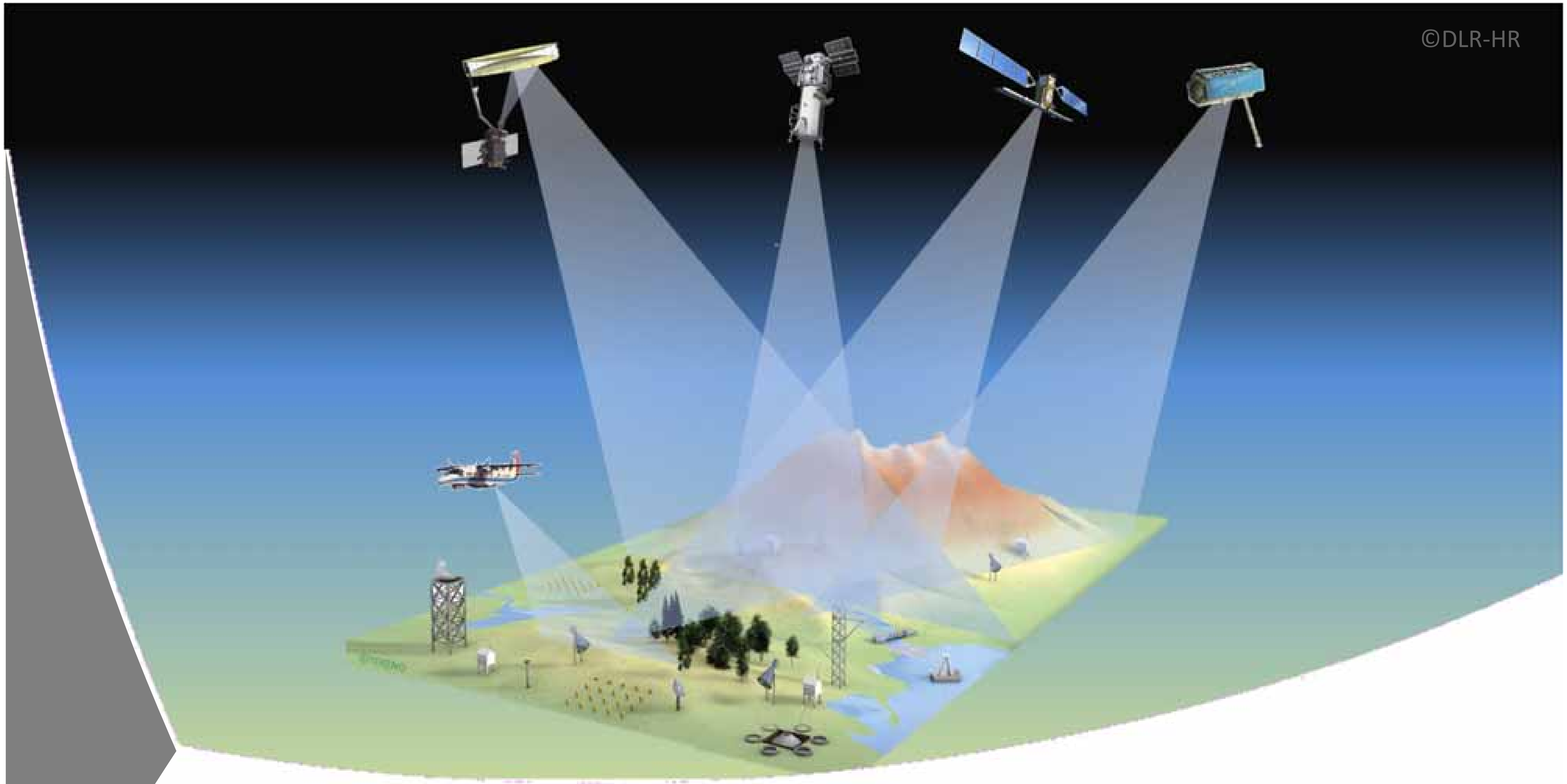

SAR Applications - Examples in SAR-EDU

Thomas Jagdhuber[1] & Entire SAR EDU Team

[1]Microwaves and Radar Institute, German Aerospace Center

Thomas.Jagdhuber@dlr.de

Overview on Content

- SAR EDU Portal at a Glance
- Overview on Radar Sensor Types
- Sentinel-1: A SAR Mapping Revolution
- Application Examples in SAR EDU
  - Ocean
  - Forest
  - Agriculture
  - Urban
  - Cryosphere

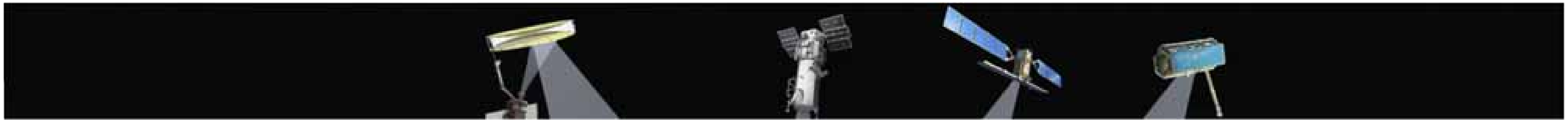

On-line SAR Education Portal "SAR EDU" (http://saredu.dlr.de)

Start Page

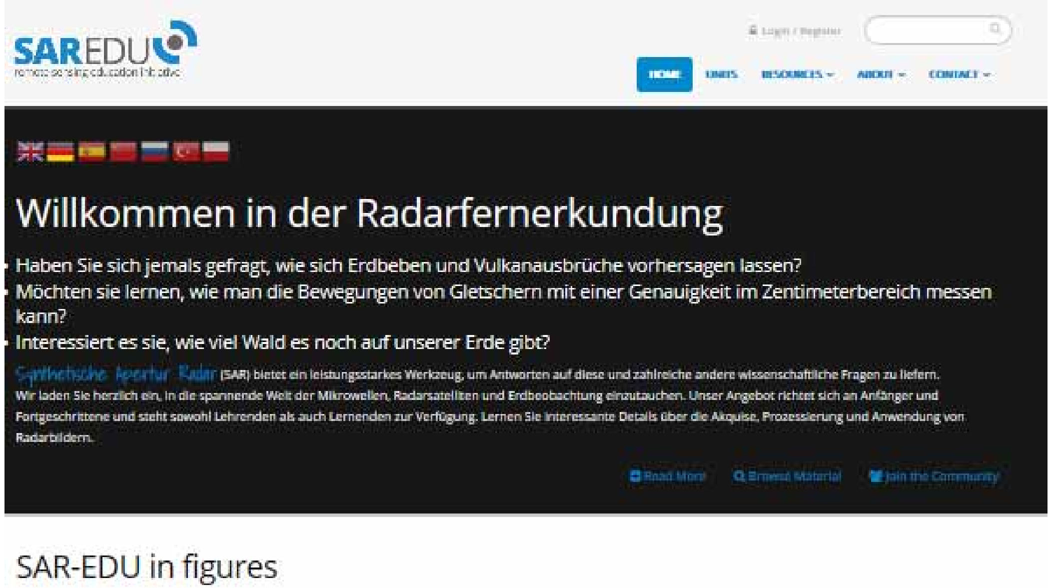

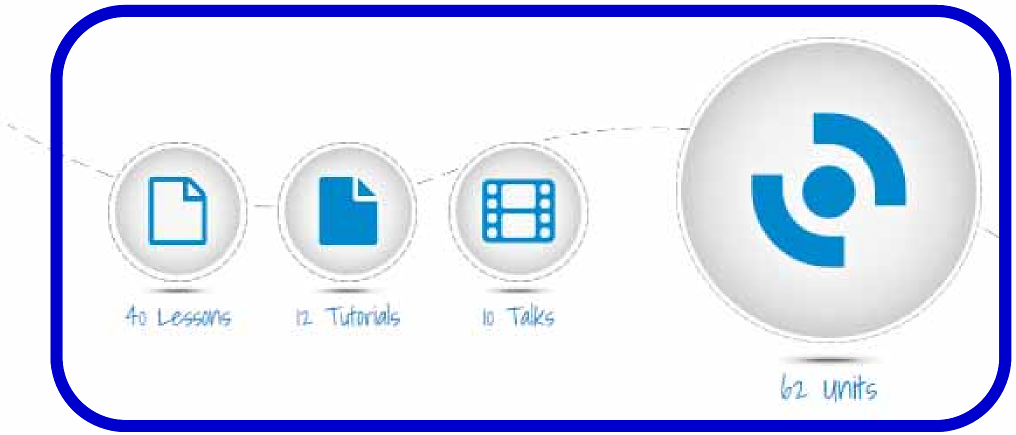

- ***Lectures***
- ***Exercises***
- ***Tutorials***
- ***Data***
- ***Talks***
- ***Discussion Forum***

SAR Remote Sensing Education Initiative

SAREDU

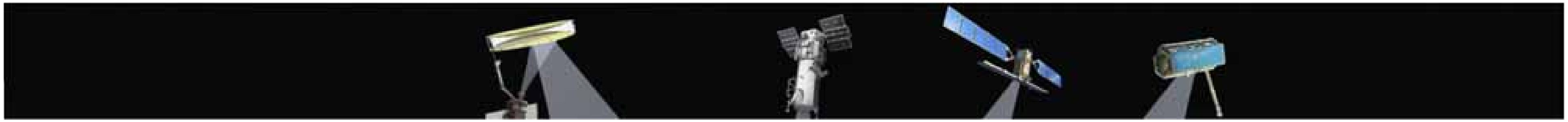

Online - Tutorial on Polarimetric SAR (PolSAR) within SAR EDU Portal (http://saredu.dlr.de)

Selection from 40 Different SAR Lessons

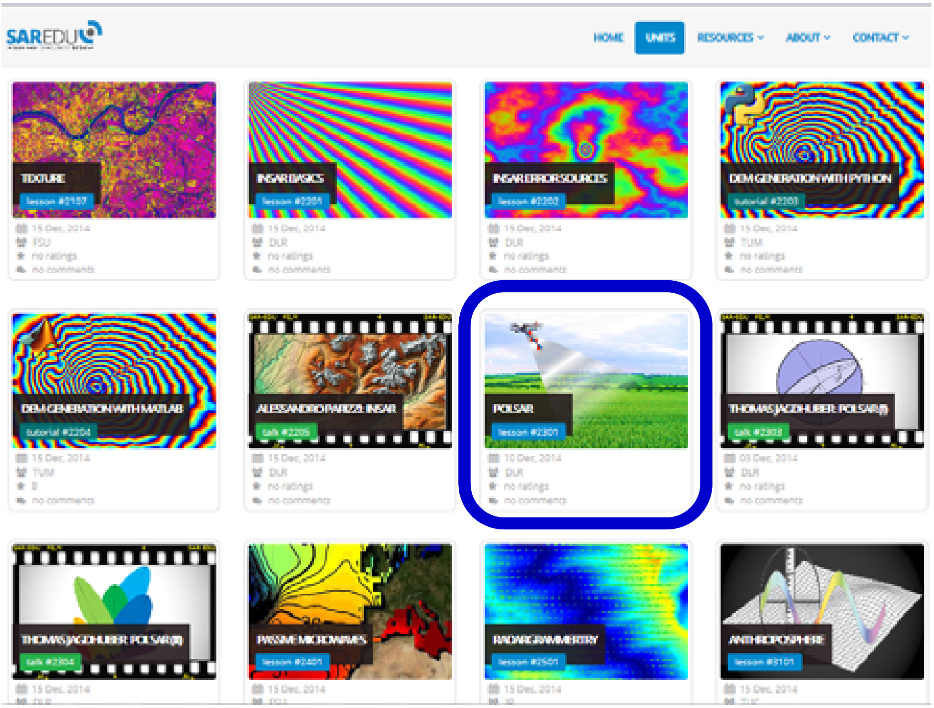

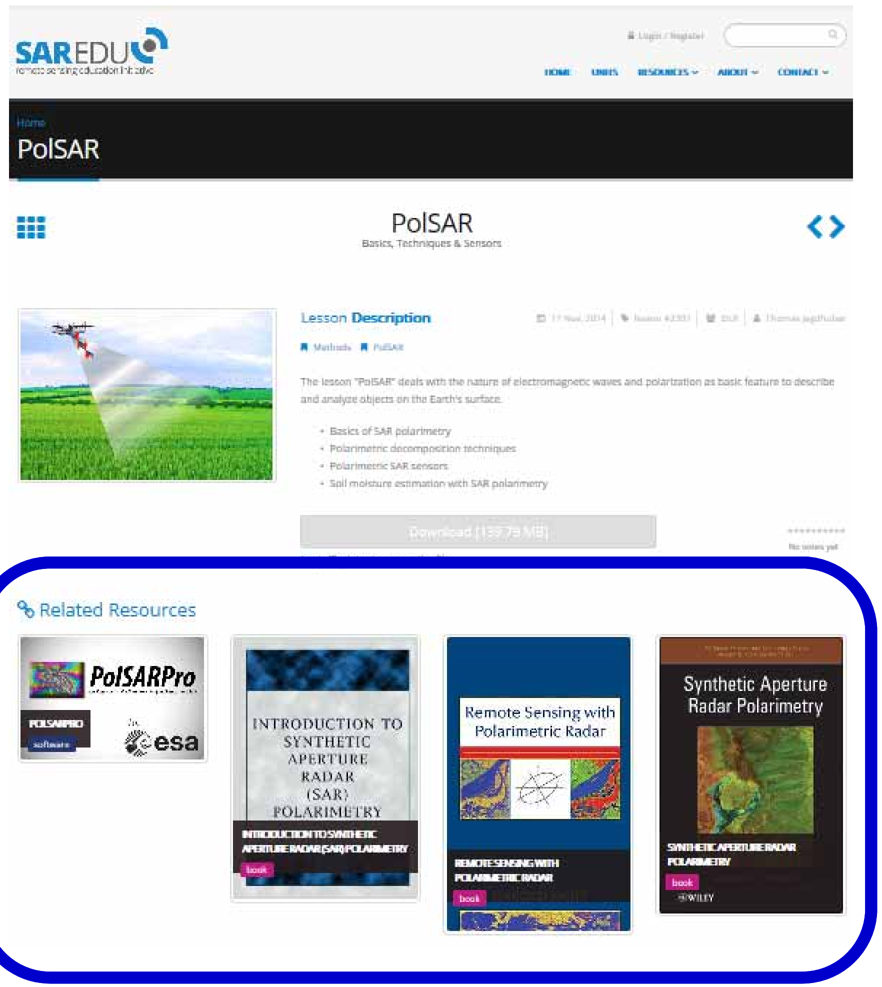

Literature & Software

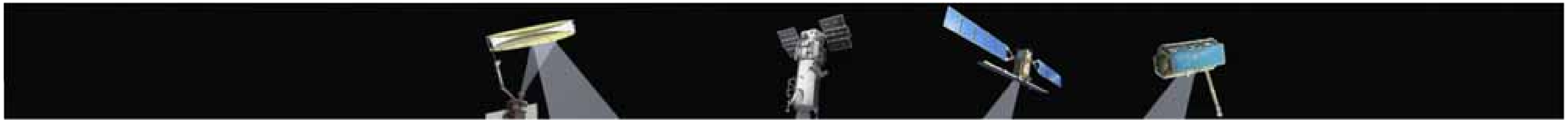

Exemplary Data and Software within SAR EDU Portal (http://saredu.dlr.de)

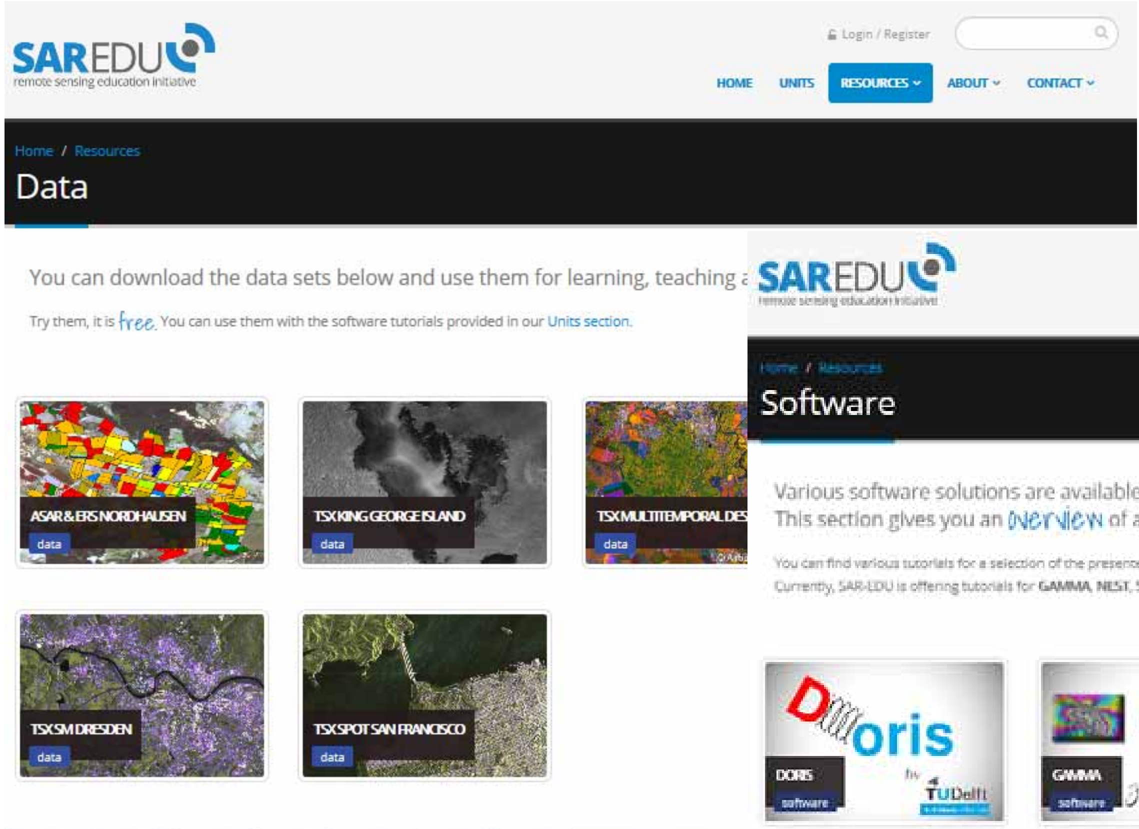

Exemplary Data Sets for Training

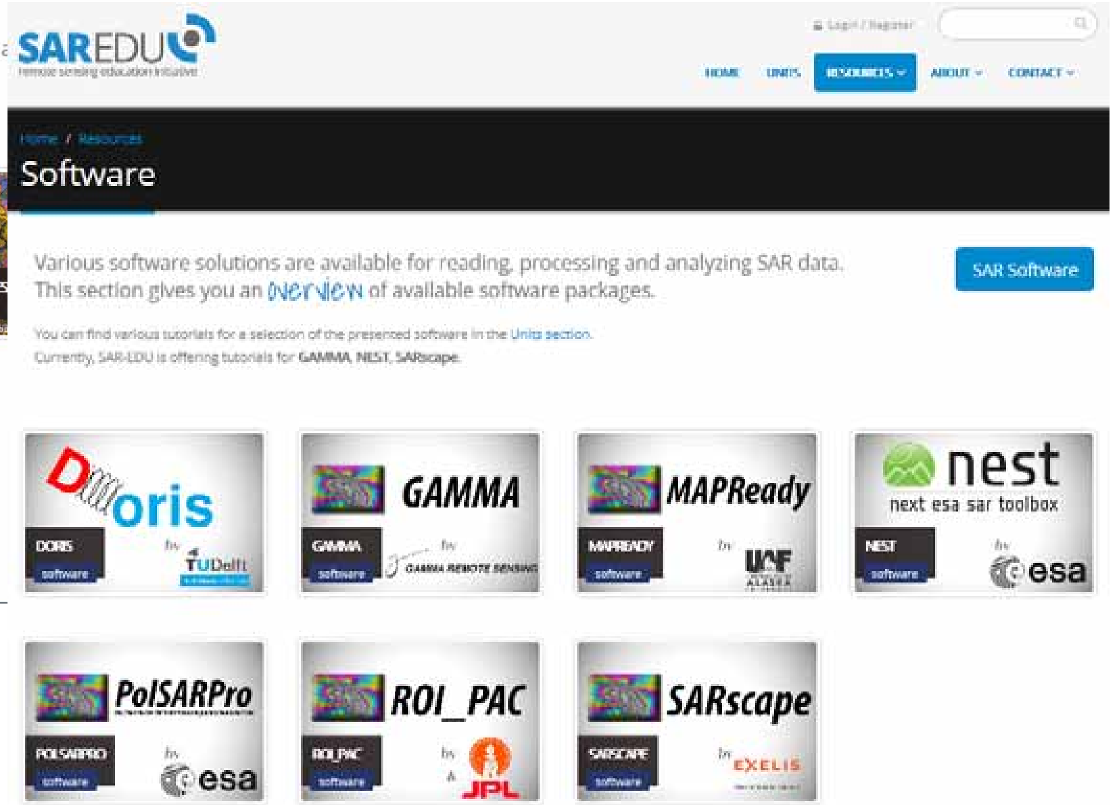

(Open-Source) Software

Remote Sensing Education Initiative

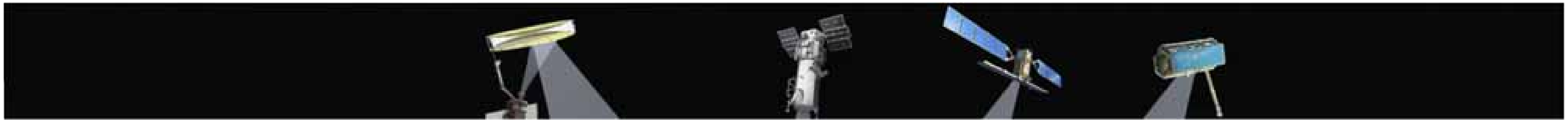

Active and Passive Radar Sensors

SAR = Synthetic Aperture Radar

RADAR = Radio Detection And Ranging

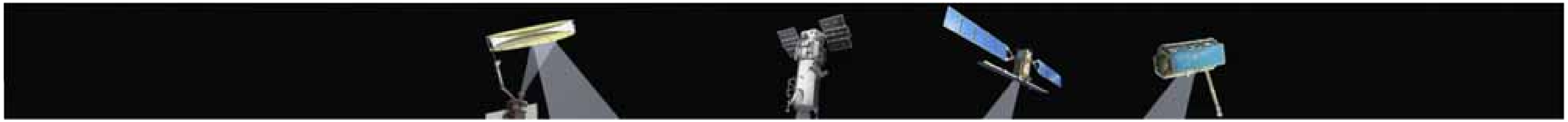

Short Review of Radar Sensors

- Four main types of spaceborne radar systems:

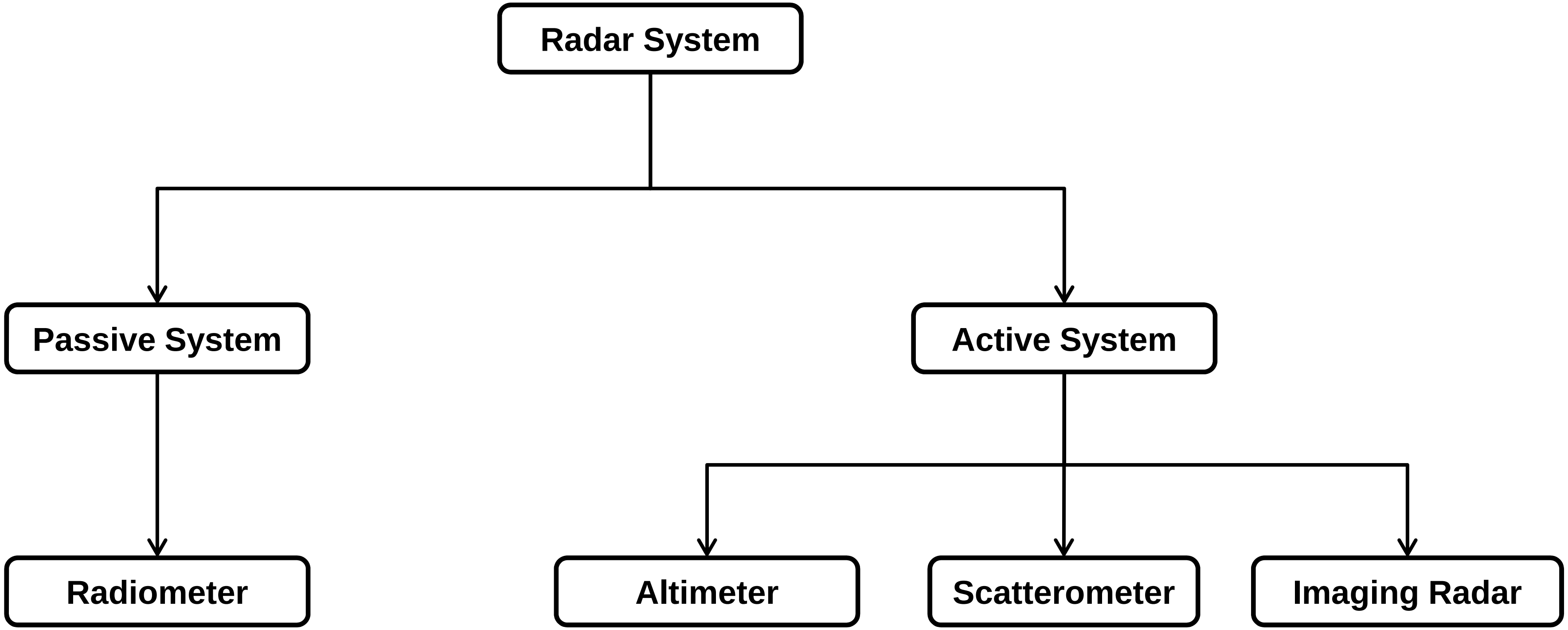

SAR Remote Sensing Education Initiative
SAREDU

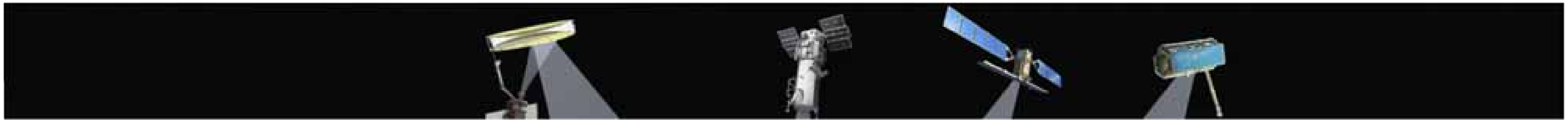

Short Review of Radar Systems

- **Radiometers**
  - Passive devices
  - Measure the self-emission of the Earth's surface in the microwave region of electromagnetic spectrum
  - Basic assumption: Increasing moisture leads to decreasing emissivity in the microwave region of the electromagnetic spectrum
- **Altimeters**
  - Active devices
  - Measures distances (calculated from signal travel time and speed of light)

SAR Remote Sensing Education Initiative

SAREDU

Short Review of Radar Systems

- **Scatterometers**
  - Active device
  - Measure the energy scattered back from the surface with high radiometric resolution
  - Low spatial resolution (25-50 km)
  - High temporal resolution (up to two measurements per day)

- **SAR**
  - Active device
  - Measure the energy scattered back from the surface with high geometric resolution
  - High spatial resolution (up to 2 m)
  - Low temporal resolution (3 [ScanSAR] -31 days)

Temporal vs. Spatial Resolution

- Temporal and spatial resolution of space-borne radar systems are interrelated
  - High spatial resolution, small swath width, low temporal resolution
  - Low spatial resolution, large swath width, high temporal resolution

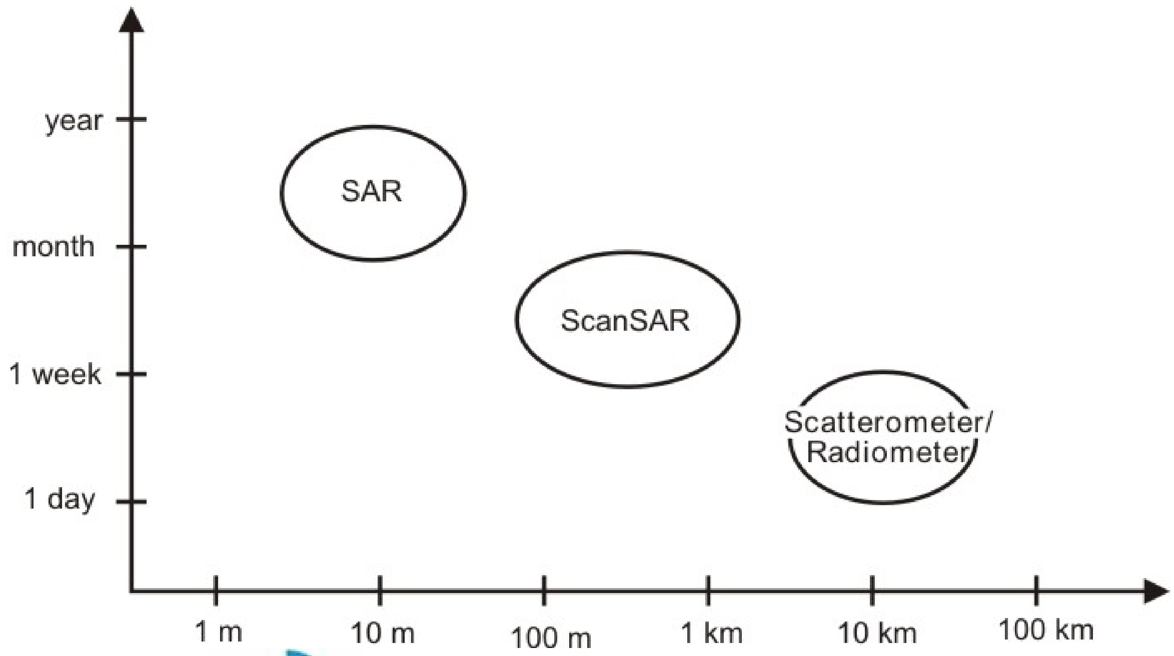

Fig.: Relation between temporal and spatial resolution (© I.P.F., Vienna University of Technology, 2012)

SAR Remote Sensing Education Initiative

SAREDU

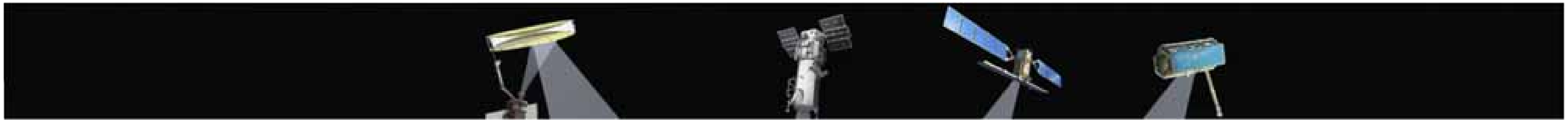

Short Review of Radar Sensors

- Four main types of spaceborne radar systems:

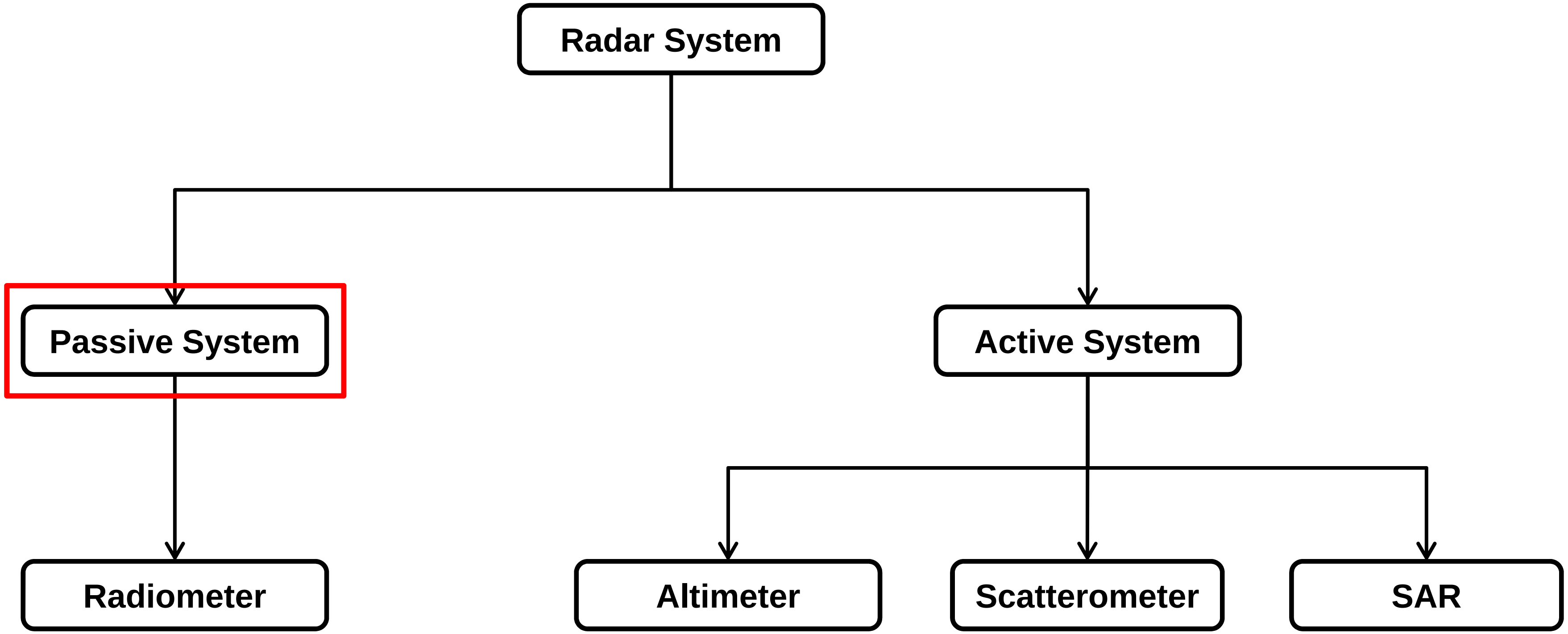

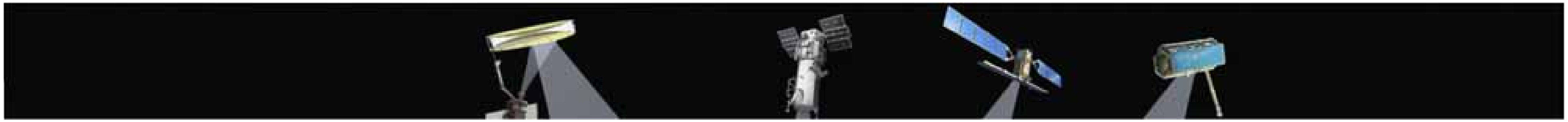

Source Components of Passive Microwave Signals

1. Emitted component of the atmosphere
2. Emitted component (depending on the surface temperature of the object)
3. Surface-reflected component
4. Transmitted component (from subsurface)

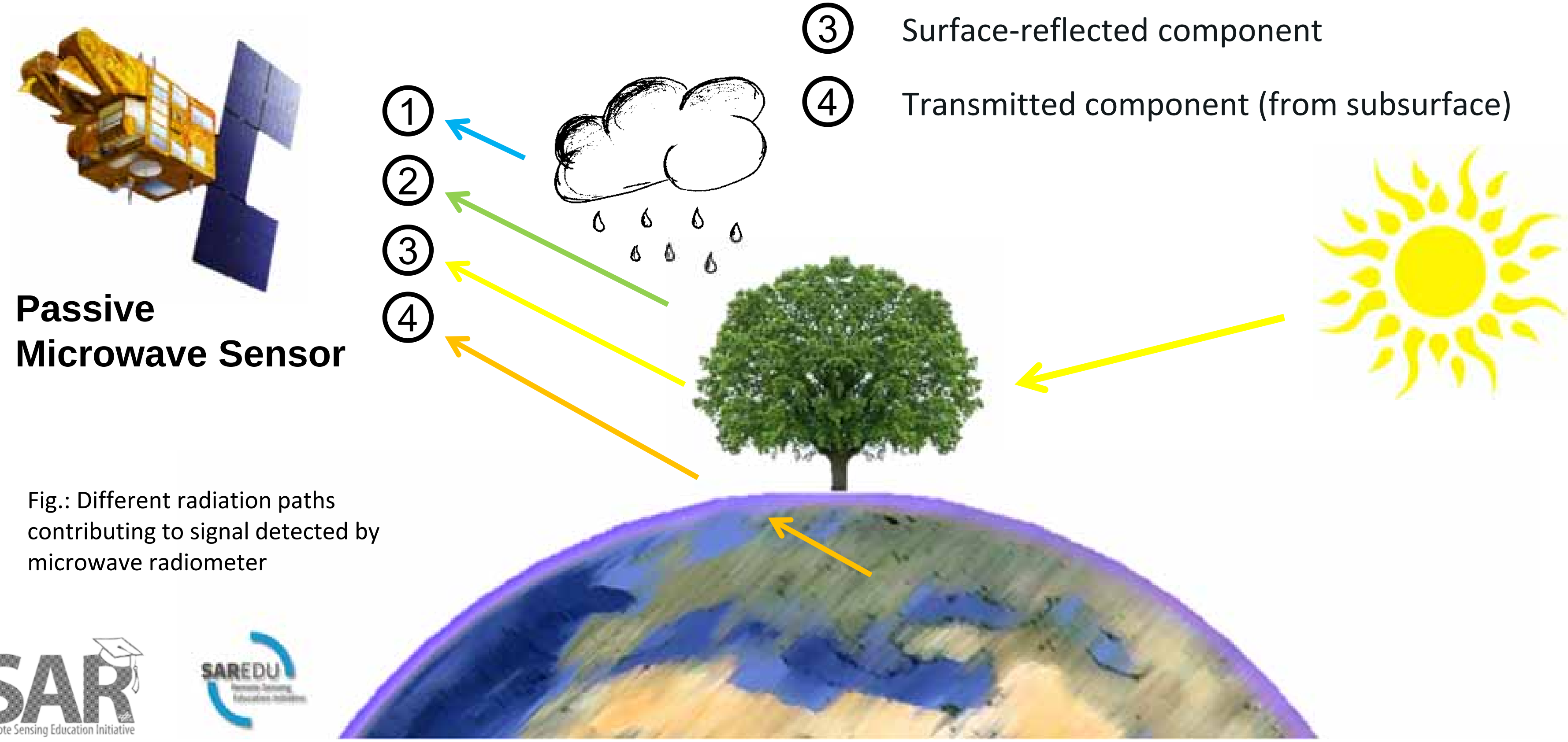

Fig.: Different radiation paths contributing to signal detected by microwave radiometer

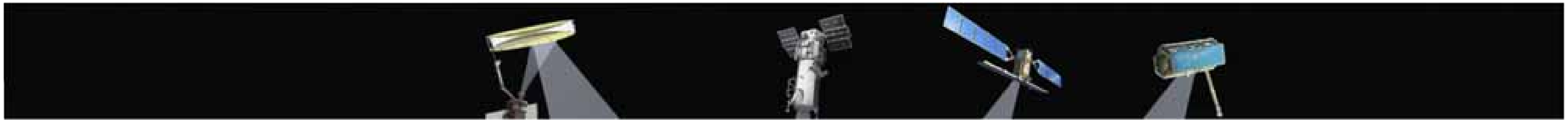

SMOS – Soil Moisture and Ocean Salinity Mission

- Web: http://www.esa.int/esaLP/LPsmos.html
- ESA Earth Explorer mission
- Launched in 2009
- Objectives:
  - **Monitoring of soil moisture and ocean salinity**
- Sensor:
  - Passive interferometric L-band radiometer (λ = 21 cm), receives signals in V and H polarization at incidence angles from 20° - 60°
  - Spatial resolution: 35-50 km
  - Temporal resolution: 3 days

Fig.: SMOS in orbit (artist's view)
(© ESA Multi-media gallery, 2012)

SAR Remote Sensing Education Initiative

SAREDU

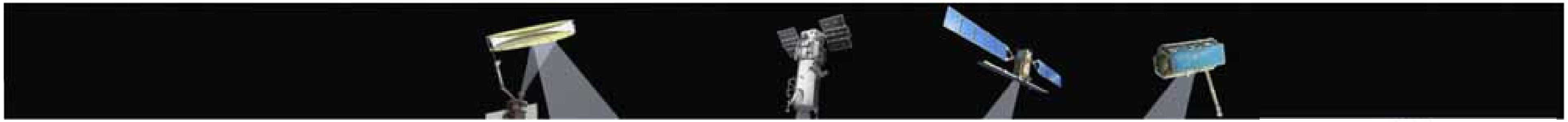

Source Components of Active Microwave Signals

① Scattered component of the atmosphere

② Scattered component (depending on the surface geometry and dielectric content of the object)

③ Surface-reflected component

④ Reflected component (from subsurface)

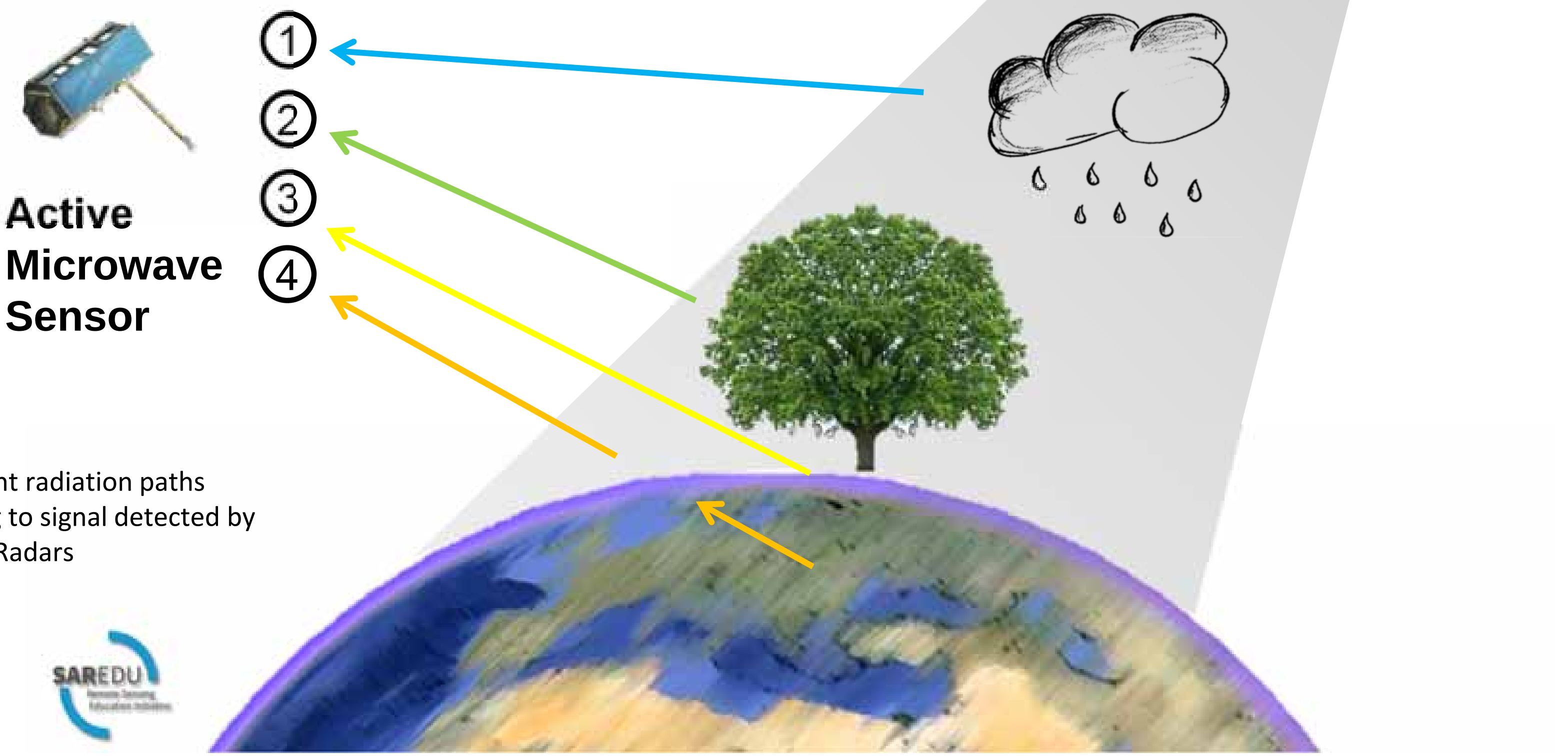

Fig.: Different radiation paths contributing to signal detected by microwave Radars

SAR Remote Sensing Education Initiative
SAREDU

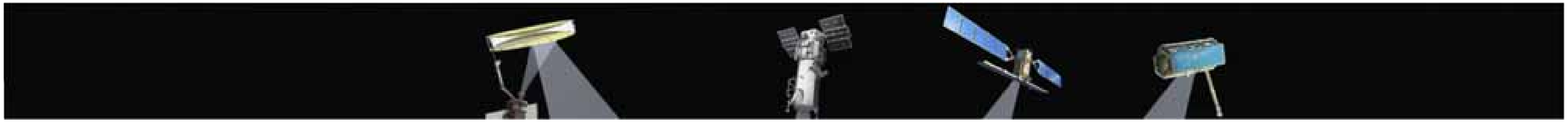

Short review of radar sensors

- Four main types of spaceborne radar systems:

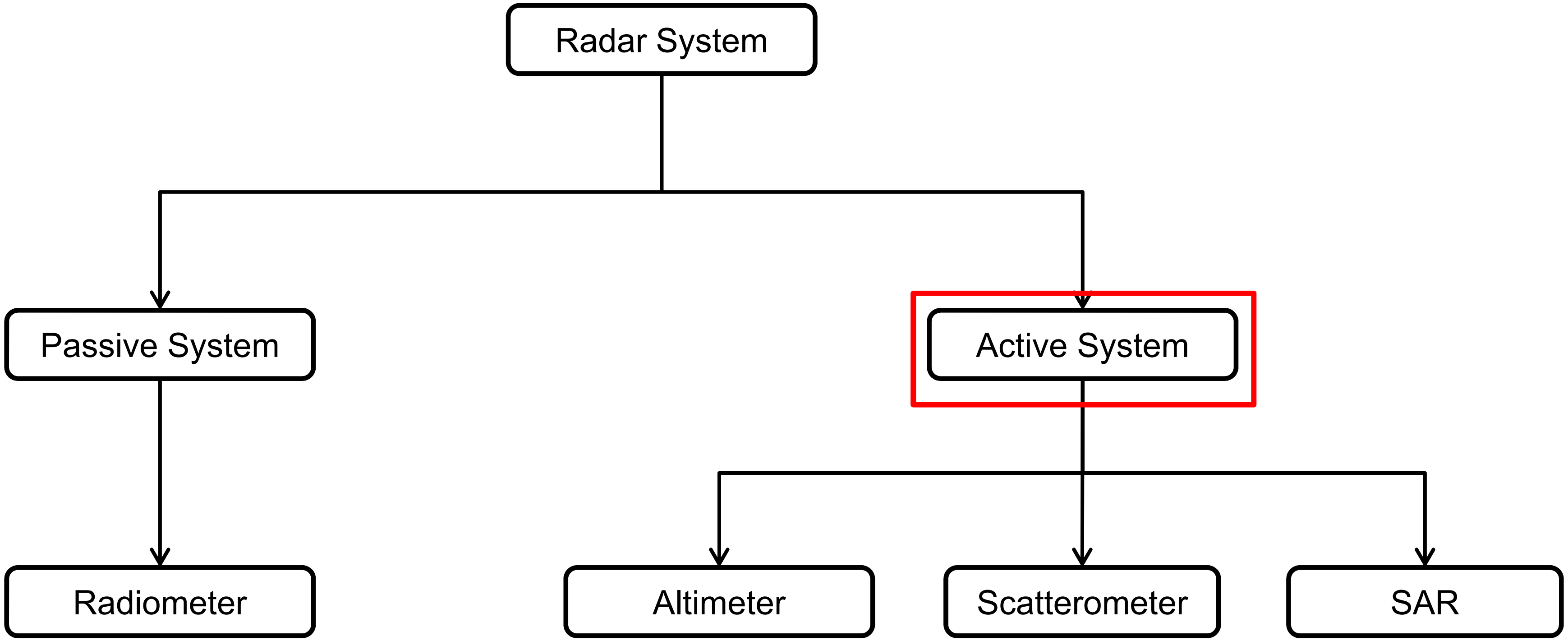

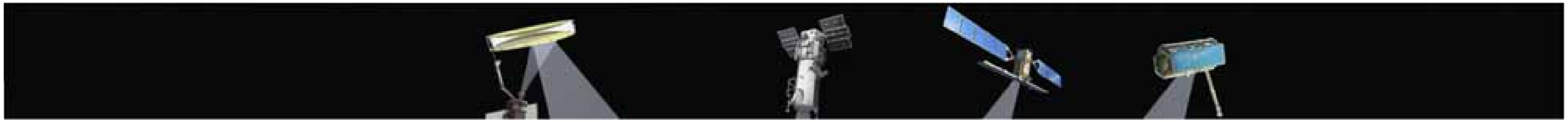

ERS-1/2 Altimeter

Fig.: Radar altimeter on ERS (© ESA, 2012)

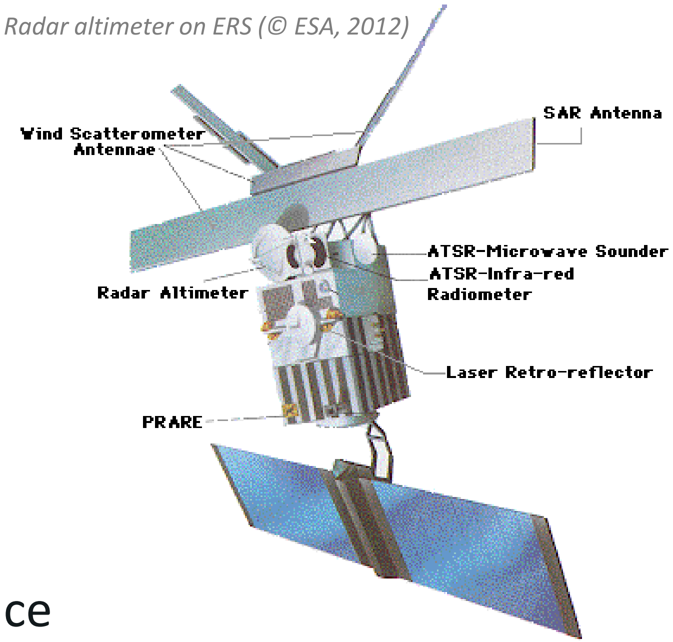

- Web: https://earth.esa.int/web/guest/missions/esa-operational-eo-missions/ers/instruments/ra
- Launched in 1991 (ERS-1) and 1995 (ERS-2)
- Objectives:
  - Oceanography (meso-scale topography, variability, sea level trends)
  - Ice/sea ice (occurrence, trends, thickness of ice shields)

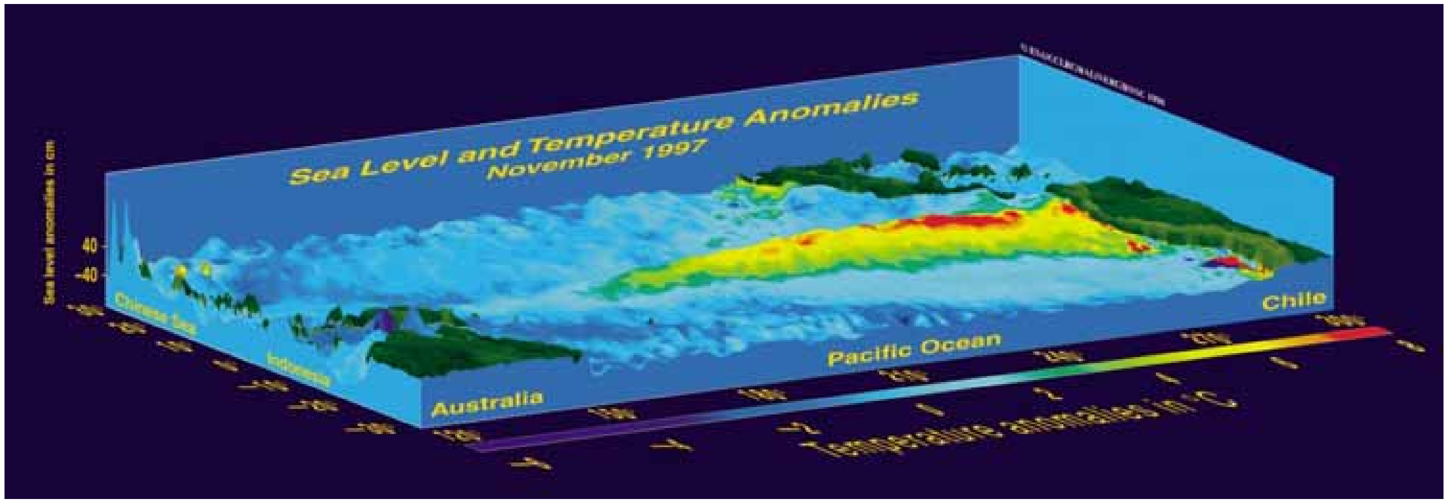

Fig.: Three-dimensional representation of the fully developed 1997 El Niño (© ESA Multi-media gallery, 2012)

MetOp ASCAT (Advanced Scatterometer)

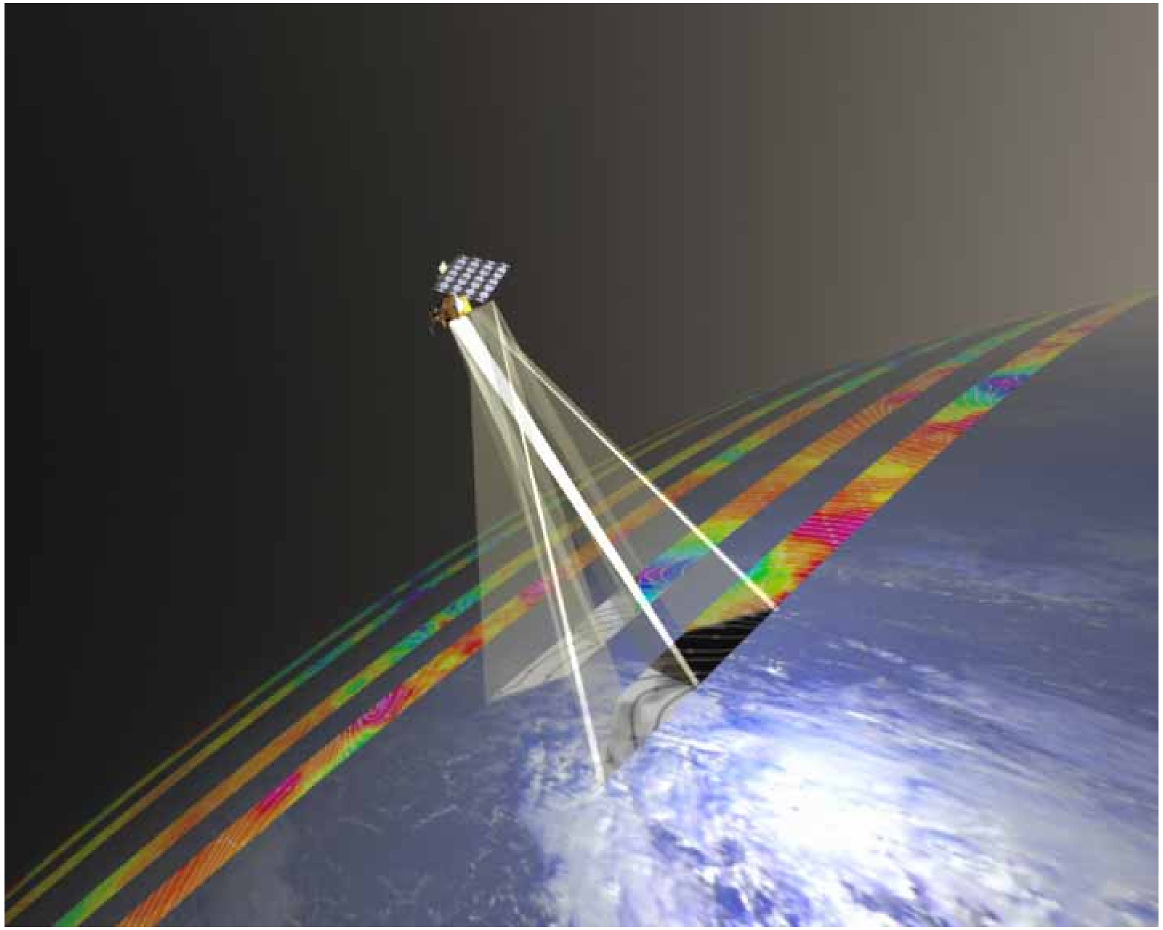

Fig.: Illustration of ASCAT achieving near global coverage in five days with a repeat cycle of 29 days (© ESA Multi-media gallery, 2012)


Sentinel-1
esa
P.CARRIL 2007

Sentinel-1

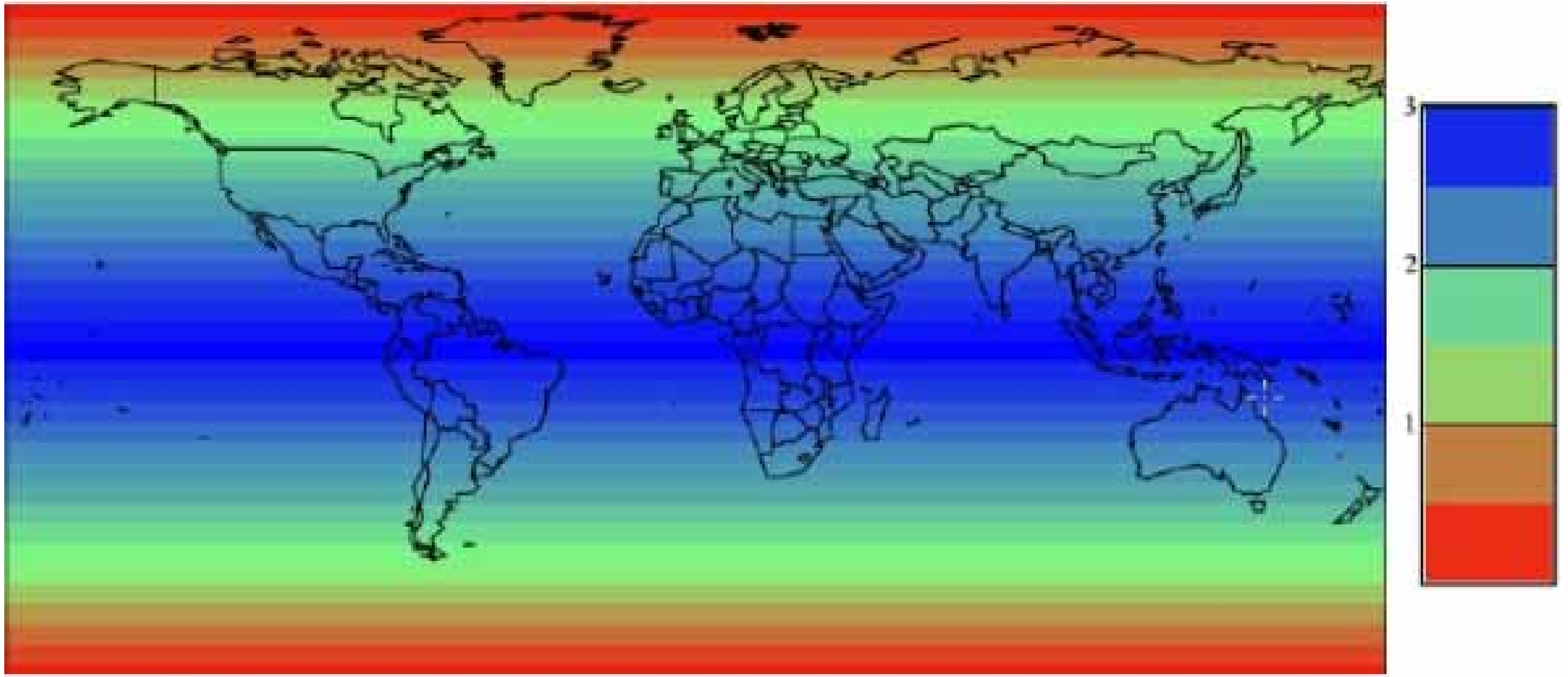

- ✓ Two satellites in a 12 day orbit
- ✓ Repeat frequency: 6 days (important for coherence)
- ✓ Revisit frequency: (asc/desc & overlap): 3 days at the equator, <1 day at high latitudes (Europe ~ 2 days)

Sentinel-1

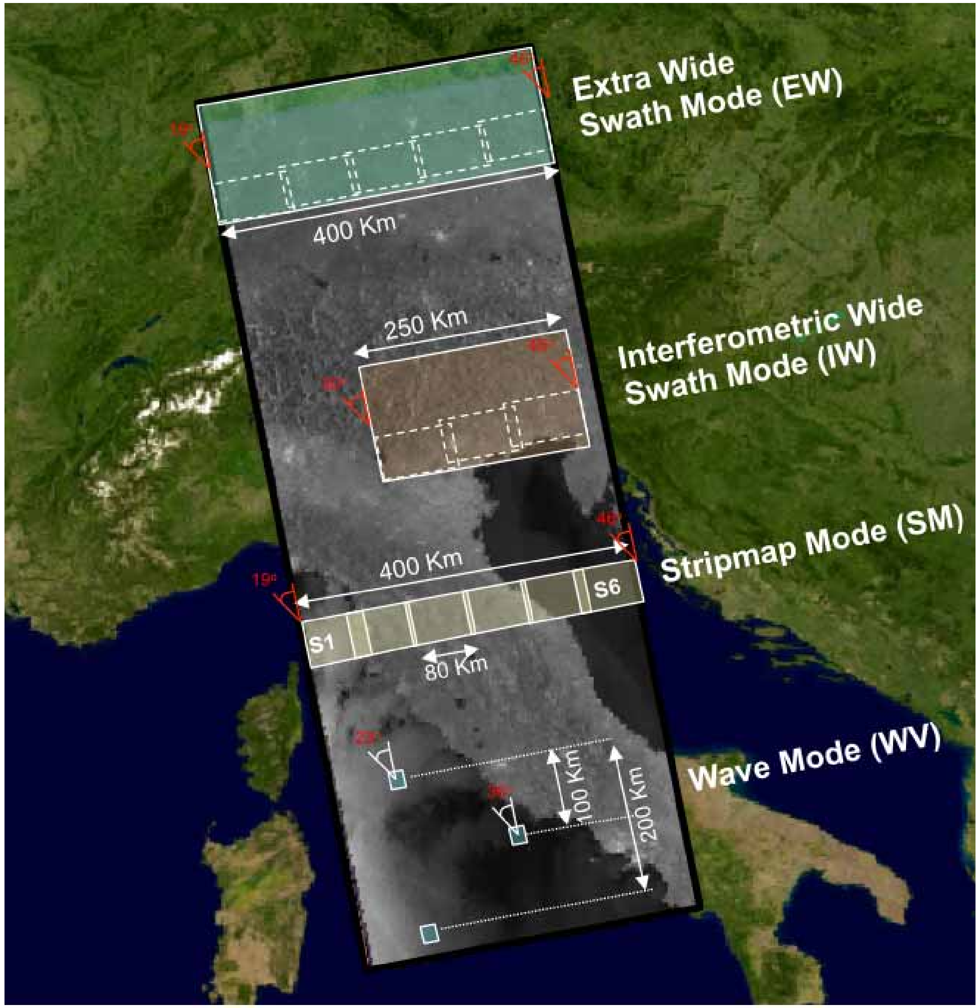

Acquisition Modes

Extra wide-swath mode (HH+HV,VV+VH)
400 km and 20×40 m resolution

Interferometric wide-swath (HH+HV,VV+VH)
250 km and 5×20 m resolution

Strip map mode (HH+HV,VV+VH)
80 km swath and 5×5 m resolution

Wave-mode images (HH, VV)
20×20 km and 5×5 m resolution (at 100 km intervals)

Sentinel-1

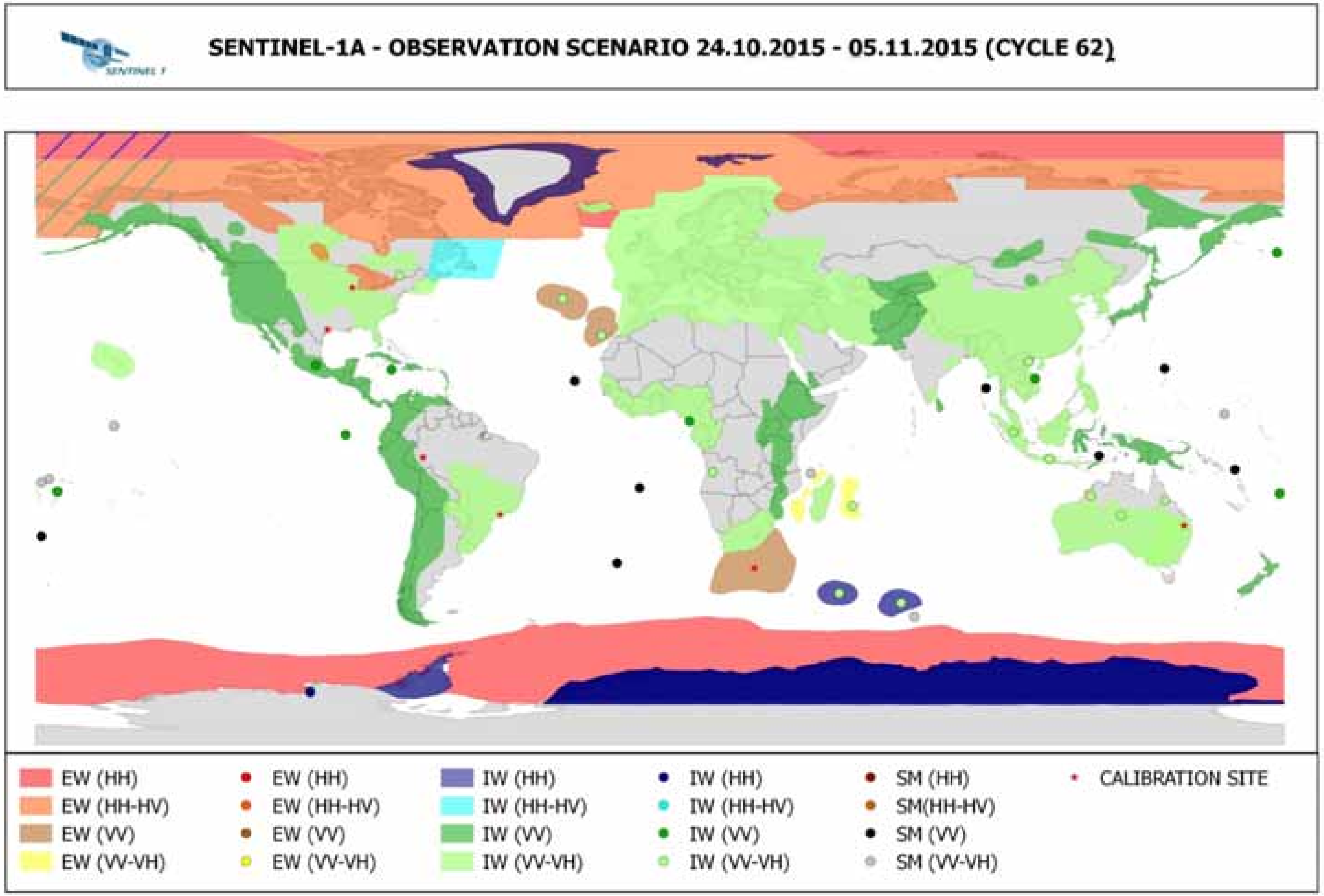
SENTINEL-1A - OBSERVATION SCENARIO 24.10.2015 - 05.11.2015 (CYCLE 62)
EW (HH)
EW (HH-HV)
EW (VV)
EW (VV-VH)
EW (HH)
EW (HH-HV)
EW (VV)
EW (VV-VH)
IW (HH)
IW (HH-HV)
IW (VV)
IW (VV-VH)
IW (HH)
IW (HH-HV)
IW (VV)
IW (VV-VH)
SM (HH)
SM(HH-HV)
SM (VV)
SM (VV-VH)
CALIBRATION SITE

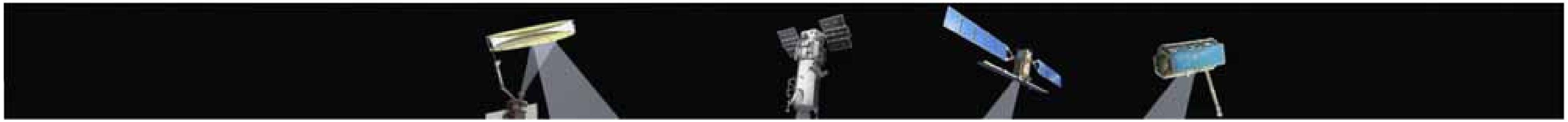

Short Review of Radar Sensors

- Four main types of spaceborne radar systems:

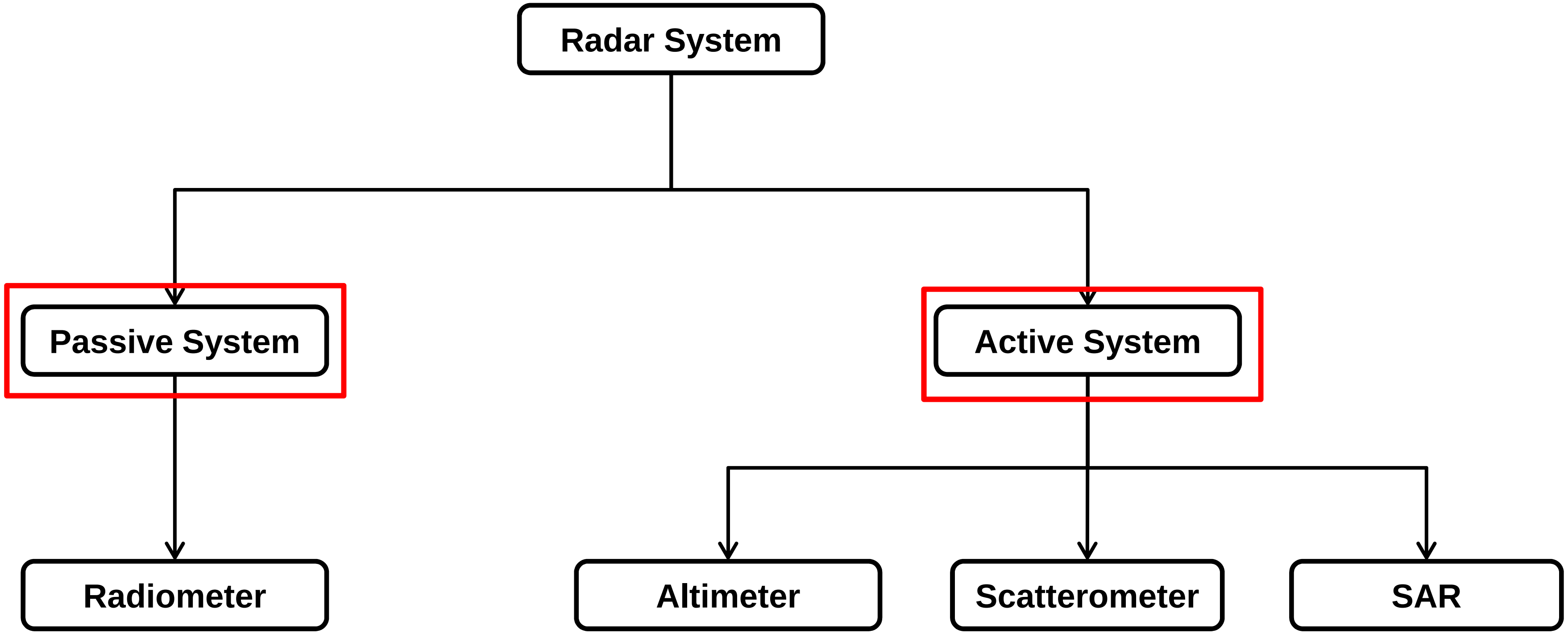

SAR Remote Sensing Education Initiative
SAREDU

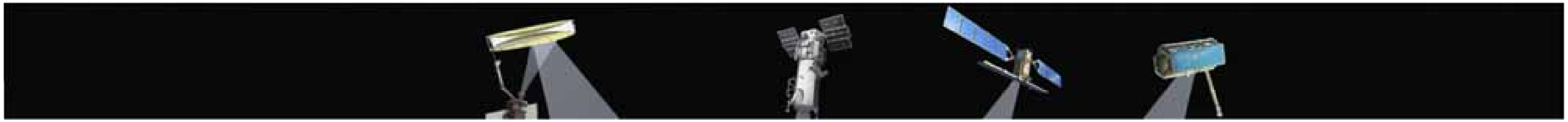

SMAP – Soil Moisture Active Passive

- Web: http://smap.jpl.nasa.gov/
- NASA Science mission
- Launched in January 31st 2015
- Objectives:
  - Soil moisture
  - Freeze-thaw state of land surface
  - Improve net carbon flux estimation in boreal landscapes
  - Improve drought/flood prediction

Fig.: SMAP Spacecraft. 3D rendering of the SMAP Spacecraft (© NASA's Earth Observatory, 2012)

SAR Remote Sensing Education Initiative

SAREDU

SAR Applications for Oceanography

Dr. Susanne Lehner, Dr. Andrey Pleskachevsky
Dr. Xiao-Ming Li, Dr. Stephan Brusch
Miguel Bruck, Domenico Velotto

German Aerospace Center (DLR)
Remote Sensing Technology Institute
SAR Signal Processing

DLR

TECHNISCHE UNIVERSITÄT MÜNCHEN

SAREDU Remote Sensing Education Initiative

Processes and Objects in Oceans Observed by SAR

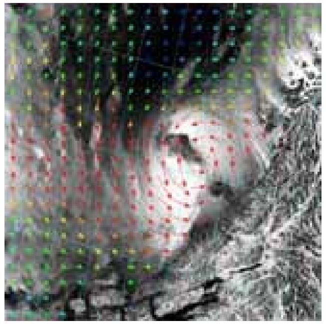

Wind

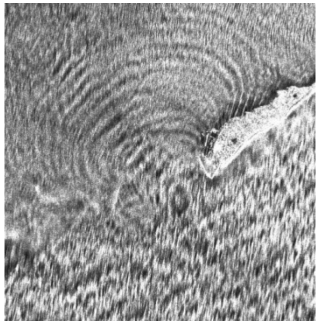

Sea State

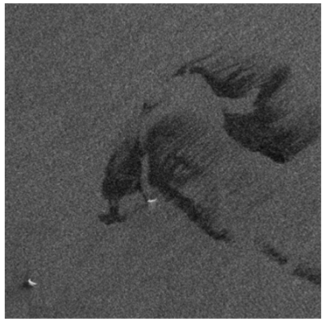

Oil

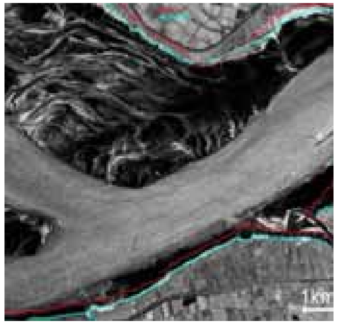

Land-Water Line

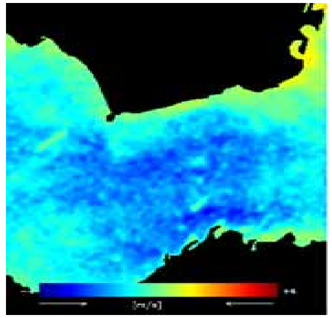

Surface Currents

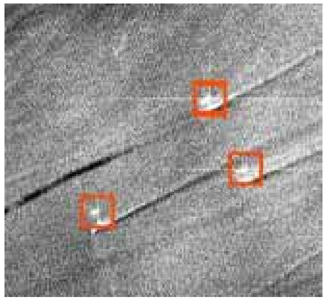

Ships

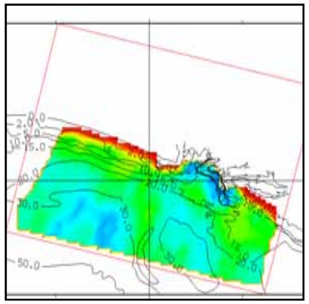

Bathymetry
by Wave Refraction

Wave Breaking

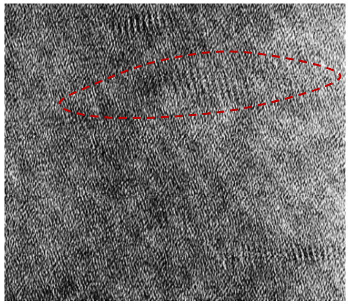

Wave Groups

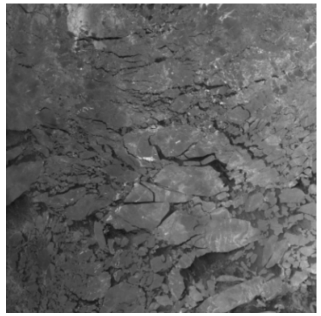

Ice and Icebergs

Fig. 1: Examples of processes observed by SAR at ocean surface (© DLR)

ERS

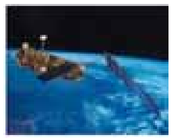

ENVISAT

TerraSAR-X

Remote sensing helps improving forecast systems

wave height in Atlantic : forecast wave model results from DWD (German Weather Services)

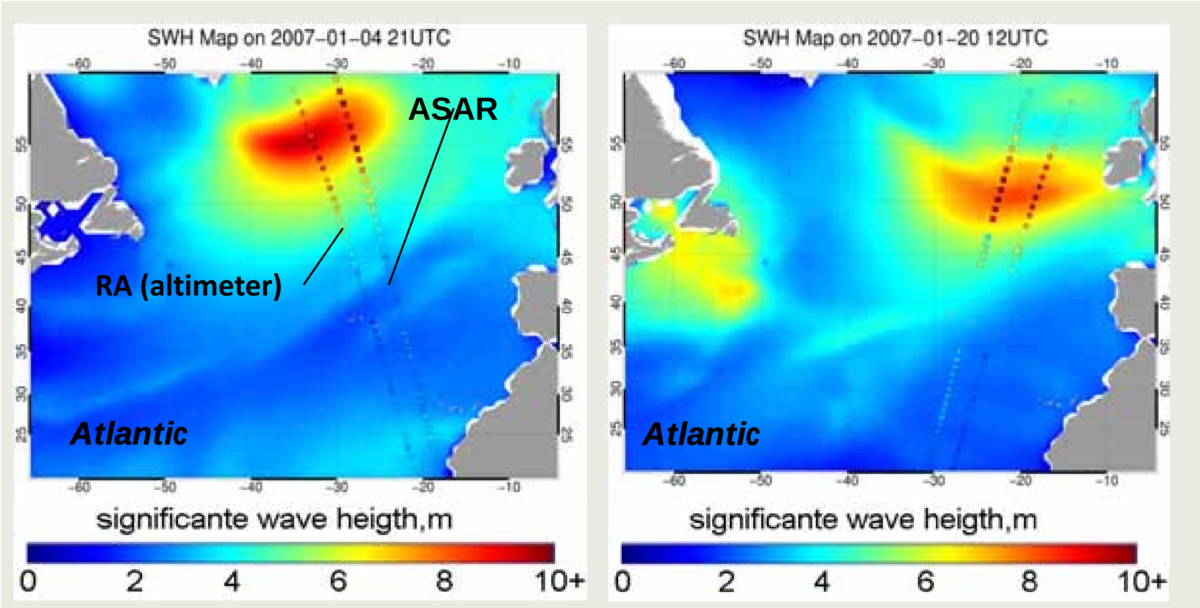

ASAR images covering 6/10km×5km acquired along the orbit every 100 km.

Fig. 2: Sea state from satellites over storms in North-Atlantic and DWD model forecasting:
two independent measurements on board ENVISAT show storm peak underestimation by wave model (© DLR, Li)

Comparison of SAR sensors for maritime applications

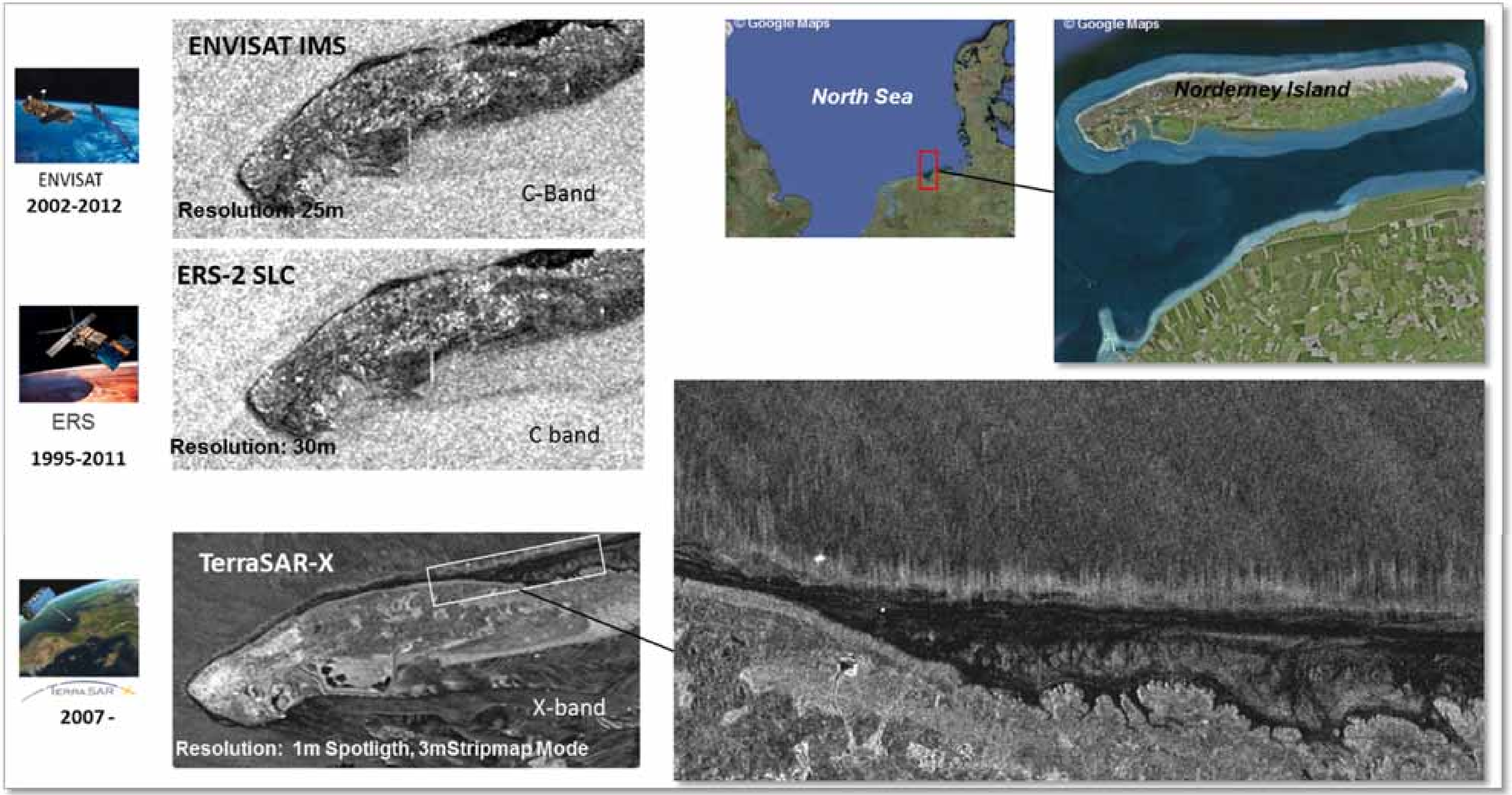

Fig. 3: Comparison of SAR sensors for coastal maritime applications (© DLR). Resolution of TS-X allows to see individual waves up to 20m wavelength and to observe details of coastal processes like wave breaking

Wind, Waves and Currents in TerraSAR-X SAR Images

TerraSAR-X
TanDEM-X

2007 -

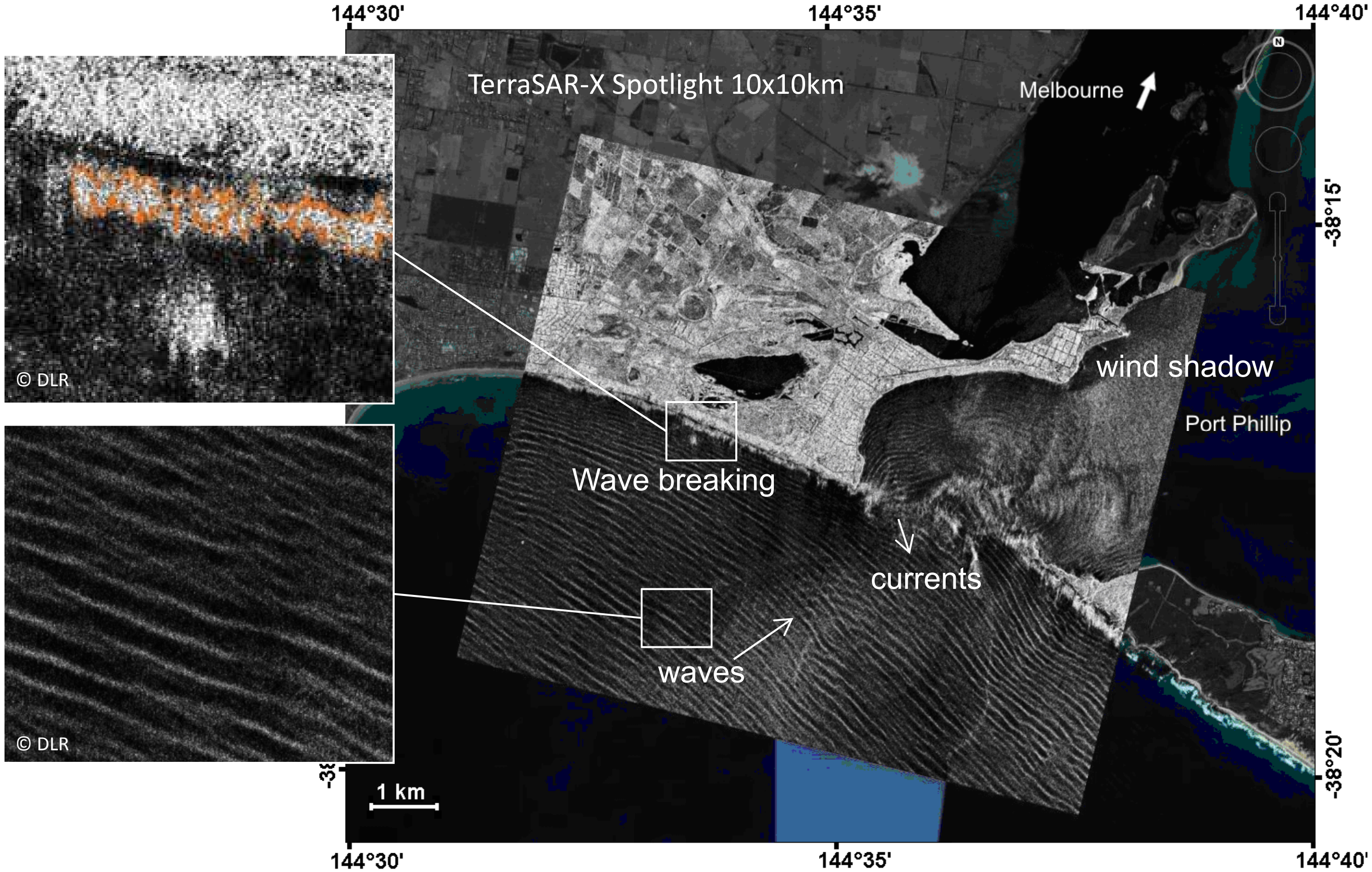

Fig. 4: Wind, waves and currents in TerraSAR-X SAR images (Brusch et al., 2011)

SAREDU

TerraSAR-X example for coastal application

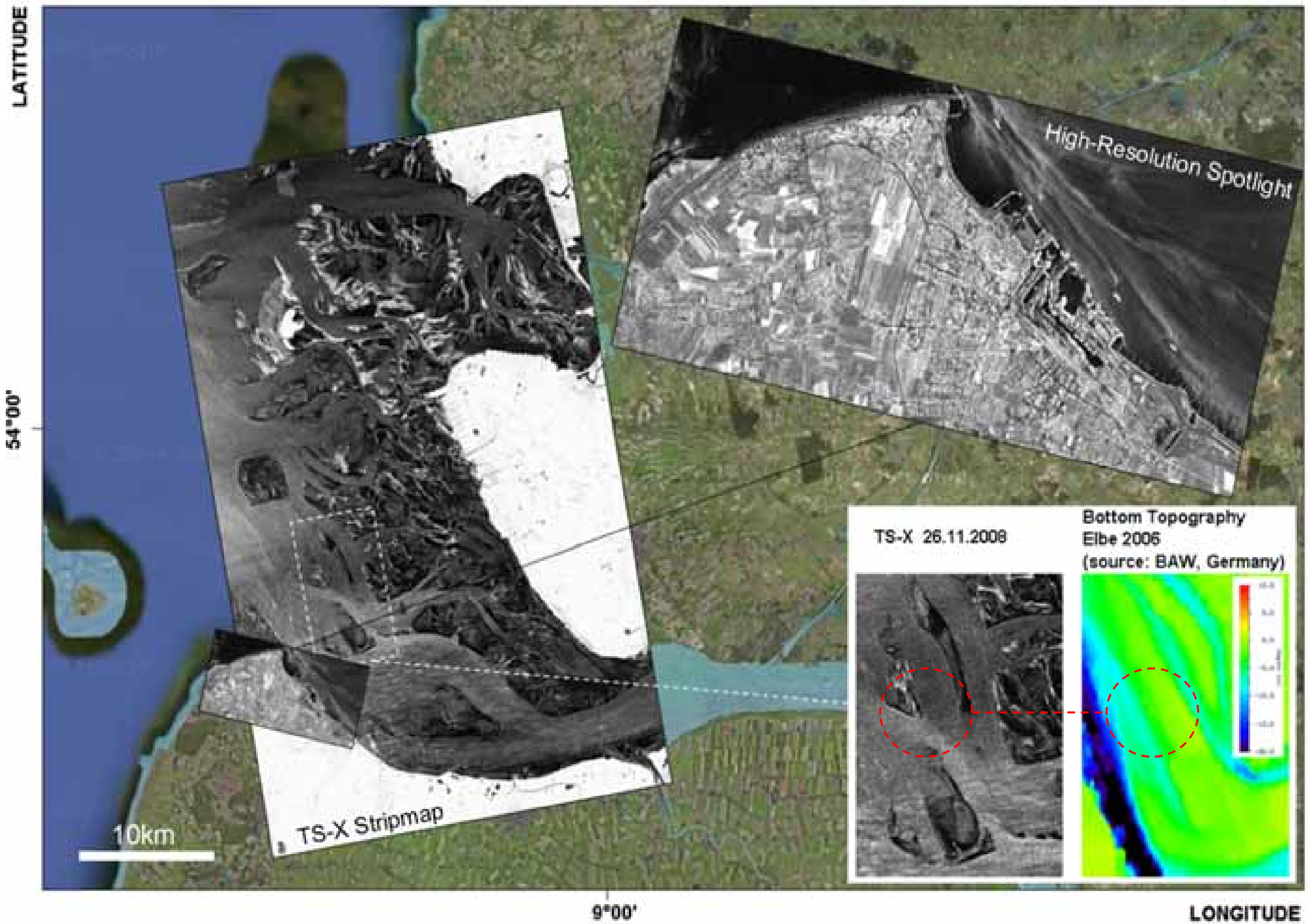

TerraSAR-X
TanDEM-X

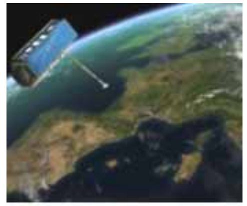

2007 -

Fig. 5: TerraSAR-X scenes acquired over Elbe Estuary, German Bight, North Sea (background image © Google Maps): Stripmap scene acquired on November 26, 2008, at 17:10 and depicts the change of bathymetry in the estuary in comparison to bathymetry processed by BAW (German Federal Waterways Engineering and Research Institute) in 2006. As the TS-X image shows, a long sandbank was partially eroded in the centre and split by a tidal inlet (Lehner et al., 2012).

Imaging of long ocean surface waves by TerraSAR-X: different modes

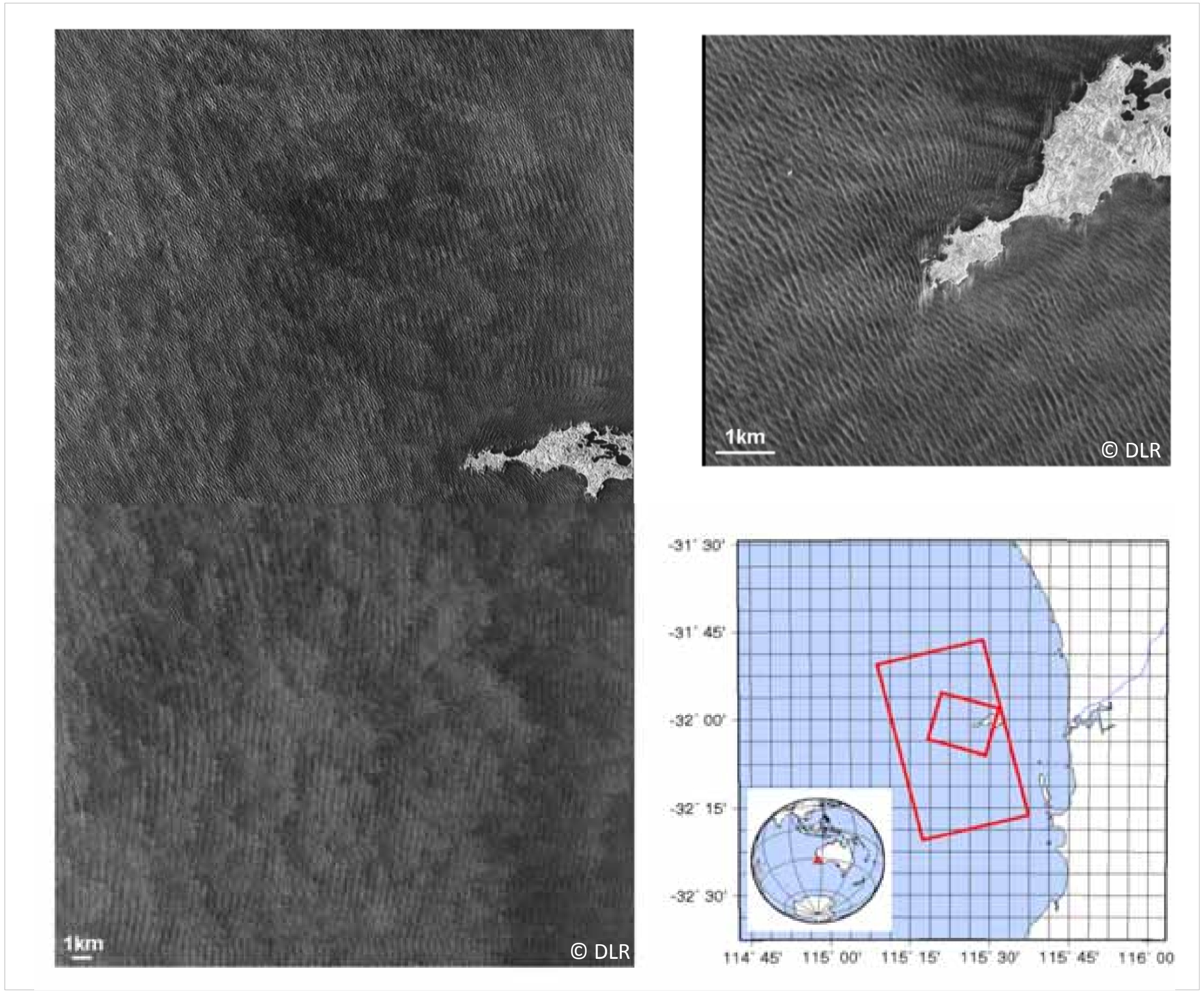

TerraSAR-X Spotlight and StripMap modes for sea state assessment

Fig. 45: Different modes of TerraSAR-X images acquired over Rottenest Island: VV polarized Stripmap on September 23, 2009 at 10:53 UTC (left) and Spotlight on October 20, 2009 at 21:36 UTC (right). (Pleskachevsky et al., 2011)

SAREDU Remote Sensing Education Initiative

Effect of achieved resolution by TerraSAR-X

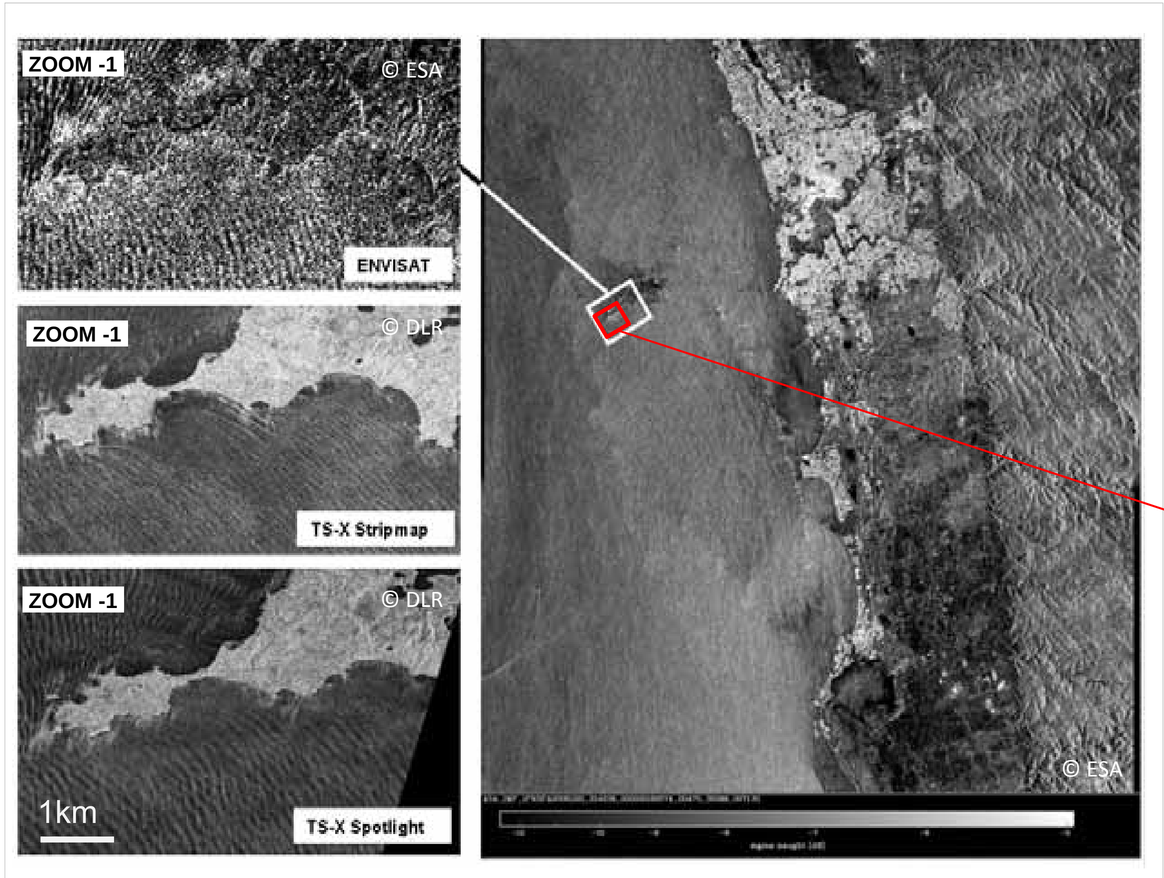

Fig. 46: ENVISAT ASAR image from December 21, 2008 acquired over Rottenest Island (right). TerraSAR-X Stripmap and Spotlight images sub-scenes (left) (Pleskachevsky et al., 2011)

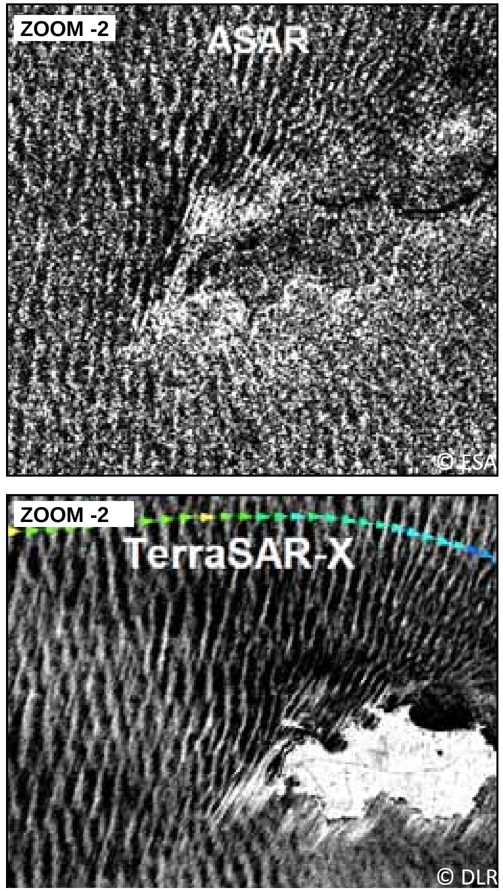

Rottenest-Island, ASAR (resolution~25m, image pixel size 12m) and TerraSAR-X Spotlight (resolution~2m, image pixel size 0.75m): Although the waves are detectable in ASAR images, extraction of wavelength <200m and obtaining refraction is not possible.

SAREDU Remote Sensing Education Initiative

Sea state measurements examples using TerraSAR-X

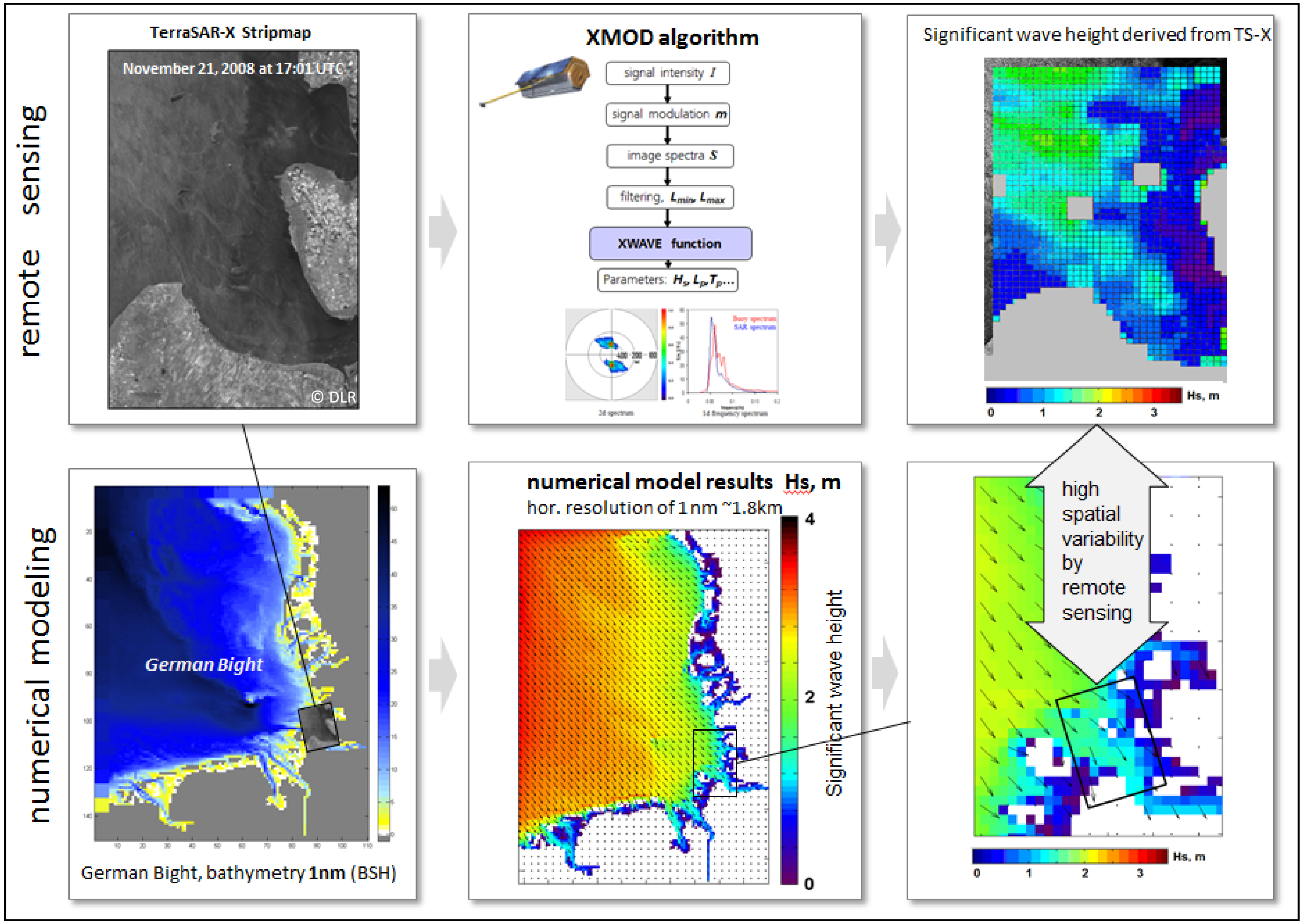

Fig. 56: XMOD example for the North Sea - November 21, 2008 at 17:01 UTC near Elbe Estuary and significant wave height field in comparison to results of wave model with resolution of 1nm (© DLR, Pleskachevsky)

SAREDU

Surface Wind

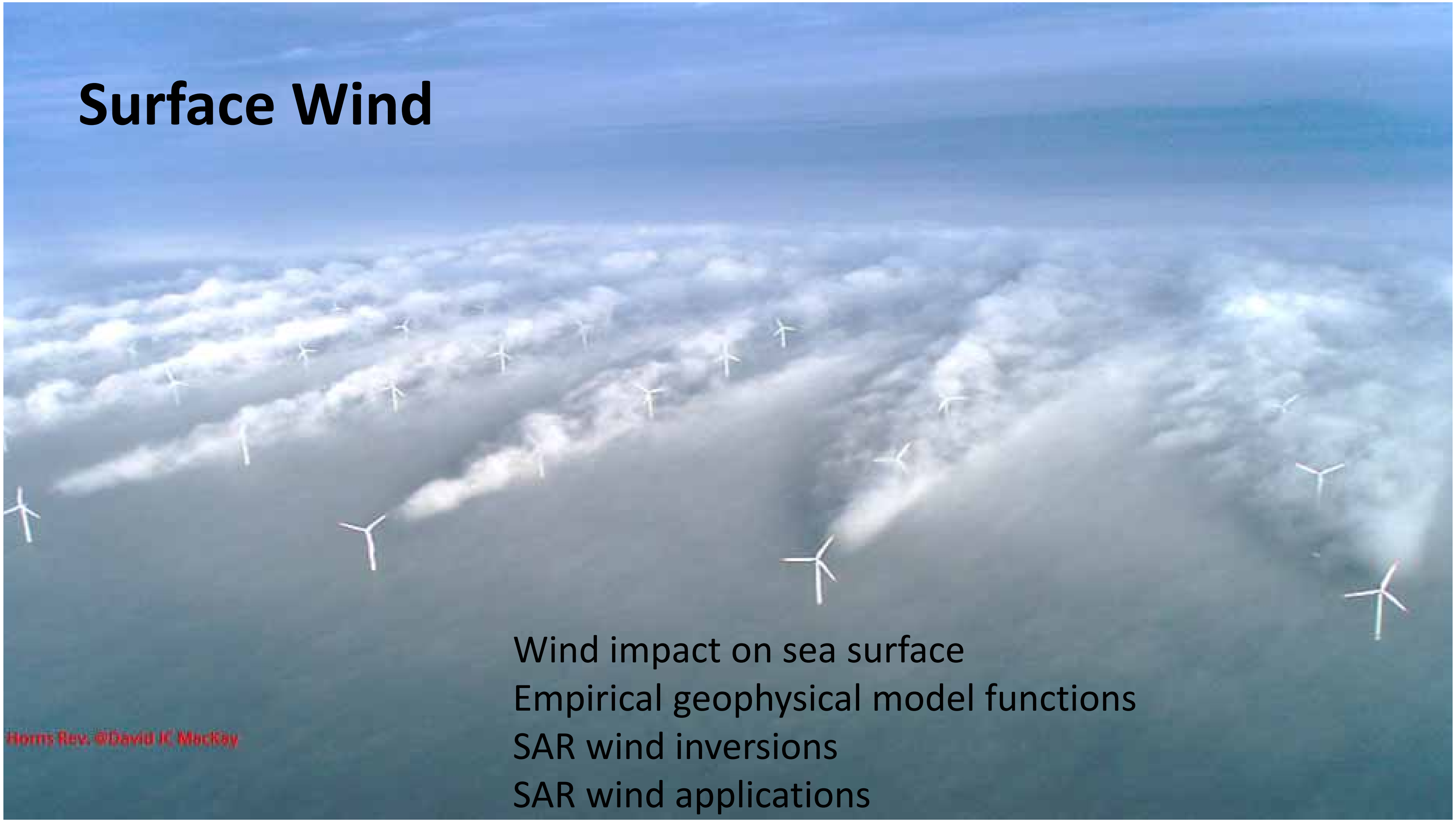

Wind impact on sea surface
Empirical geophysical model functions
SAR wind inversions
SAR wind applications

Applications of SAR Winds : different SAR sensors

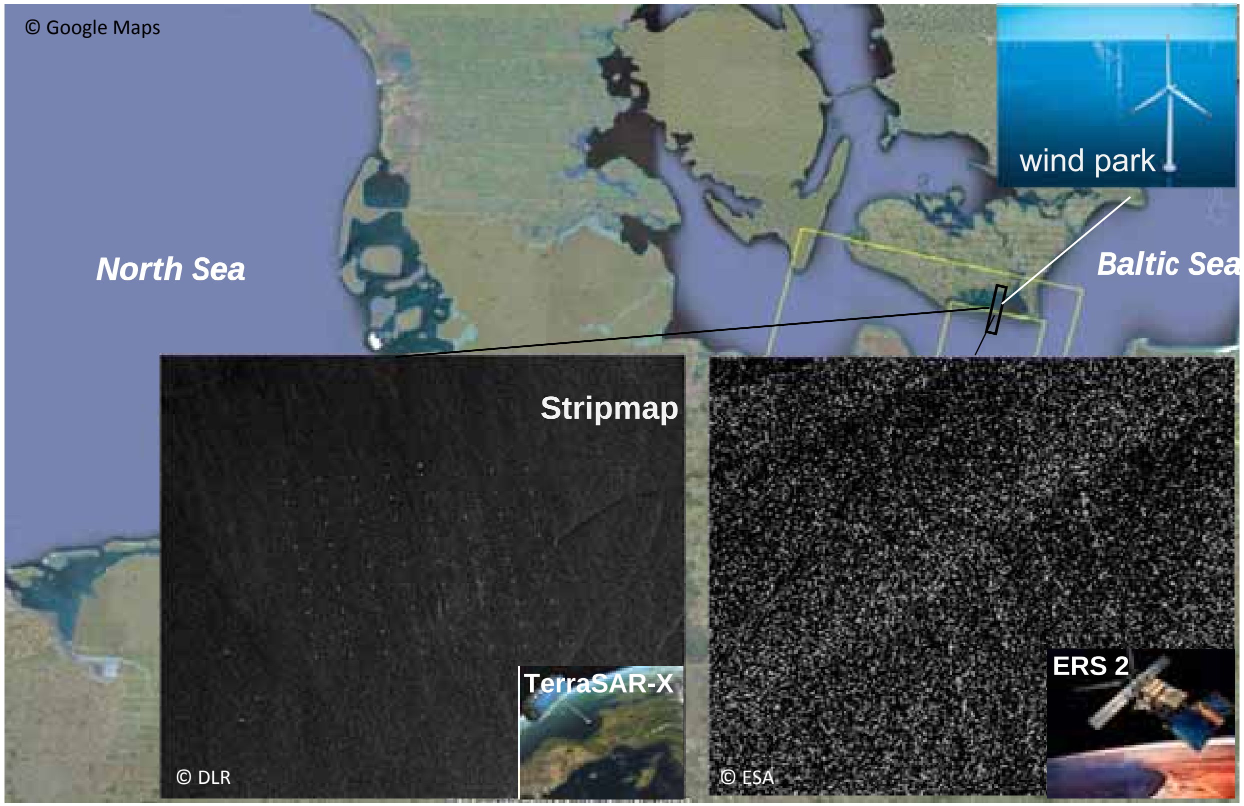

Fig. 6: High resolution SAR data show highly detailed spatial variability at ocean surface (© DLR). Due to its high spatial resolution, the SAR retrieved sea surface wind field is particularly used for coastal monitoring, to improve and assimilate into weather predictions, to monitor tropical and extra-tropical cyclones, to map katabatic and gap winds, to investigate atmospheric vortex streets and boundary layer rolls, as well as in support of offshore wind farming (see references). The following is focused on using TerraSAR-X and Tandem-X high spatial resolution data to monitor coastal wind field. The figure illuminates improvement of spatial resolution of TerraSAR-X (3 m for Stripmap in this case) compared to the previous ERS-2 SAR data (25 m). The bright points on the TerraSAR-X image are the offshore wind turbines over the Baltic Sea.

Wind Field from SAR Data: Alpha Ventus Wind Park

Alpha Ventus: Offshore Wind park in the North Sea

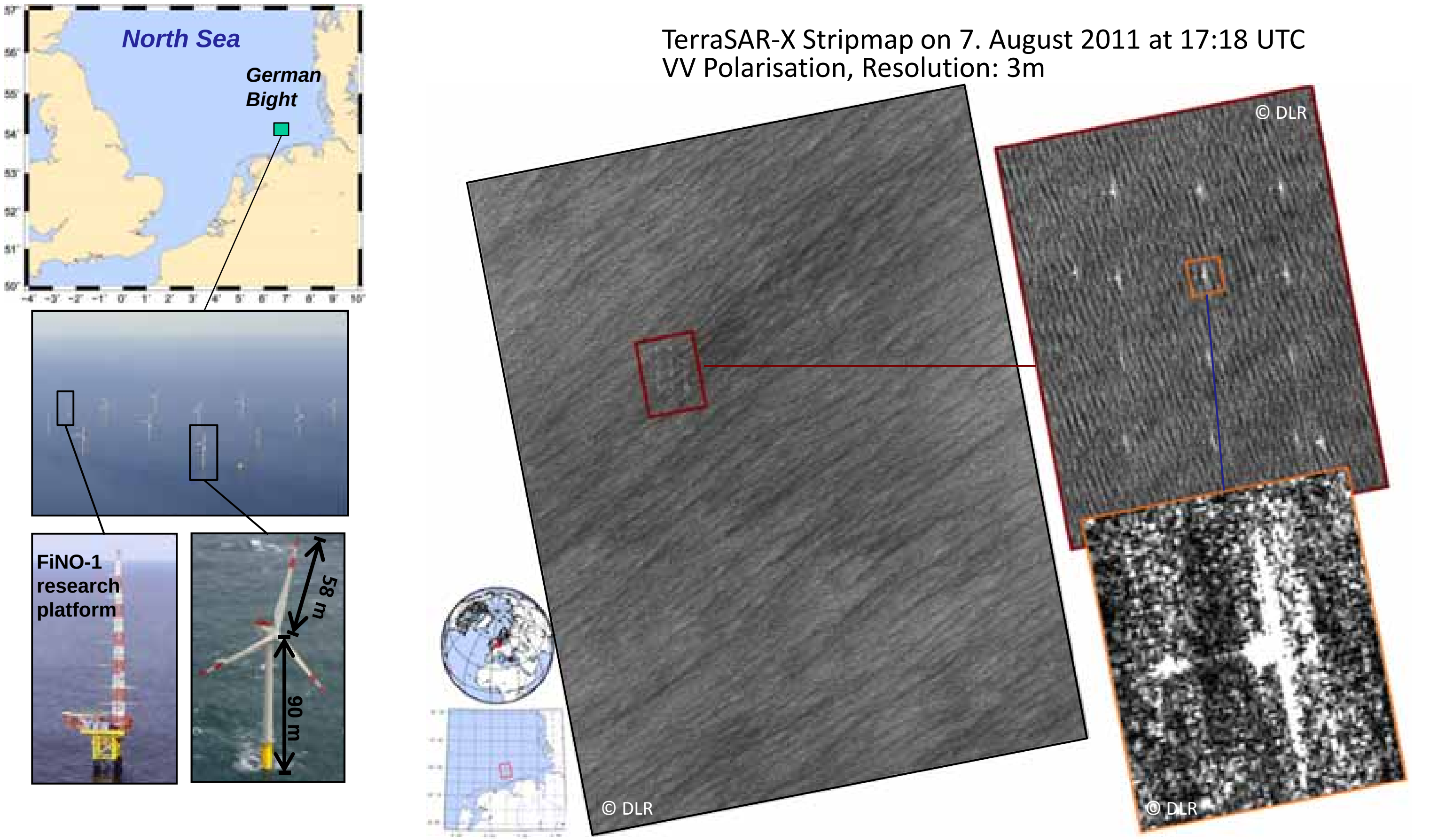

Fig. 17: Wind estimation from TerraSAR-X Stripmap image for *Alpha Ventus* Offshore Wind Park in the North Sea (© DLR, Li)

Wind Field from SAR Data: Alpha Ventus Wind Park

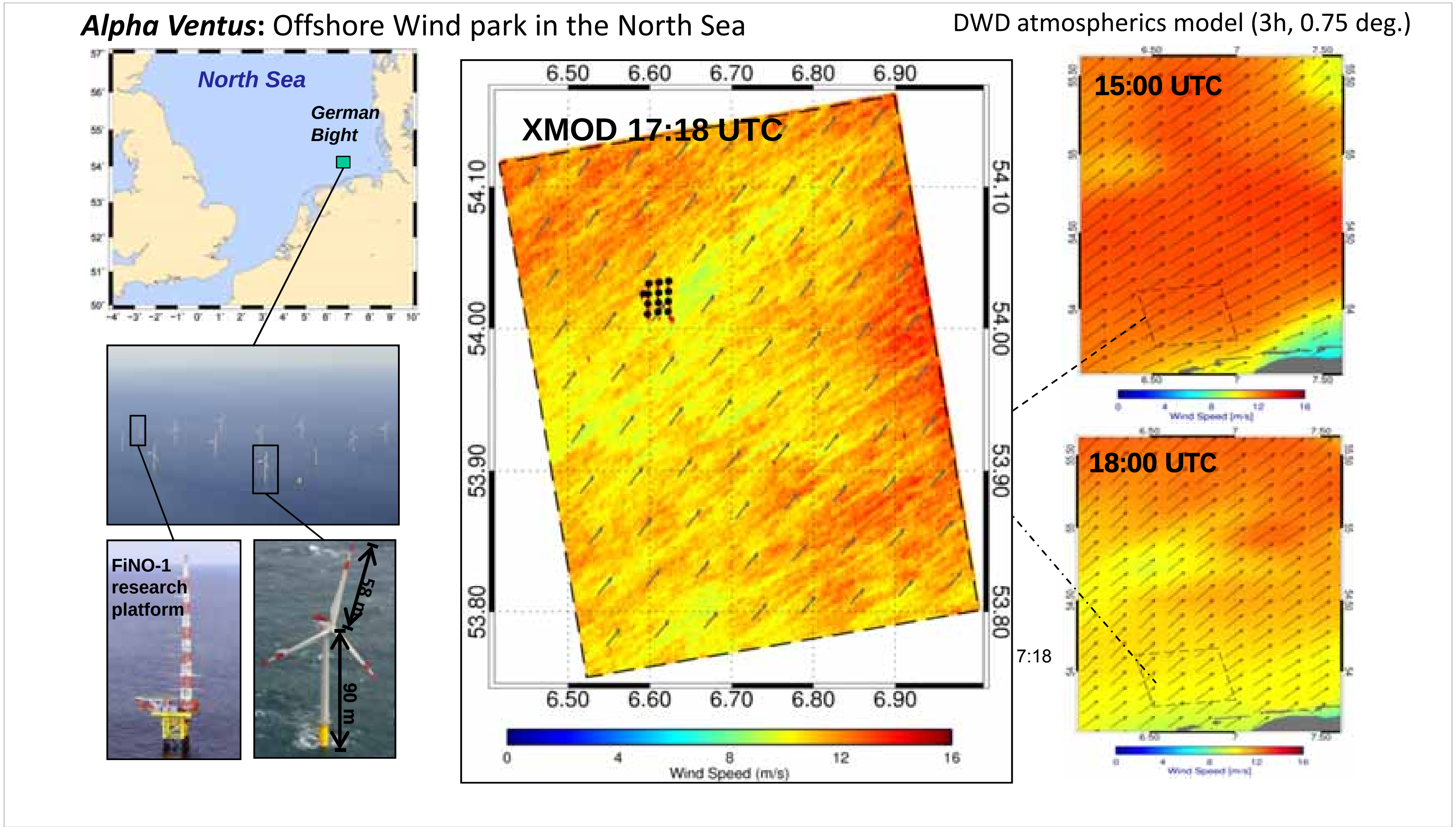

Fig. 18: Wind estimation from TerraSAR-X Stripmap image for *Alpha Ventus* Offshore Wind Park in the North Sea. Comparison to DWD model (© DLR)

Wind Field from SAR Data: Alpha Ventus Wind Park

Alpha Ventus: Offshore Wind park in the North Sea

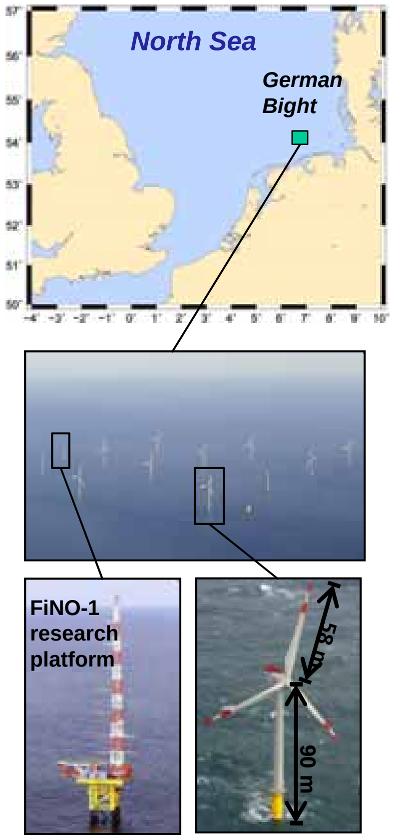

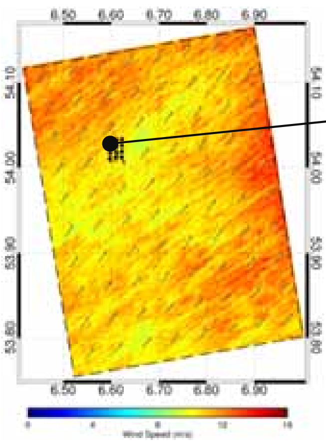

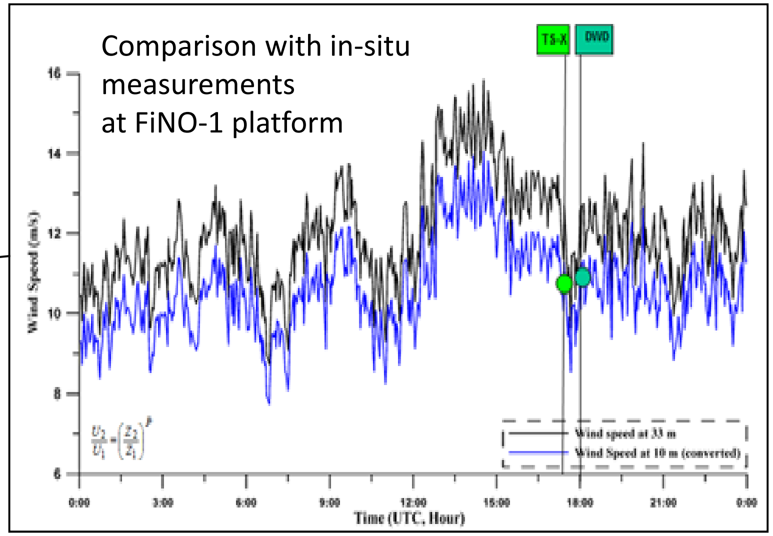

comparison	Wind speed U_{10} (m/s)	time (UTC)	distance (km)
In situ / DWD	11.2 / 10.5	18:00	0.9
In situ / XMOD	10.5 / 10.3	17:18	0.1

Fig. 19: Wind estimation from TerraSAR-X Stripmap image for *Alpha Ventus* Offshore Wind Park in the North Sea. Comparison to in-situ measurements (© DLR)

Wind field from SAR data: *Typhoon*

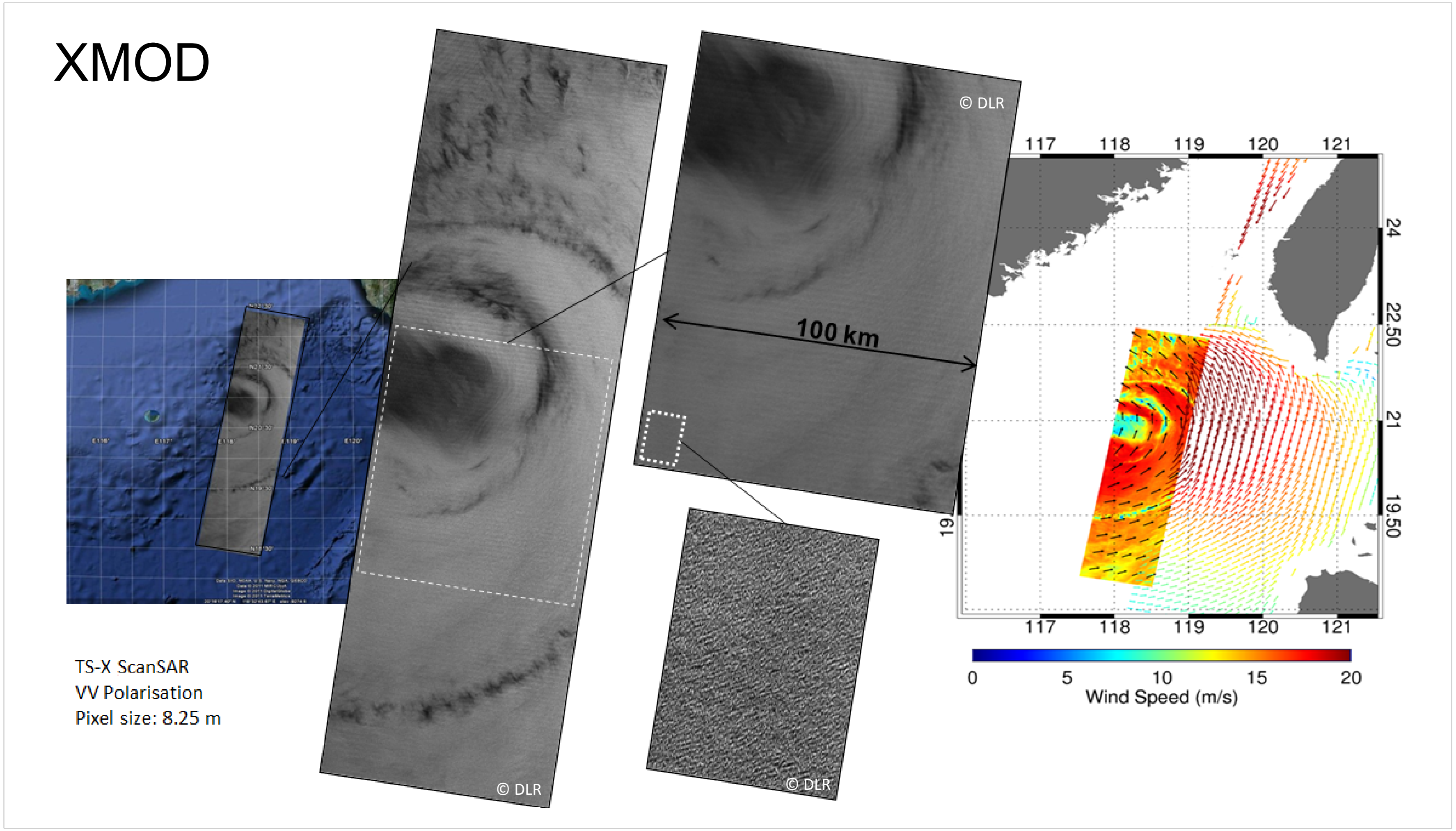

Fig. 20: Tropical Cyclone Eye “MEGI” SSW measurement of Typhoon using TSX-SC data (© DLR)

Wind field from SAR data: *Hurricanes*

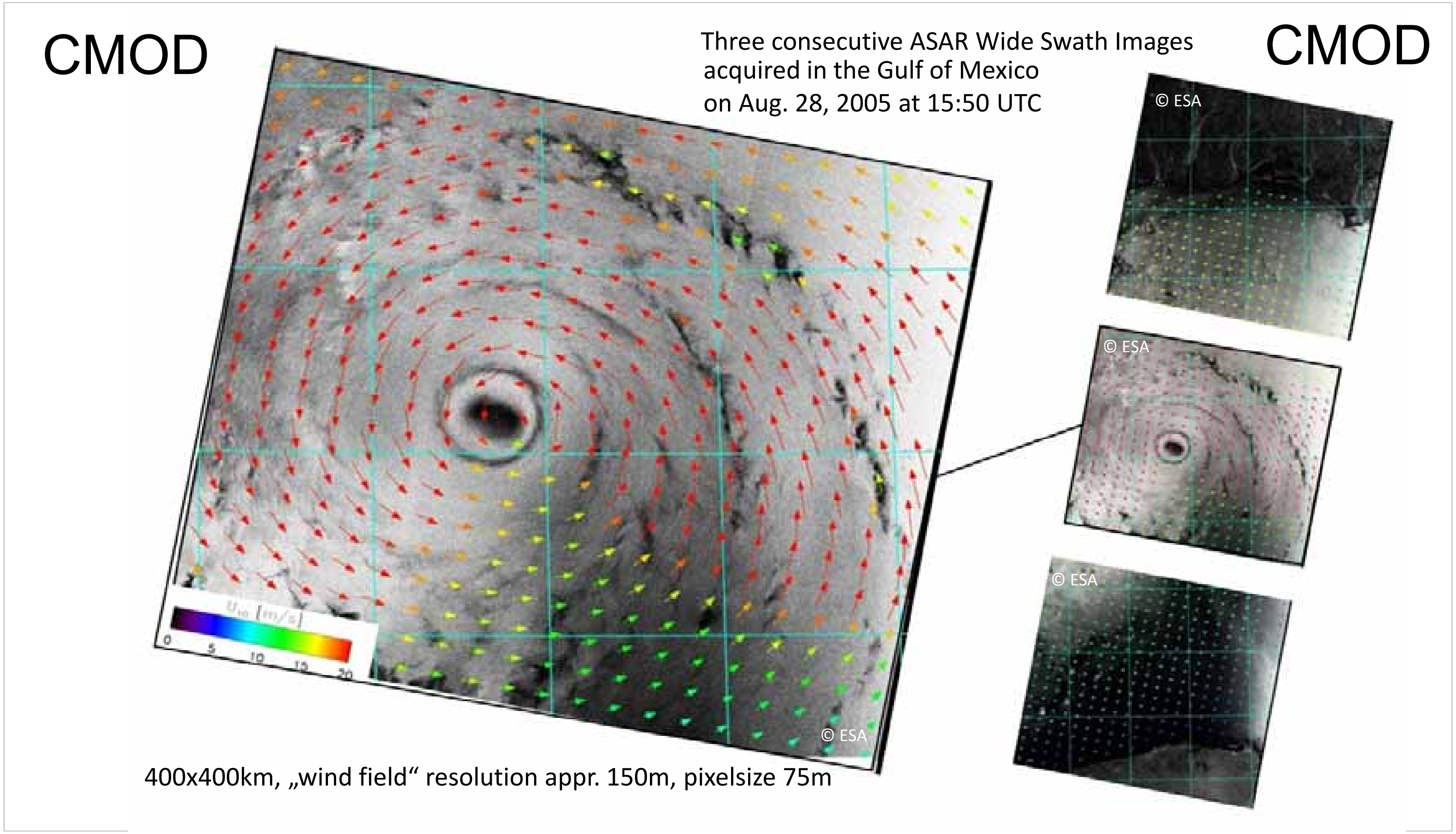

Fig. 21: SAR sea surface wind field for tropical cyclones: Hurricane Katrina, August, 2005 (© DLR, Lehner)

Remote Sensing and Oil Spill

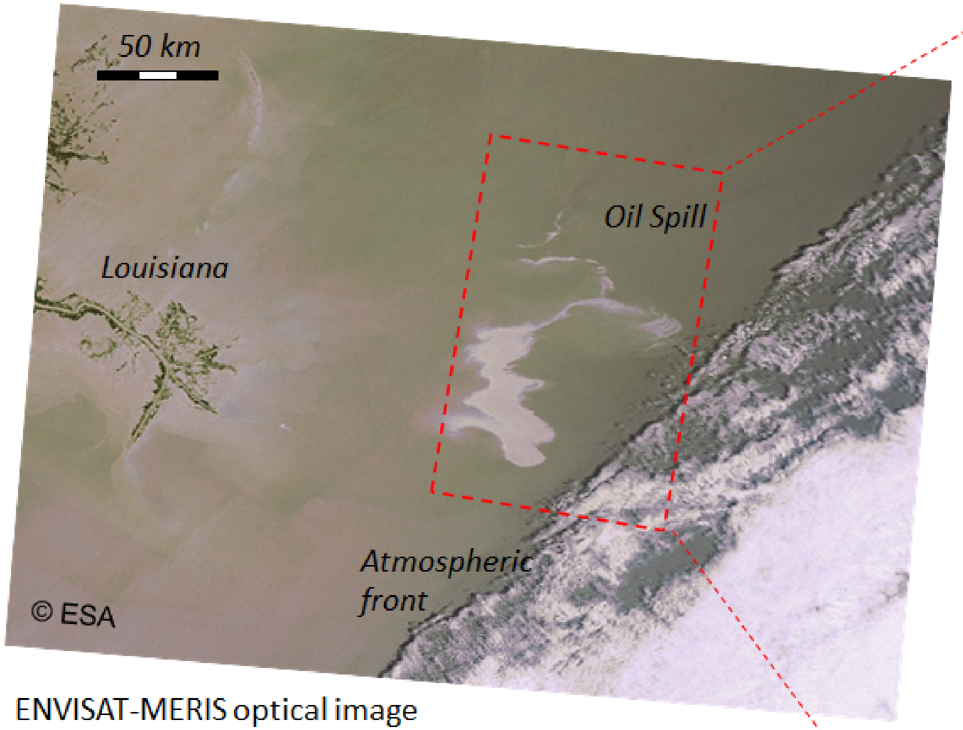

ENVISAT-MERIS optical image
April 25, 2010 at 16:28 UTC

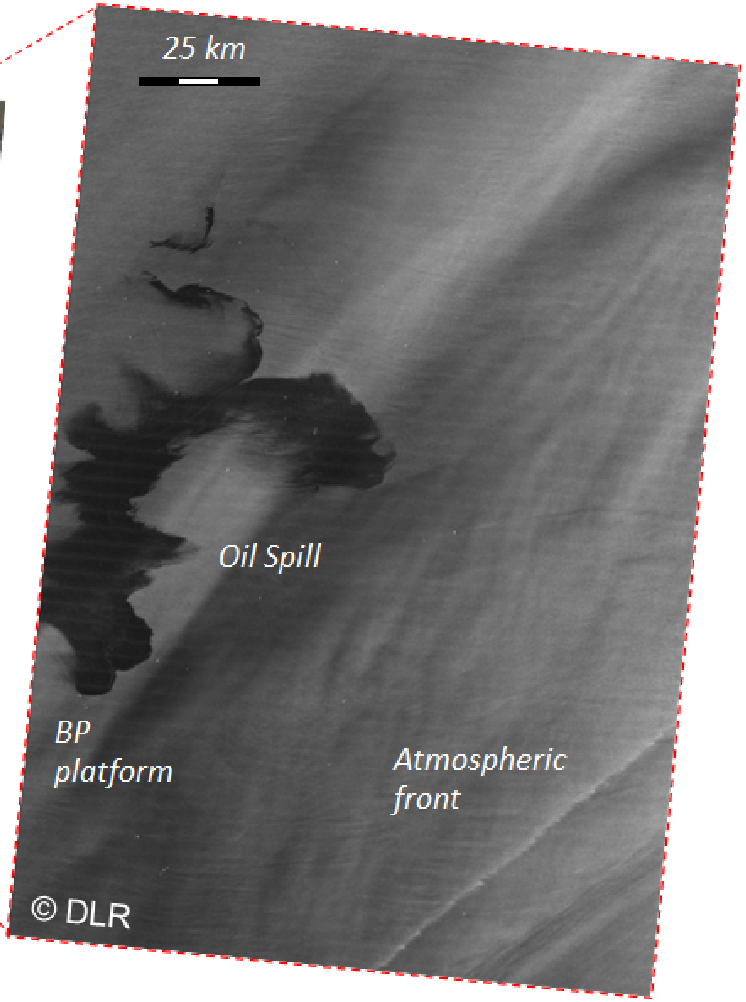

TerraSAR-X radar image
April 25, 2010 at 11:50 UTC
BP oil spill in Gulf of Mexico

Fig. 63: Oil split example - BP oil spill in Gulf of Mexico in 2010.

Weathering Processes of Oil Spilled at Sea and SAR Interpretation

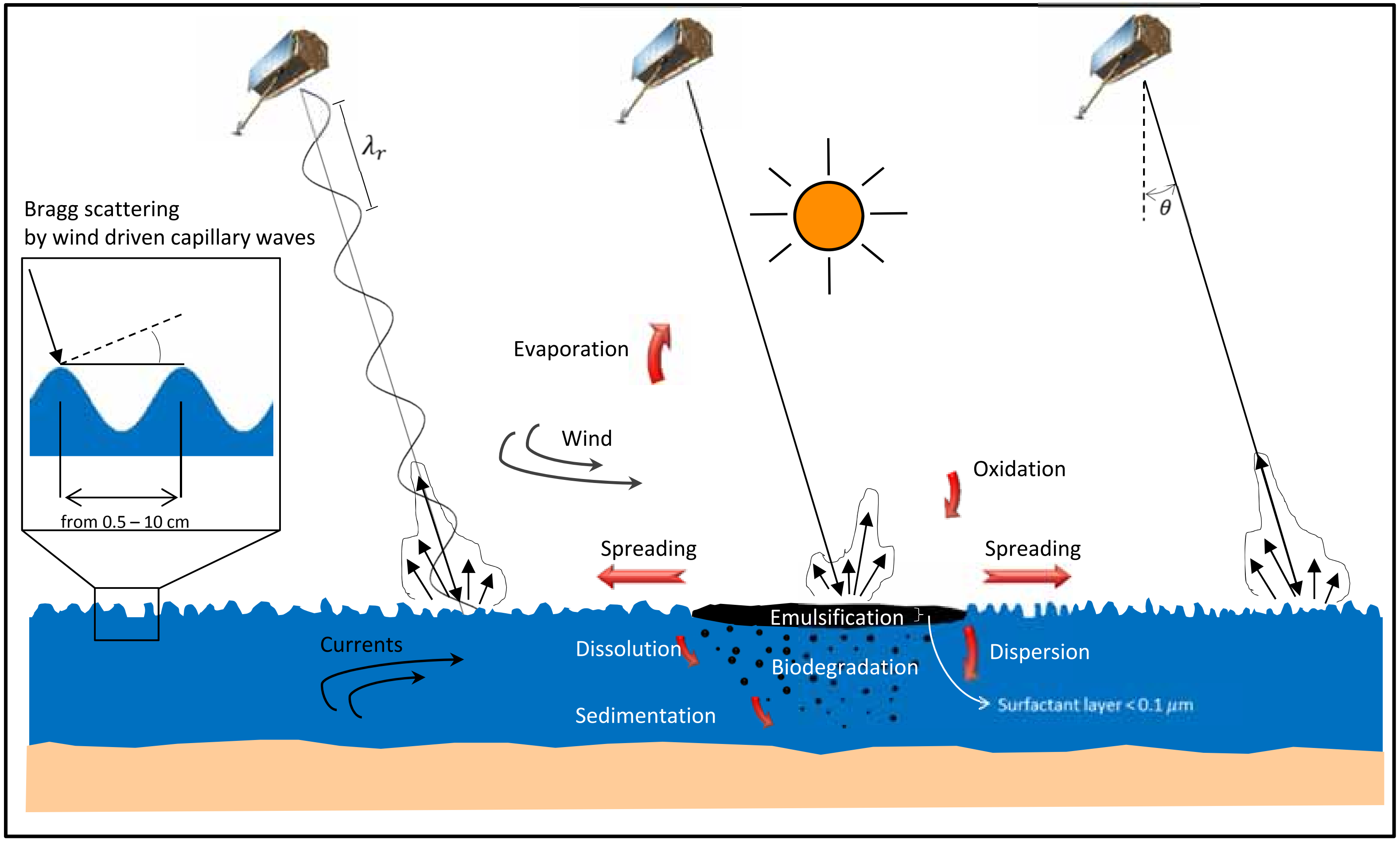

Fig. 64: Schema for oil detection by SAR (© DLR)

Examples of look-alike

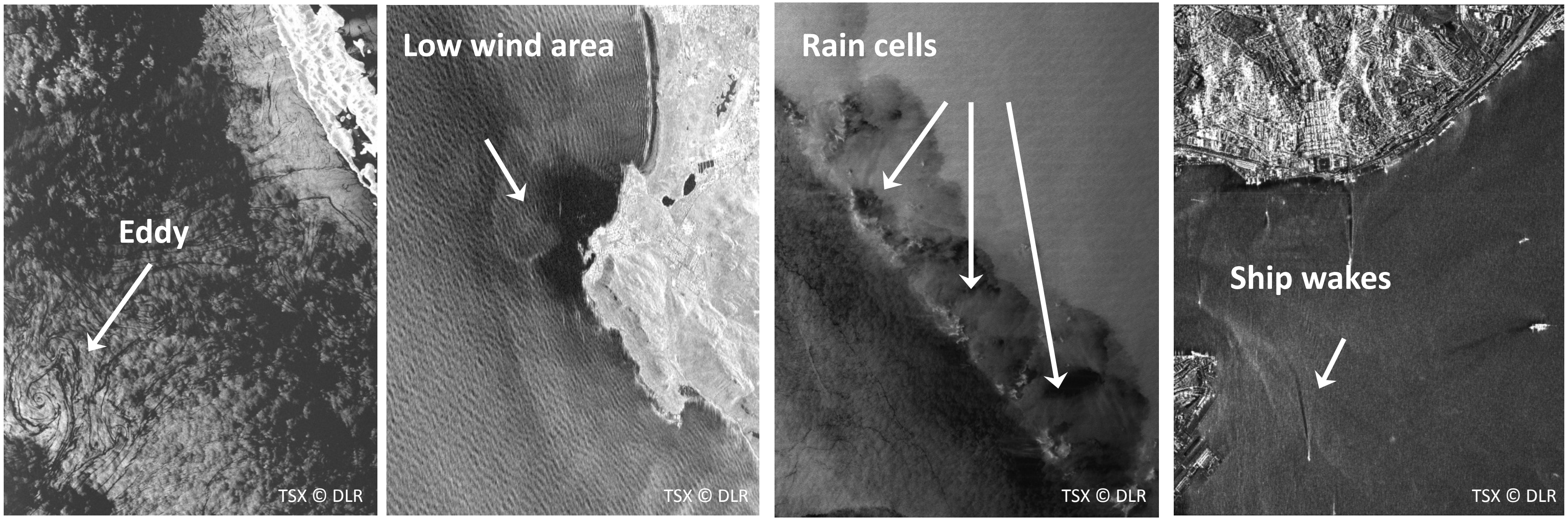

Fig. 65: Interpretation of different natural, atmospheric and man-made phenomena causing low backscattering (© DLR)

Differences of oil and oil-like structures in SAR imaging

Discrimination methods used for TerraSAR-X:

- Method 1: **neural network** (single-pol SAR data)
- Method 2: **co-polarized phase differences-CPD** (dual-pol SAR data, complex)

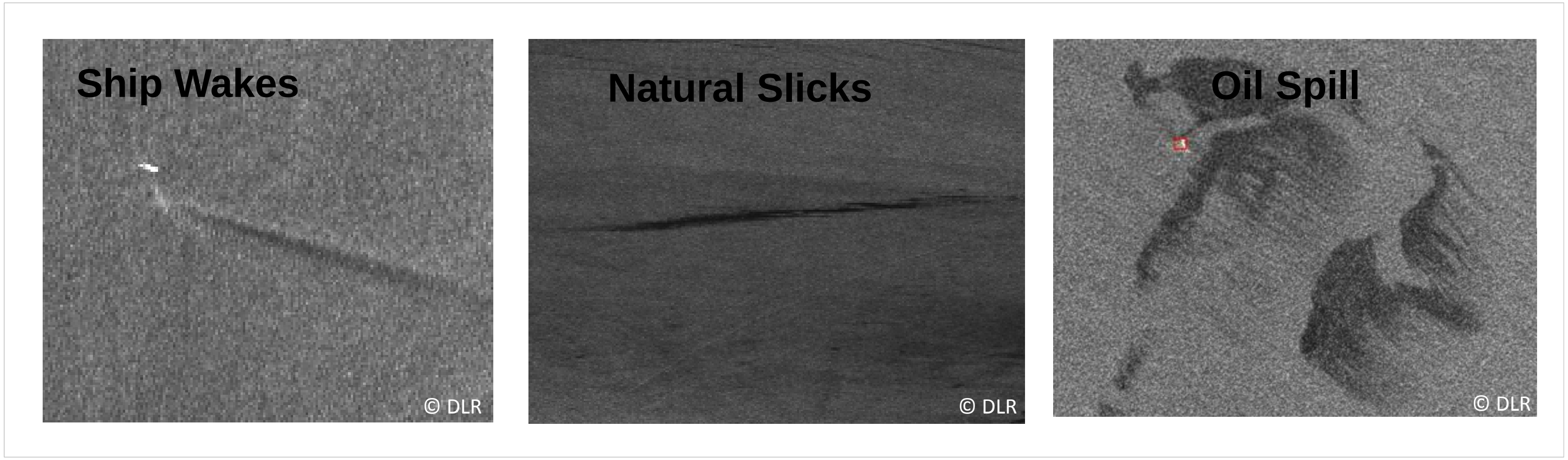

Fig. 72: Examples for oil and oil-like structures in SAR images (© DLR, Velotto)

First Oil Spills Detected by Sentinel-1

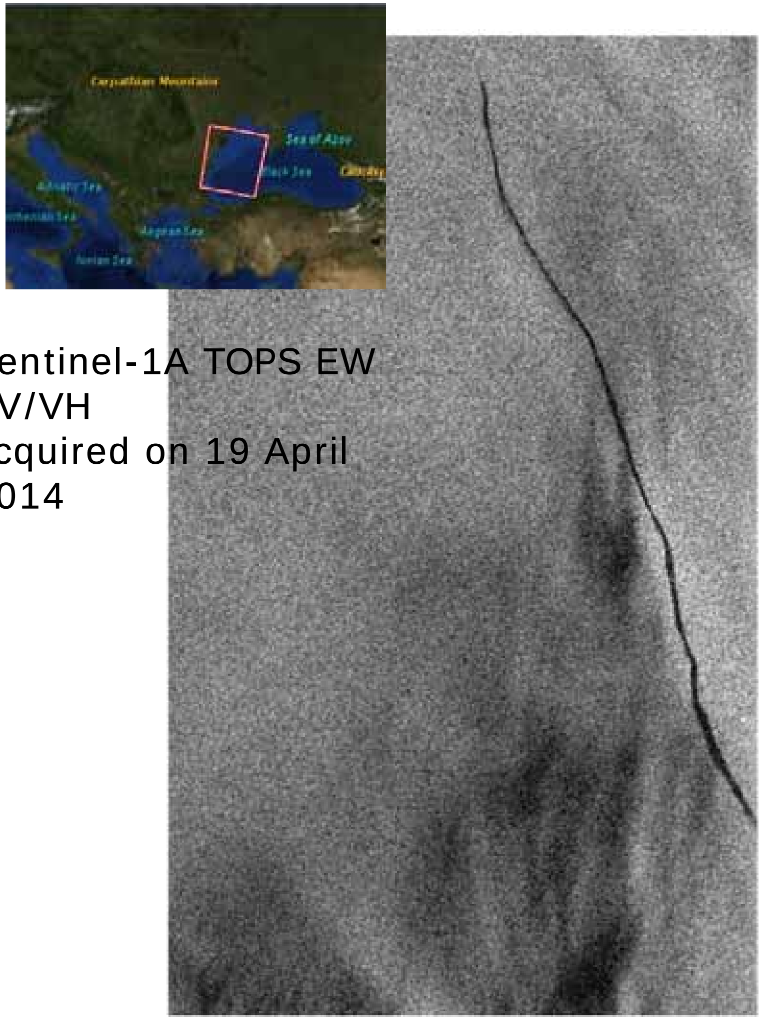

Sentinel-1A TOPS EW VV/VH
acquired on 19 April 2014

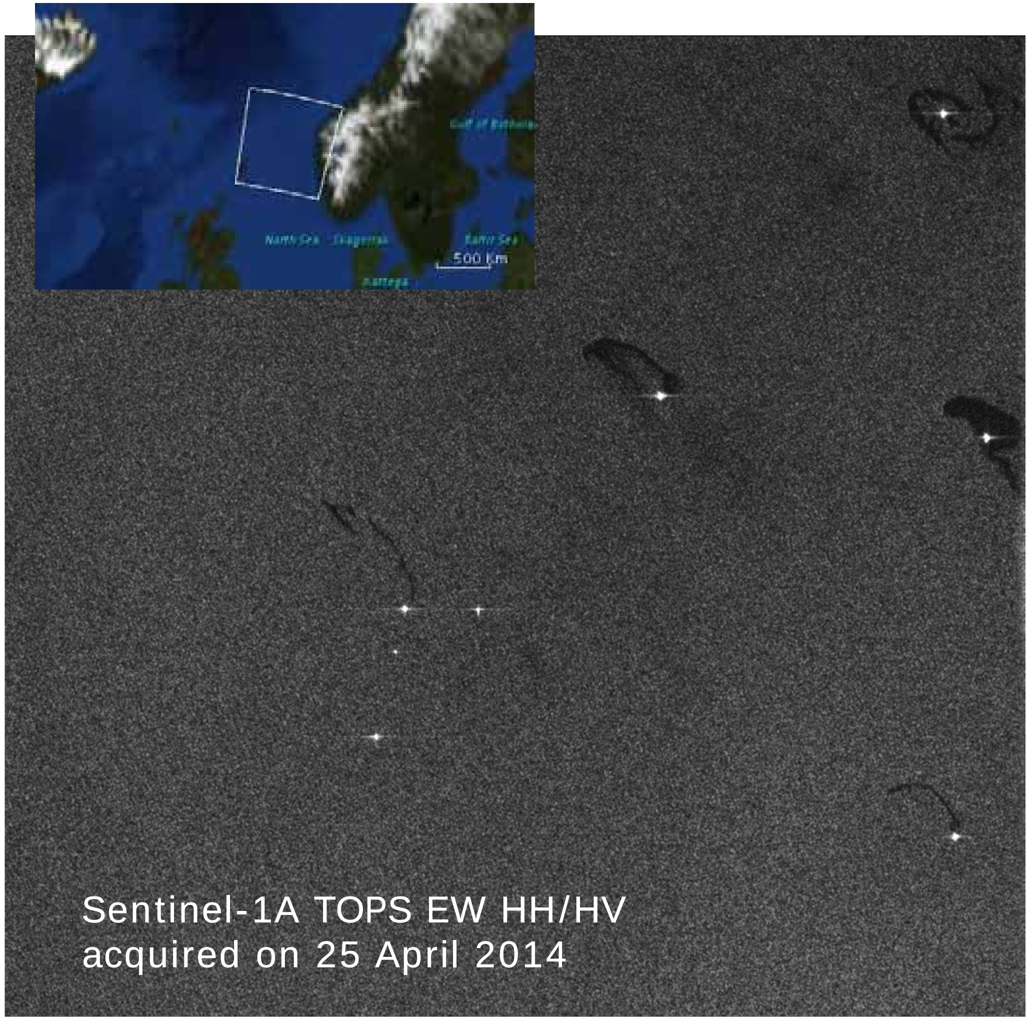

Sentinel-1A TOPS EW HH/HV
acquired on 25 April 2014

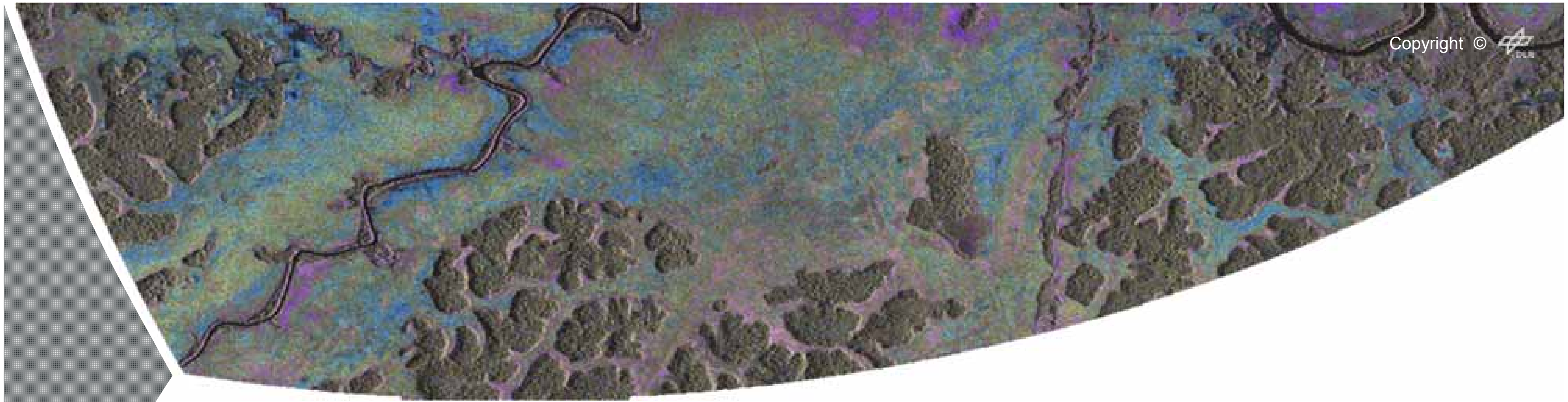

SAR Applications of the Biosphere

Nicole Richter

Christian Thiel

Christiane Schmullius

Robert Eckardt

Friedrich-Schiller-University Jena
Department for Earth Observation
Jena, Germany

TECHNISCHE UNIVERSITÄT MÜNCHEN

SAREDU Remote Sensing Education Initiative

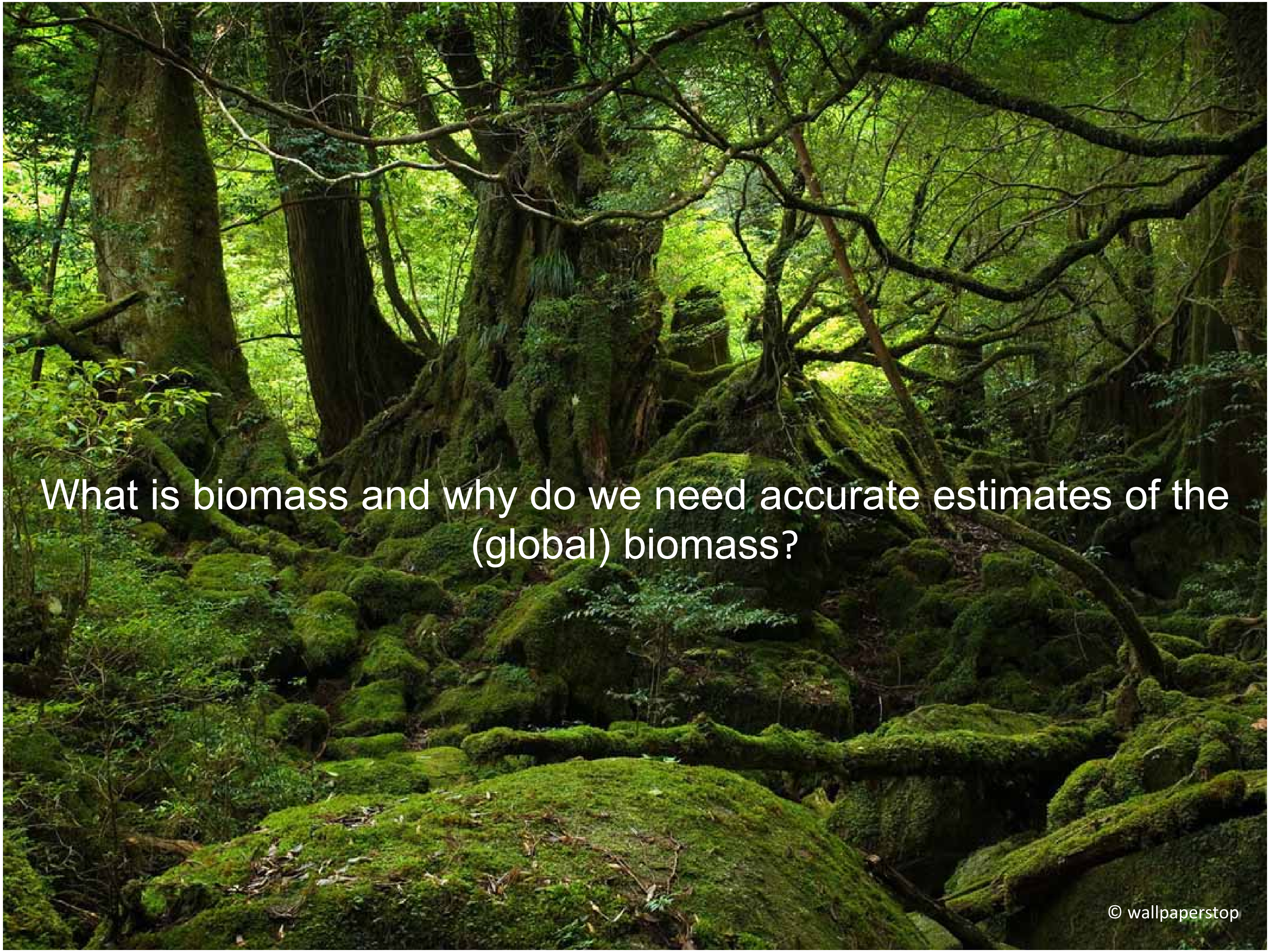

What is biomass and why do we need accurate estimates of the (global) biomass?

Advantages of SAR data

(compared to optical remote sensing data or in-situ measurements)

- Higher spatial coverage
- Higher temporal resolution (repeat cycle e.g. 11 days)

⇒ Remotely sensed data therefore can be used to fill spatial, attributional, and temporal gaps in forest inventory data

- Contactless

⇒ Detection of unknown regions

- Retrospective analysis
  (archived SAR data since 1991 (but not globally))
- Microwaves enable a weather- and illumination-independent imaging process

FAO, 2009, Balzter, 2001

Biomass from forest height

1 - FOREST HEIGHT
↓
2 - CONVERSION
↓
3 - FOREST BIOMASS

Forest height estimates from single frequency, fully polarimetric-interferometric SAR data through model-based inversion

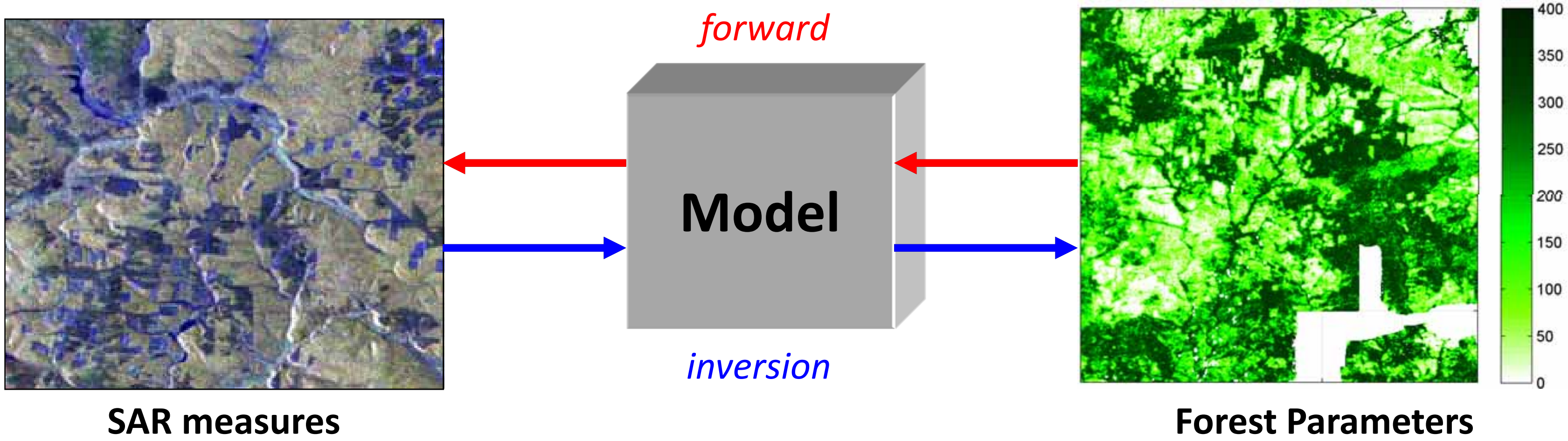

Fig.: Linking SAR measures and forest parameters (THIEL, 2012).

Biomass from forest height

1 - Forest Height
↓
2 - Conversion
↓
3 - Forest Biomass

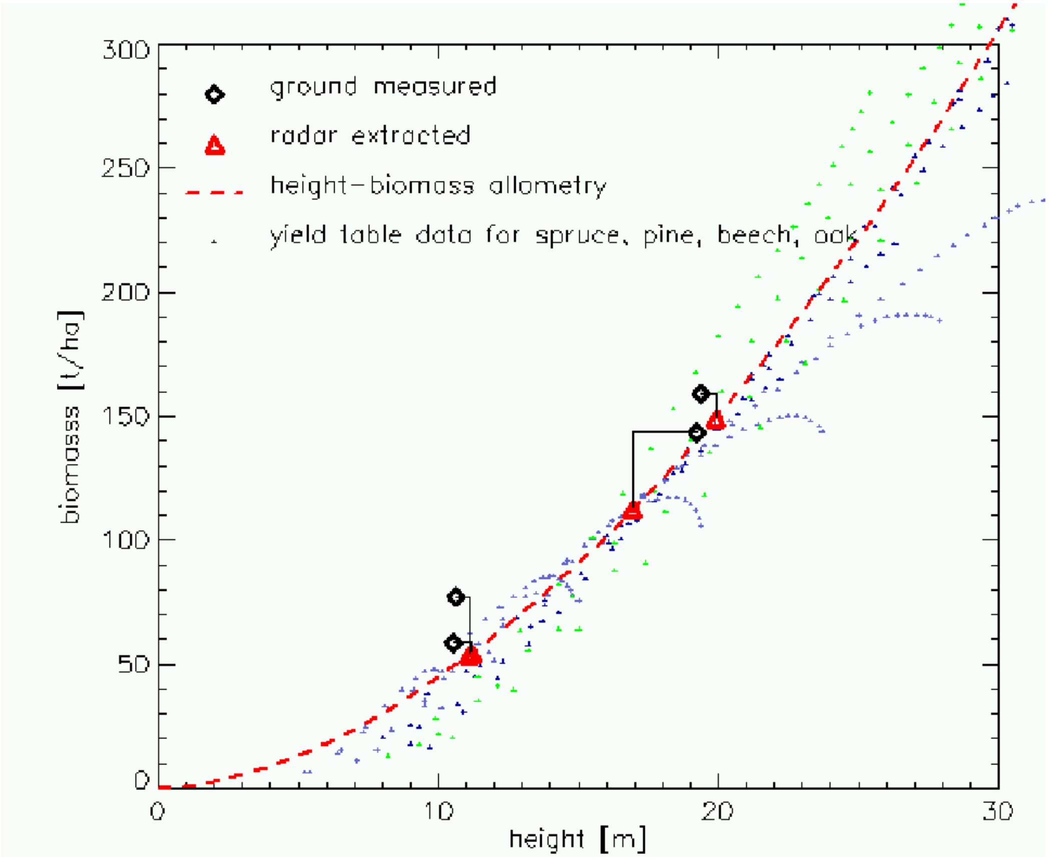

Fig.: Correlation of forest heights vs. biomass for the ground measurements and Pol-InSAR extracted heights that were converted to biomass through height-biomass allometry **[Biomass = 0.801 x $h_{100}^{1.748}$]** (Mette et al., 2004).

SAREDU

Biomass from forest height

1 - FOREST HEIGHT
↓
2 - CONVERSION
↓
3 - FOREST BIOMASS

Multi-temporal combination of single biomass estimates

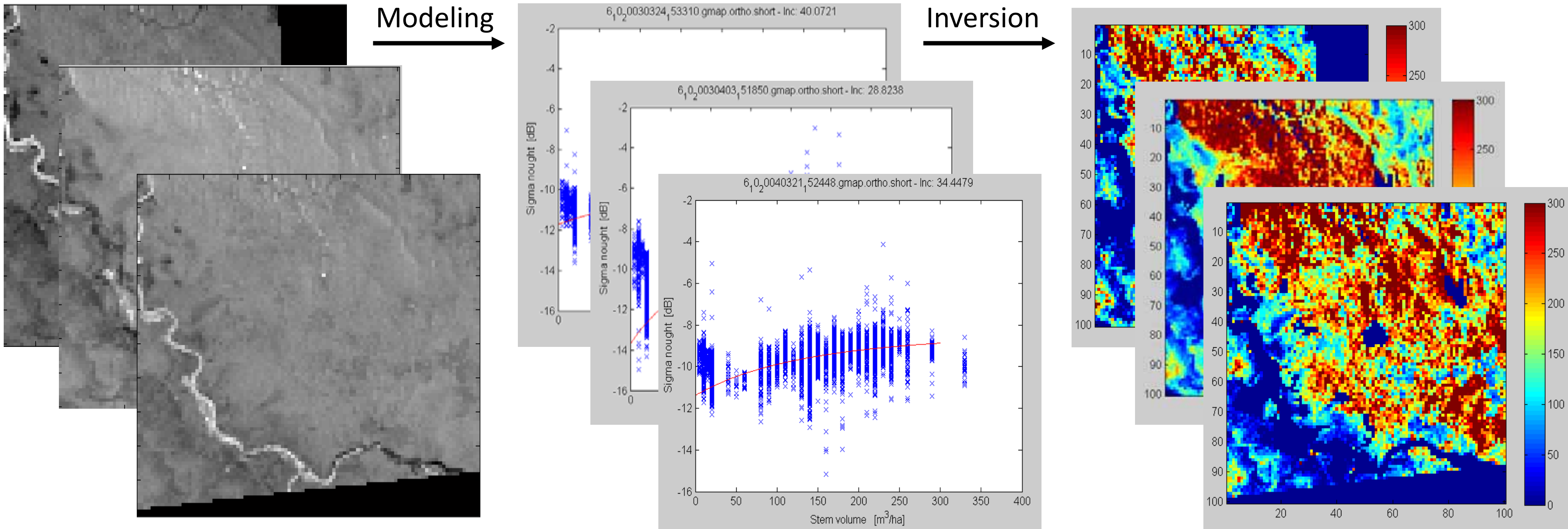

A multi-temporal combination of single estimates with weights determined by the backscatter contrast σ^0_{veg} - σ^0_{gr} allows obtaining the final estimate

[ESA BIOMASAR Project, MAURIZIO SANTORO, 2007]

SAREDU Remote Sensing Education Initiative

Biomass from forest height

1 - Forest Height
↓
2 - Conversion
↓
3 - Forest Biomass

Multi-temporal combination of single biomass estimates

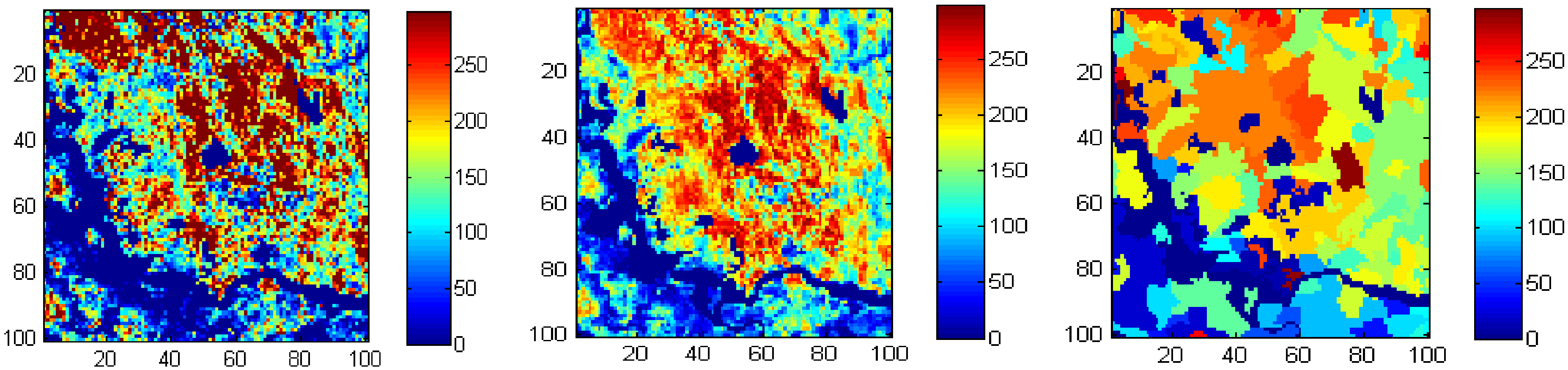

Single-image | Multi-temporal (29 images) | Inventory

- From a single image it is possible to identify sparse/dense forest patterns at most
- From multi-temporal combination it is possible to identify biomass levels

[ESA BIOMASAR Project, Maurizio Santoro, 2007]

Application examples

- SIBERIA - Biomass mapping in Siberia
- ESA DRAGON – Biomass mapping in China
- BIOMASAR – Panboreal forest growing stock volume maps
- SARvanna – Vegetation structure mapping in the Kruger National Park
- Biomass from forest height – Fichtelgebirge, Germany

BIOMASAR Growing Stock Volume products

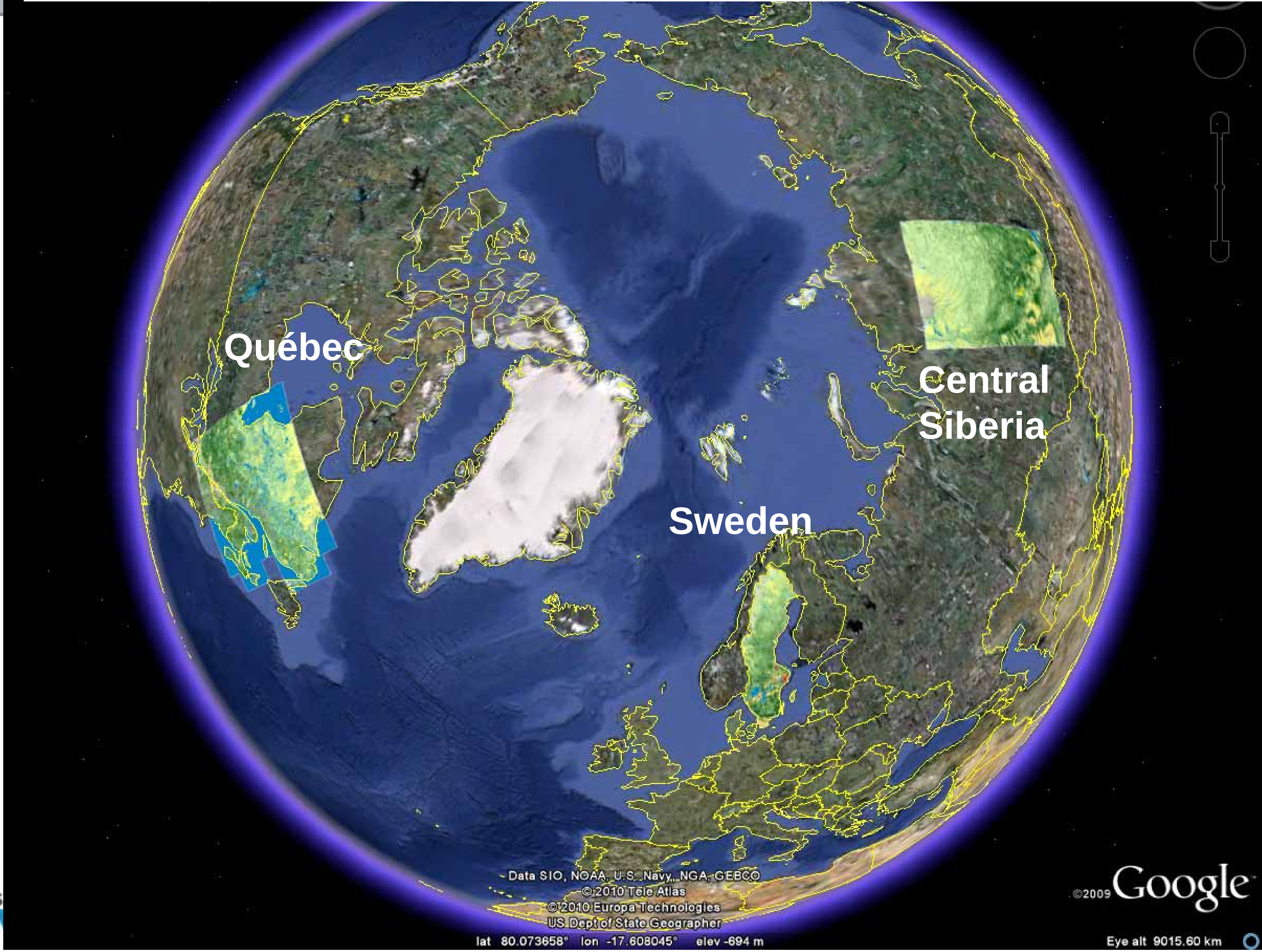

BIOMASAR Project

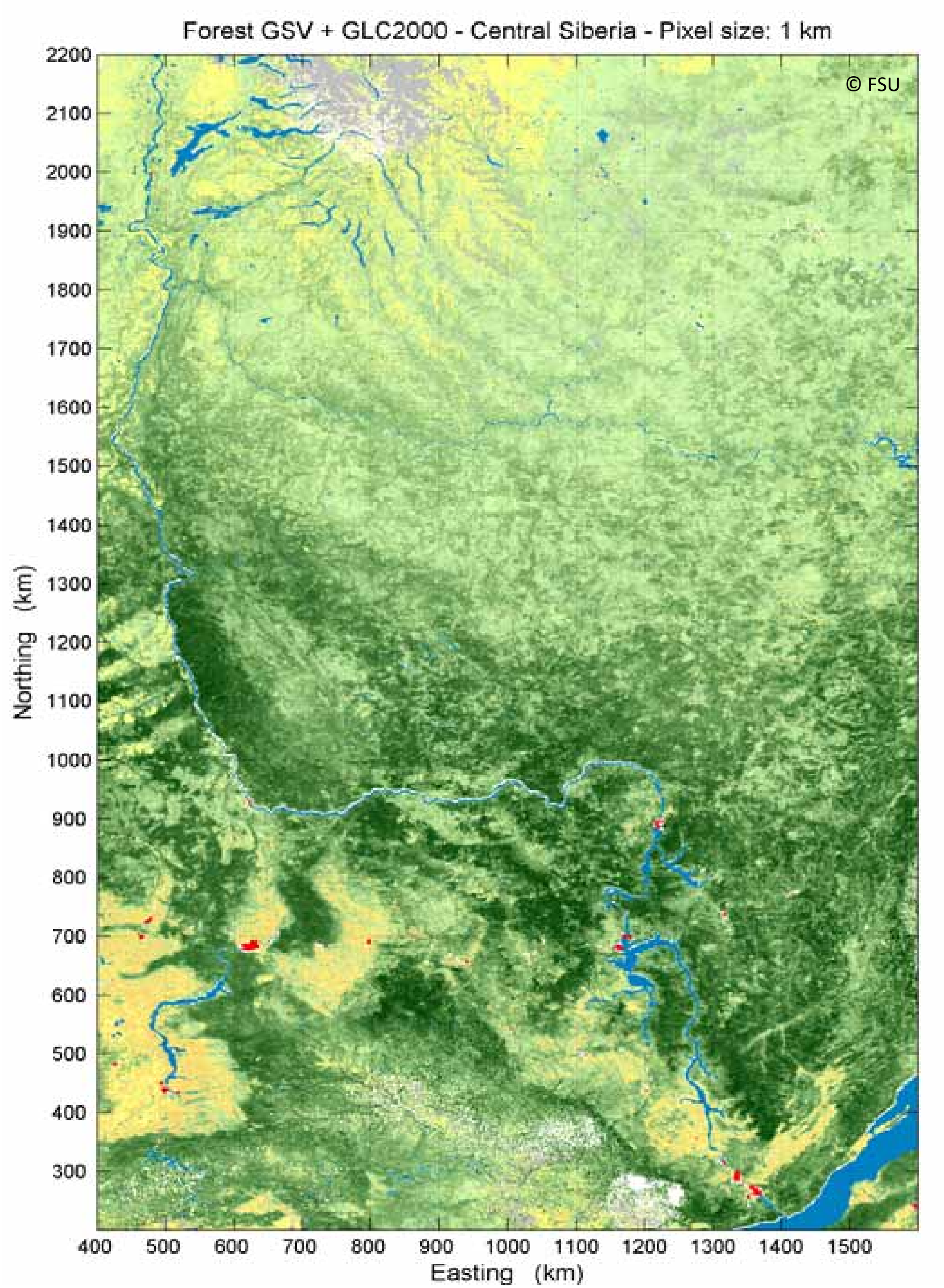

1-km forest Growing Stock Volume (GSV) map of Central Siberia

- 2,400,000 km²
- ENVISAT ASAR Global Monitoring mode (Jan. 2005 – Feb. 2006)
- GLC 2000 land cover used as background

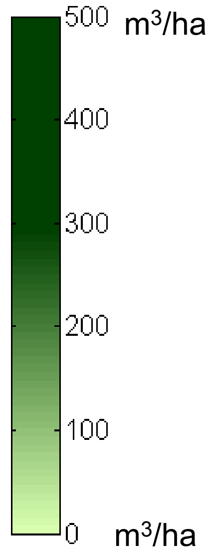

BIOMASAR Project

Pan-boreal growing stock volume

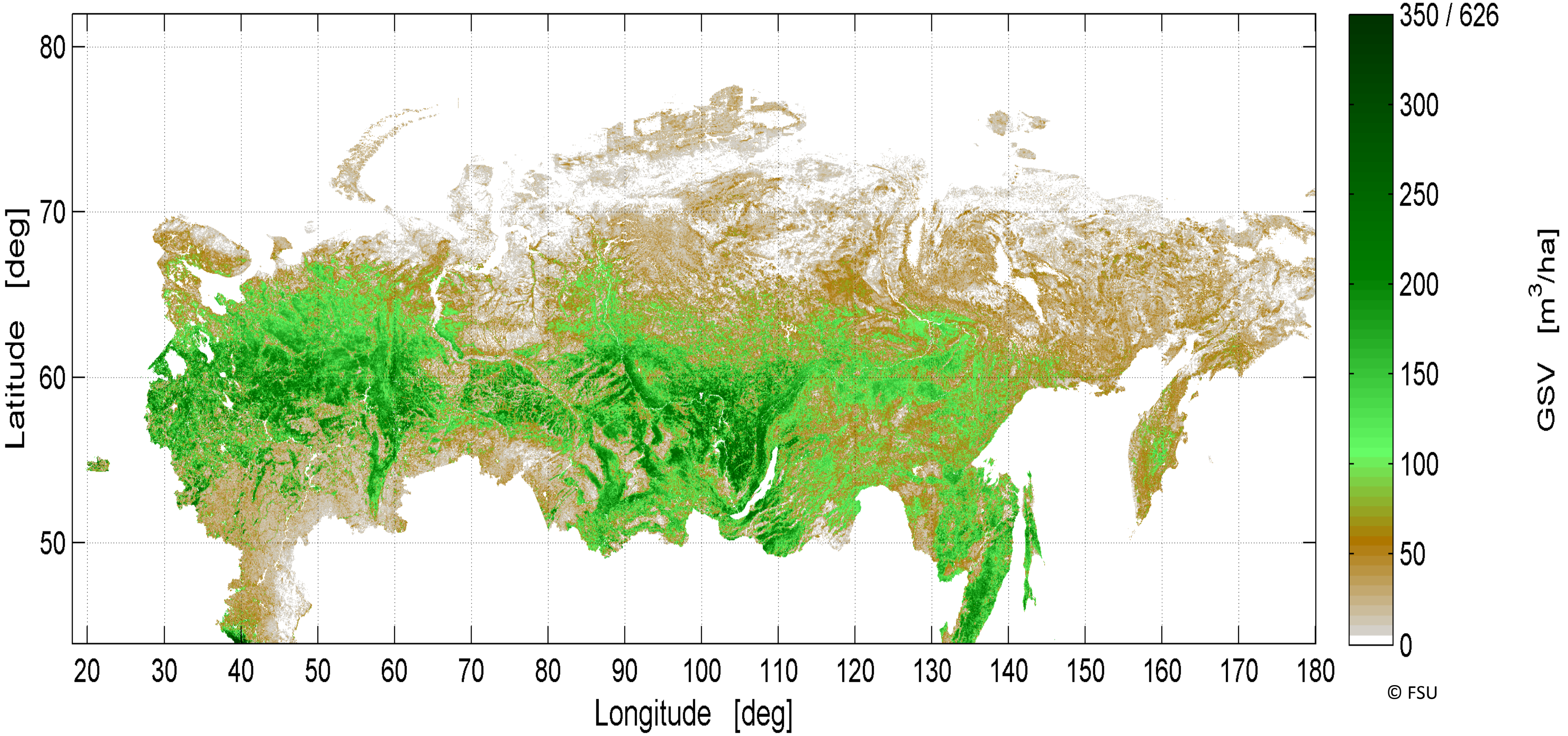

BIOMASAR Project

Radar-retrieved growing stock volume map of Mexico

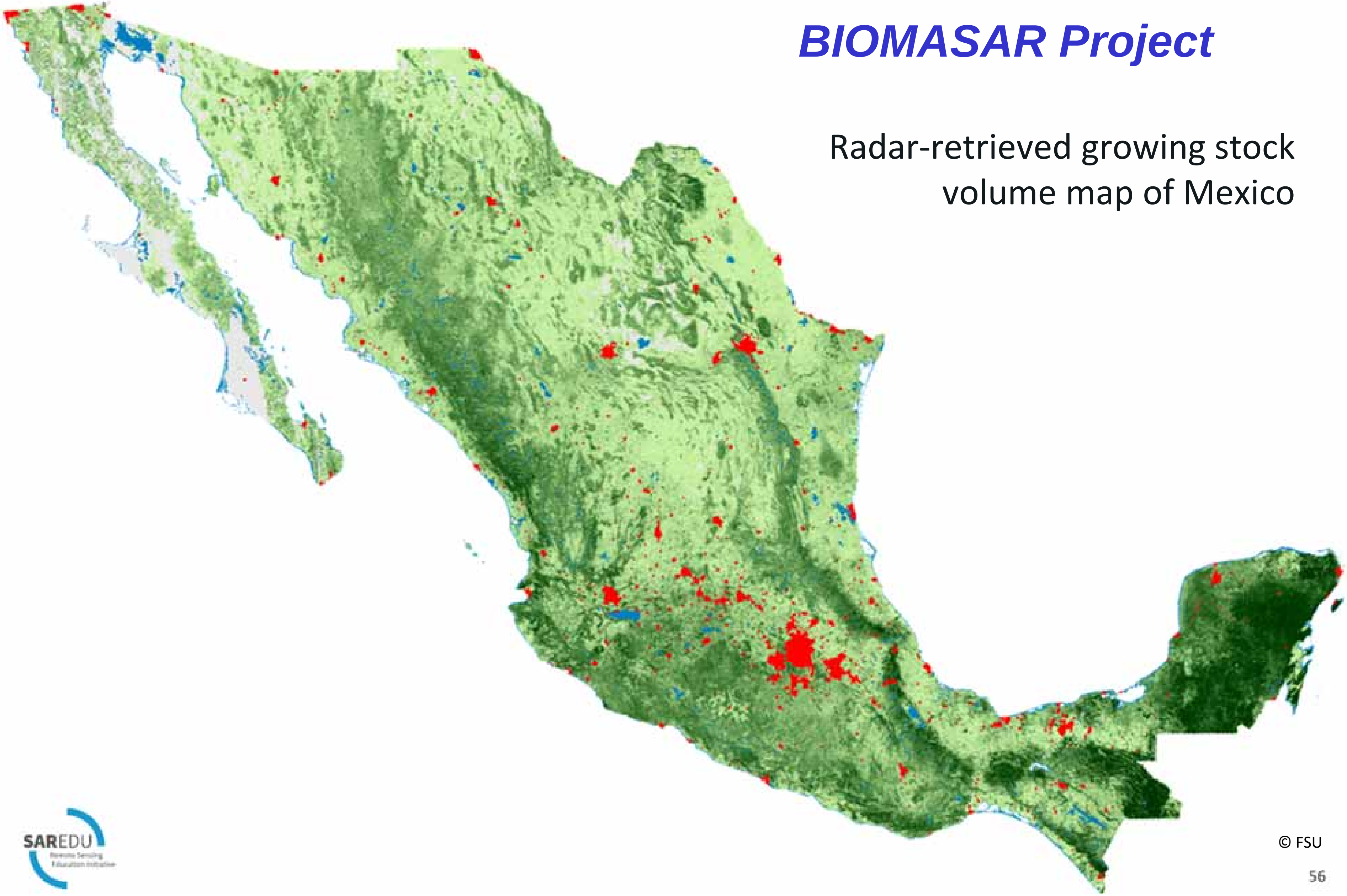

BIOMASAR Project

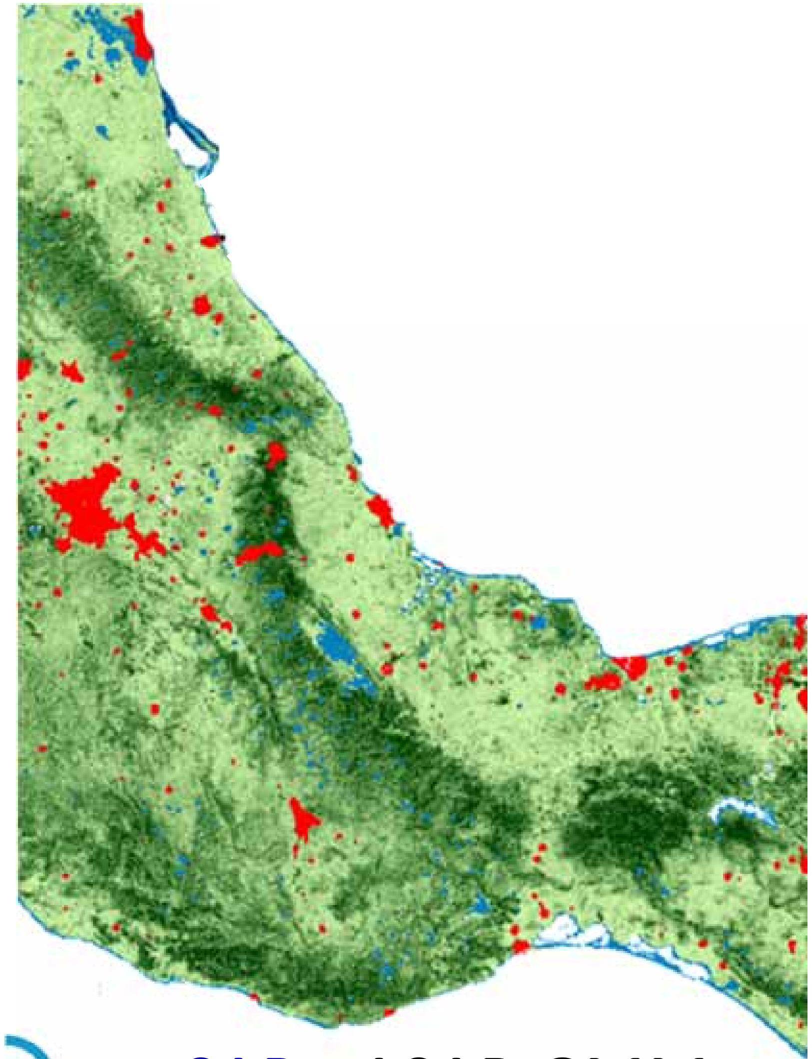

SAR - ASAR GMM © FSU

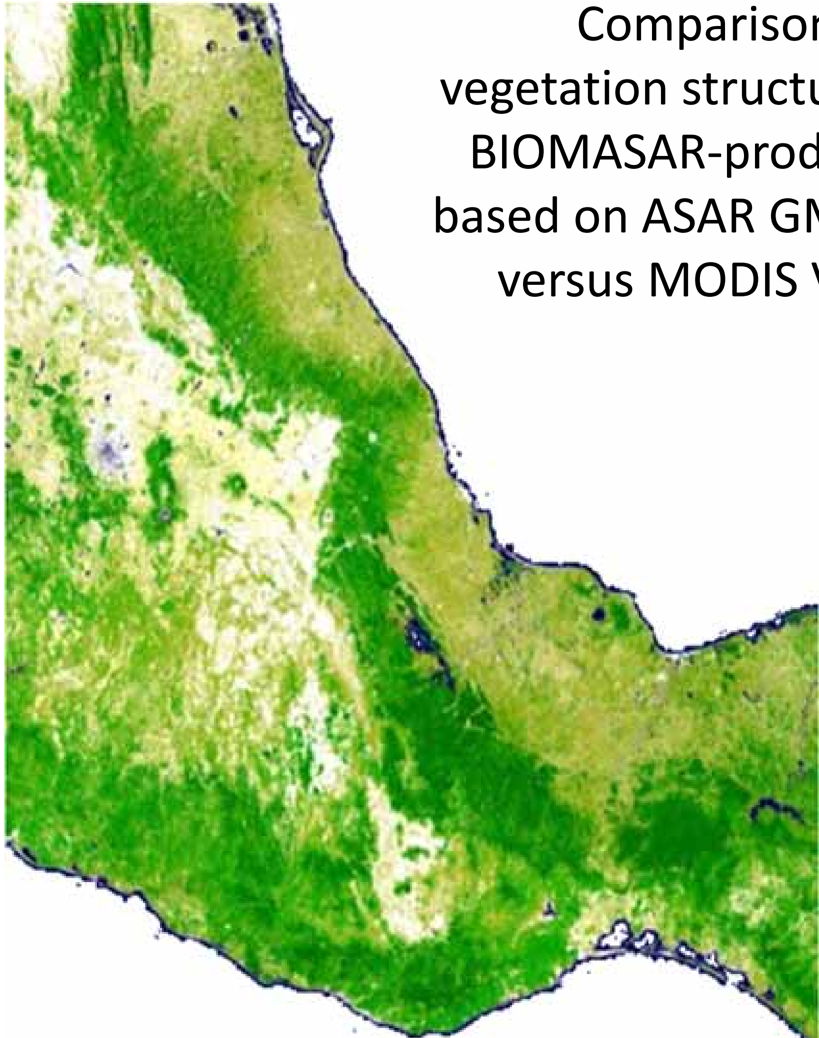

Comparison of vegetation structure: BIOMASAR-product based on ASAR GMM versus MODIS VCF

Optics - MODIS VCF © GLCF

Kruger National Park Woody Cover Maps based on April 1994 SIR-C C- (right) and L-band data (left) at 37 deg incidence angle.
Retrieval algorithm: Volume Component from Freeman Decomposition

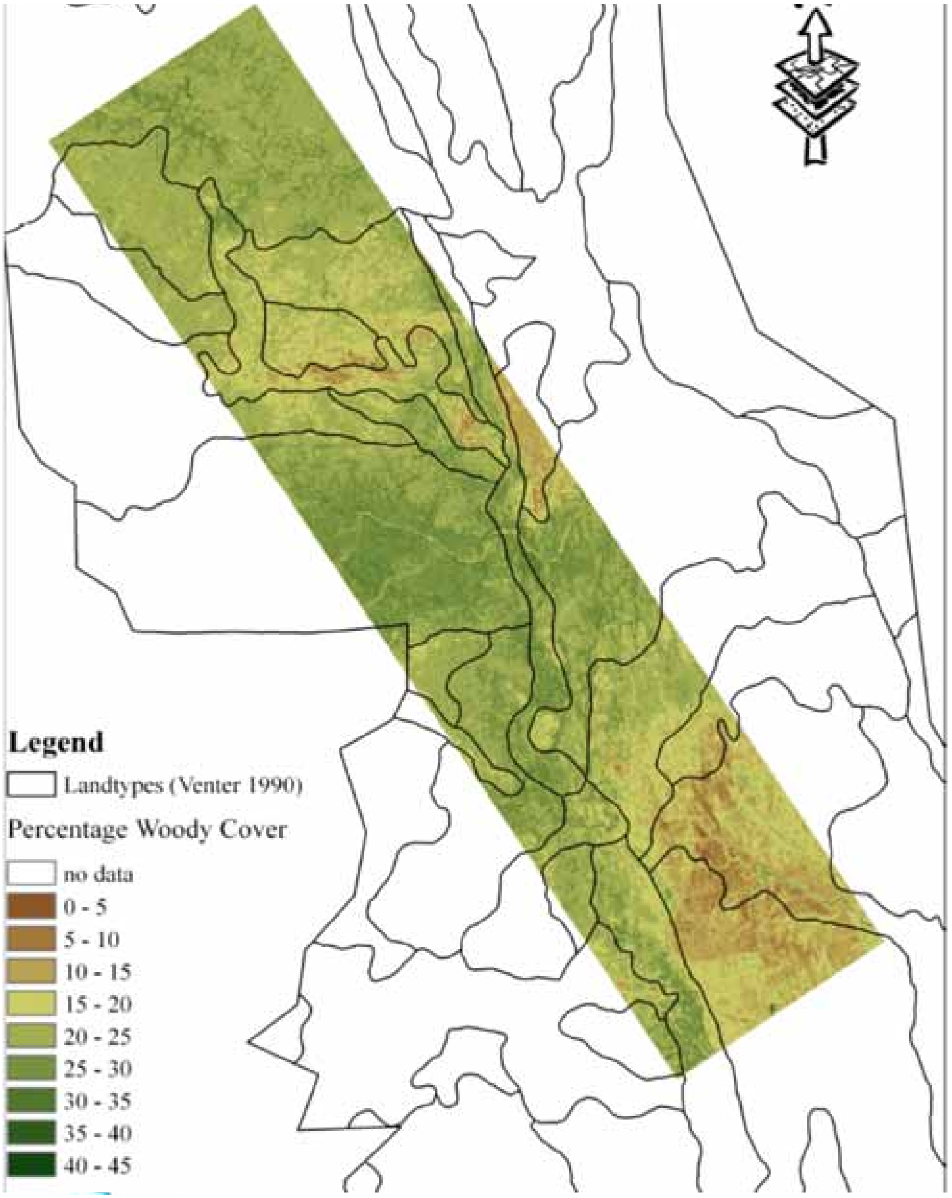

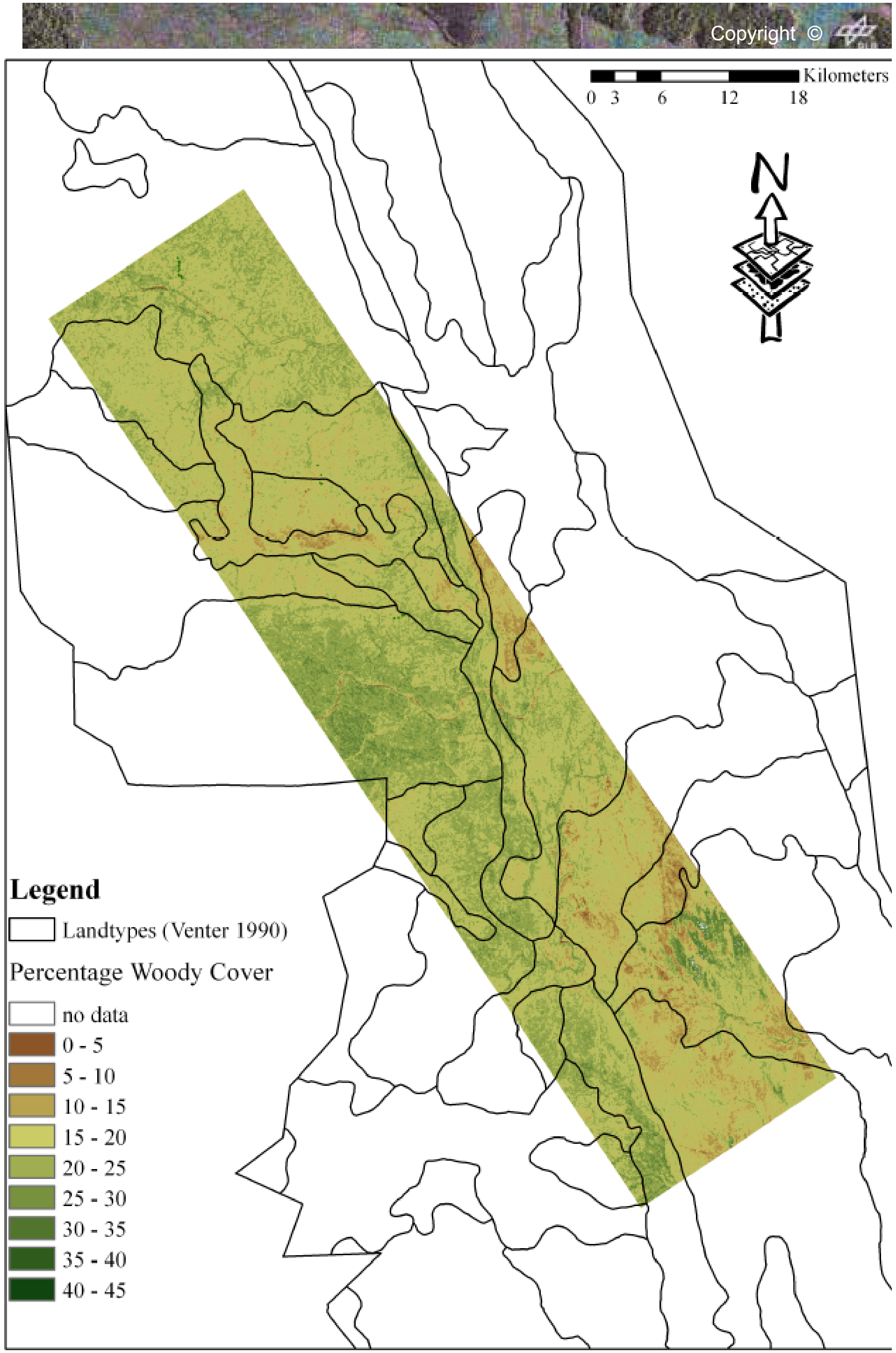

SARvanna project

Methodology – Jena IWC-model – excursus

Chunsky North – Regression Analysis for ALOS PALSAR Data

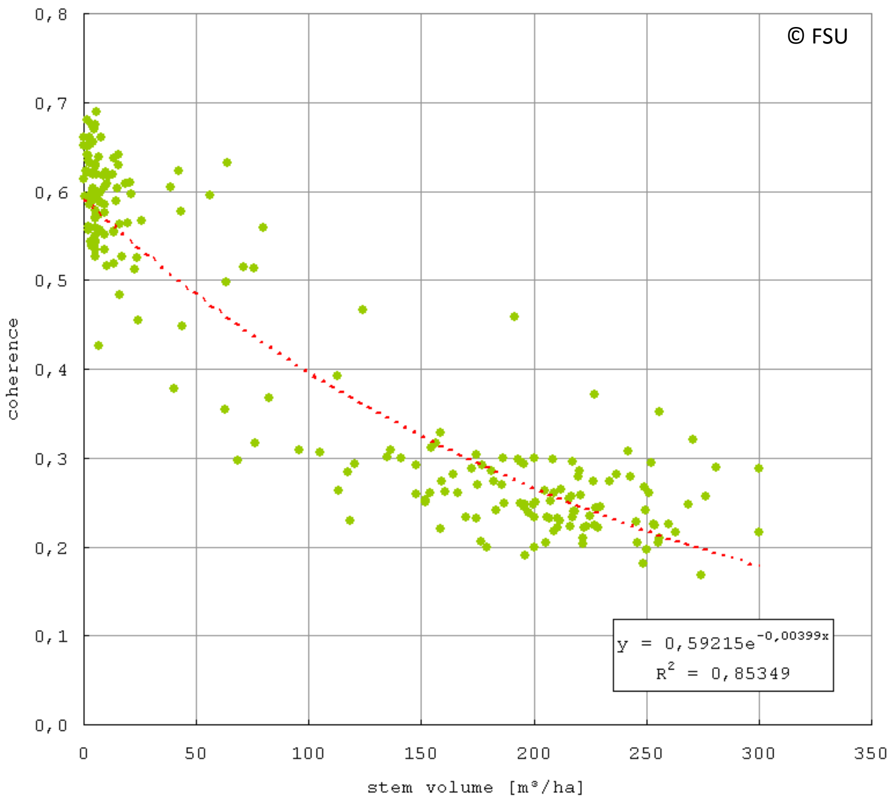

Stem volume vs. coherence
(05feb2008-22mar2008) – 12.5 m data

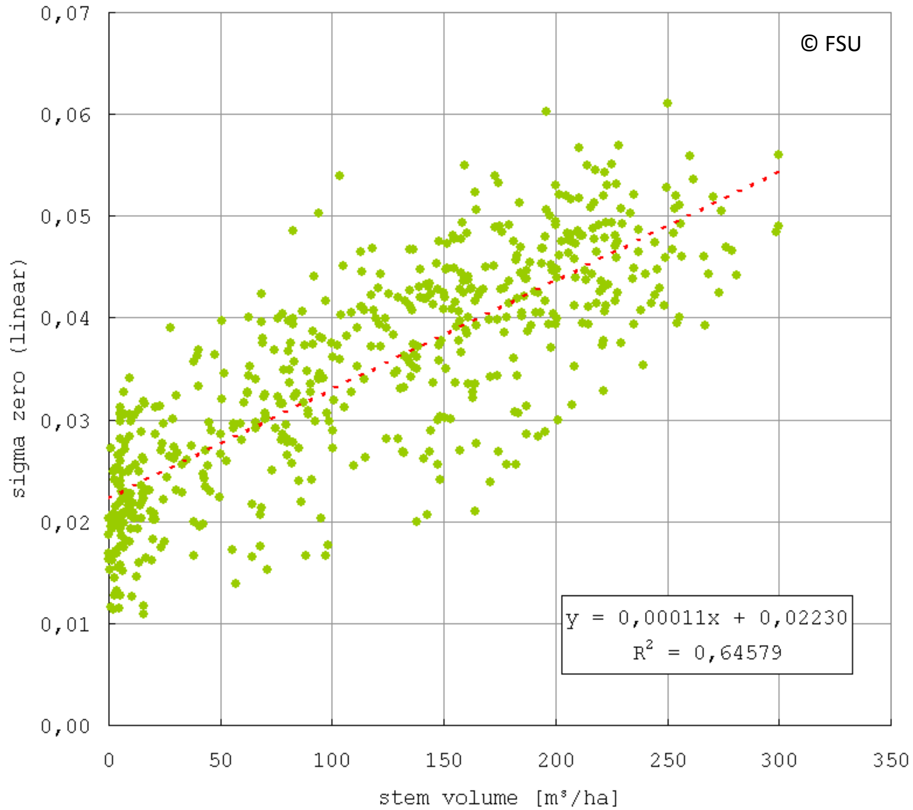

Stem volume vs. backscatter (HV)
(05aug2007) – 12.5 m data

SAREDU

Very significant correlation between SAR data and stem volume!

SARvanna project

Methodology – backscatter model

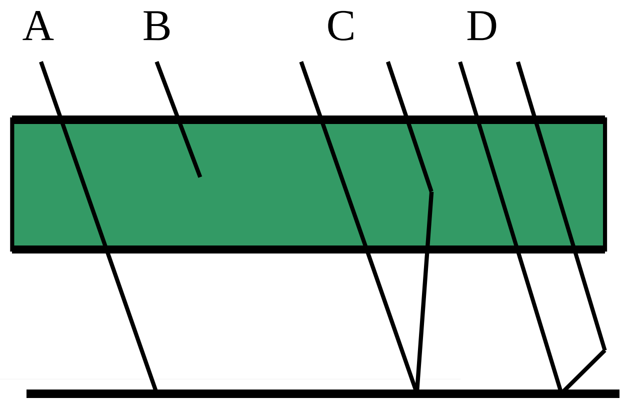

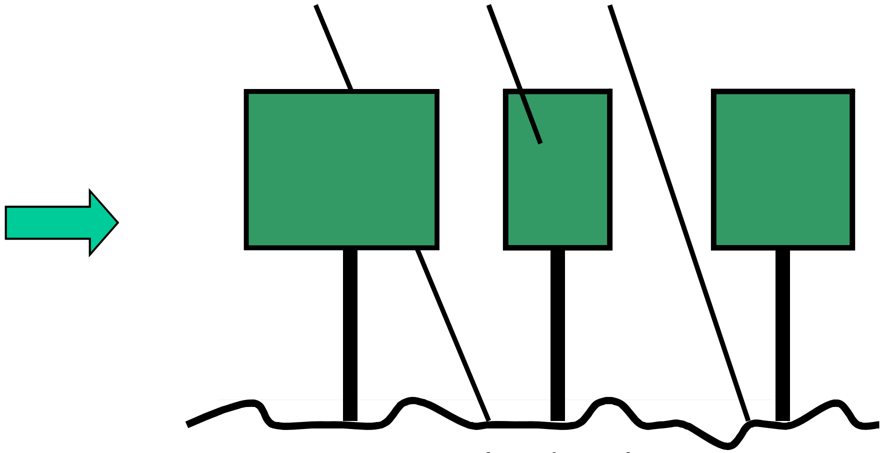

- A water cloud with gaps is closer to reality and easy to handle

$$\sigma^o_{for} = \sigma^o_{gr} e^{-\beta V} + \sigma^o_{veg}\left(1 - e^{-\beta V}\right)$$

Ground backscatter

Forest transmissivity

Vegetation backscatter

- Forest transmissivity is related to canopy closure and tree attenuation

SARvanna project

Coherence modelling - Interferometric Water Cloud Model (IWCM)

$$\gamma_{for} = \gamma_{gr} \frac{\sigma^{o}_{gr}}{\sigma^{o}_{for}} e^{-\beta V} + \gamma_{veg} \frac{\sigma^{o}_{veg}}{\sigma^{o}_{for}} \left(\frac{1-e^{-\beta V}}{1-e^{-\alpha h}} \right) \left(\frac{\alpha}{\alpha - j\omega} \right) \left(e^{-j\omega h} - e^{-\alpha h} \right)$$

The total forest coherence is a sum of 2 contributions:

Ground coherence, Γ_{gr}

Vegetation coherence, Γ_{veg}

Model considers tree attenuation (α), gaps (β), InSAR geometry (ω)

Empirical relationship

$$\gamma_{for} = \gamma_{gr} e^{-\beta V} + \gamma_{veg} \left(1 - e^{-\beta V}\right)$$

No dependence upon InSAR geometry, forest backscatter and canopy structure

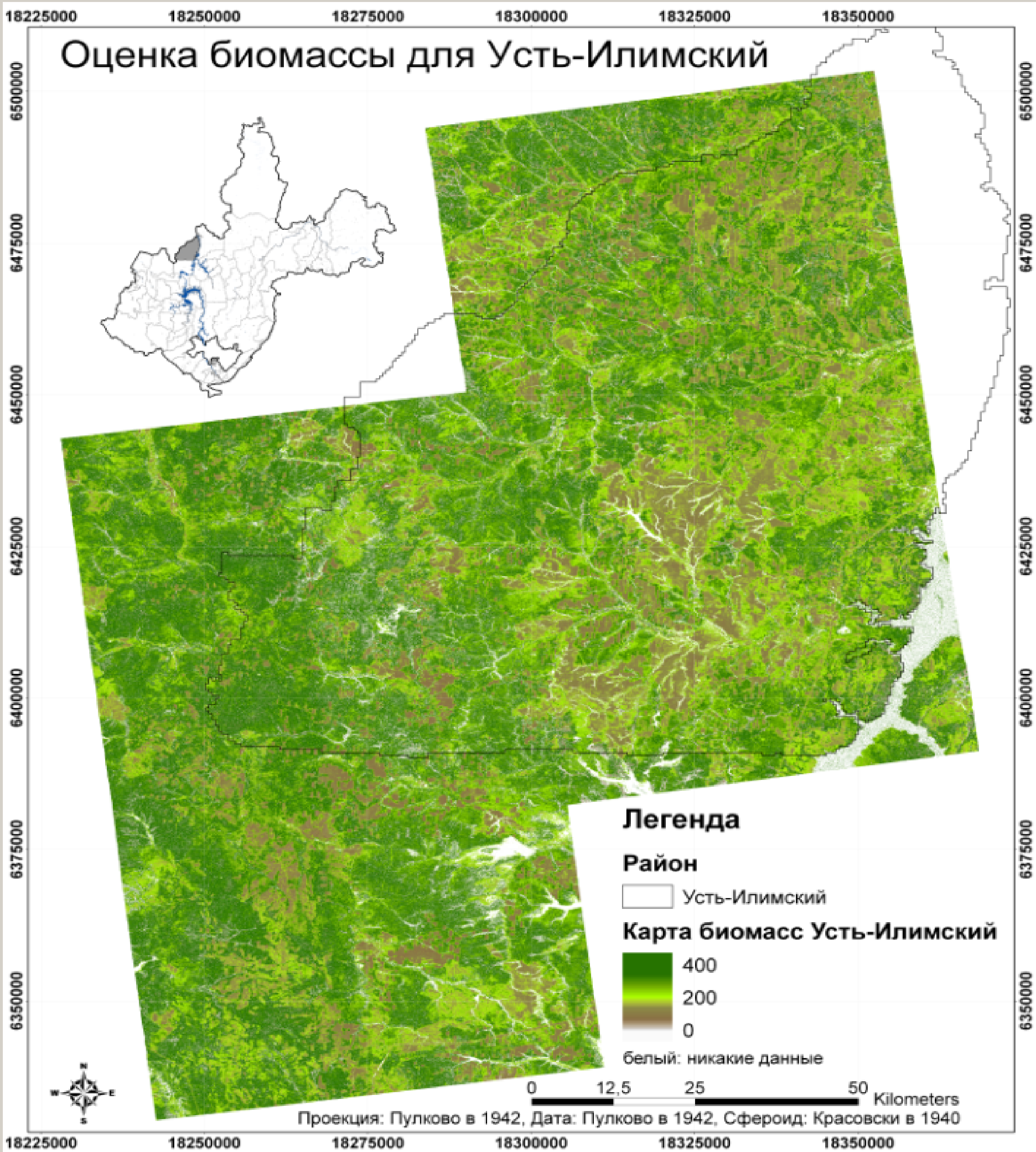

SARvanna project

Biomass map based on the **Jena IWC-Model** (Interferometric Water Cloud Model). Resolution 12,5 m.

Data Source:
ALOS PALSAR,
L-HH coherence from December 2008 until February 2009.

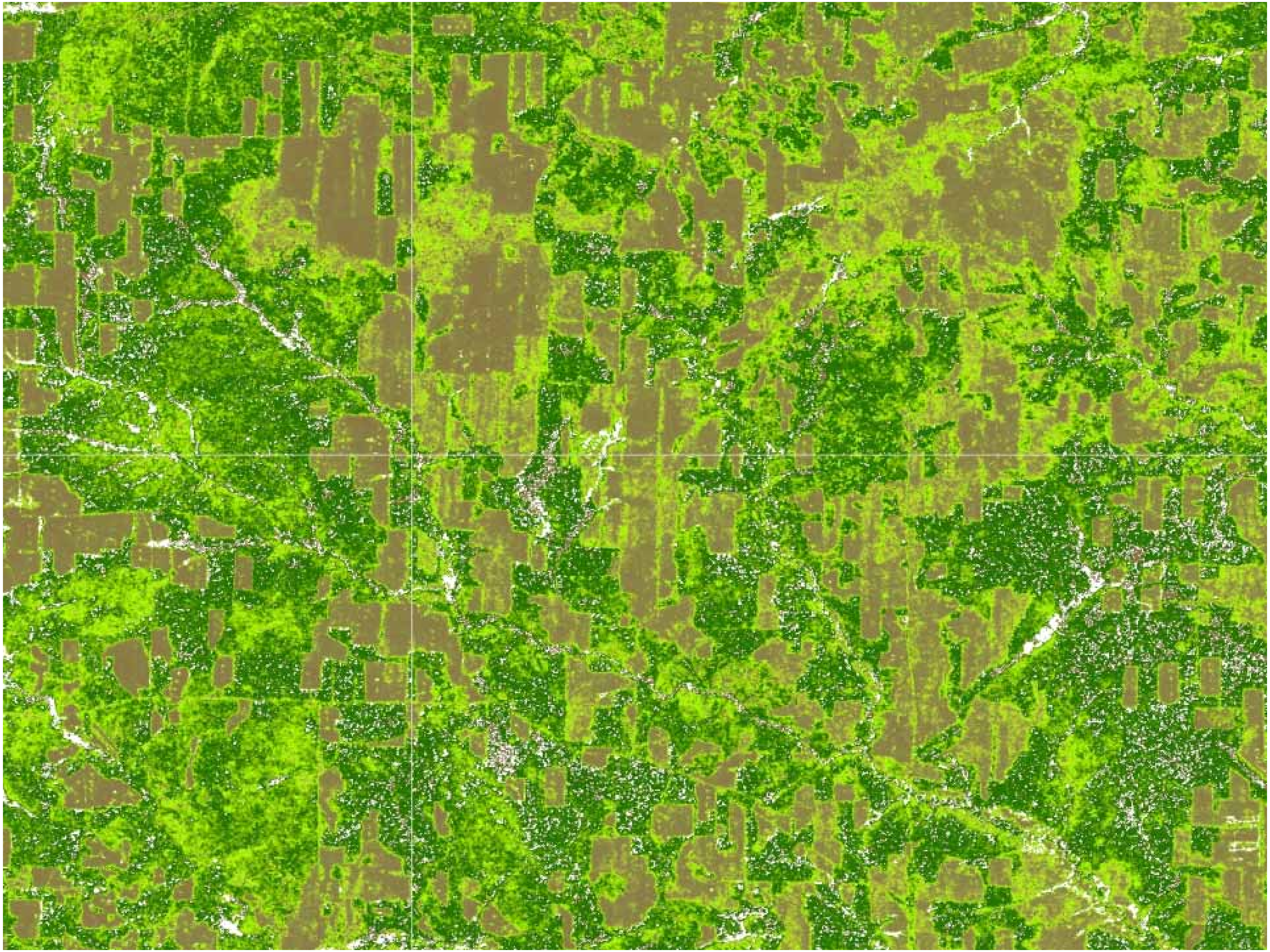

Sentinel-1A Deforestation over Brazil

Acquisition: 21 April 2014
Mode: TOPS IW HH/HV

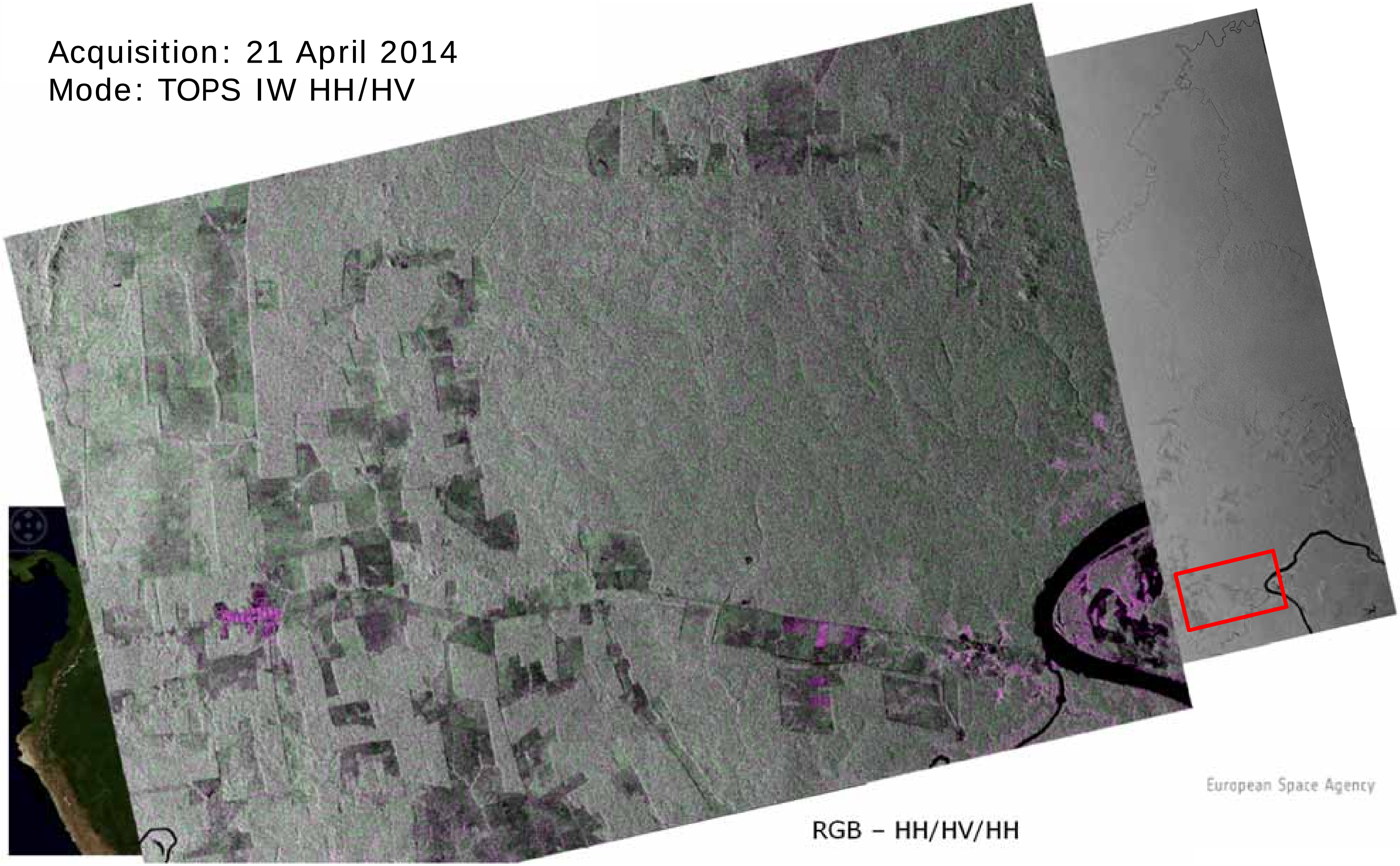

European Space Agency

Agricultural Applications of SAR Data

Tanja Riedel

Robert Eckardt

Earth Observation
Institute of Geography
Friedrich-Schiller-University Jena

SAREDU
Remote Sensing Education Initiative

System Parameters - Frequency

Airborne E-SAR data acquired on June 14, 2000 near Alling, Bavaria, Germany

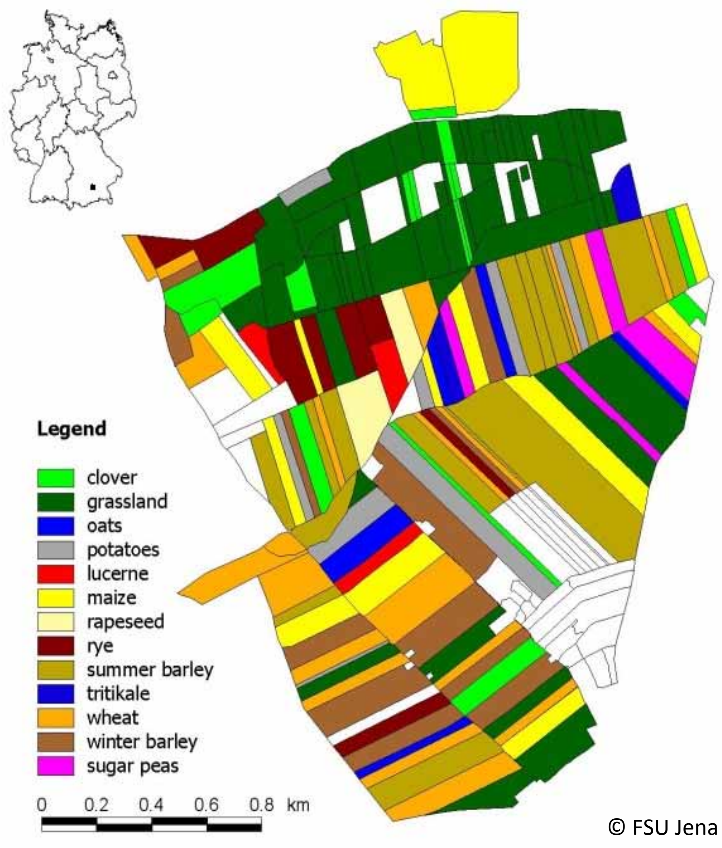

Fig.: X-VV / C-VV / L-VV composite (left) and crop type map (right)

System Parameters - Polarisation

Airborne E-SAR data acquired on June 14, 2000 near Alling, Bavaria, Germany

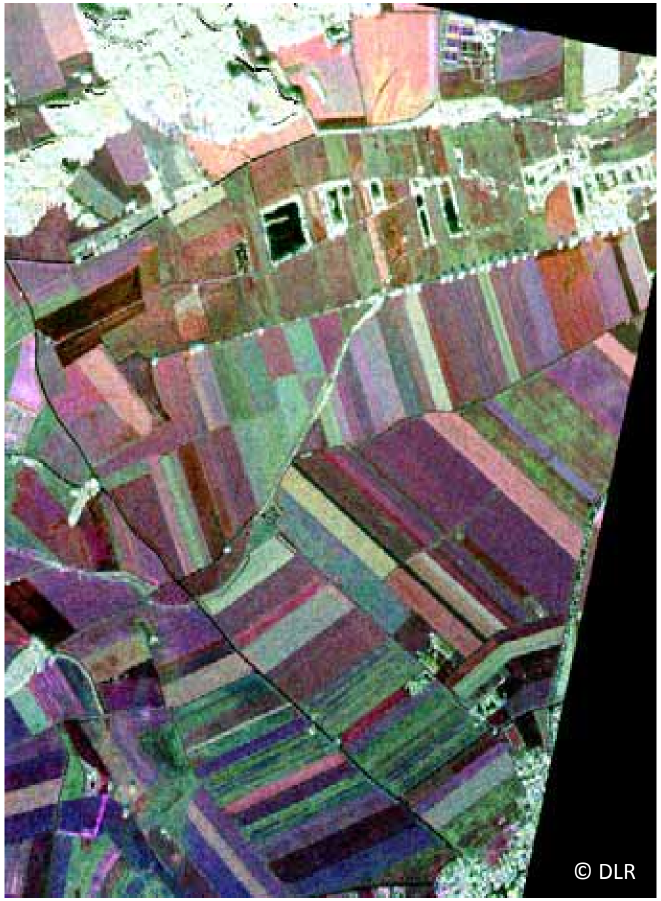

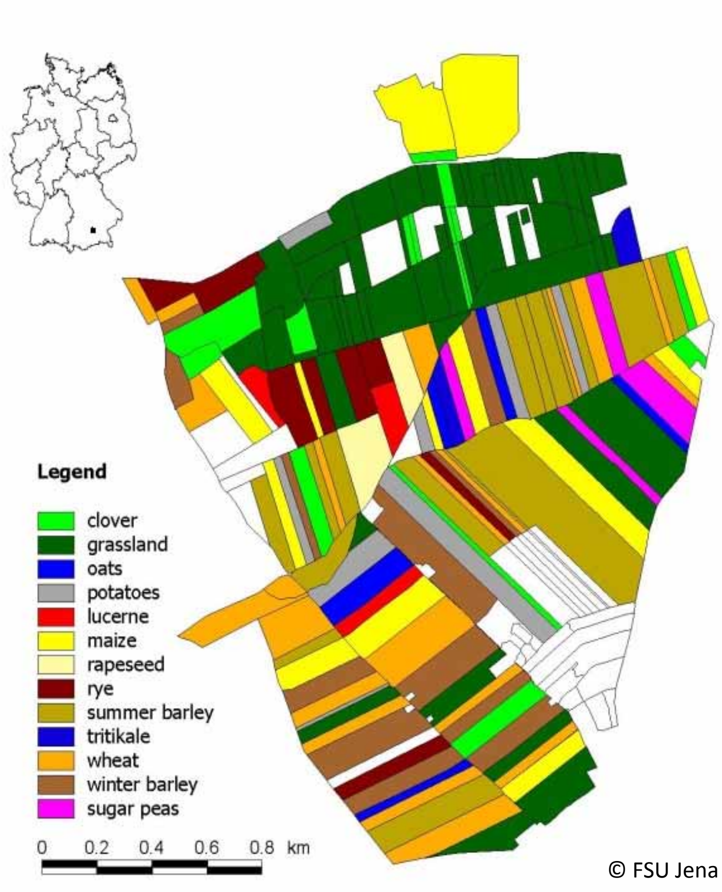

Fig.: L-VV-L-HV-L-HH composite (left) and crop map (right)

Crop type mapping – selected image features

Winter vs. spring crops

Early growing season

Spring crops → bare fields → surface scattering

Winter crops → some degree of volume scattering

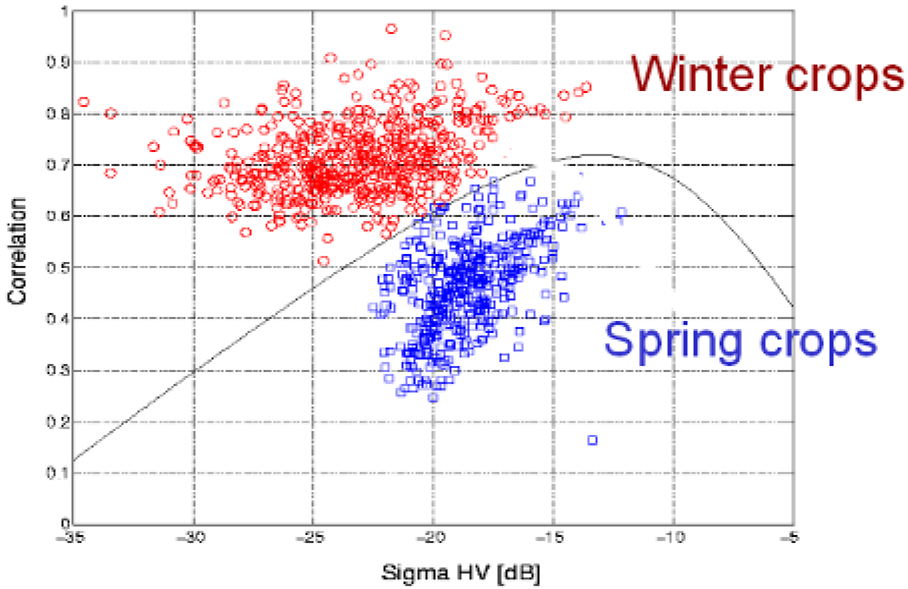

Fig.: HH-VV correlation versus HV backscatter for winter (red) and spring (blue) crops – airborne EMISAR data, April 17, Foulum test site (Quegan et al., 2003)

Parameter 1	*Parameter 2*	*Spring OK (No. & %)*	*Spring Bad (No. & %)*	*Winter OK (No. & %)*	*Winter Bad (No. & %)*	*Overall (%)*
VV	*HV*	524 (94.2)	32 (5.8)	395 (88.0)	54 (12.0)	92.6
Correlation	*HV*	524 (94.2)	32 (5.8)	432 (96.2)	17 (3.8)	95.1
Alpha	*Entropy*	535 (96.2)	21 (3.8)	413 (92.0)	36 (8.0)	94.2
Correlation	*Entropy*	539 (96.9)	17 (3.1)	392 (87.3)	57 (12.7)	92.6
HV-HH	*HV-VV*	512 (92.0)	44 (8.0)	421 (93.7)	28 (6.3)	92.8
RR-RL	*HV-VV*	506 (91.0)	50 (9.0)	428 (95.3)	21 (4.7)	92.9
HH	*HV*	452 (81.3)	104 (18.7)	424 (94.4)	25 (5.6)	87.1
Entropy	*RR-RL*	531 (95.5)	25 (4.5)	418 (93.1)	31 (6.9)	94.4

Tab.: Potential of various parameters for differentiation of winter and spring crops – airborne EMISAR data, April 17, Foulum test site (Quegan et al., 2003)

Quegan et al., 2003

Crop type mapping – selected image features

Rice

- Mapping of paddy rice fields
- HH/VV ratio at X- or C-band
- Dynamic range (sowing – plant maturity phase)
  - C-band: 4 – 7 dB
  - X-band: 8 – 12 dB

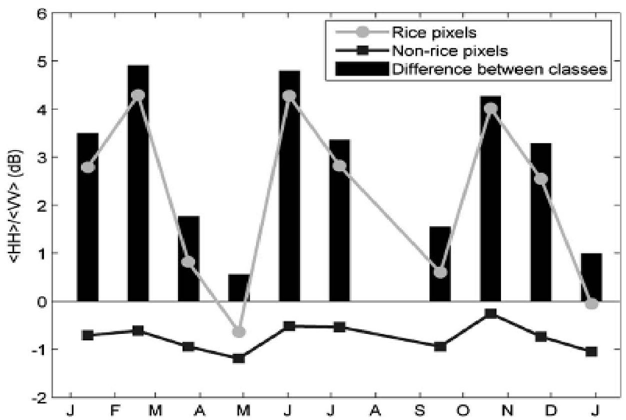

Fig.: Envisat ASAR polarization ratio of the mean intensities HH/VV for pixels defined as (grey circles) rice and (black square) non-rice in the GIS database. Black bars represent the difference of this ratio between the two classes (Bouvet et al., 2009)

Fig.: TerraSAR-X false colour composite image (HH / VV / HH-VV) of a test site in the mouth of the Guadalquivir river, SW of Spain, acquired on August 4. Cultivated rice fields are identified in pink colour (Lopez-Sanchez et al., 2011)

SAREDU Remote Sensing Education Initiative

PRELIMINAY RESULTS
RICE MONITORING

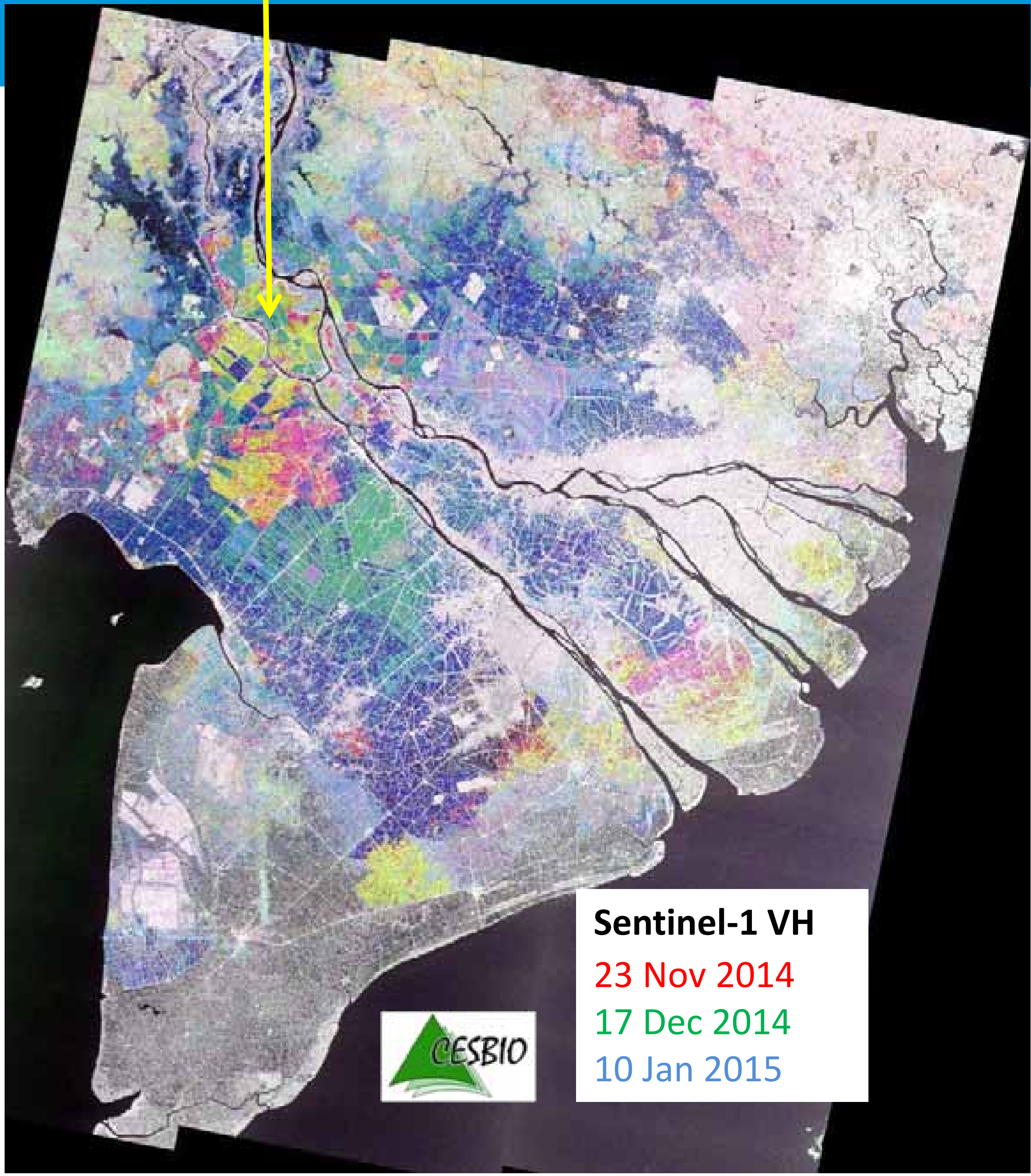

Asia- RICE
Technical Demonstration Site:
The Mekong River Delta
(~250 x 300 km)

Sentinel-1 data acquired every 12 days (resolution 40m or 10m):

1 - 30 Oct 2014
2 - 11 Nov 2014
3 - 23 Nov 2014
4 - 5 Dec 2014
5- 17 Dec 2014
6- 10 Jan 2015

The period corresponds to
. Recession of flood waters
. For fields protected by dykes: the end of Autumn-Winter crop and the beginning of Winter-Spring crop
(e.g. in the An Giang Province)

Bouvet & Le Toan

PRELIMINAY RESULTS
RICE MONITORING
Rice crop calendar for local/regional survey and inputs to rice growth models

The An Giang province (80 km x 80 km)

Crop calendar in the An Giang Province

Crop season	Nov.	Dec.	Jan.	Feb.	Mar.	Apr.	May	June	July	Aug.	Sep.	Oct.	Nov.	Dec.
Winter-Spring crop														
Summer-Autumn crop														
Autumn-Winter crop														

November-December: end of Autumn-Winter crop and beginning of Winter-Spring crop

Crop calendar using the first Sentinel-1 data

- Planted around 11-12- 2014
- Planted between 11-11 and 23-11
- Planted on 23 -11
- Harvested between 23-11 and 5 -12, and planted again around 5-12
- Harvested between 23-11 and 5-12, and planted again between 5 and 17 -12
- Harvested between 17 -12 and 10 -01-2015

Bouvet & Le Toan

European Space Agency

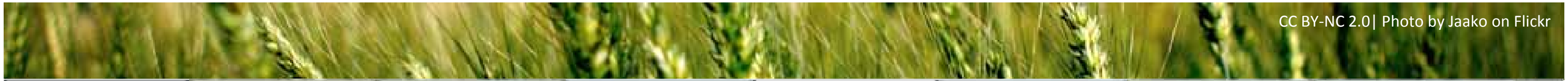

Crop Type Mapping

Potential of multipolarized SAR data @ C-band

- Rape: cross-polarized backscatter from twigs and pods
- Corn: dominant soil backscatter
- Cereals: attenuated soil backscatter
- Sugar beets: soil backscattering and scattering from leaves

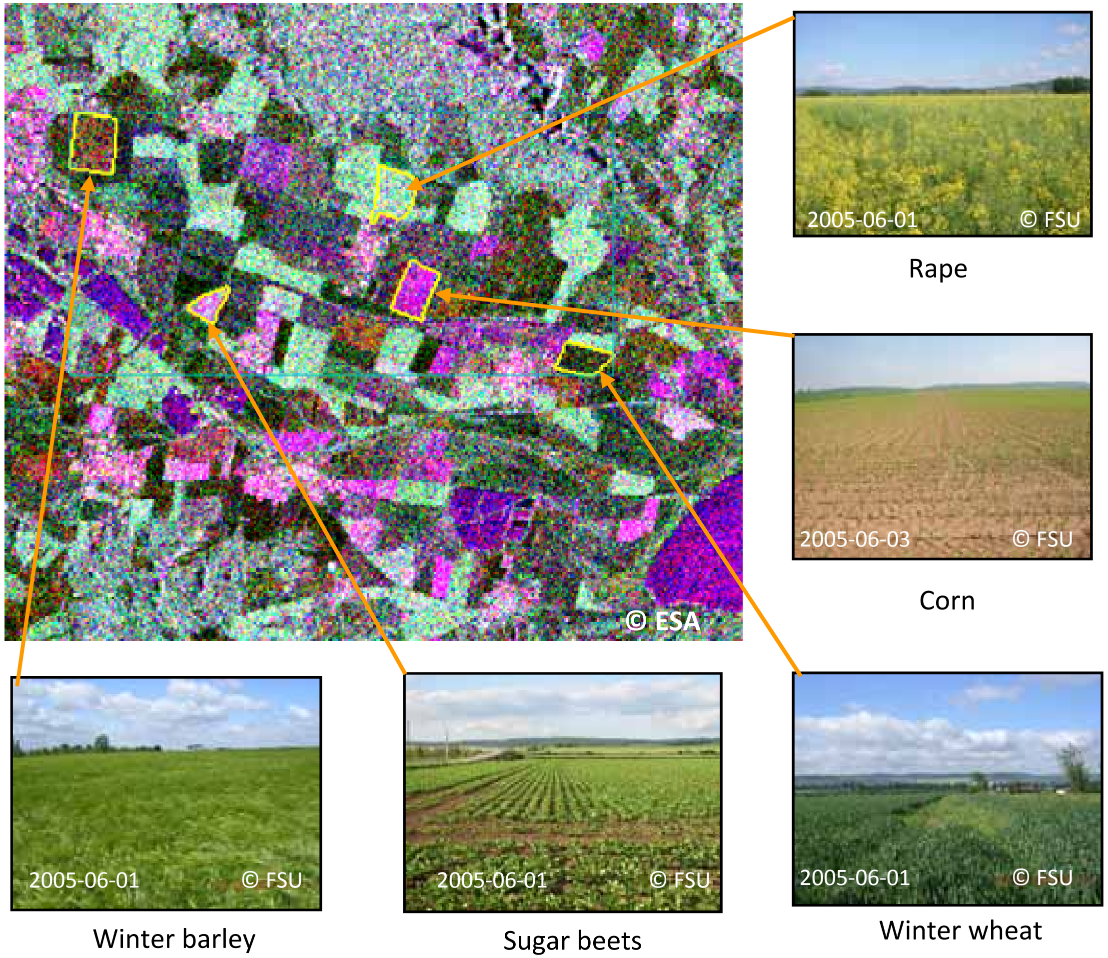

Fig: Potential of multipolarized SAR data for crop-type classification – C-band RGB composite ASAR HH / ASAR HV / ERS-2 acquired on June 6, 2005 over the Nordhausen test site, Germany (© FSU Jena)

SAREDU

Crop monitoring / biophysical parameters

Could we recognize cultivation problems / field heterogeneities in SAR data? Example 1

summer barl
south: 60 – 70 cm / north

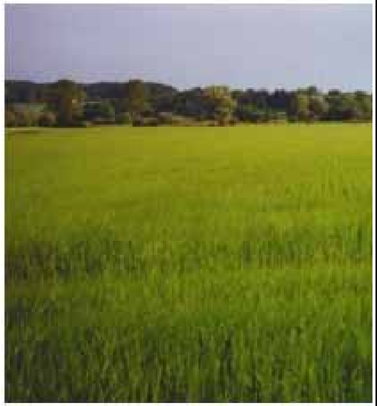

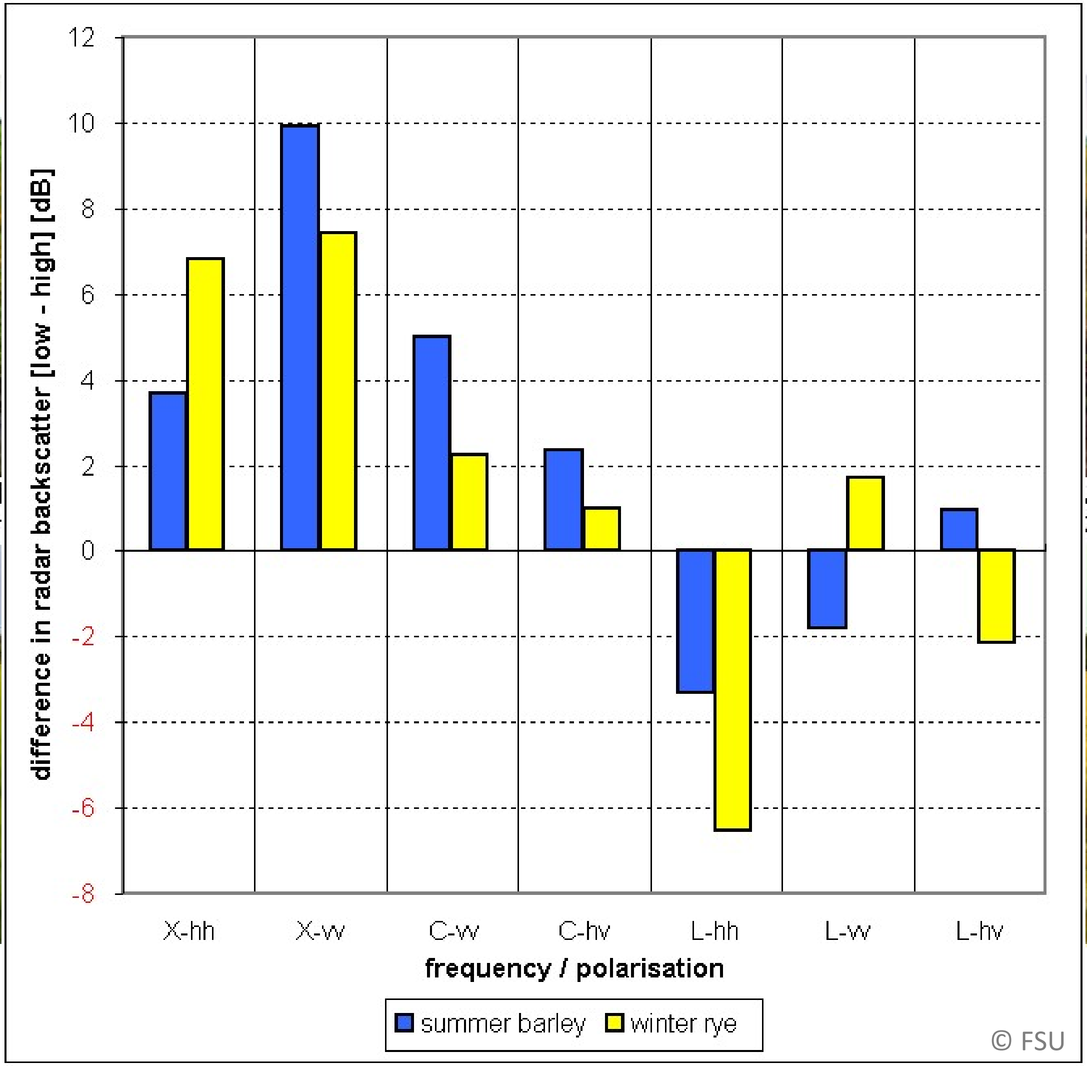

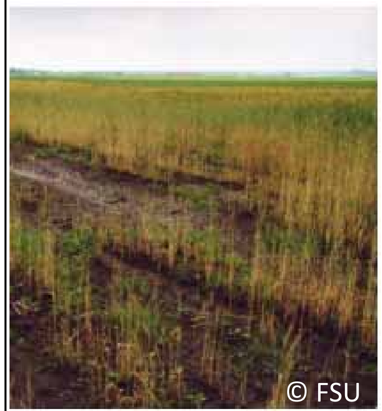

vinter rye
20 cm / north: 30 – 60 cm

Crop type mapping – classification example 4

C-band

- Multitemporal ASAR & ERS-2 from 2005, test site Nordhausen, Thuringia, Germany

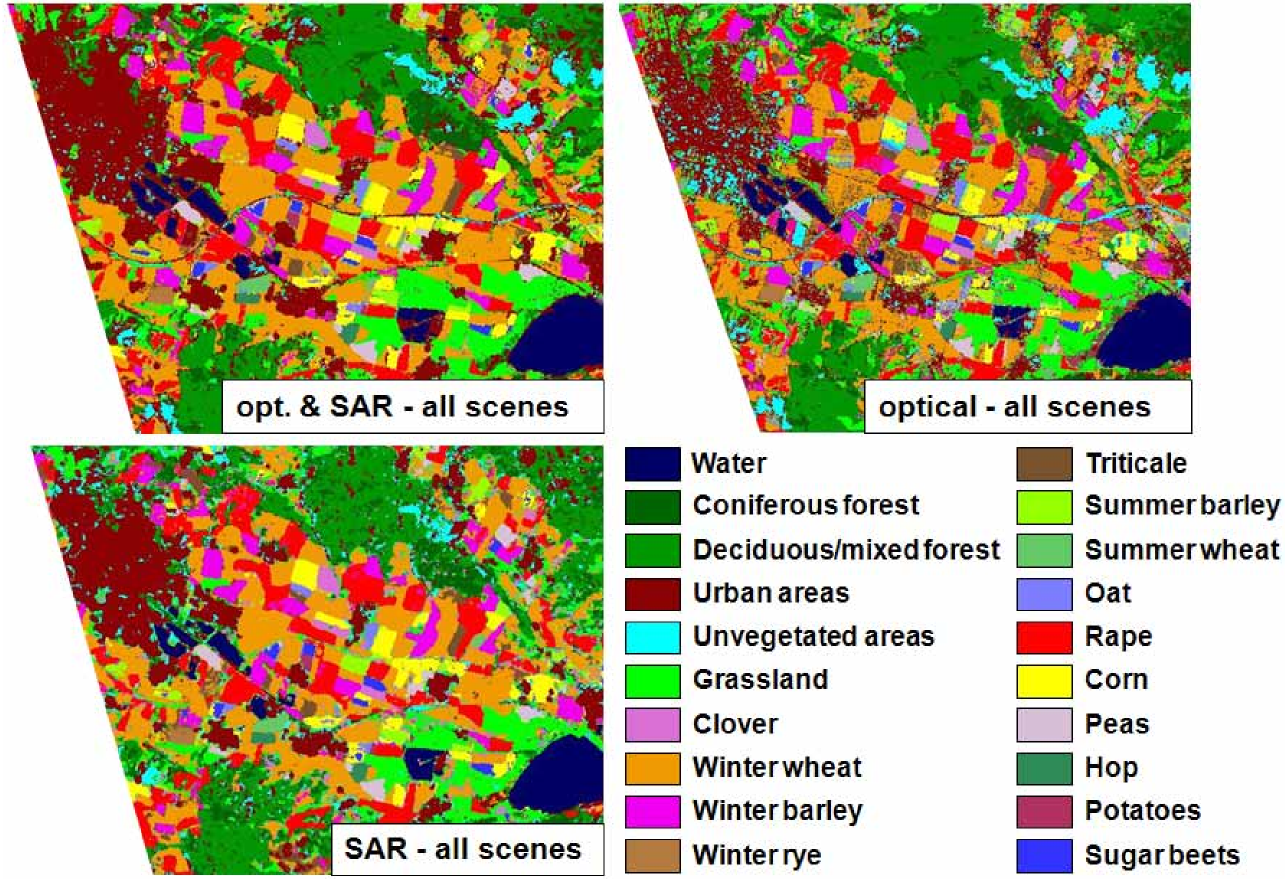

Fig.: Land cover maps – achieved overall accuracies:
optical & SAR: 83,7%;
optical: 77,9%;
SAR: 80,2%
(© FSU, 2007)

SAREDU

Soil parameter retrieval – application example 4

Soil moisture under vegetation – SAR polarimetry

- Airborne L-band E-SAR data acquired within the AgriSAR, OPAQUE and SARTEO campaign over three test sites in Germany
- Comparison of different decomposition approaches

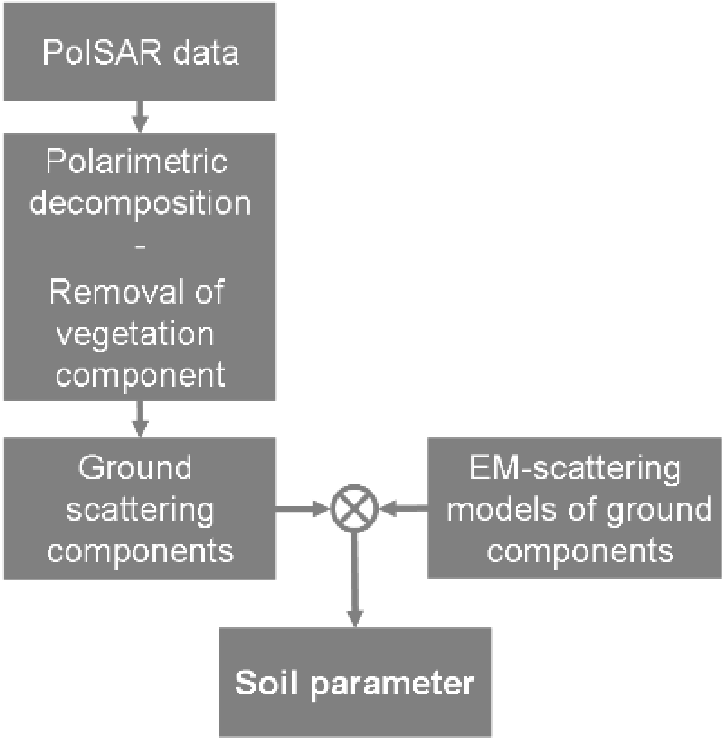

Fig.: General workflow of soil parameter retrieval from polarimetric SAR data using polarimetric decomposition techniques (Jagdhuber, 2012)

Jagdhuber, 2012

Soil parameter retrieval – application example 4

Soil moisture under vegetation – SAR polarimetry

- **Results**
  - High potential → single angular hybrid decomposition approach (rmse: 5-11%; inversion rate: 97%)
  - Further improvement using multi-angular SAR data (not necessarily true)

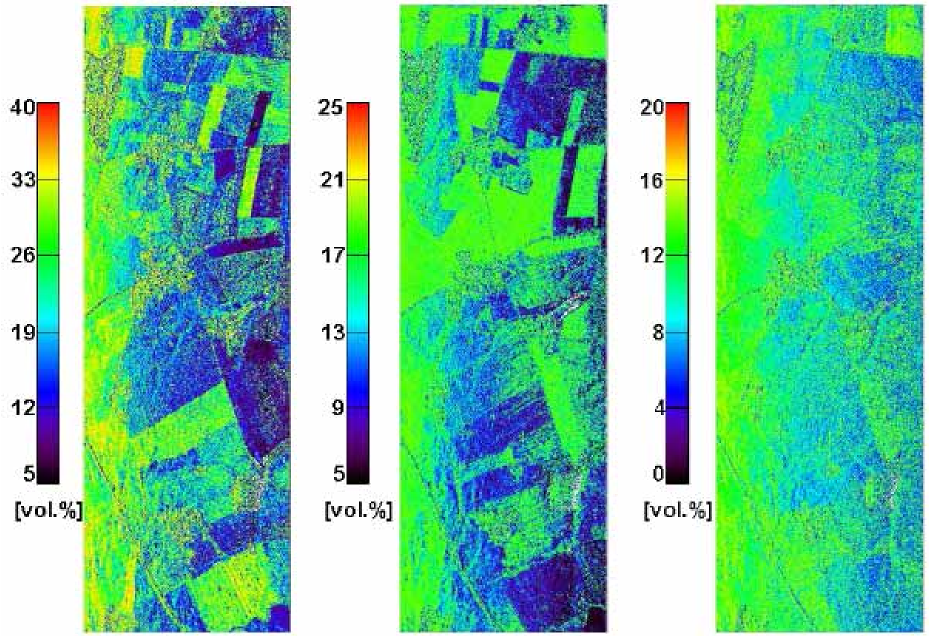

For more details see module 2300: radar polarimetry

Fig.: Results for soil moisture inversion under vegetation cover using a single angular hybrid decomposition and inversion approach – AgriSAR campaign. Left – April 19, 2006; middle: June 7, 2006; right: July 5, 2006; SO – summer oat, WW – winter wheat (Jagdhuber, 2012)

Jagdhuber, 2012

Soil parameter retrieval – application example 5

Soil surface roughness under vegetation – SAR polarimetry

- Airborne L-band E-SAR data acquired within the AgriSAR campaign over Demmin, Germany
- Methodology: modified X-Bragg ratio

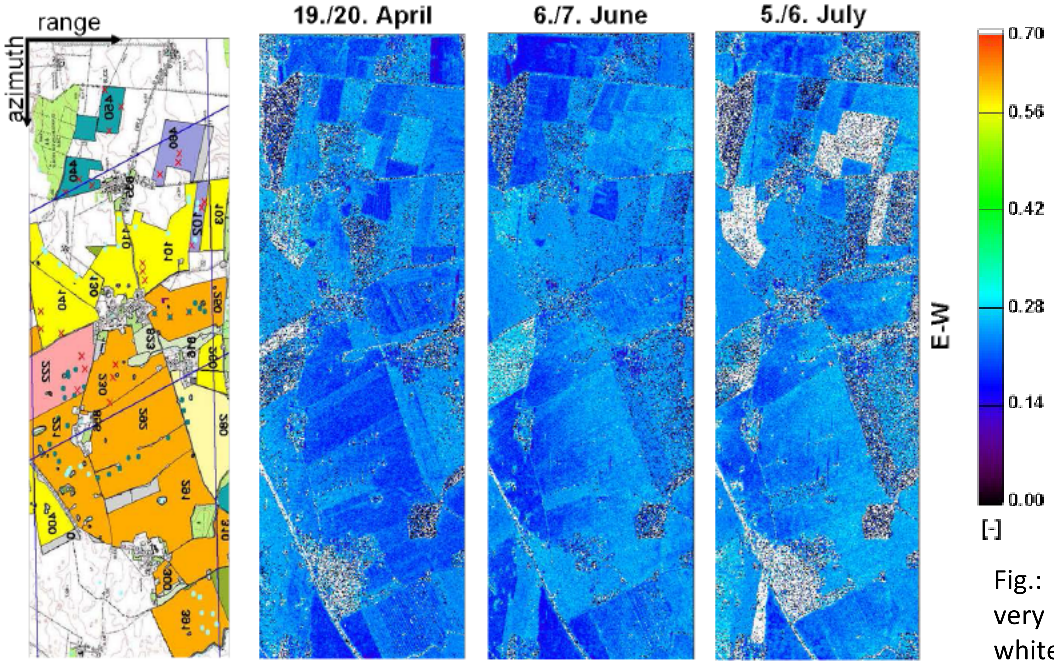

Fig.: Estimated soil roughness (ks). Areas with very rough soil conditions (ks>0.7) are masked white (Jagdhuber, 2012)

Jagdhuber, 2012

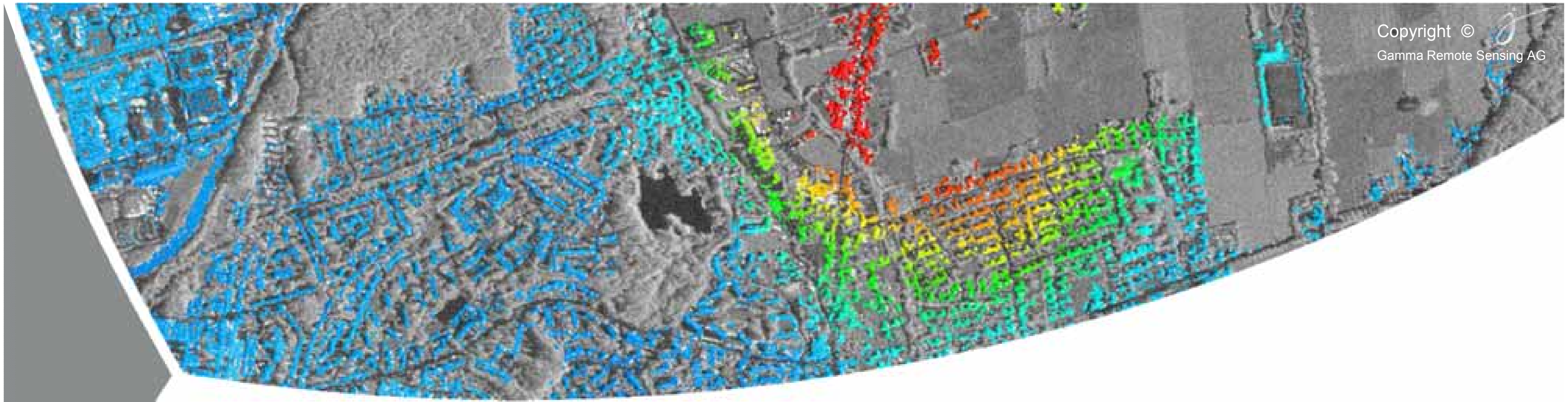

SAR Applications of the Anthroposphere

Dr.-Ing. Diana Walter

Institute of Geotechnical Engineering
and Mine Surveying, TU Clausthal

DLR

TECHNISCHE UNIVERSITÄT MÜNCHEN

TU Clausthal

SAREDU Remote Sensing Education Initiative

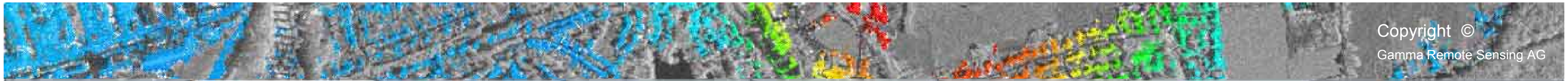

Anthropogenic activities with strong impacts on the environment

- Landscaping, e.g. dumps, reservoir dams and dikes
- Construction works, e.g. bridges
- Tunneling
- Mining (oil, gas, coal, salt, ore, ...)
  - Opencast
  - Underground
- Groundwater extraction
- Nuclear weapons testing
- etc.

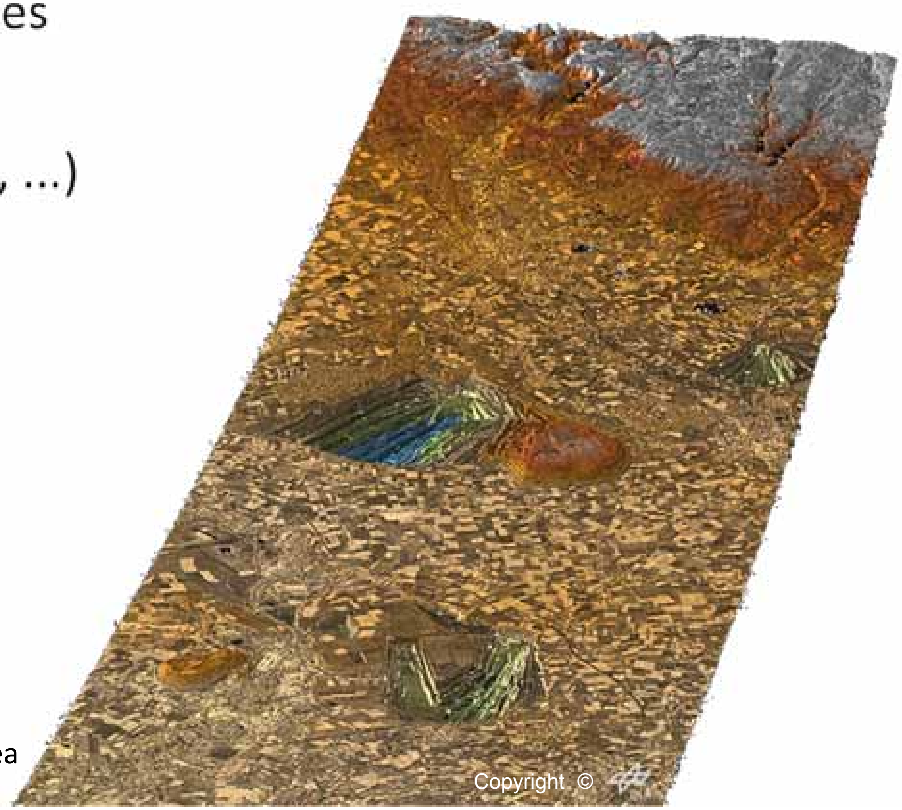

Fig. 1: TanDEM-X DEM of opencast area Garzweiler/ Germany (© DLR)

Geometrical impacts

- Movements of surface points and rigid objects [mm] = Translation
  - Vertical displacements
    - Positive: uplift/heaving
    - Negative: subsidence, setting, sagging, contraction
  - Horizontal displacements

- Surface and object deformations [mm/m]
  - Vertical: tilting ↑↓
  - Horizontal: compression (→ ←) and extension (← →)

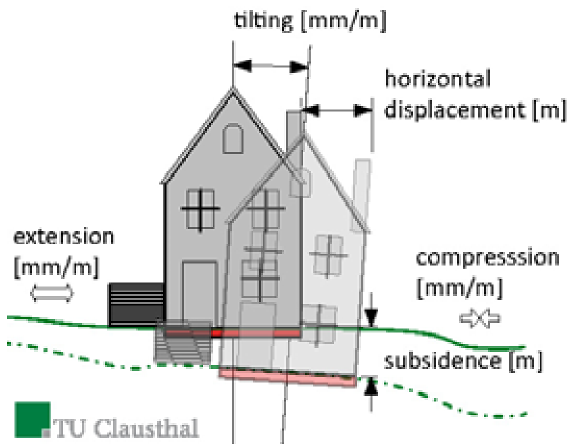

Fig. 2: Translation and deformation (© TUC, D. Walter)

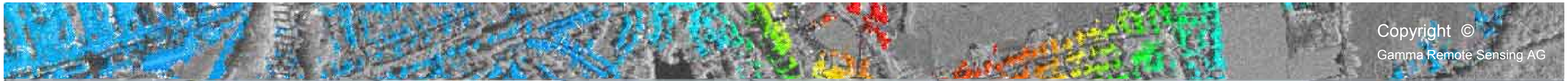

Measurement techniques for displacements at the surface

- Terrestrial methods (levelling, GPS)
- Photogrammetry
- Laser Scanning (ALS)
- **Differential SAR interferometry**
  - **Classical DInSAR**
  - **Stacking**
  - **Small-BAseline Subset technique (SBAS)**
  - **Persistent Scatterer Interferometry (PSI)**
  - **…**

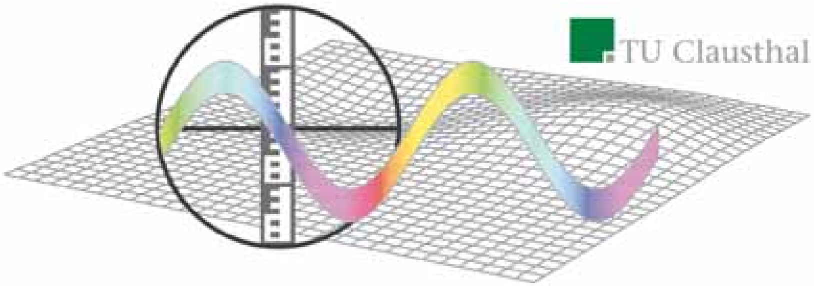

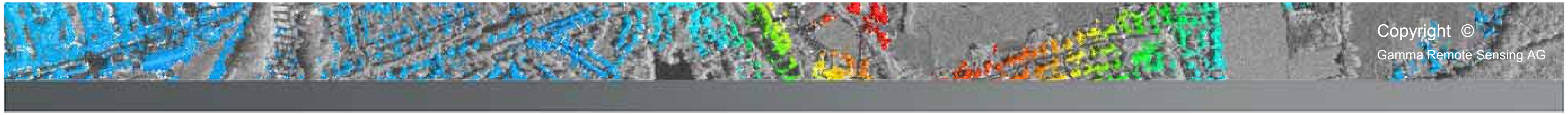

Across-Track Interferometry - Digital Elevation Models

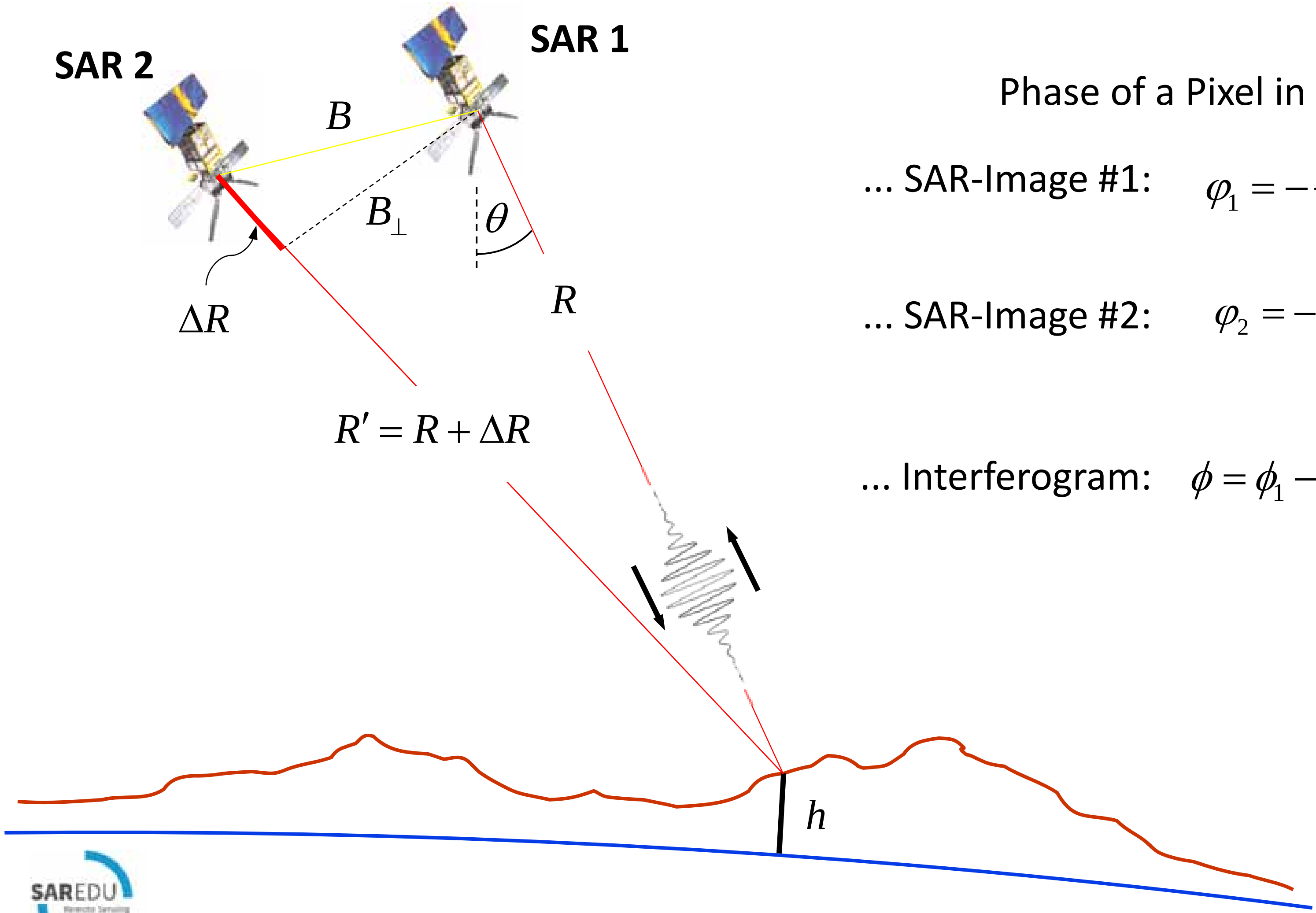

Phase of a Pixel in ...

... SAR-Image #1: $\varphi_1 = -\frac{4\pi}{\lambda} R$

... SAR-Image #2: $\varphi_2 = -\frac{4\pi}{\lambda} (R + \Delta R)$

... Interferogram: $\phi = \phi_1 - \phi_2 = \frac{4\pi}{\lambda} \Delta R$

Fig.: © DLR

SAREDU Remote Sensing Education Initiative

First Capture of an Earthquake by Sentinel-1 Napa Valley (California) M6.0R

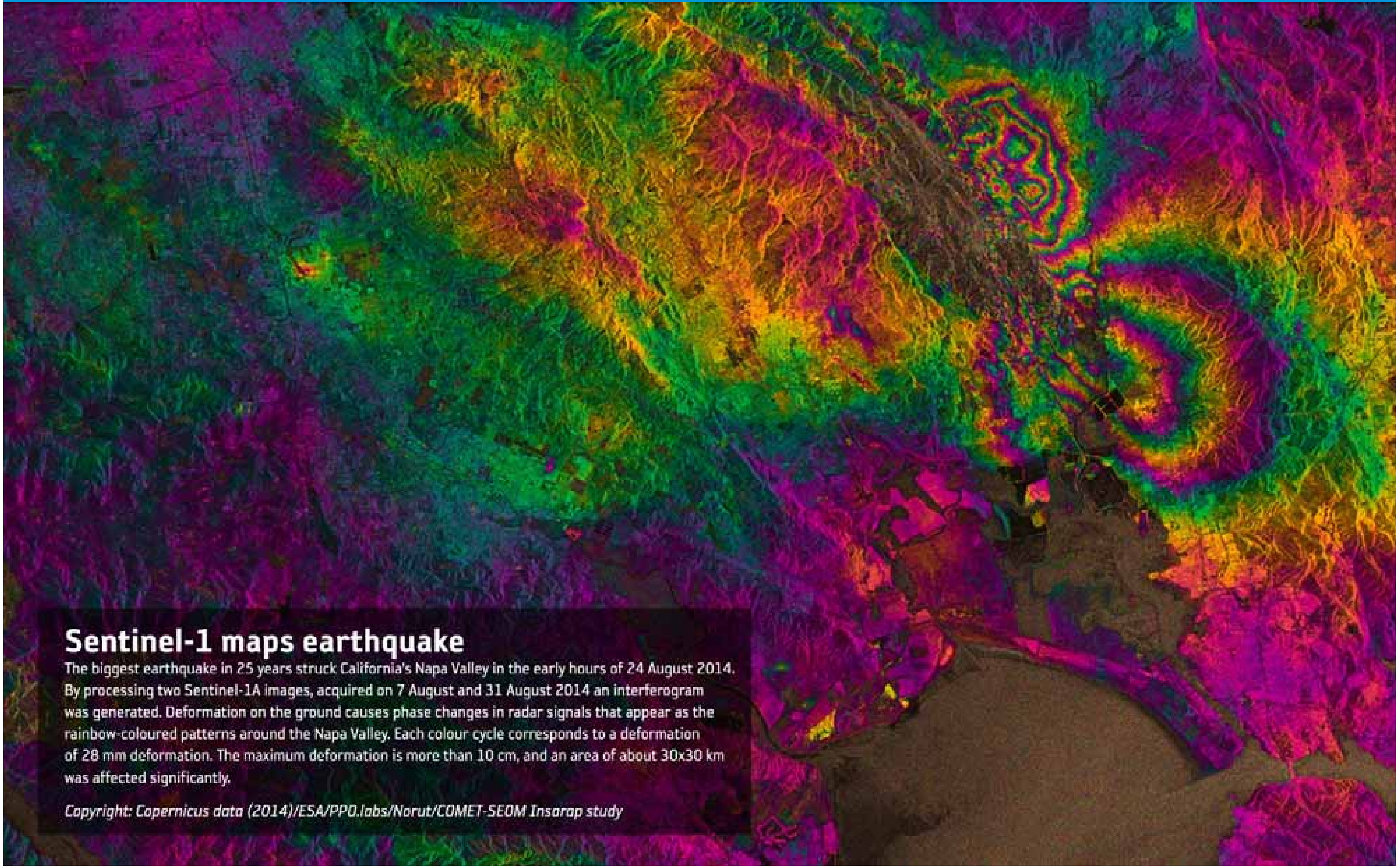

Sentinel-1 maps earthquake

The biggest earthquake in 25 years struck California's Napa Valley in the early hours of 24 August 2014. By processing two Sentinel-1A images, acquired on 7 August and 31 August 2014 an interferogram was generated. Deformation on the ground causes phase changes in radar signals that appear as the rainbow-coloured patterns around the Napa Valley. Each colour cycle corresponds to a deformation of 28 mm deformation. The maximum deformation is more than 10 cm, and an area of about 30x30 km was affected significantly.

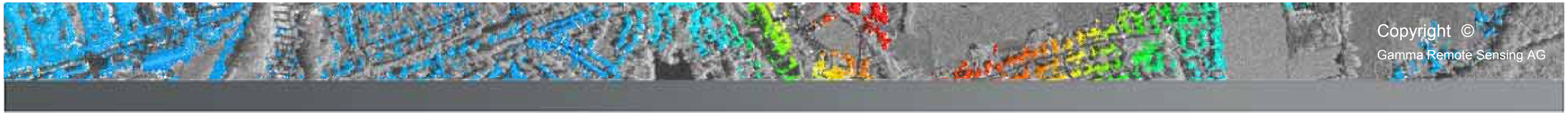

Differential Interferometry

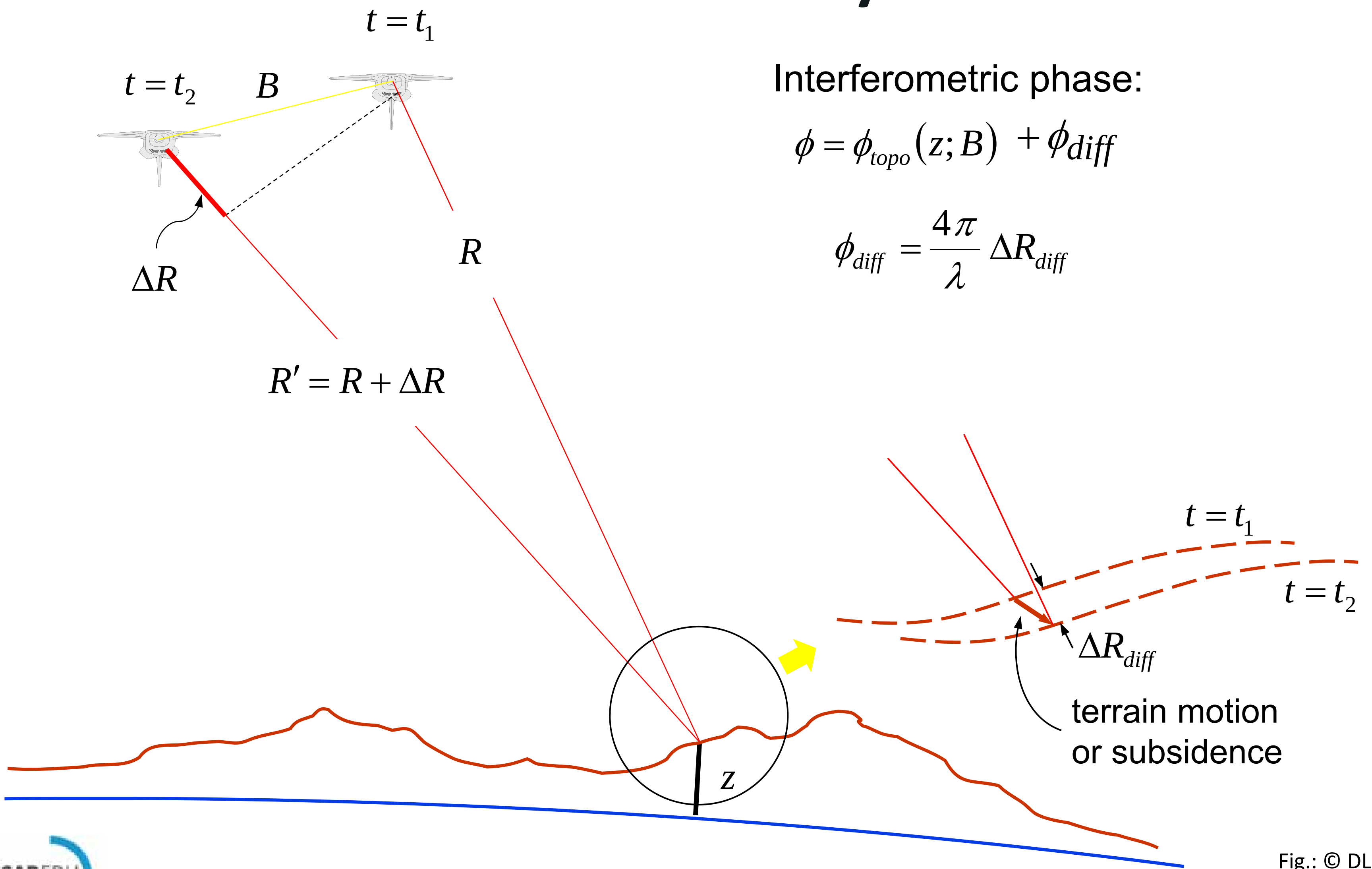

Interferometric phase:

$$\phi = \phi_{topo}(z; B) + \phi_{diff}$$

$$\phi_{diff} = \frac{4\pi}{\lambda} \Delta R_{diff}$$

Fig.: © DLR

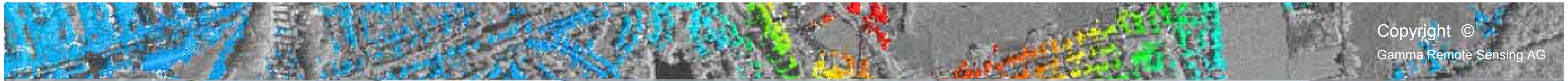

Advantages of SAR interferometry

(compared to terrestrial methods)

- Higher spatial resolution (density of points)
- Higher temporal resolution (repeat cycle e.g. 11 days)
  - Better cost-benefit ratio
- Contactless
- Area-wide deformation monitoring for
  - Large-scale areas
  - Specific objects
- Detection of unknown deformation regions
- Retrospective analysis
  (archived SAR data since 1991, but not global)

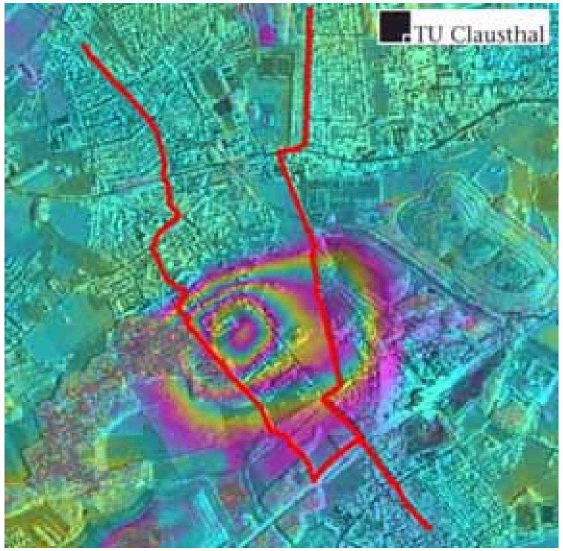

Fig. 3: Spatial resolution - Levelling (red) and DInSAR (background) (© D. Walter)

SAREDU Remote Sensing Education Initiative

I. Underground hard coal mining

- **SAR data:** TerraSAR-X (Stripmap)
- **AOI:** Ruhr region, Germany
- **Time:** Spring 2008
- **Deformation:** Subsidence trough
- **Cause:** Underground mining of hard coal without backfilling of cavities
- **Processing:** Classical DInSAR and Stacking
- **Problems:**
  - Decorrelations in vegetated areas
  - Atmospheric influences → summation of these effects in stacking processing
- **Features:**
  - Changes of deformation rates (doubling after the second period B-C)
  - Shift of subsidence centre (maximum)

SAREDU Remote Sensing Education Initiative

Underground Hard Coal Mining with DInSAR

subsidence trough

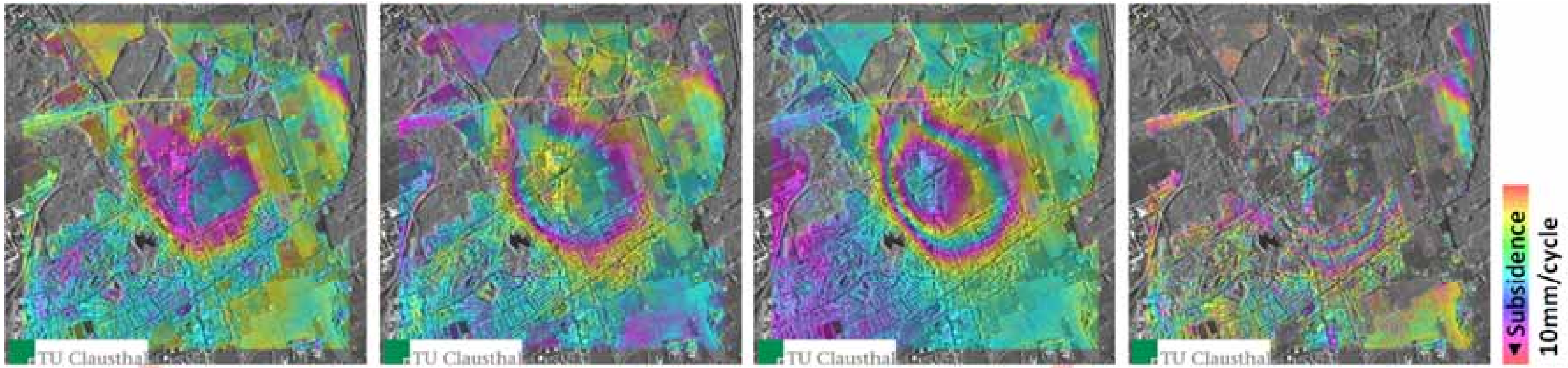

A-B: 11 days, B= 163m
Max: 22mm/month

B-C: 11 days, B = 171m
Max: 27mm/month

C-D: 11 days, B = 28m
Max: 55mm/month

D-E: 22 days, B = 313m
Max: 55mm/month

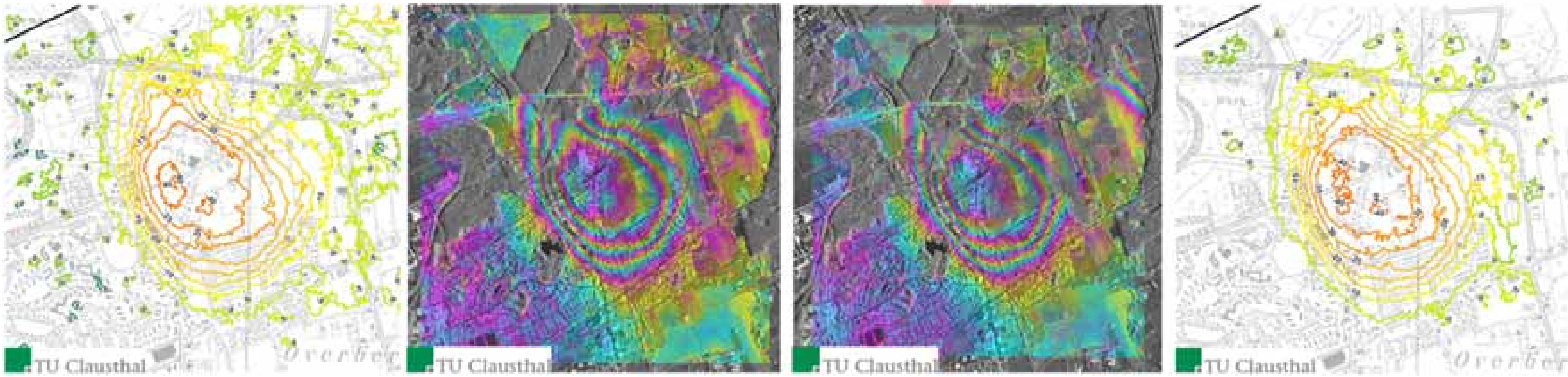

Stacking result (A-B)+(B-C)+(C-D)
Left: Isolines [mm], Right: vertical displacement map

A-D: 33 days, B = 36m
Max: 36mm/month

A-D: Isolines of subsidence [mm]

Fig. 31: © TU Clausthal

SAREDU Remote Sensing Education Initiative

Sentinel-1 First Subsidence Monitoring
Mexico City

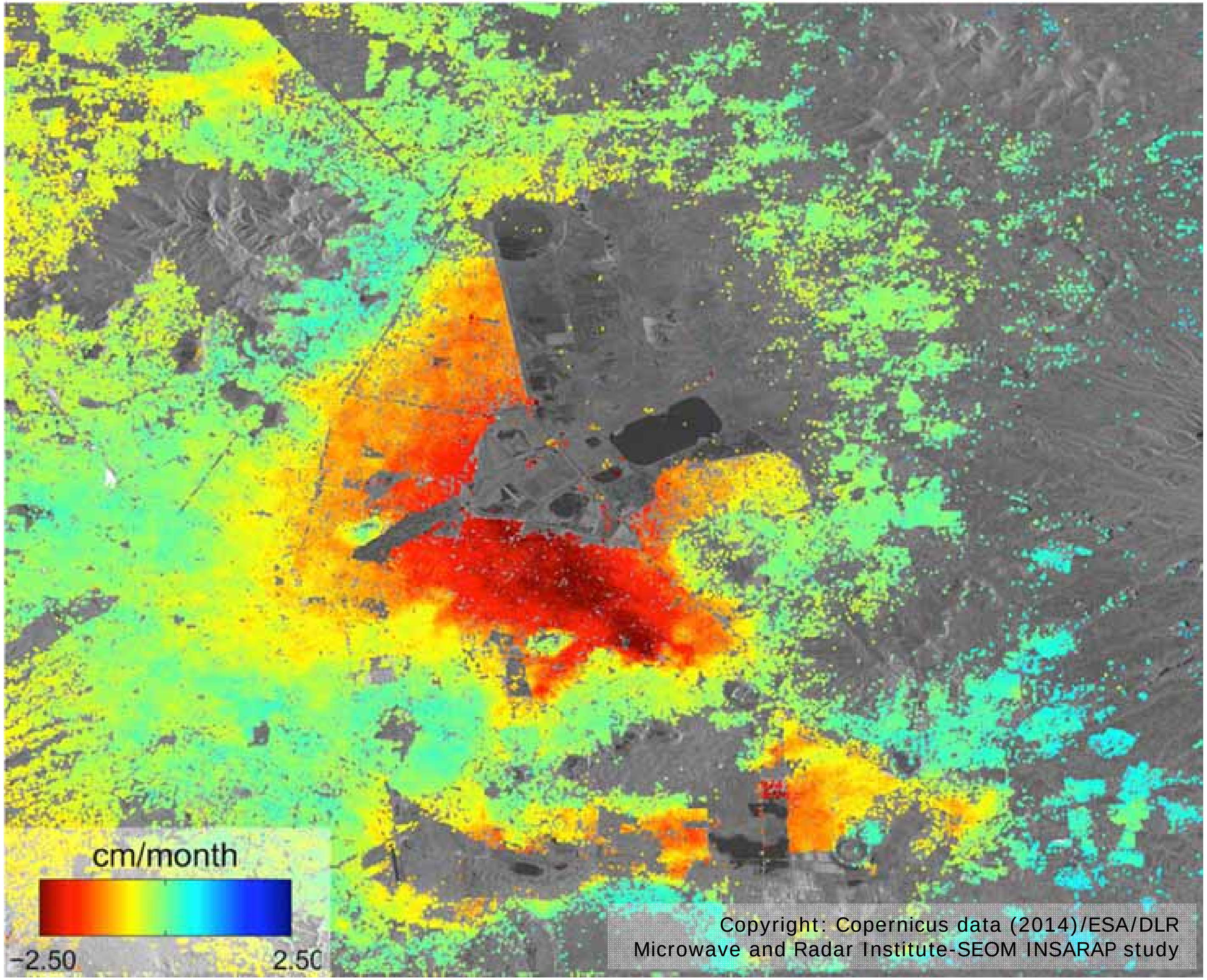

Five Sentinel-1A radar TOPS scans acquired between 3 October and 2 December 2014 were combined to create this image of ground deformation in Mexico City.

The deformation is caused by ground water extraction, with some areas of the city subsiding at up to 2.5 cm/month (red).

seom
scientific exploitation of operational missions
European Space Agency

‘Big Deformation’
Mexico City - Recap

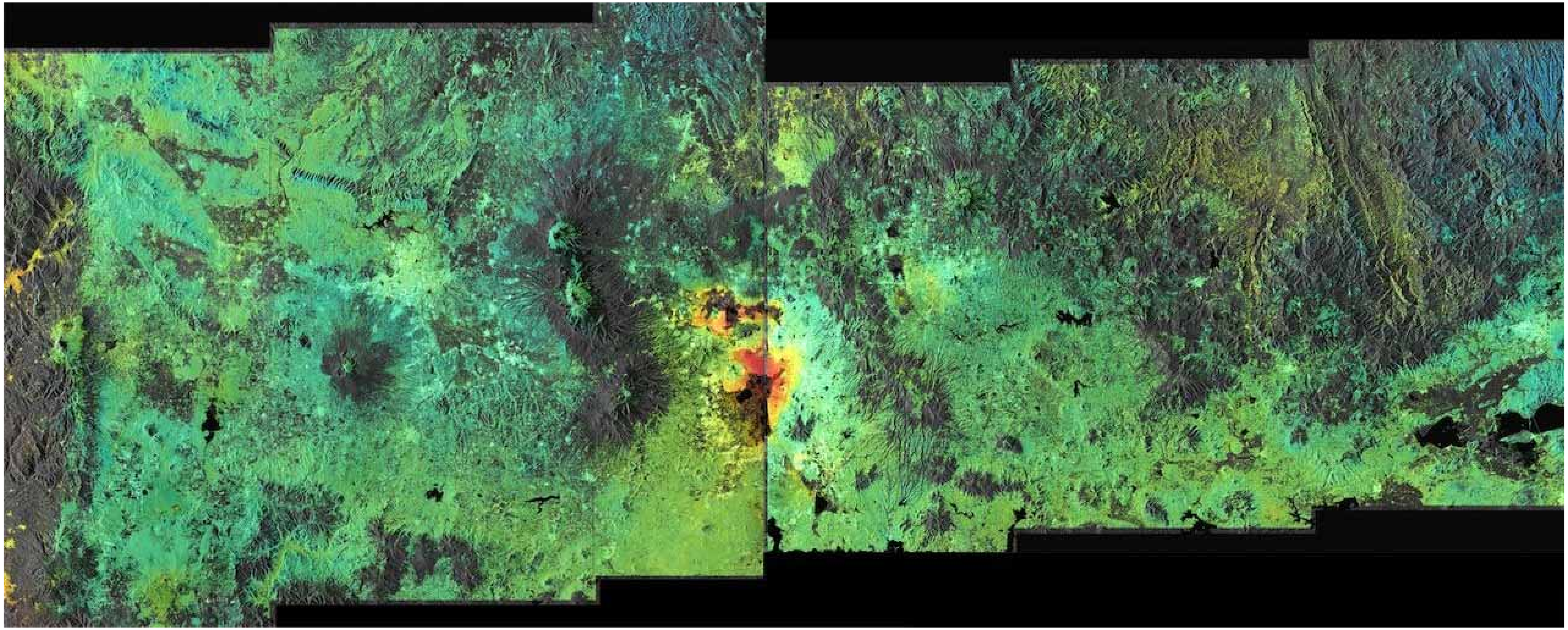

~**500km** (longitude)

European Space Agency

II. Mining coal dump

- **SAR data:** TerraSAR-X (Stripmap)
- **AOI:** Ruhr region, Germany
- **Object size:** ≈ 900 m x 700 m
- **Time:** Spring 2008
- **Deformation:** Settings
- **Cause:** Compaction of material (grains) through imposed load
- **Processing:** Classical DInSAR and Stacking
- **Problems:**
  - Decorrelations in active embankment areas
  - Topographic phase errors, because of slightly outdated DEM of 2006
- **Features:**
  - Small-scale deformations of the dump

II. Mining coal dump

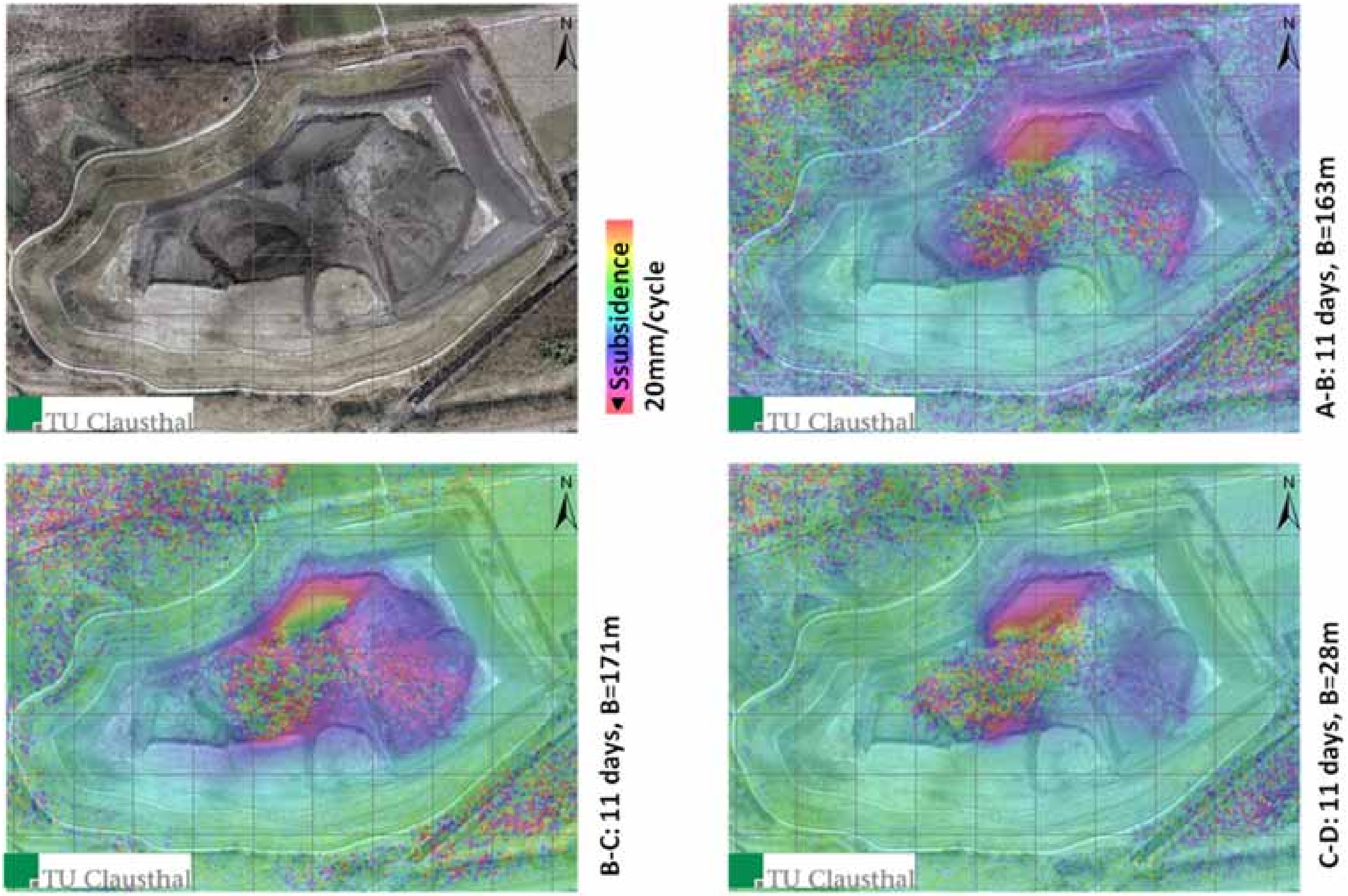

Fig. 32: Setting of a mining coal dump (© TU Clausthal)

III. Lignite opencast mining

- **SAR data:** TerraSAR-X, Envisat ASAR, ALOS PALSAR
- **AOI:** Middle Germany
- **Time:** 2005 – 2011
- **Deformation:** Subsidences (drainage in active opencast mining area)
  Uplifts (flooding of abandoned mining areas)
- **Cause:** Changes of the state of strain
- **Processing:** Stacking
- **Problems:**
  - Strong decorrelations, because of rural character of AOI
  - Strong atmospheric disturbances (see (Schäfer, 2012))
- **Features:**
  - Large-scale displacements
  - ALOS results show best area coverage

Vertical Movements in Lignite Opencast Mining with DInSAR

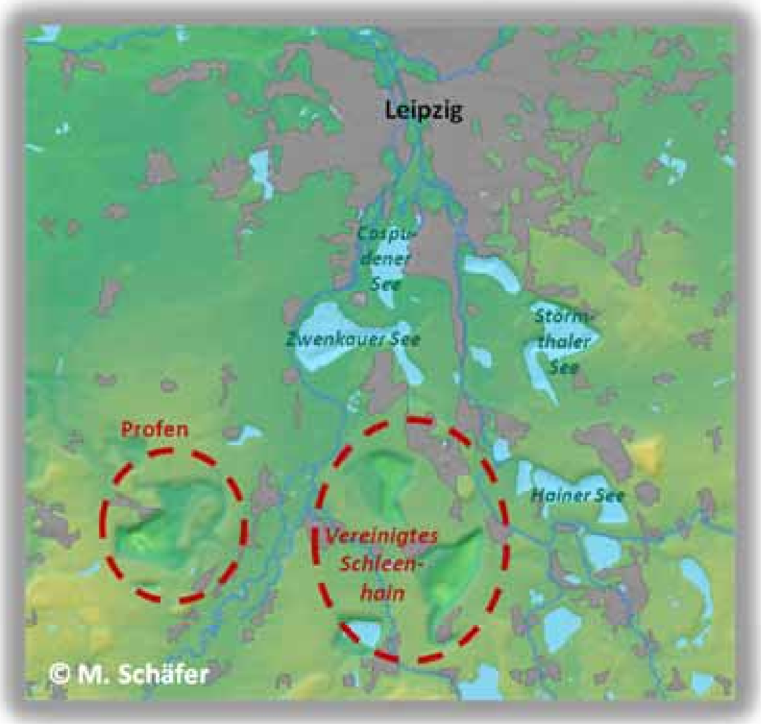

Fig. 33: Copyright © M. Schäfer
(Schäfer, 2012)

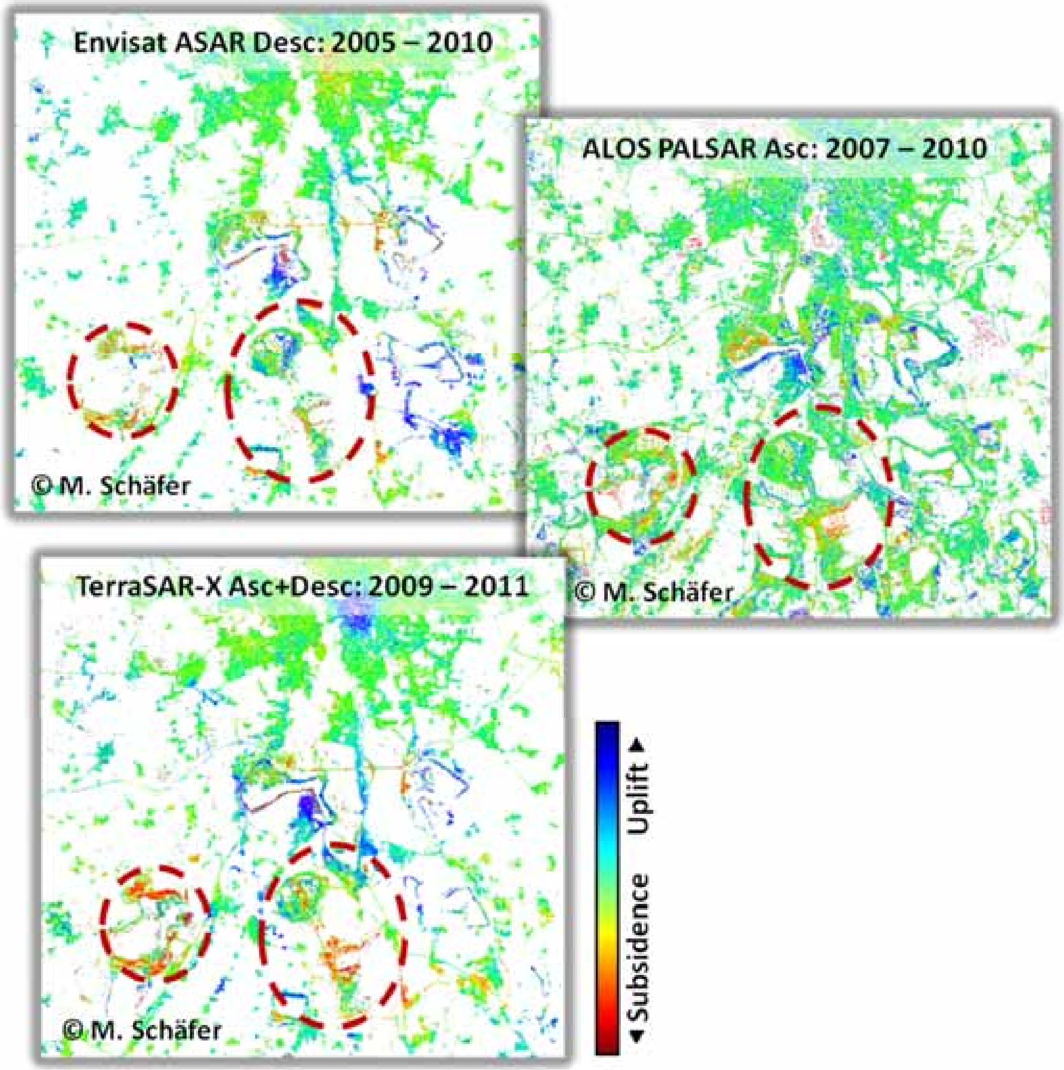

IV. Natural gas storage

- **SAR data:** ERS-1/-2, Envisat ASAR
- **AOI:** Berlin, Germany
- **Time:** 1992 – 2010
- **Deformation:** Cyclic movements with subsidence and uplift
- **Cause:** Mostly seasonal filling (increase of pressure in the injection phase) and withdrawal of natural gas from aquiferous reservoir rocks
- **Processing:** PSI
- **Problems:**
  - Very slow deformation rates in dimension of measurement accuracy of sensors
- **Features:**
  - Correlation of interferometric results with pressure data

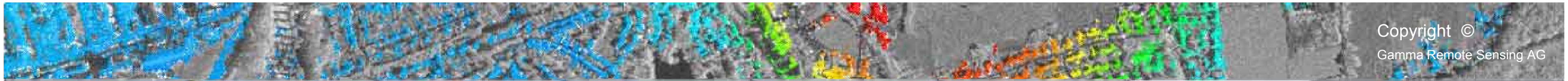

IV. Natural gas storage

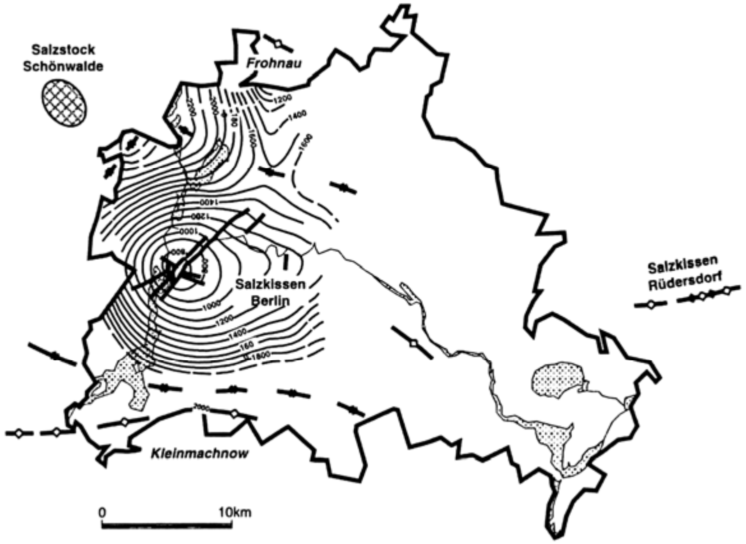

Fig. 34: Large-scale structure of storage layer above salt pillow (Burkowski, 1999)

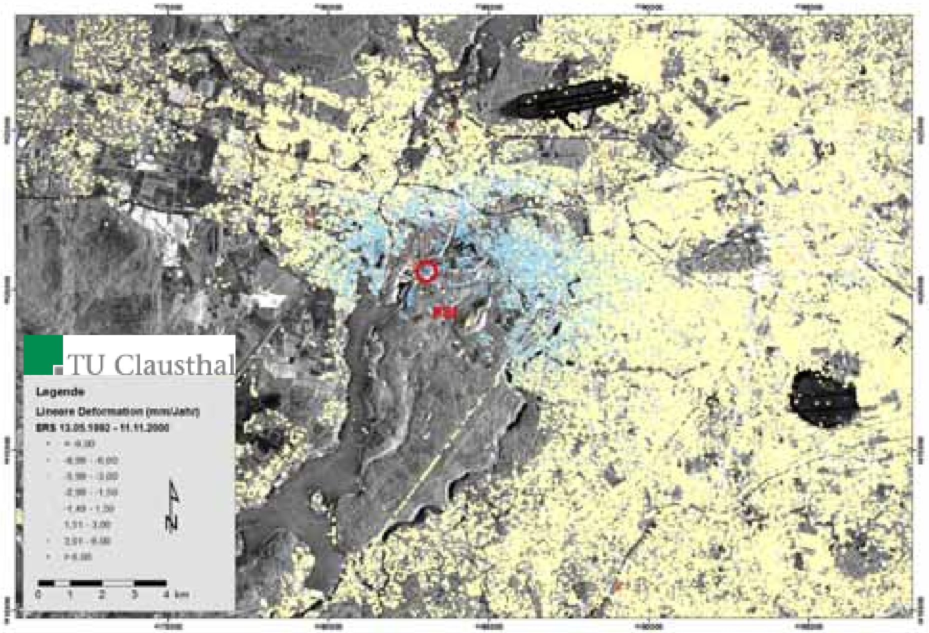

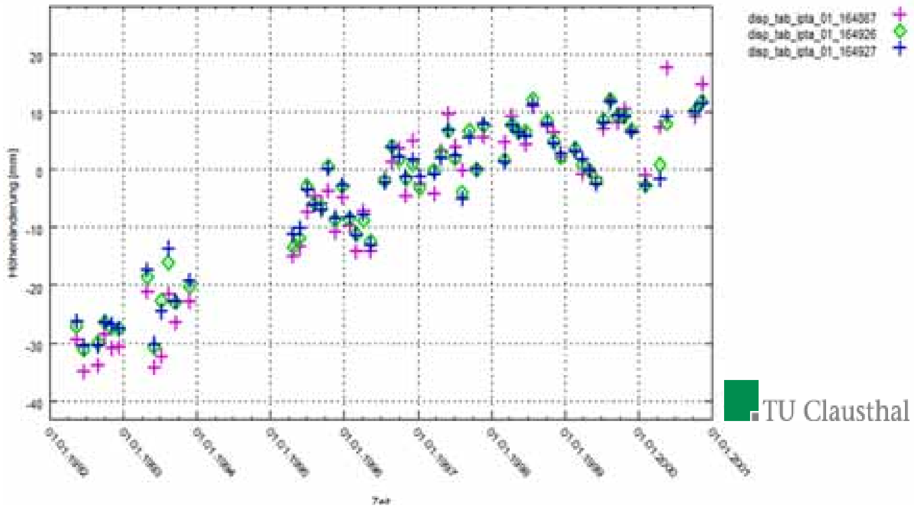

Fig. 35: Vertical displacements [mm/a] derived from ERS-1/-2 data stack (1992 – 2000) using PSI method (Schäfer et al., 2011) © TU Clausthal

IV. Natural gas storage

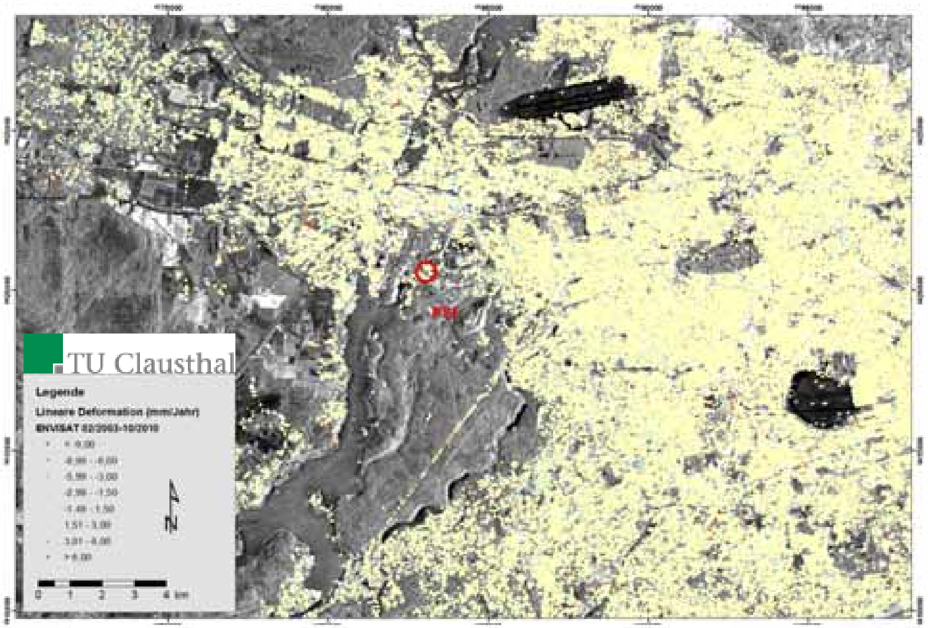

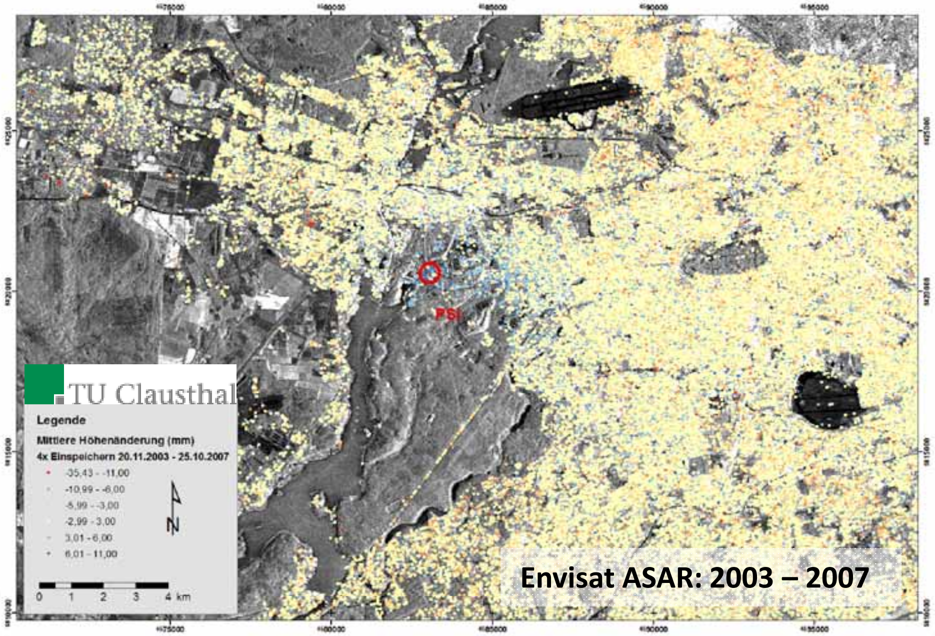

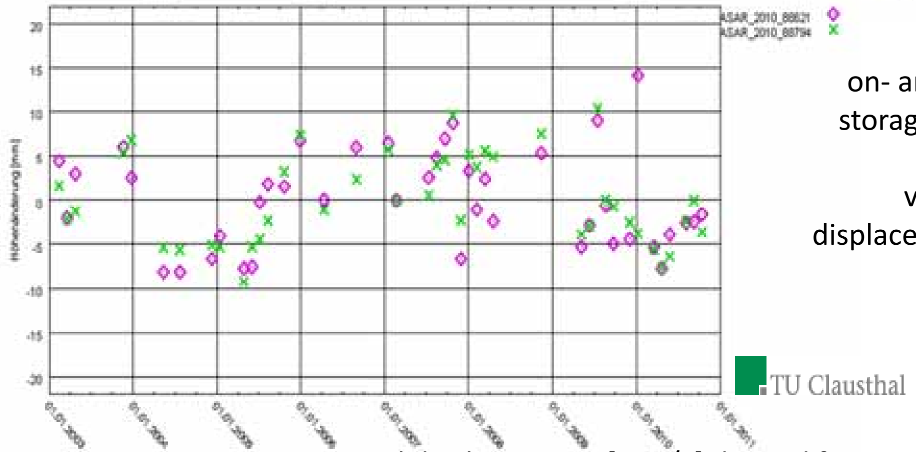

on- and off-storage data

vertical displacements [mm]

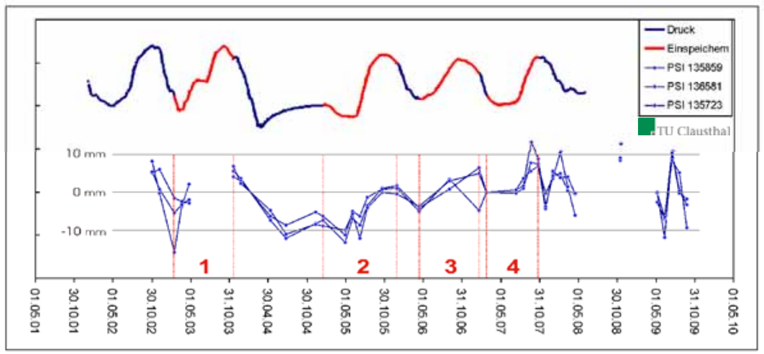

Fig. 36: Vertical displacements [mm/a] derived from Envisat ASAR using PSI method (Schäfer et al., 2011) © TU Clausthal

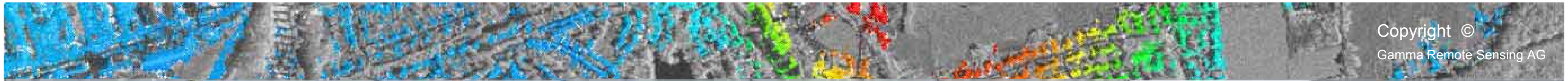

V. Nuclear weapons testing

- **SAR data:** ERS-1/-2
- **AOI:** Pahuete Mesa test area, Nevada, USA
- **Time:** 04/1992 – 05/1996
- **Deformation:** Subsidence trough
- **Cause:** Melting and rupture of rocks resulting from detonation
- **Processing:** Classical DInSAR
- **Problems:**
  - High topographic phase errors, due to mountainous area
- **Features:**
  - Slow deformation rate (-0,505 cm/month → -0,180 cm/month→ -0,206 cm/month → -0,069 cm/month)
  - Correlation between underground detonation point and maximum of subsidence trough

SAREDU Remote Sensing Education Initiative

Monitoring of Underground Nuclear Weapons Testing with DInSAR

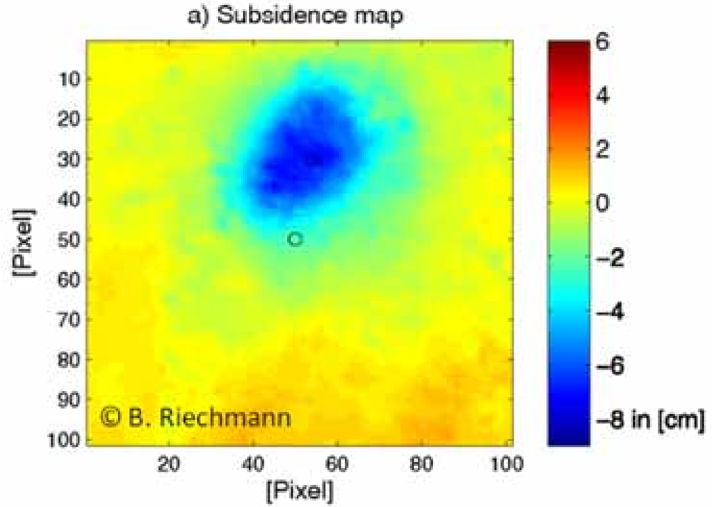

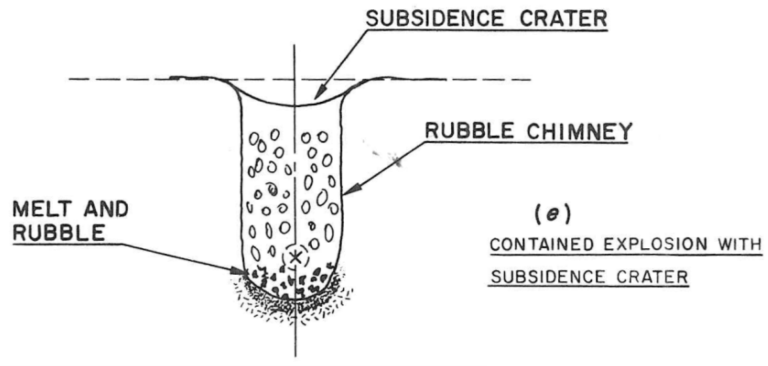

Fig. 37: Illustration of impact of nuclear detonation (Teller et al., 1968)

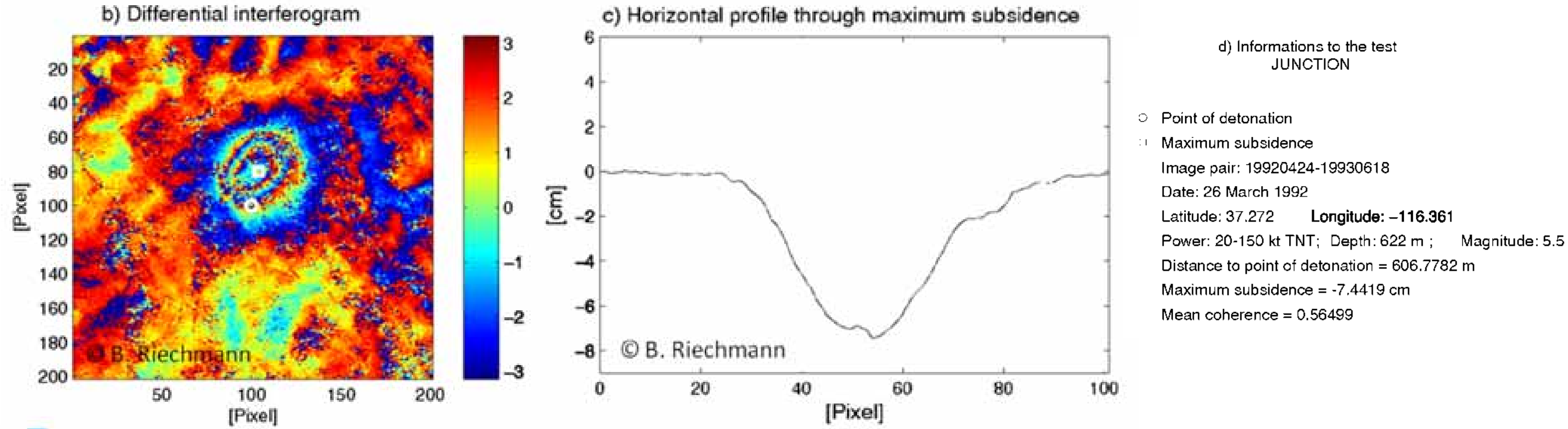

Fig. 38: Impacts of nuclear test „JUNCTION“ on the surface (24.4.1992 – 18.6.1993) (Riechmann, 2009)

VI. Structure deformation

- **SAR data:** ALOS PALSAR
- **AOI:** Okinawa, Japan
- **Object:** Reservoir dam (Taiho Subdam), 66 m height, 445 m length, 2006
- **Time:** 12/2006 – 12/2010
- **Deformation:** 3D displacements
- **Cause:** Changes of pressure because of variation of water level
- **Processing:** Classical DInSAR and SBAS
- **Analyses problems:**
  - Unknown
- **Features:**
  - Estimation of displacements in fluctuation vector direction
  - Safety management of a dam
  - High correlation between DInSAR and GPS results

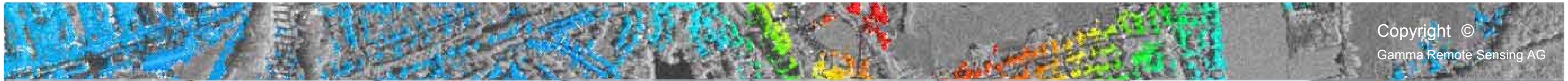

VI. Structure deformation

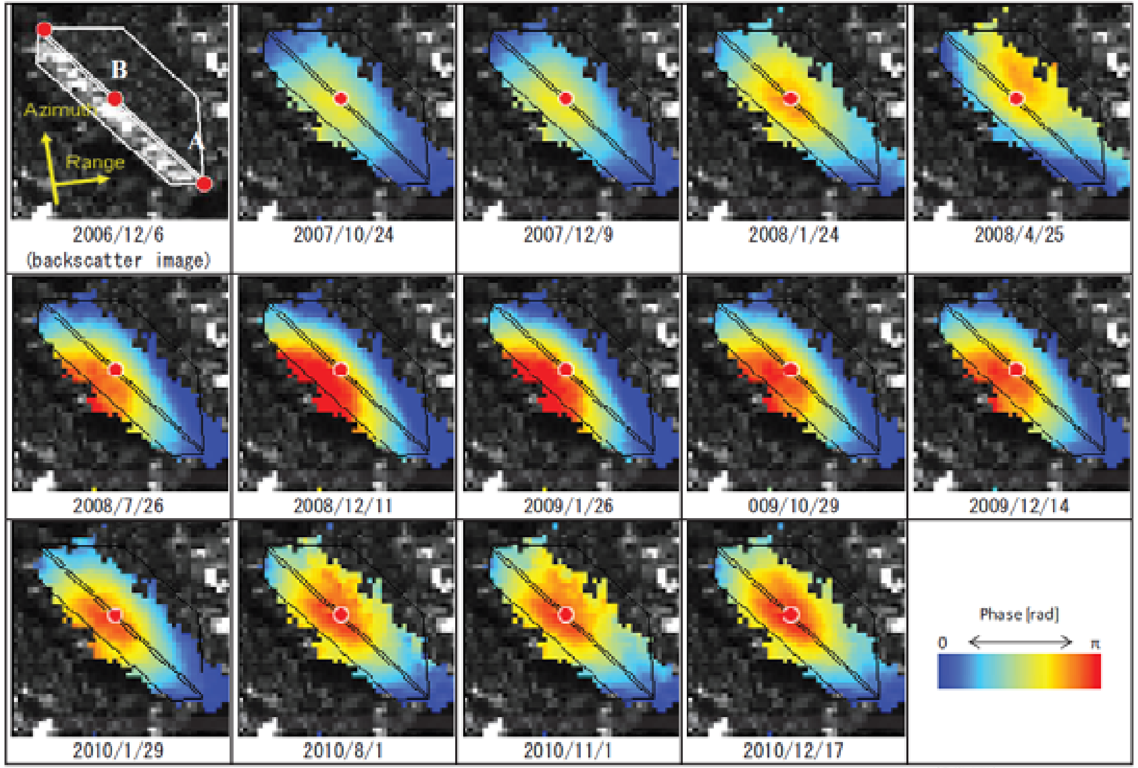

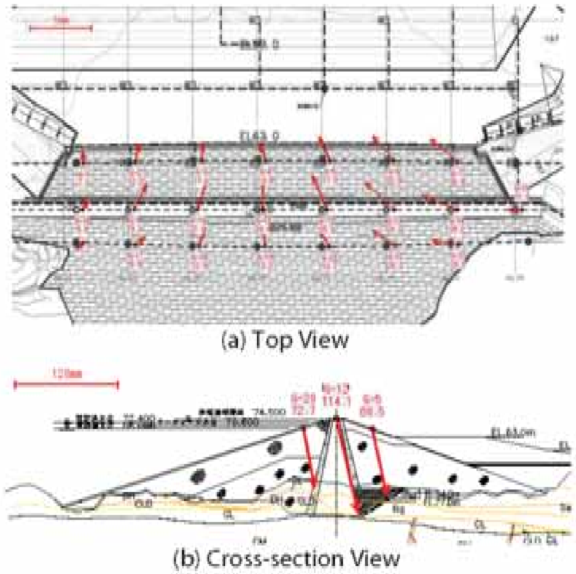

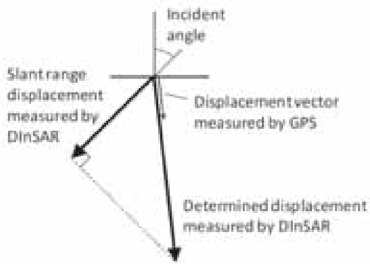

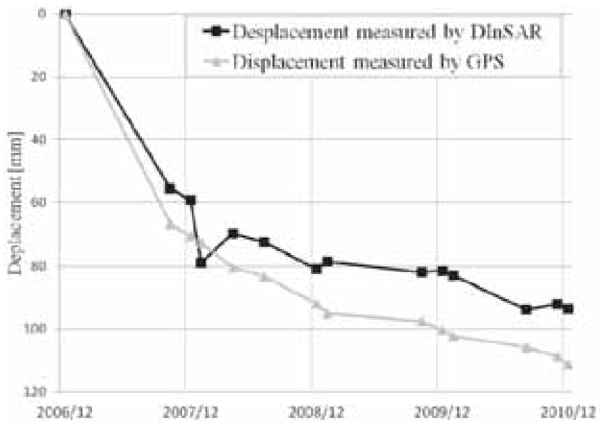

Fig. 39: Exterior deformation monitoring of dams with ALOS PALSAR and GPS (Honda et al., 2012)

SAREDU

SAR Applications of the Cryosphere

Prof. Dr. Matthias Braun

Institute of Geography, Friedrich-Alexander University Erlangen-Nuremberg

Content of Module Cryosphere

Physical principles snow & ice

Snow cover

- Extent
- Condition
- SWE
- …

Glaciers & ice sheets

- Surf. conditions
- Extent
- Structure
- Dynamics
- Elevation
- Grounding line
- …

Sea ice & icebergs

- Extent
- Movement
- Surface conditions
- …

Permafrost

- Melt-freeze
- Methane
- Lakes
- Deform.
- …

SAREDU Remote Sensing Education Initiative

Wet snow extent (09 June 2006, ENVISAT ASAR wideswath)

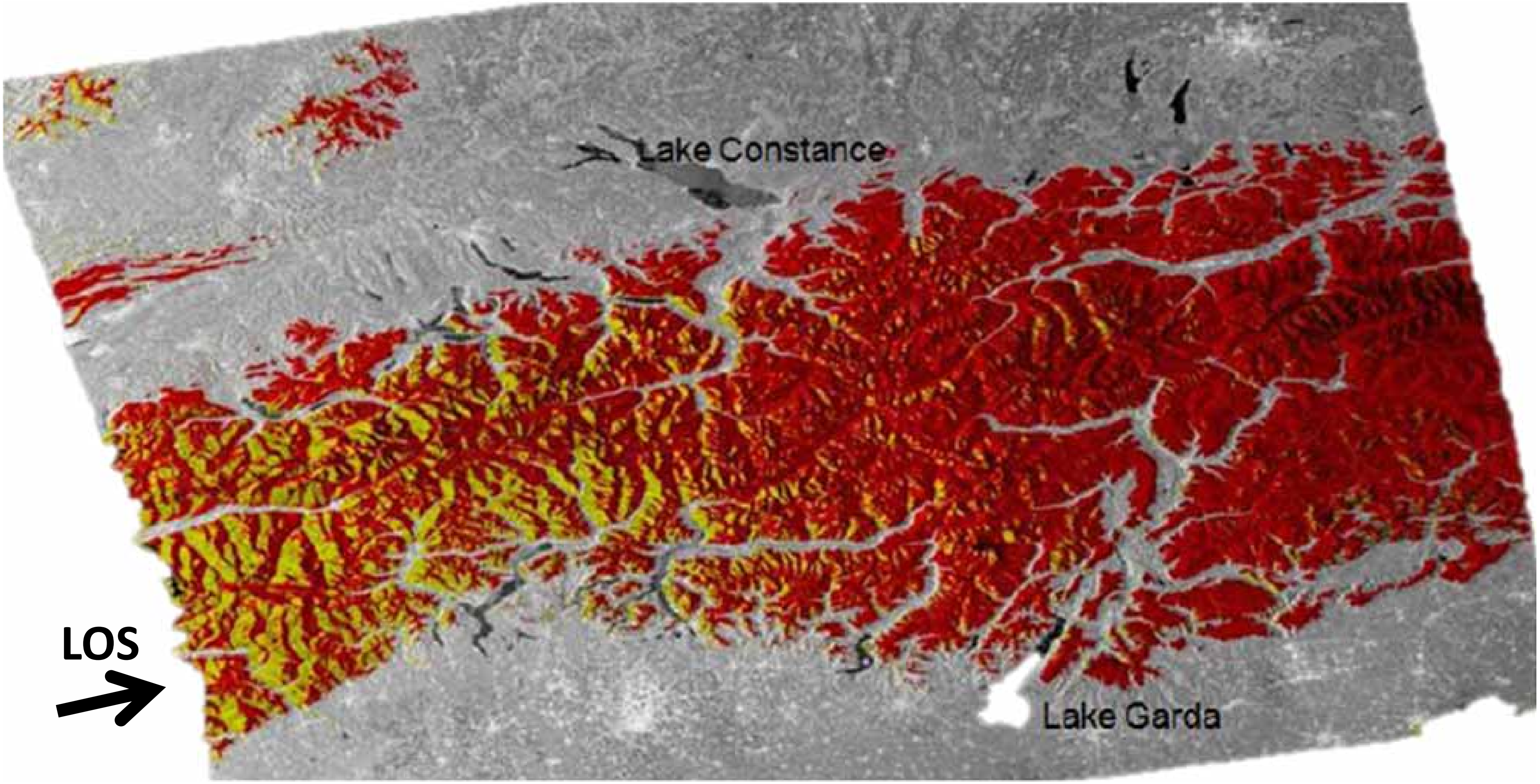

Fig. 3: Nagler et al., 2010

Multitemporal snow cover maps

ENVISAT ASAR IS6
40° incident angle

- 04 May 2004
- 08 June 2004
- 14 July 2004

- Yellow: Layover
  (6.8% of area)

LOS

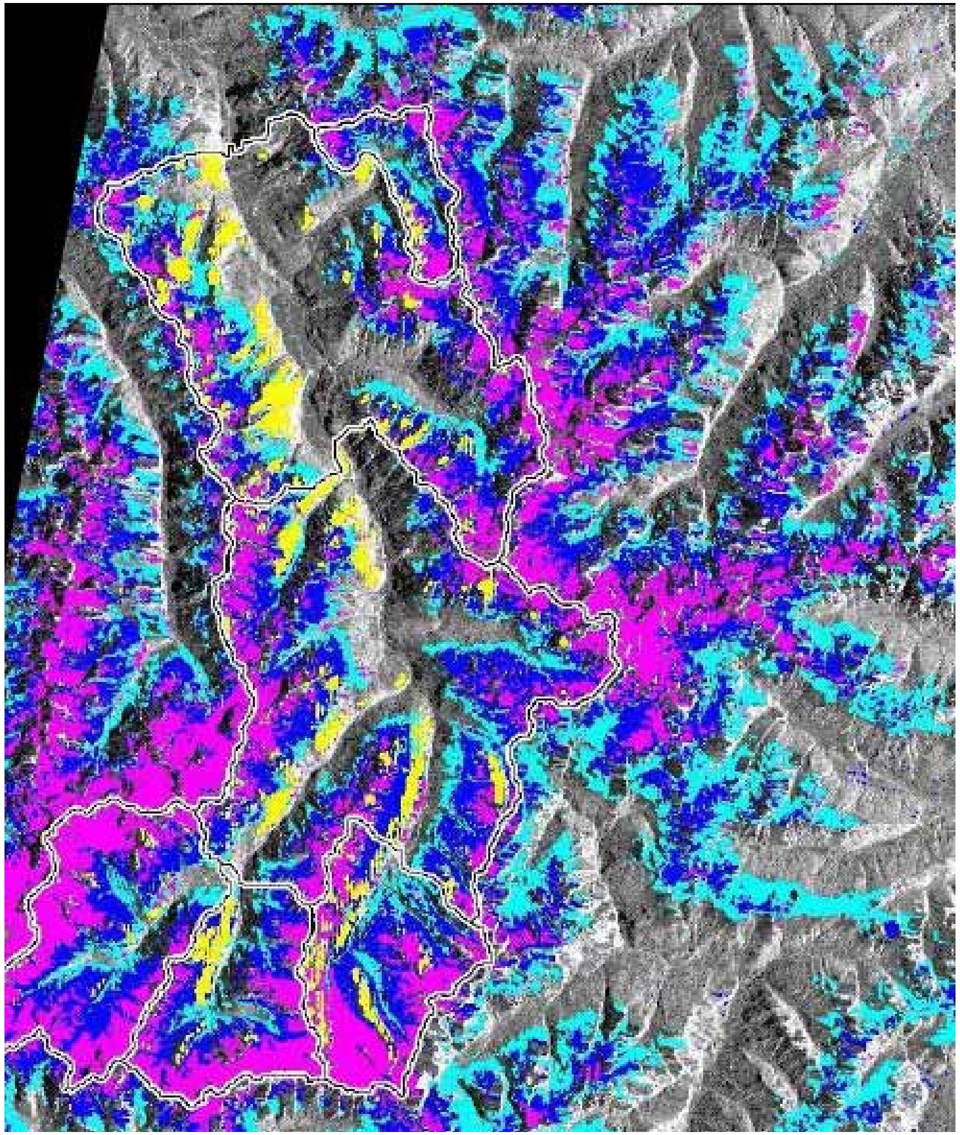

Fig. 4: Nagler et al., 2010

SAREDU

Snow covered area (SCA) MODIS-ENVISAT

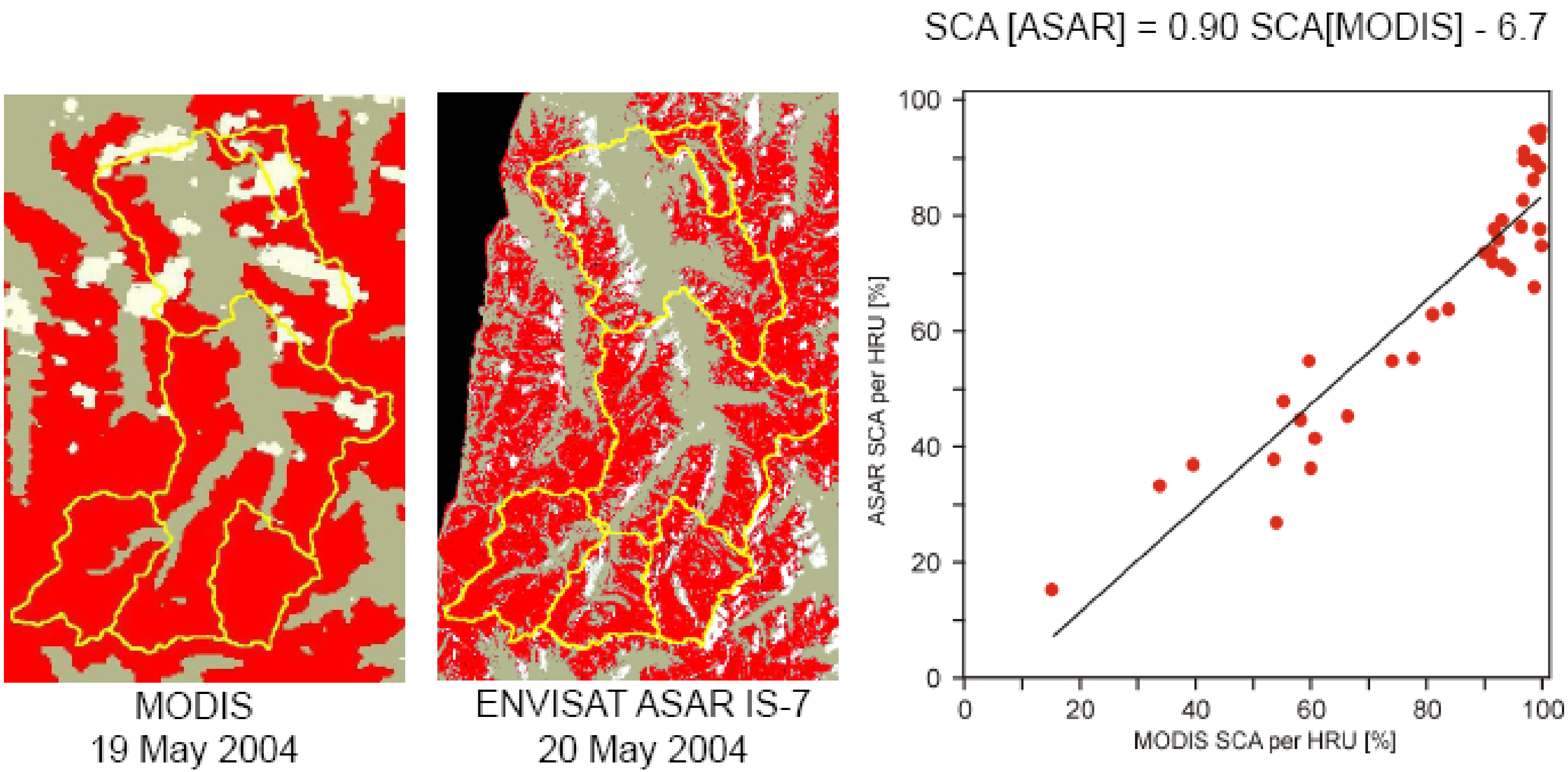

Fig. 5: Nagler et al., 2010

Snow covered area (SCA) MODIS-ENVISAT

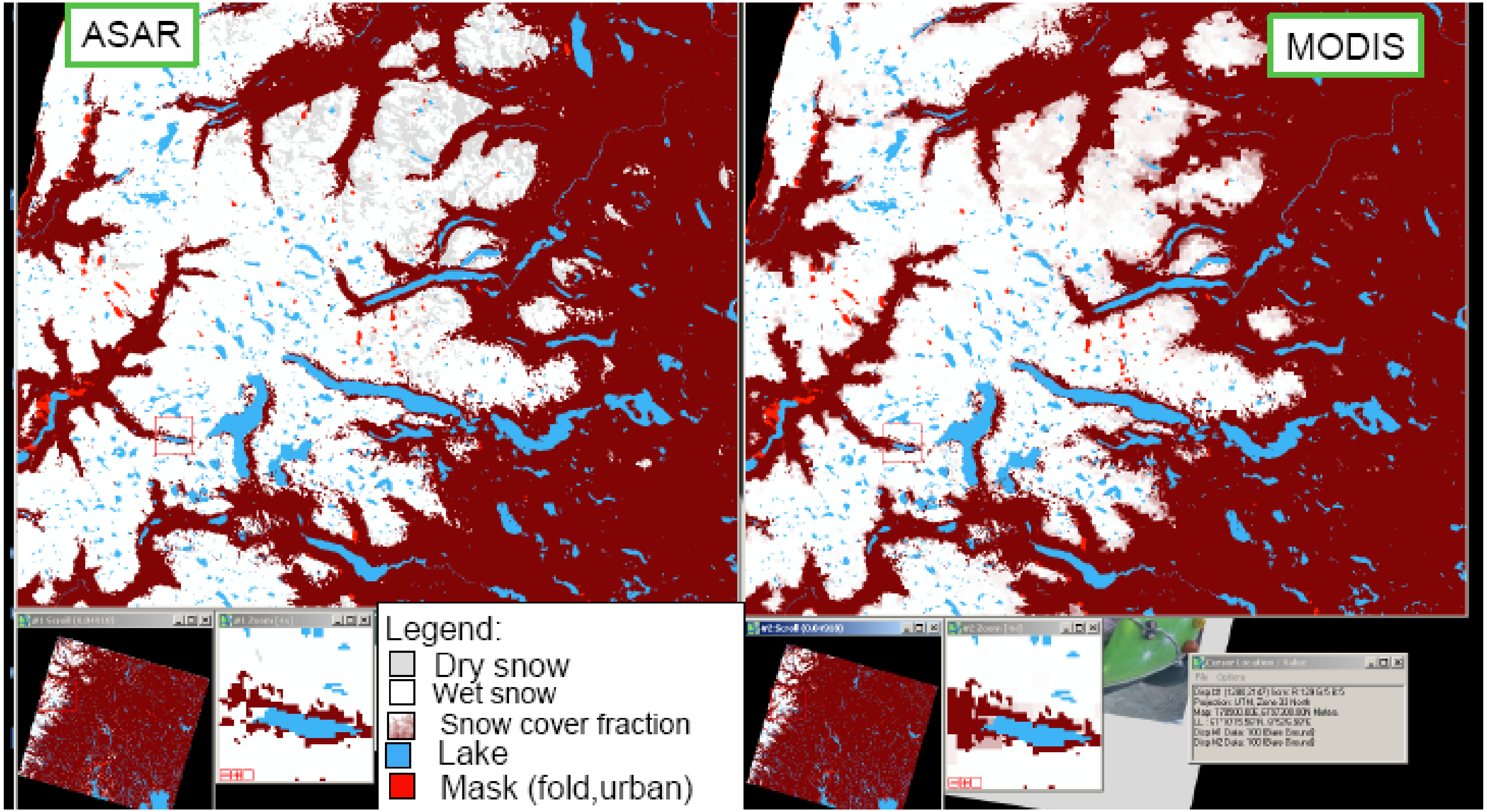

Fig. 6: Nagler et al., 2010

Snow cover extent from SAR coherence

Example from King George Island (Antarctica)

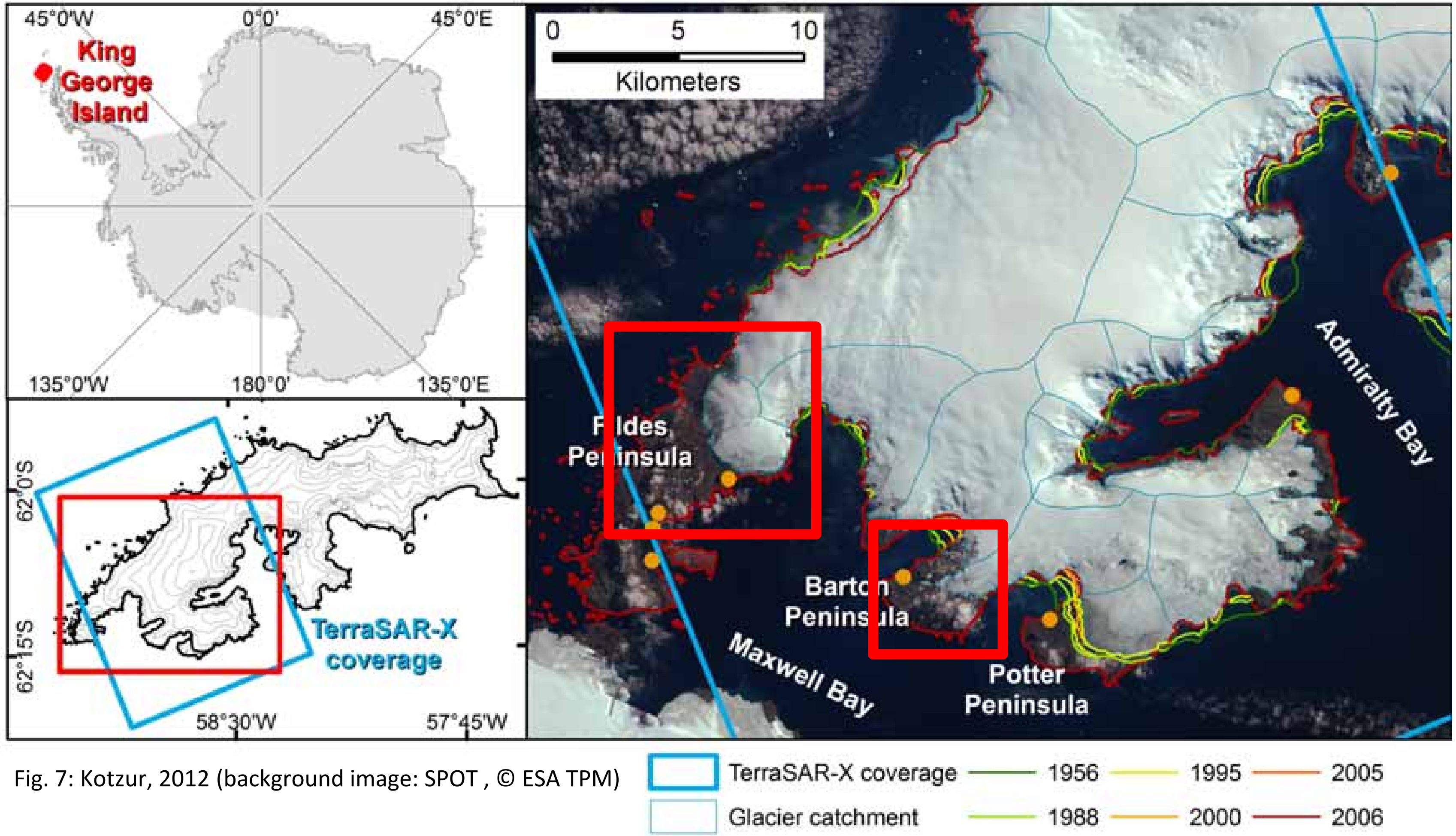

Fig. 7: Kotzur, 2012 (background image: SPOT , © ESA TPM)

SAREDU

Snow cover extent from SAR coherence

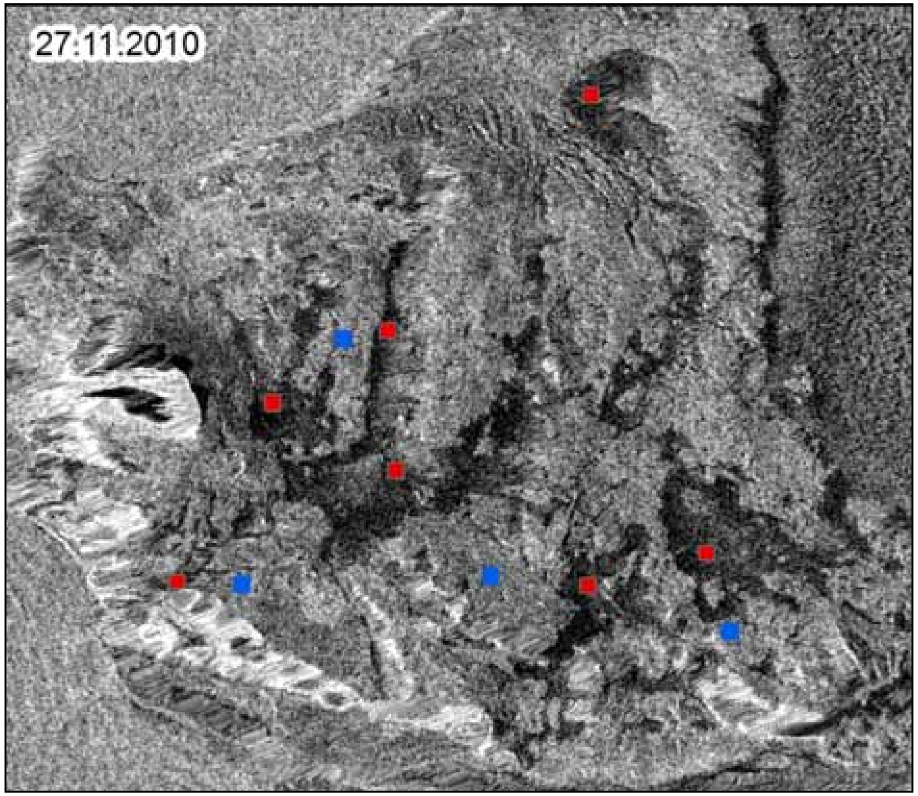

Fig. 8: Kotzur, 2012

Potter Peninsula

Amplitude (left) – 27-11-2010

Coherence (right) – 16/27-11-2010

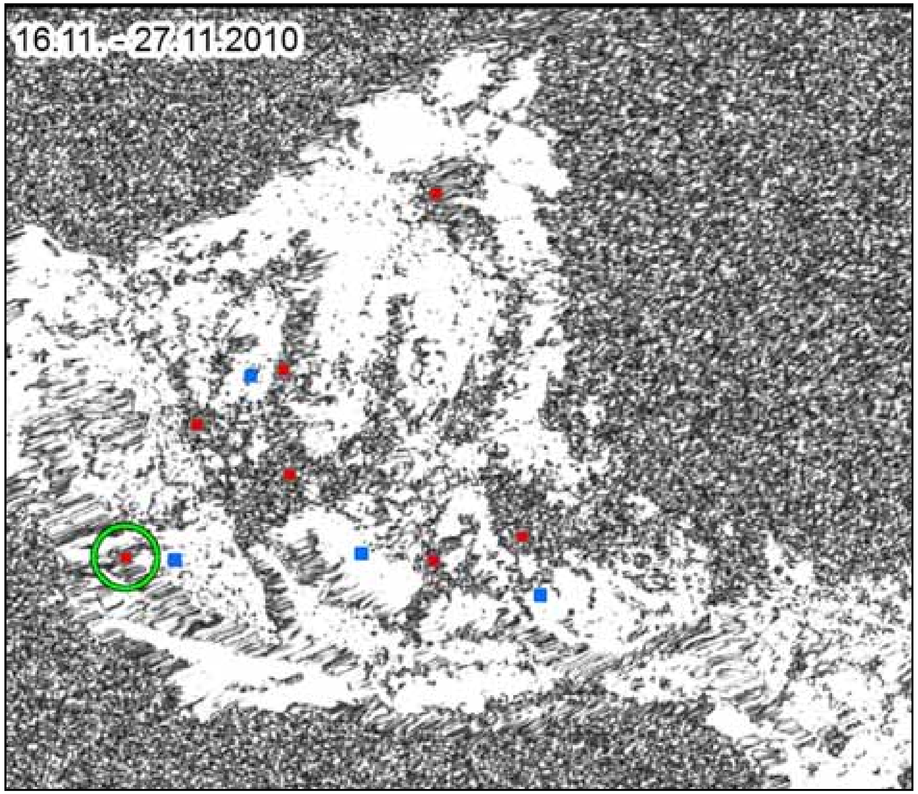

SAREDU Remote Sensing Education Initiative

Snow cover extent from SAR coherence

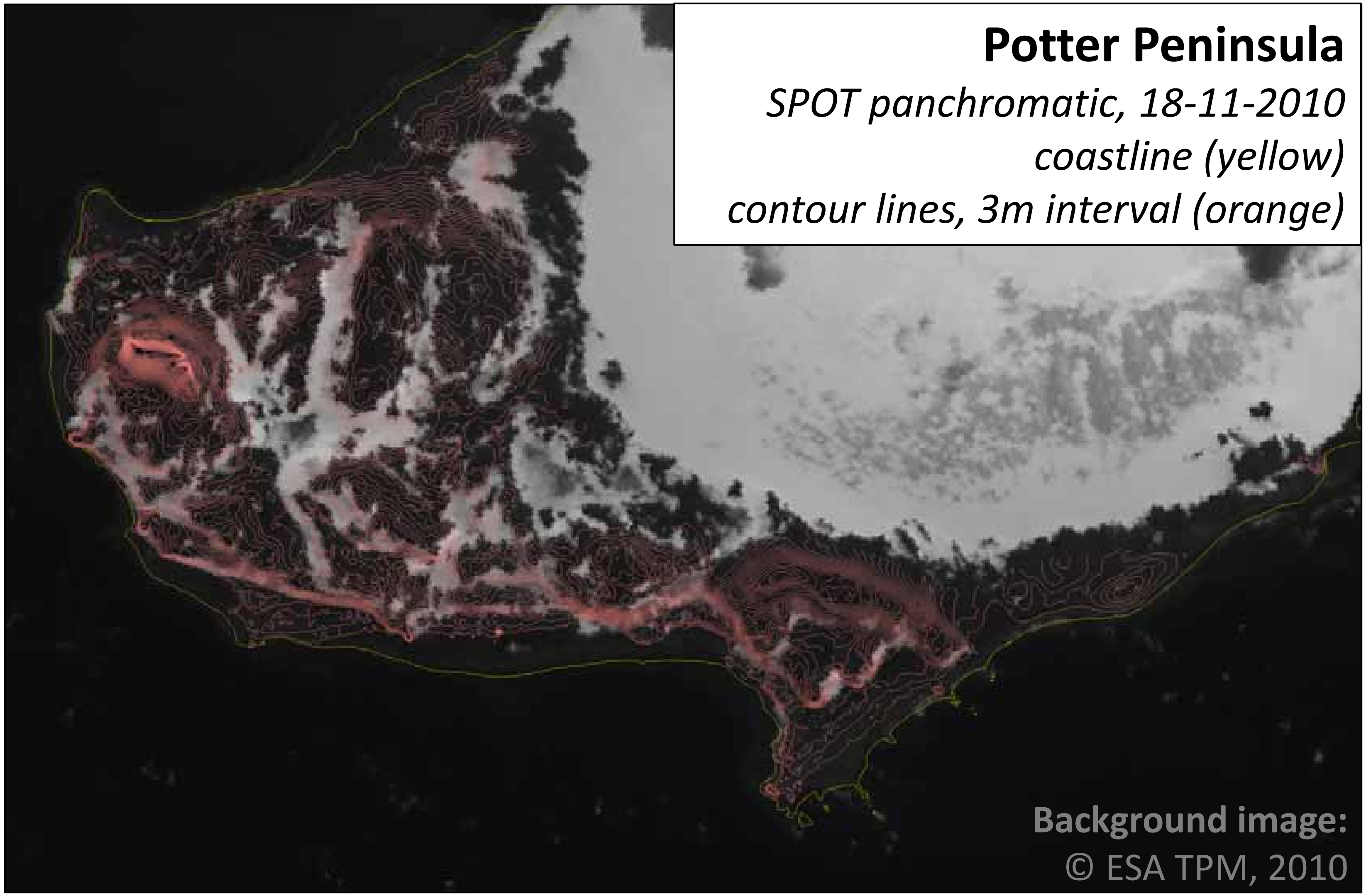

Fig. 9: Kotzur, 2012

What can you see on this SAR image?

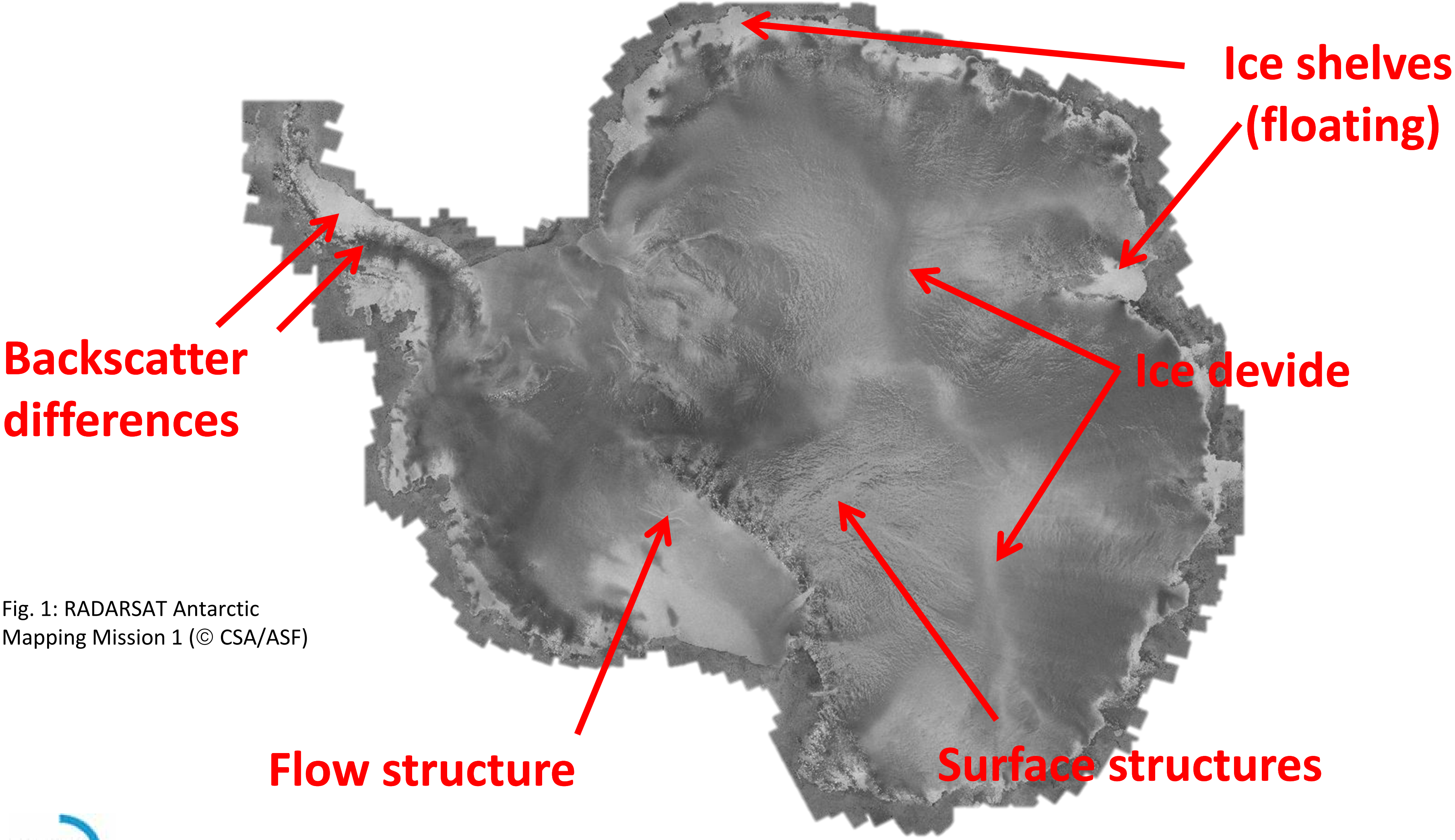

Fig. 1: RADARSAT Antarctic Mapping Mission 1 (© CSA/ASF)

RADARSAT ScanSAR mosaics, Antarctic Peninsula

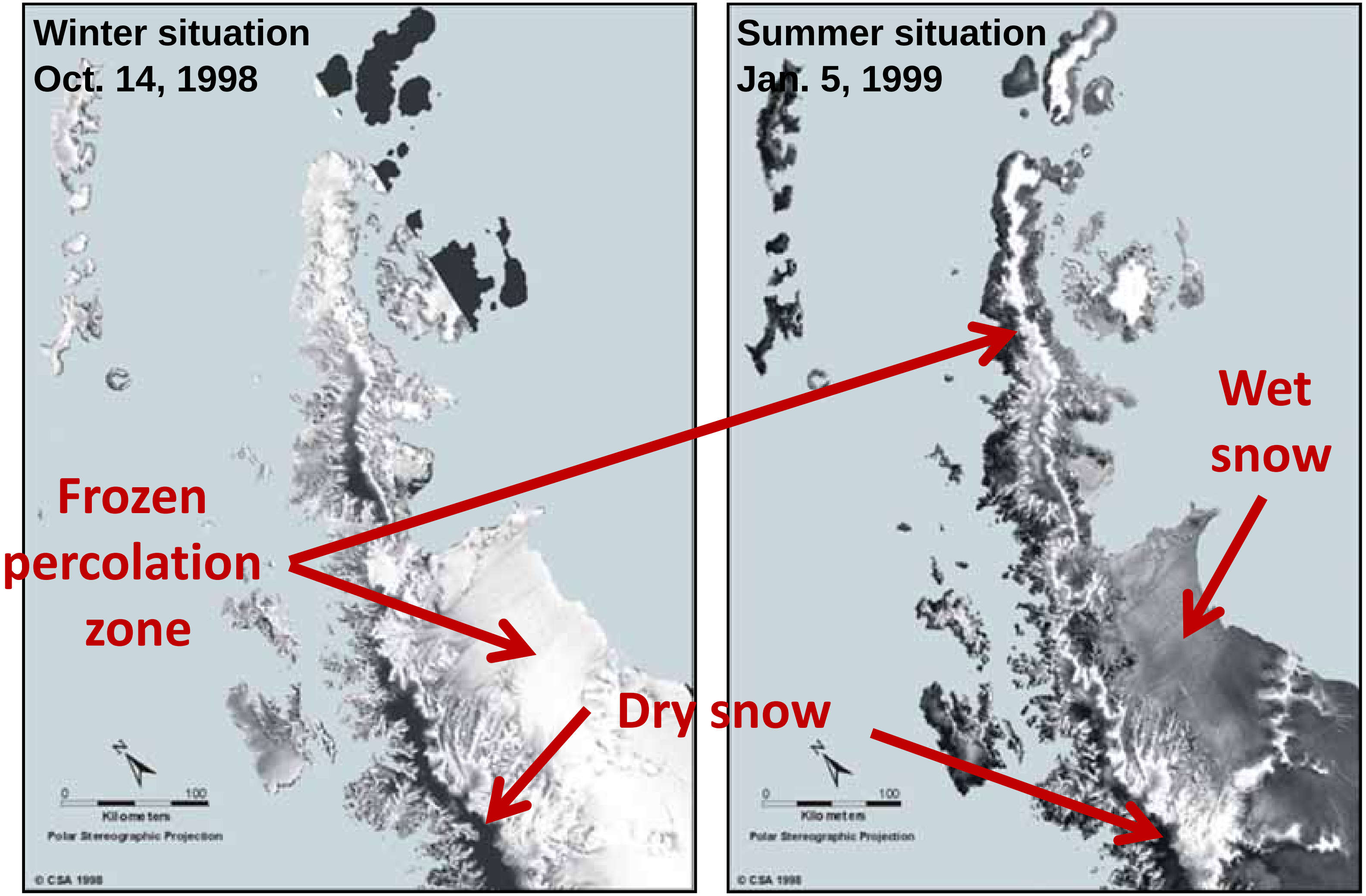

Fig. 8: Rau, 2004

Seasonal development of SAR backscatter

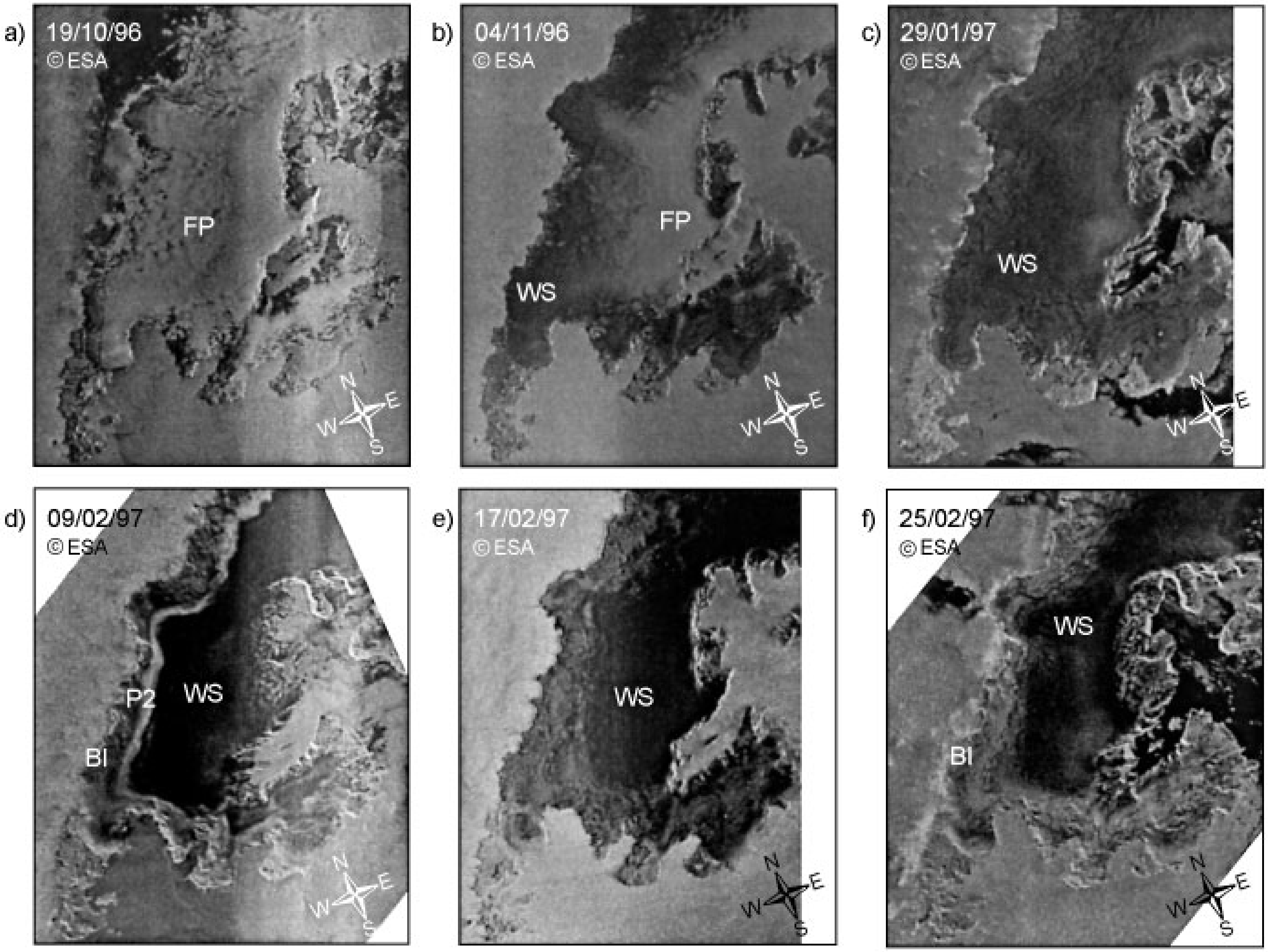

King George Island, Antarctica
C-band, VV

WS: wet snow
FP: frozen percolation
BI: bare ice
P2: rough wet snow

Fig. 9: Braun et al., 2000

Example: snow and ice classification

29 Sept. 2000 → late summer (ERS-2)

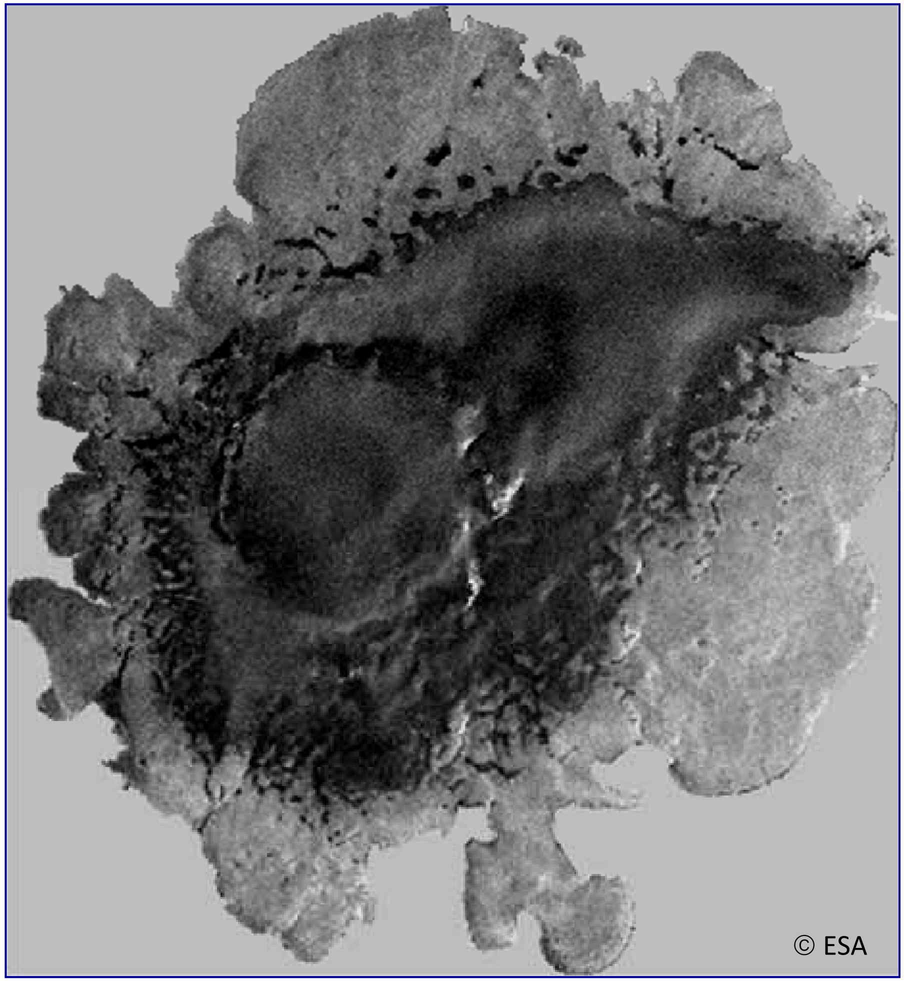

27 Dec. 2000 → winter (ERS-2)

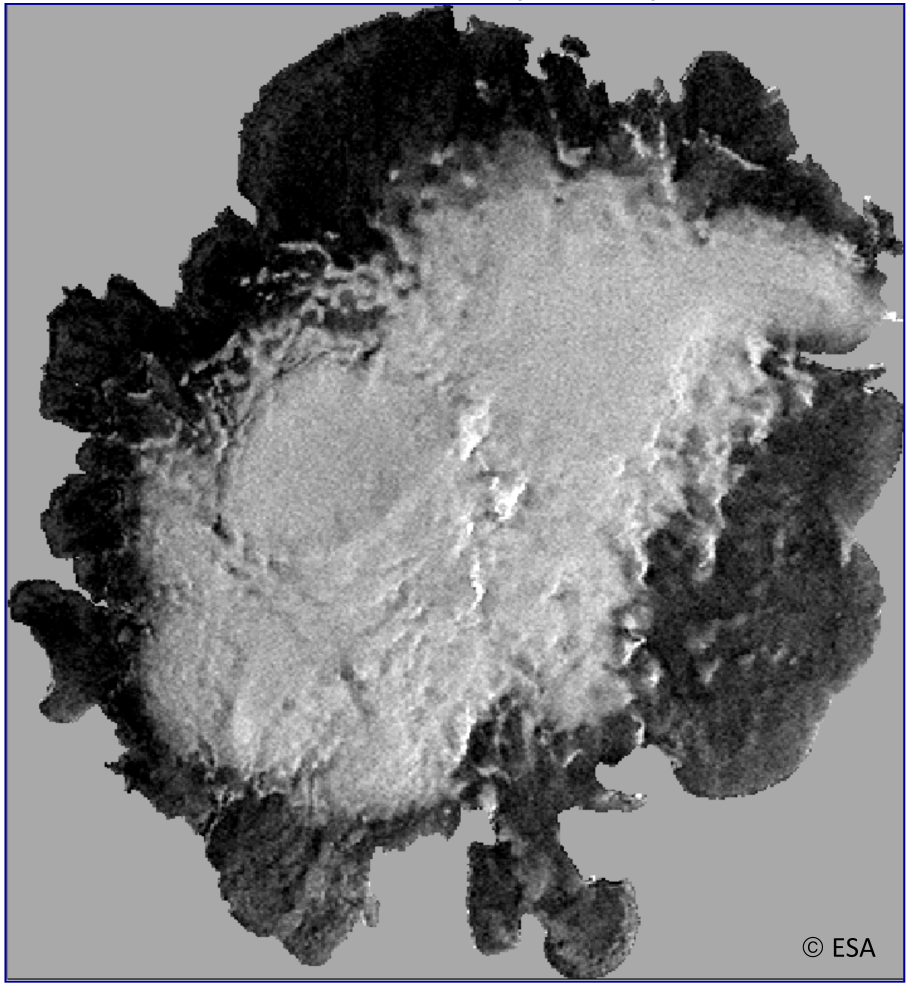

Example: snow and ice classification

29 Sept. 2000 → late summer (ERS-2)

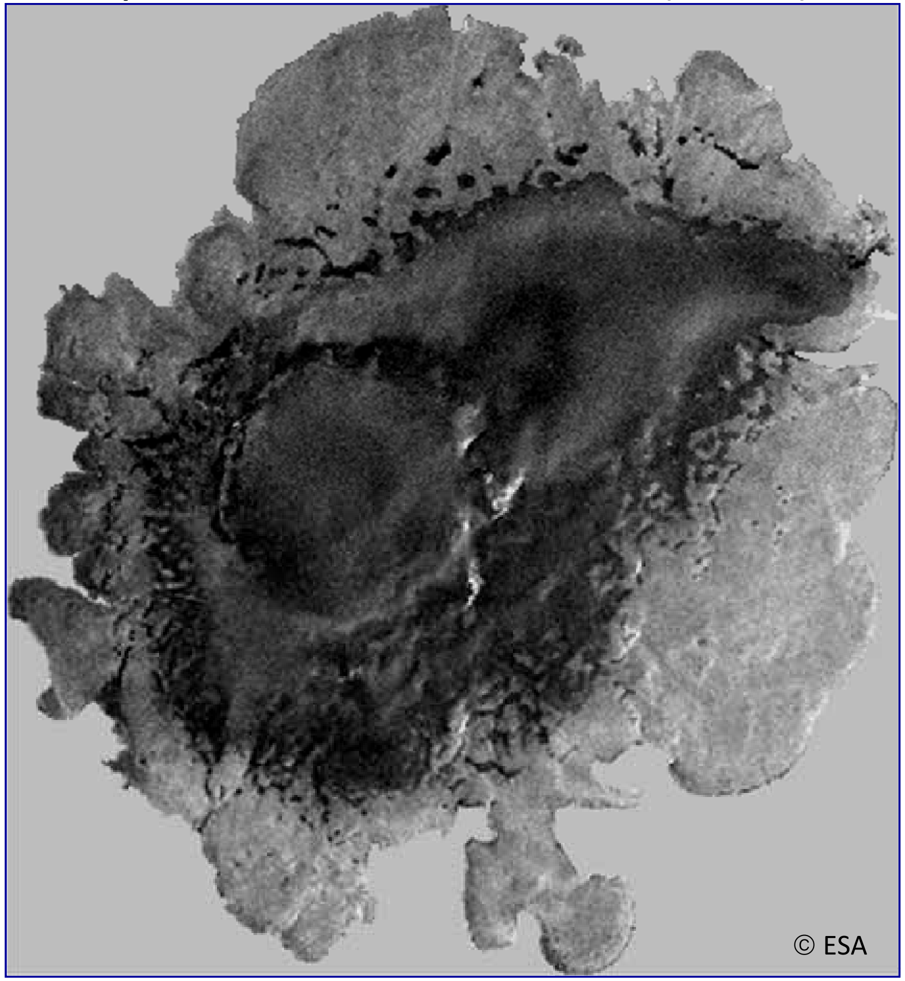

knowledgebased classification

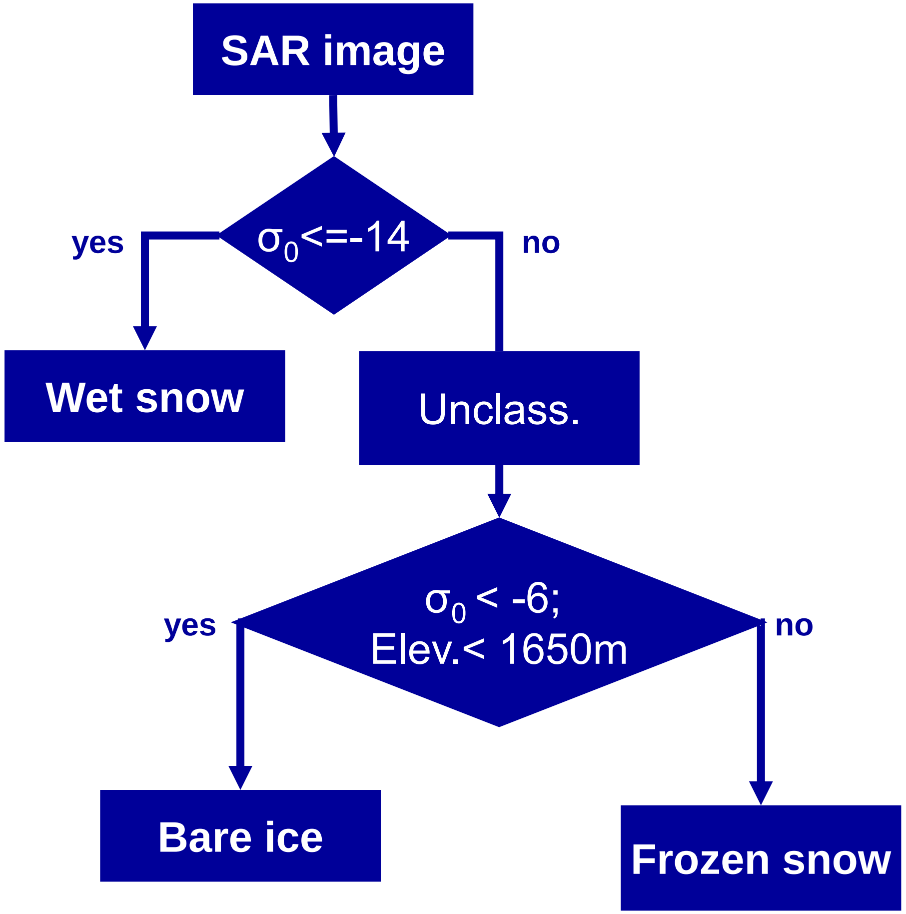

SAREDU

Example: snow and ice classification

29 Sept. 2000 → late summer (ERS-2)

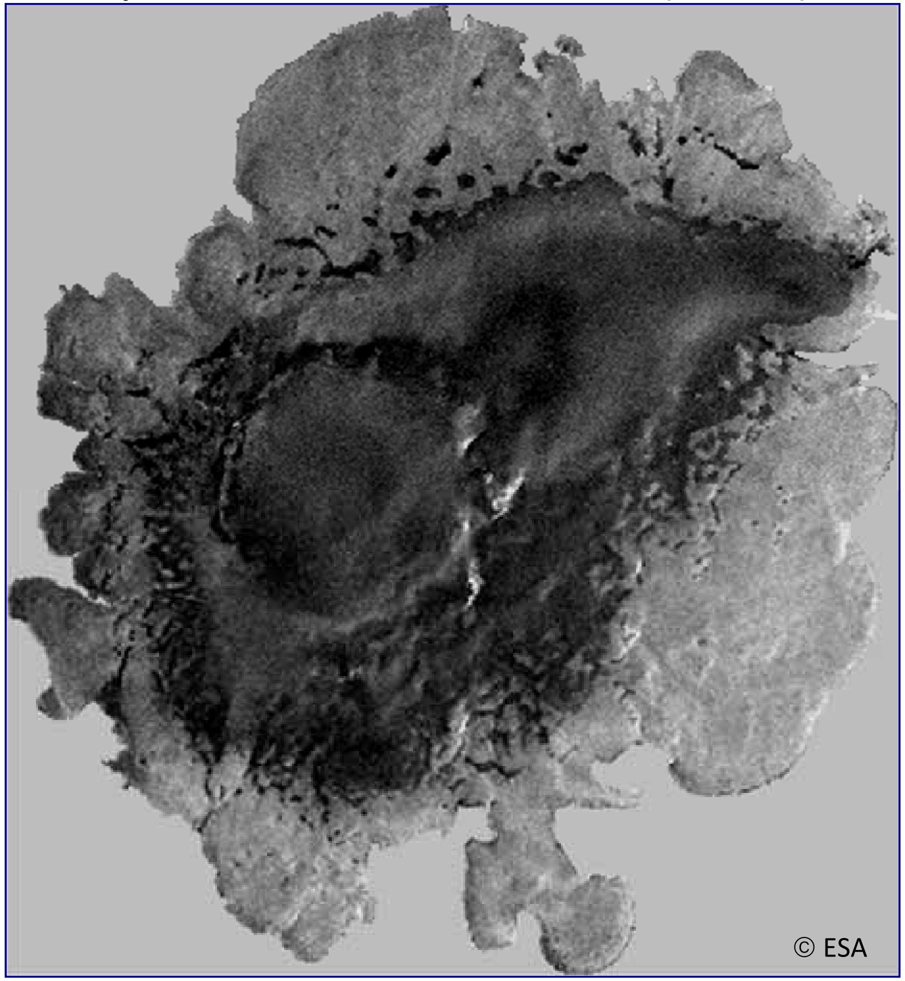

knowledgebased classification

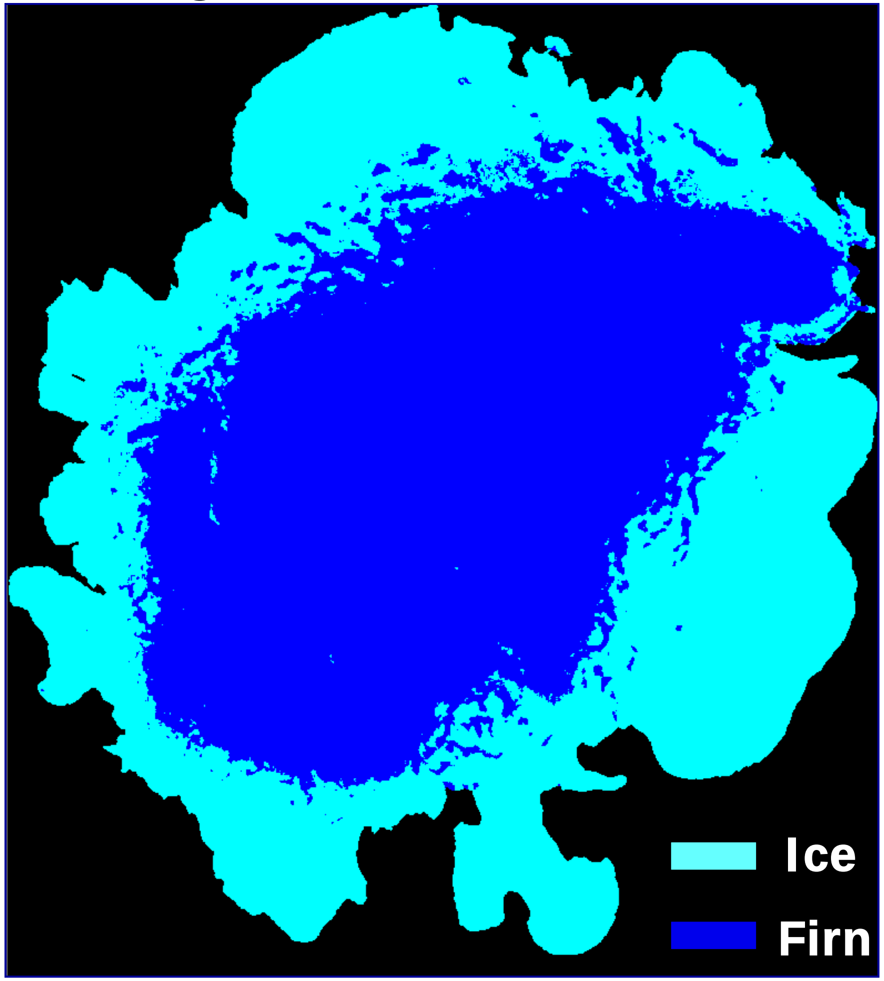

Example: snow and ice classification

Annual variation of firn and bare ice area

(1992, 2005, 2006 derive from winter imagery, all other from summer imagery

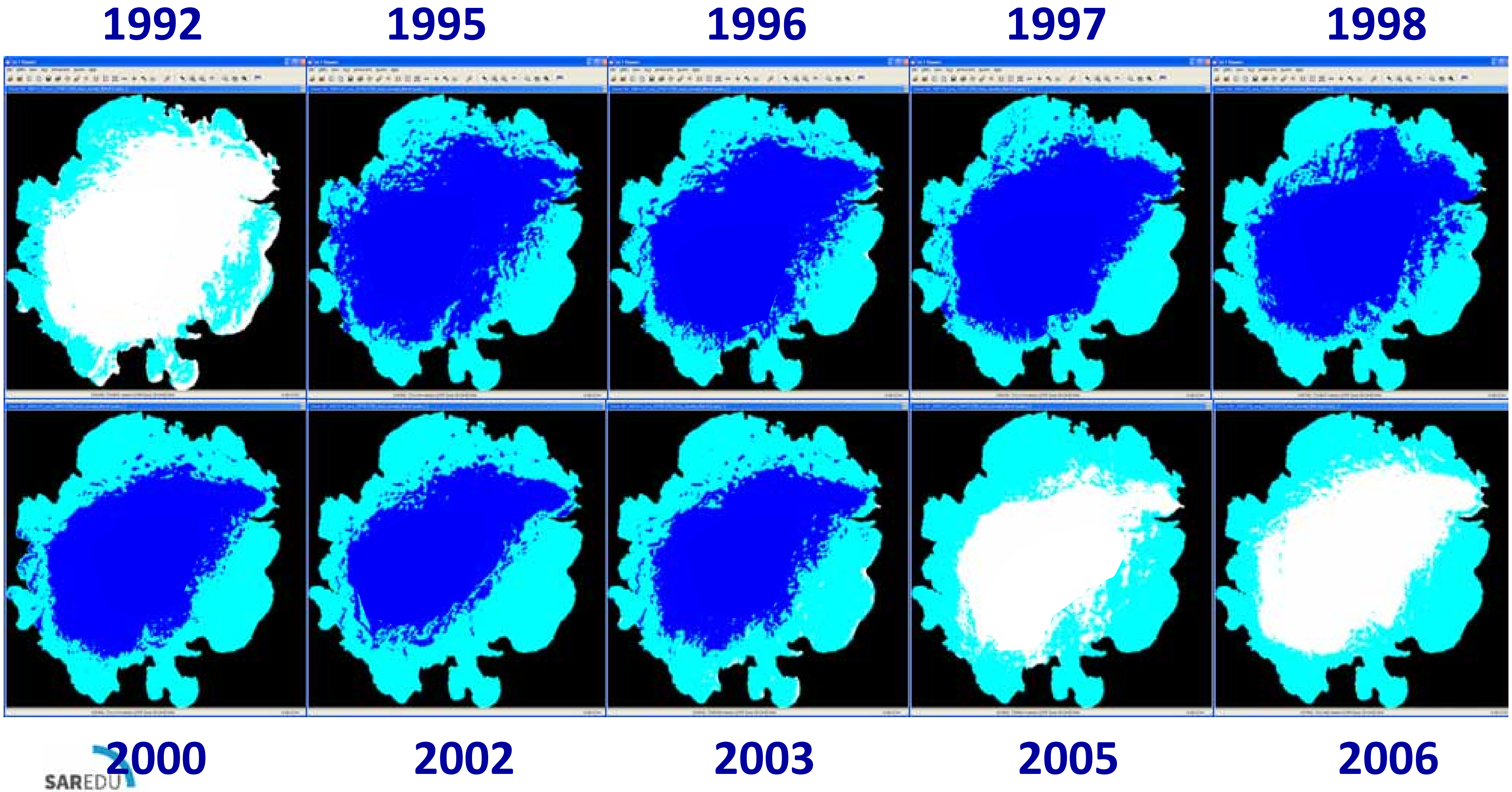

Glacier mask from TSX coherence & intensity

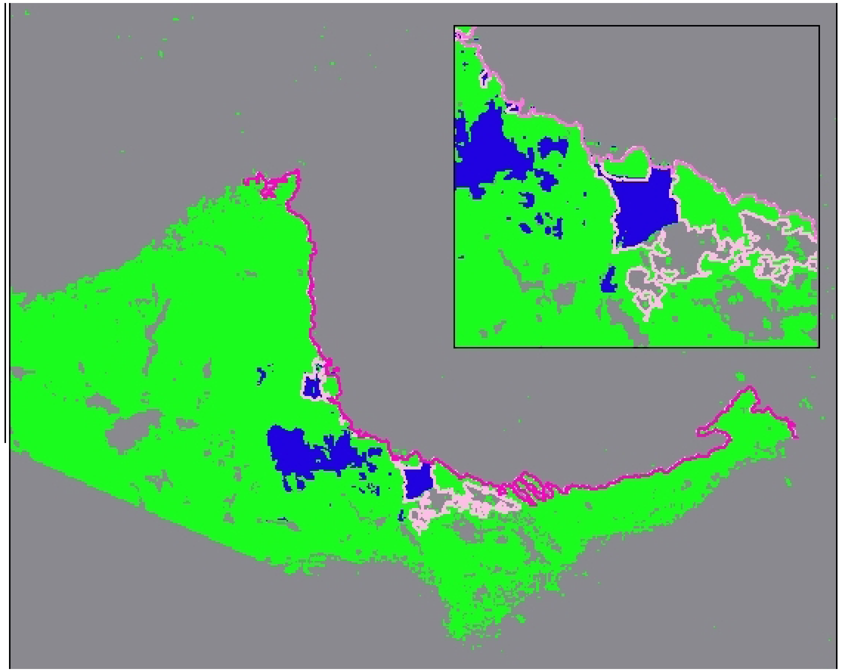

Fig. 27: Kotzur, 2012

Potter Peninsula, King George Island, Antarctica. Pink line: glacier boundary from coherence alone, magenta line: with intensity thresholding, green: ice-free areas, blue: water

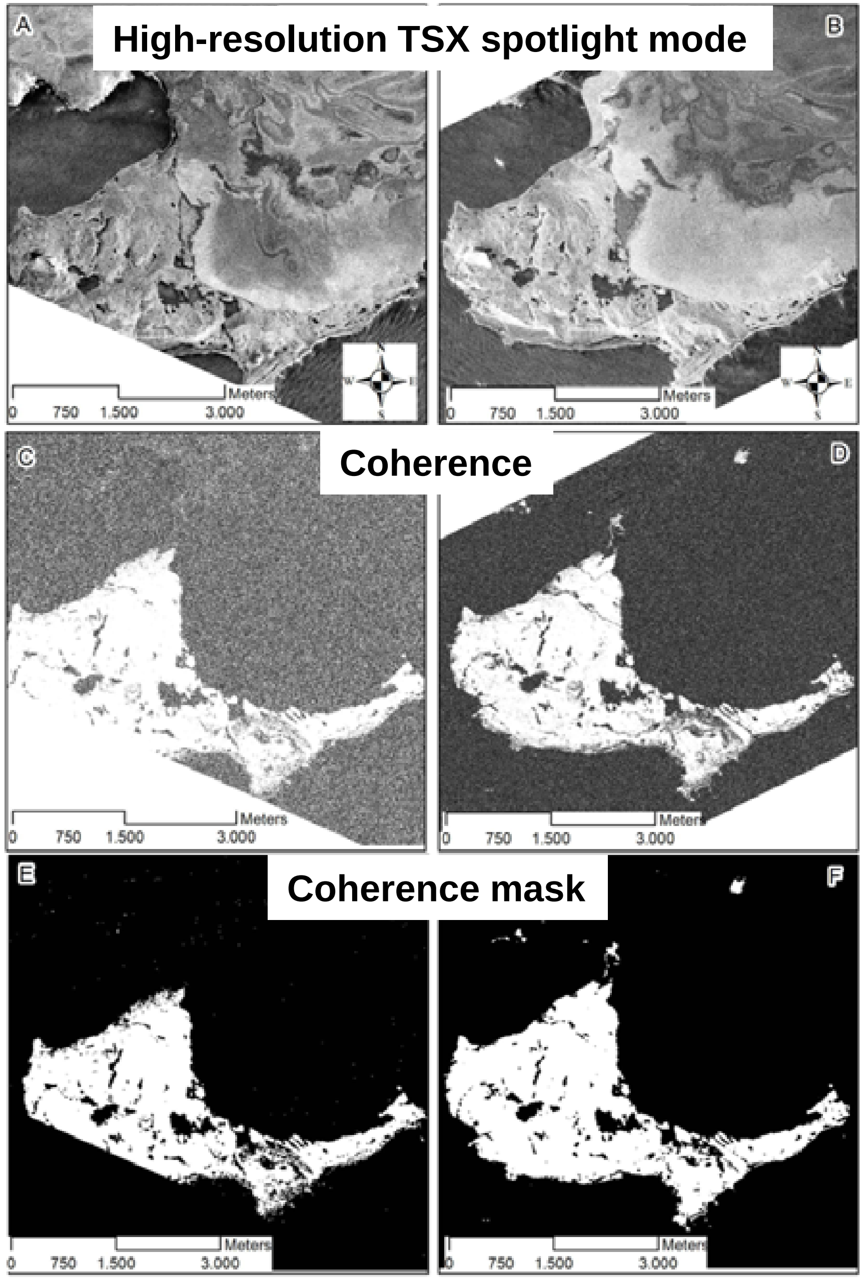

SAREDU

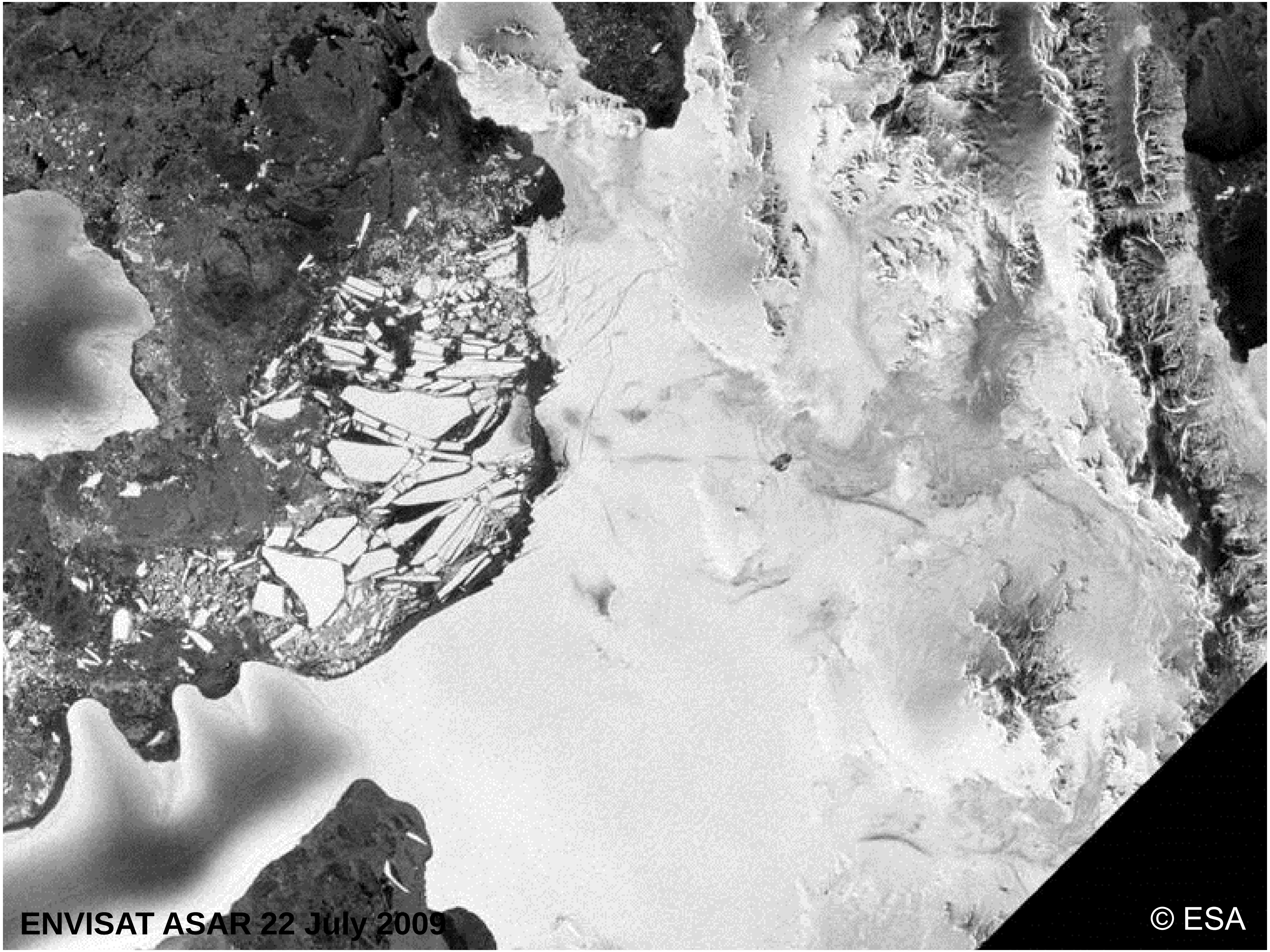
ENVISAT ASAR 22 July 2009
© ESA

Structural Glaciological Mapping

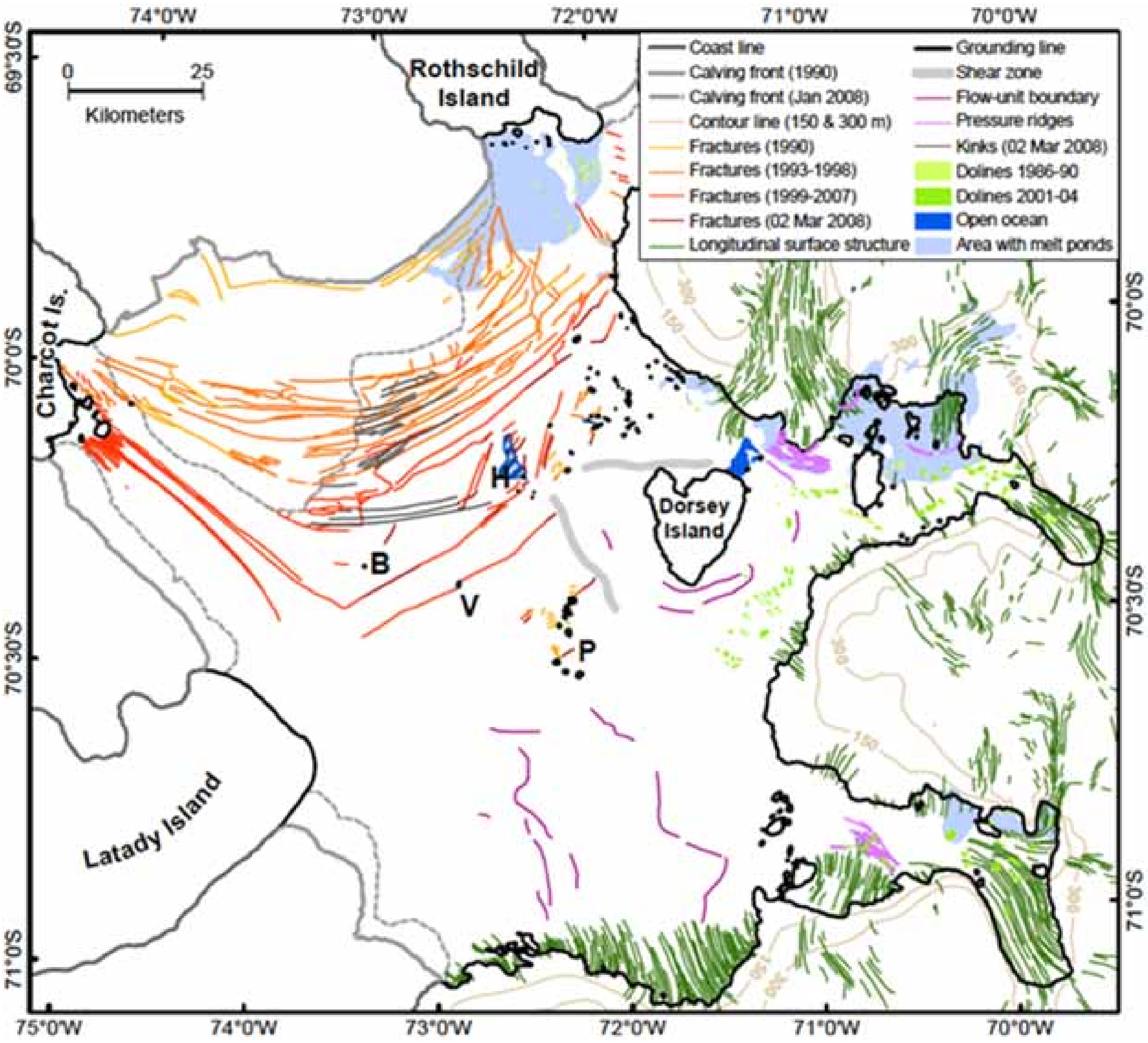

Fig. 28: Braun et al. (2009)

SAREDU

How to map glacier flow from SAR?

Three basic techniques:

- Feature or intensity offset tracking
- Coherence tracking
- Differential SAR interferometry (DInSAR)

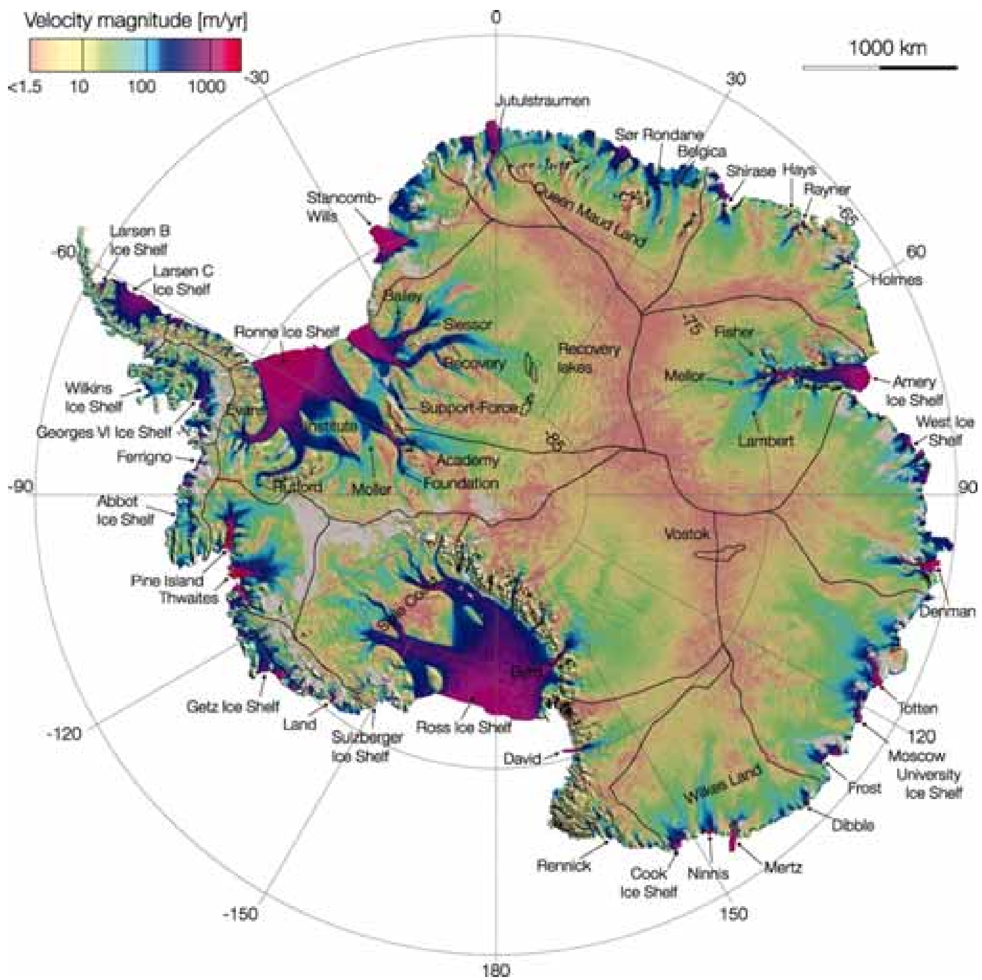

Fig. 29: First complete velocity mosaic of Antarctica (IPY 2007-09) (Rignot et al., 2011)

SAREDU Remote Sensing Education Initiative

Ice Dynamics

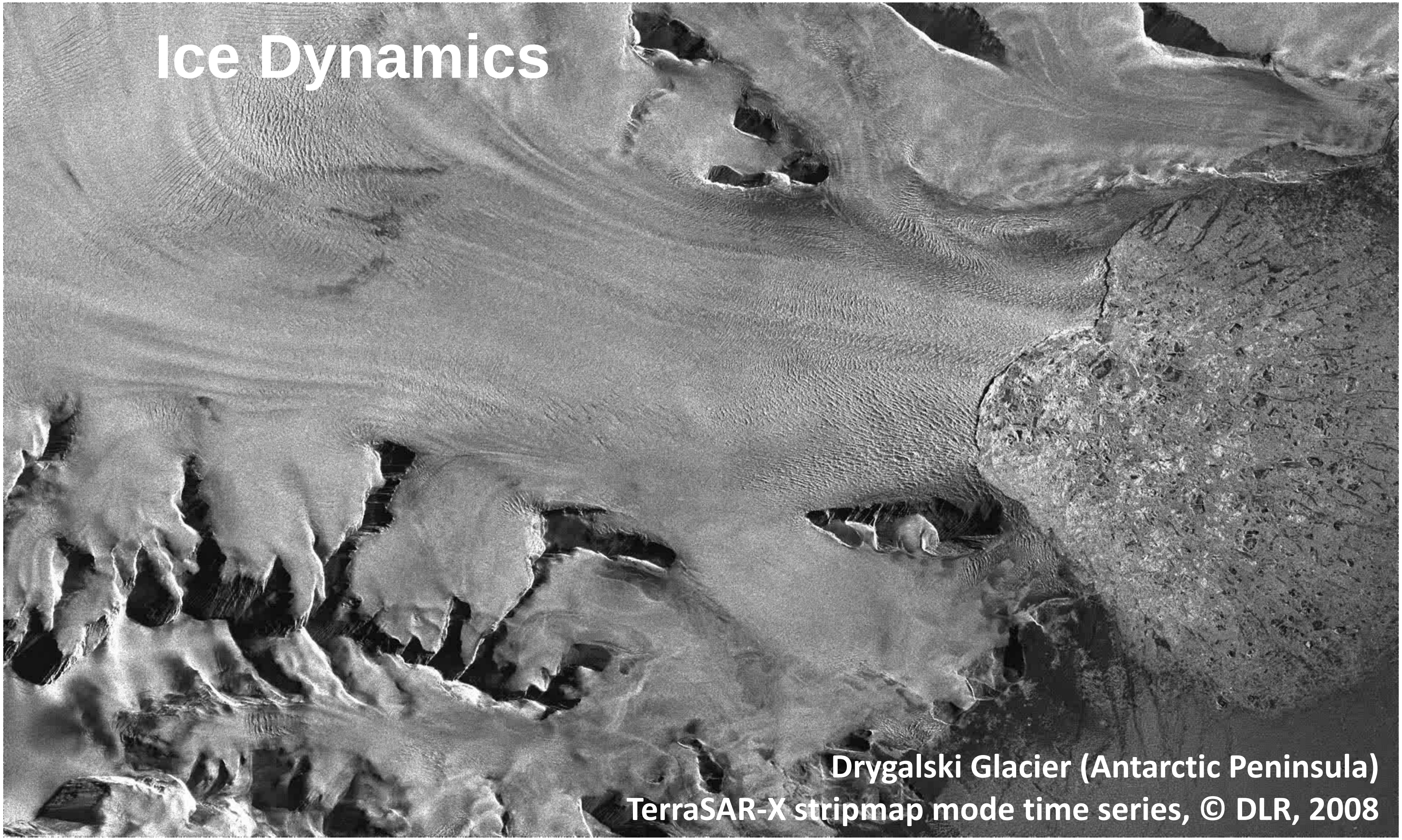

Drygalski Glacier (Antarctic Peninsula)
TerraSAR-X stripmap mode time series, © DLR, 2008

Fast Flowing Glaciers, repeated TerraSAR-X Acquisitions for Bombardie-Dinsmoor-Edgeworth Glaciers, Antarctic Peninsula

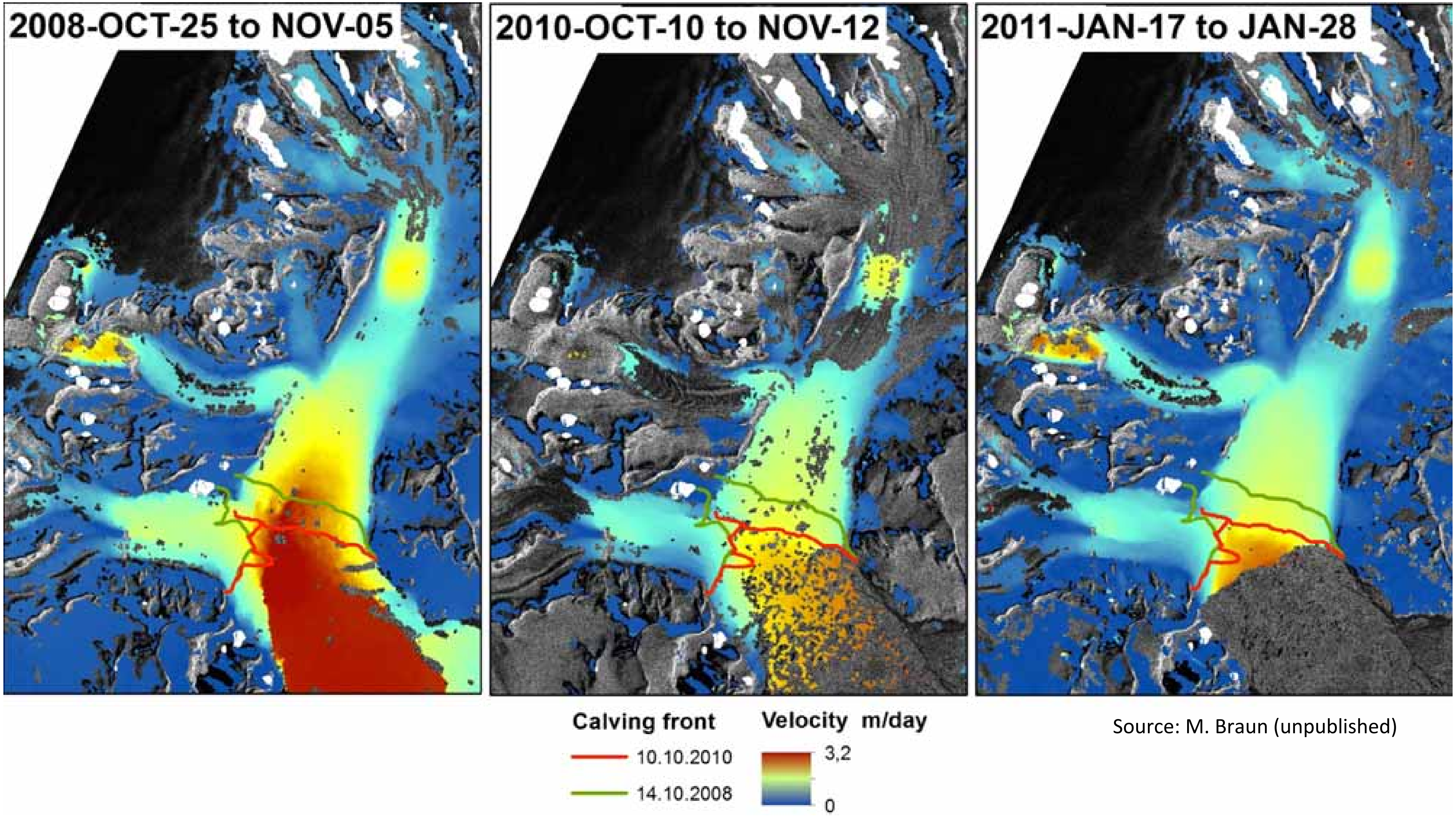

Source: M. Braun (unpublished)

Sea Ice Types

Pancake ice
(http://antarcticfudgesicles.files.wordpress.com)

Frost flowers
(http://www.newscientist.com)

Rafting
(http://www.polartrec.com)

Nilas
(http://www.polartrec.com)

Sea Ice Types & Sizes

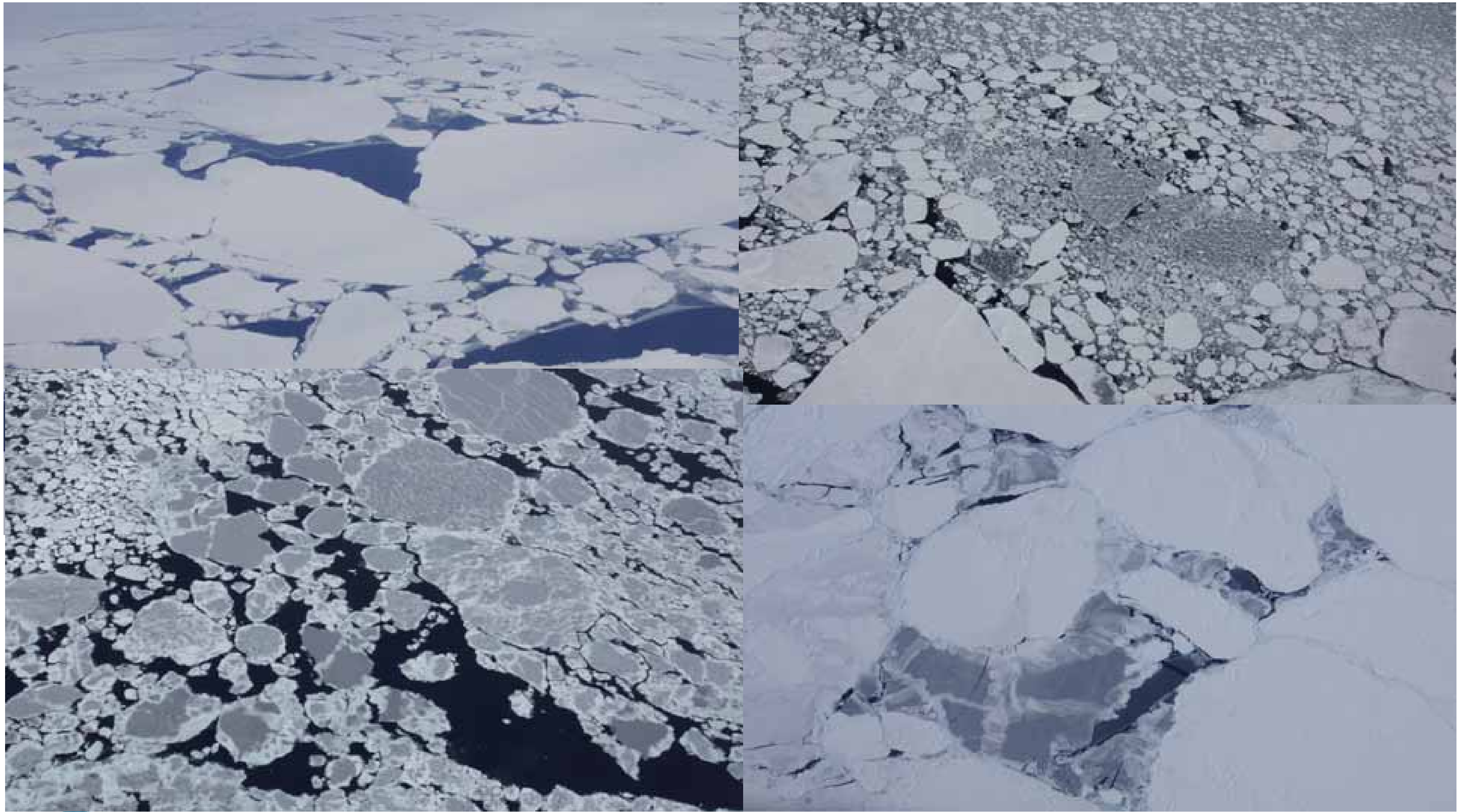

Photos: M. Braun, Bellingshausen Sea, Antarctica

Sea Ice from Multi-frequency SAR

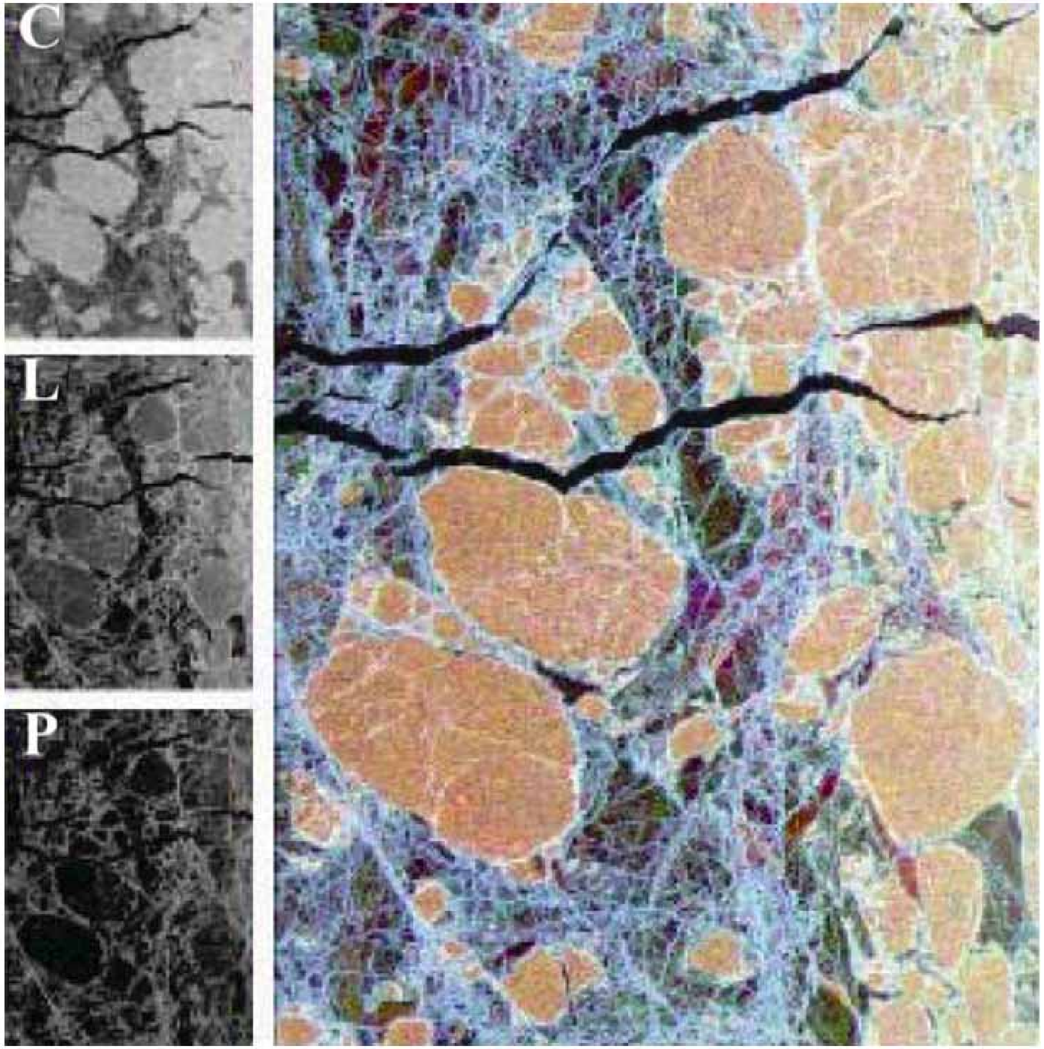

R: C-band
G: L-band
B: P-band

Fig. 6: Scheuchl, B. et al, 2004

SAREDU

Sea Ice from Multi-polarized SAR

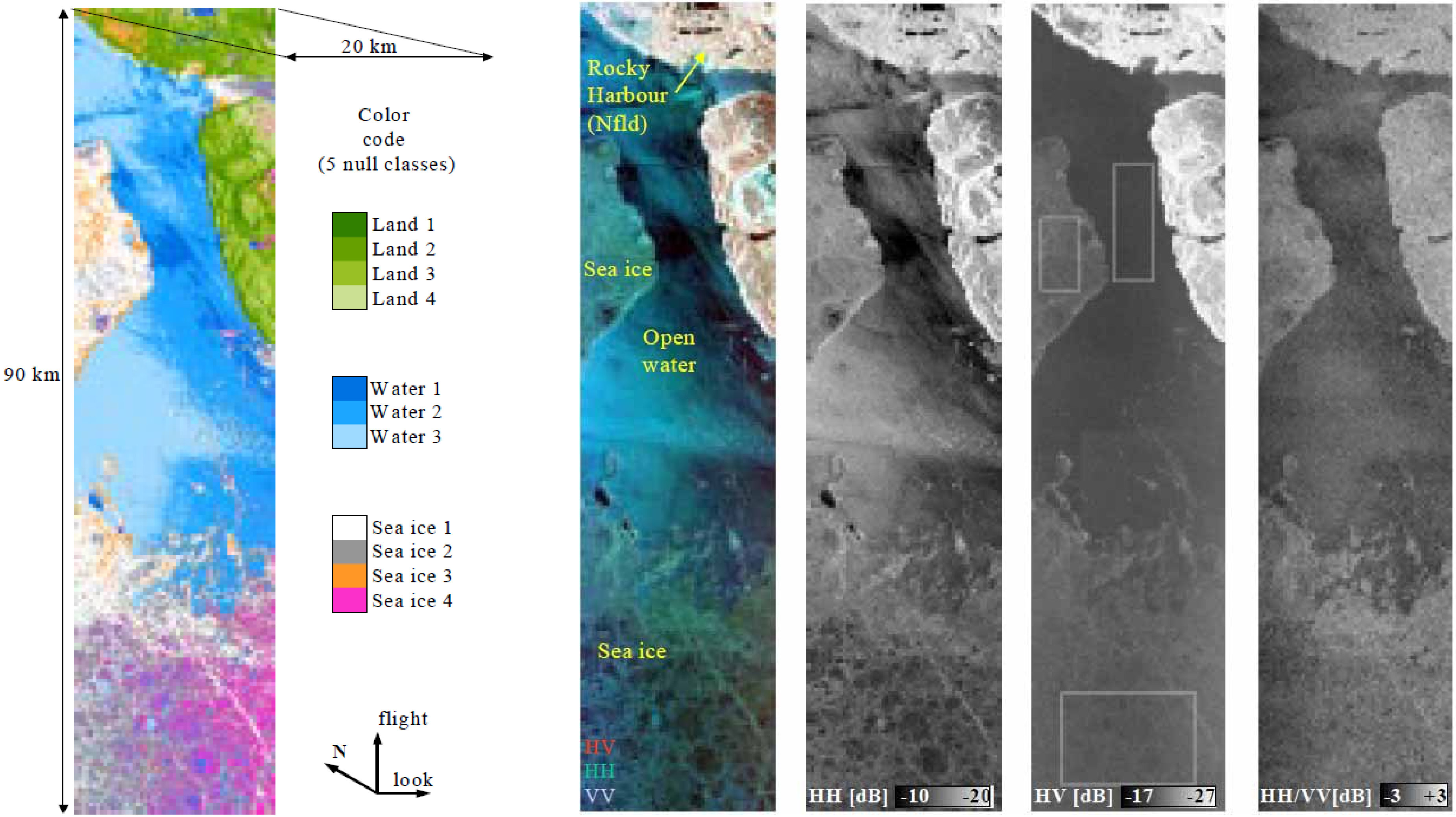

Fig. 7: Scheuchl et al, 2001

SAREDU

Sea Ice Monitoring Svalbard (Norway) VV & VH

Deutsches Zentrum
für Luft- und Raumfahrt e.V.
in der Helmholtz-Gemeinschaft
DLR

FIRST DEMONSTRATION OF SEA-ICE APPLICATIONS WITH SENTINEL-1A DATA

The first Sentinel-1 sea-ice chart

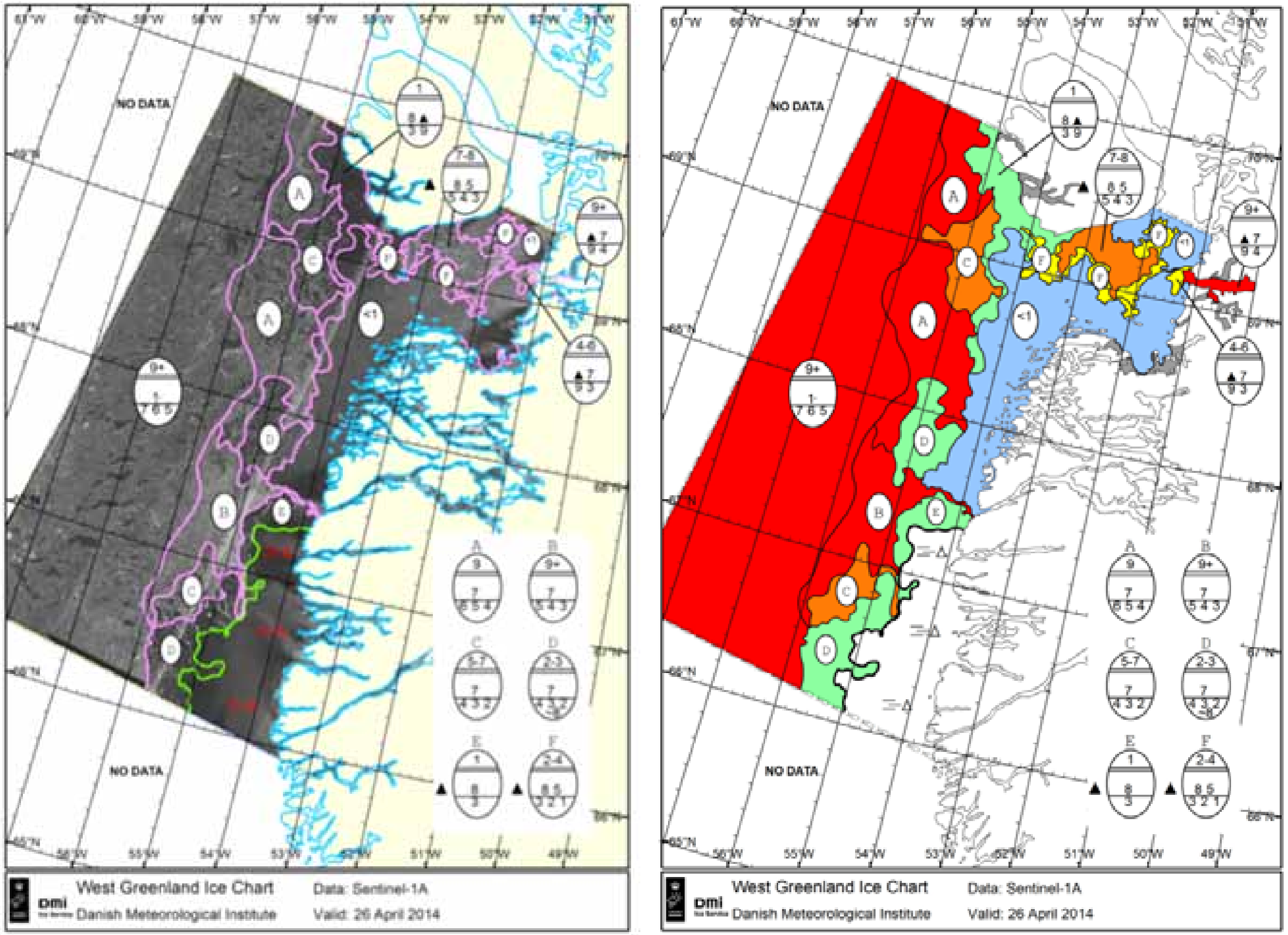

Courtesy of DMI, MyOcean

S1A image20140426 10:10 UTC, EWS, HH

First Greenland Ice Sheet Ice Surface Velocity Map based on Sentinel-1 data

esa

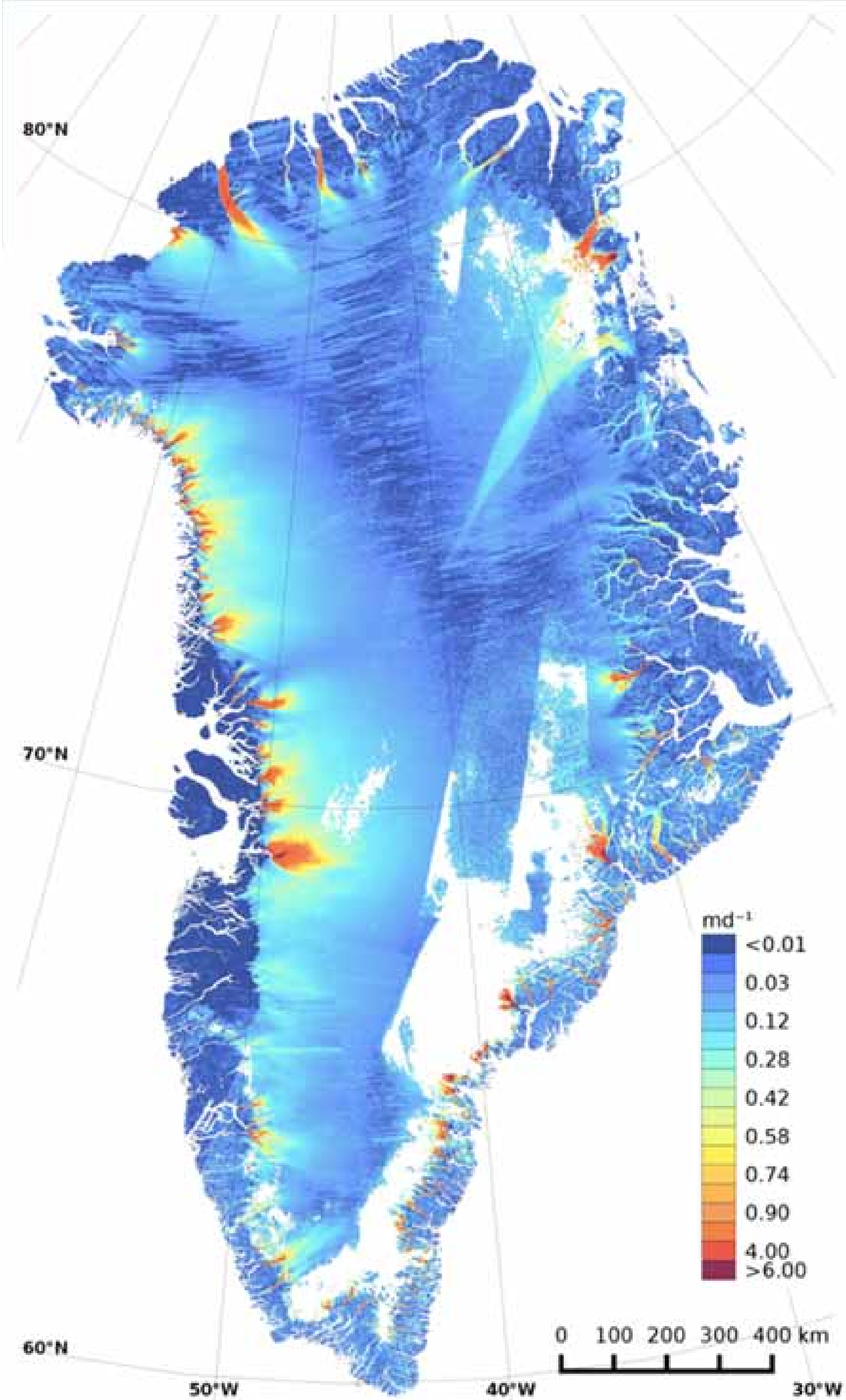

Based on SLC products from Sentinel-1 Interferometric Wide Swath mode

Period: Jan-Mar 2015
(some scenes from Oct-Dec 2014)

~ 800 scenes
~ 25 000 bursts
~ 2.7 TB of SLC data

Offset tracking technique

Courtesy ENVEO IT Gmbh / ESA CCI Ice Sheets Project

European Space Agency

Arctic multi-year sea ice cover after 2007 minimum

a) Arctic sea ice coverage from QuikSCAT (Nov. 15, 2007)
b) RADARSAT (Dec. 01, 2007)
c,d) RADARSAT-1 mosaics of respective day
© CSA, 2011

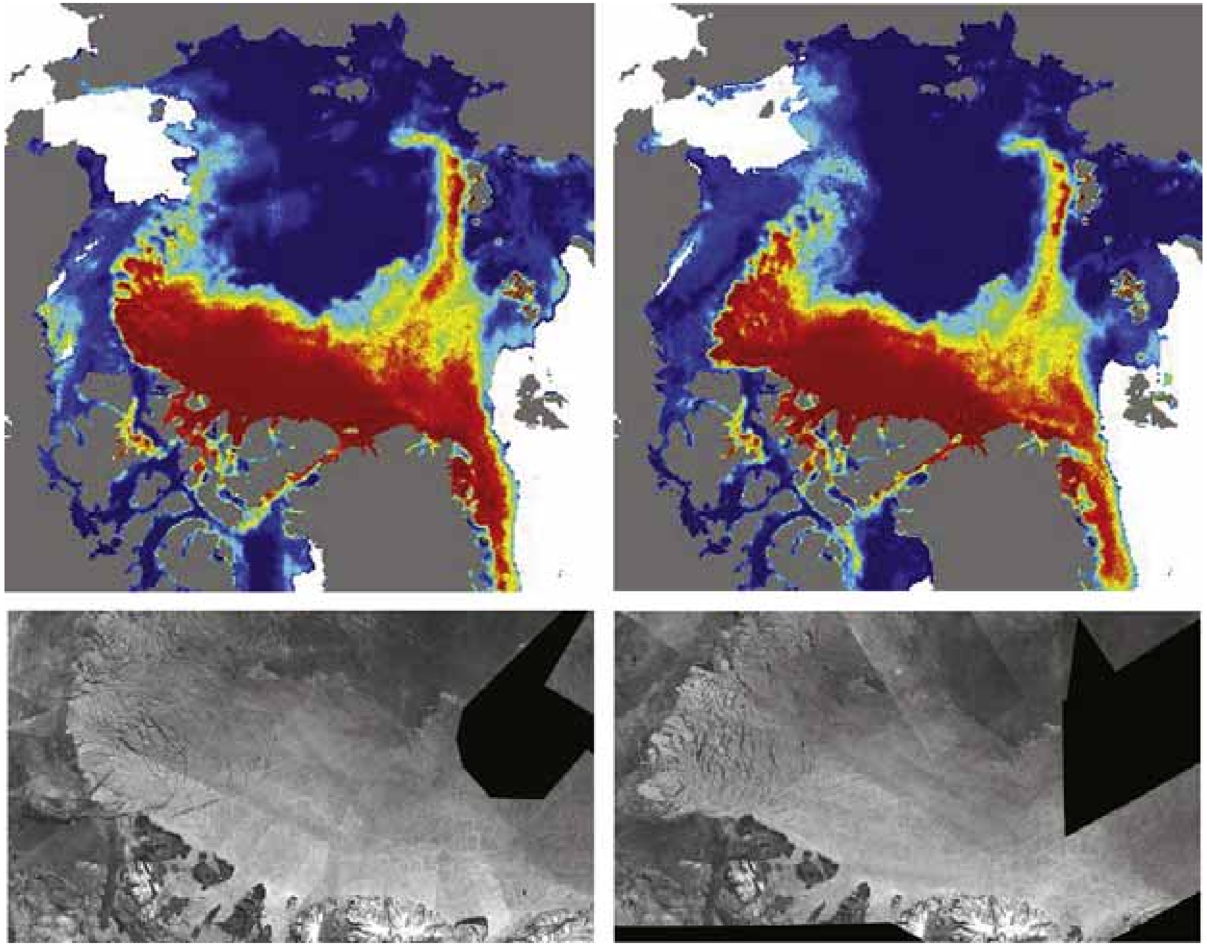

Fig. 11: Kwok & Cunningham, 2012, © CSA, 2011

Relevance

Circum-Arctic distribution of terrestrial and submarine permafrost

About 25% of the northern hemisphere (23 Mio km²)

Fig. 1: Forbes, 2011

Melt-freeze detection with SAR

- Temporal edge detection technique:

  Maximizing the convolution of backscatter time-series ($\sigma^0(t)$) and first derivative of a Gaussian distribution ($\phi(x)$):

$$max\left[\int_{-\infty}^{\infty}\phi(x)\sigma^0(t-x)dx\right]$$

  The max. value indicates the major edge of the time series and corresponding spring transition

Fig. 3: Temporal edge detection technique (Park et al., 2011)

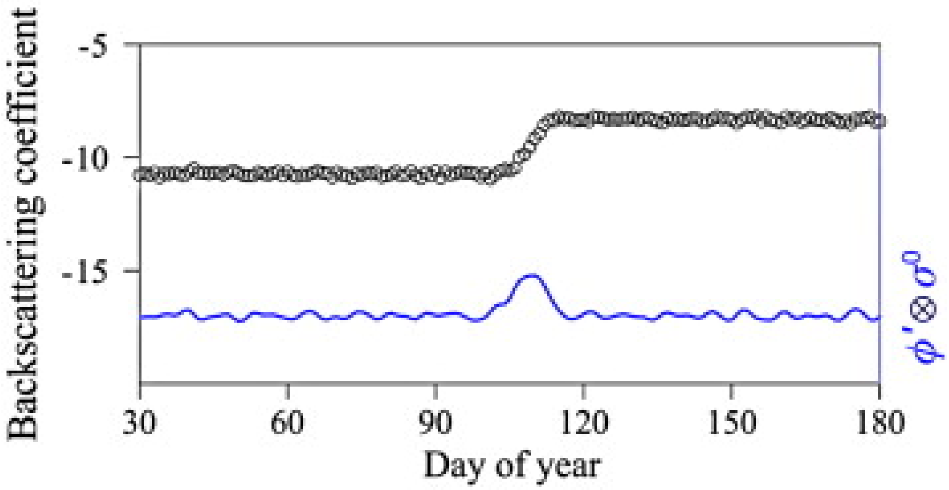

Melt-freeze detection with SAR

Piecewise functions for melt-freeze onset

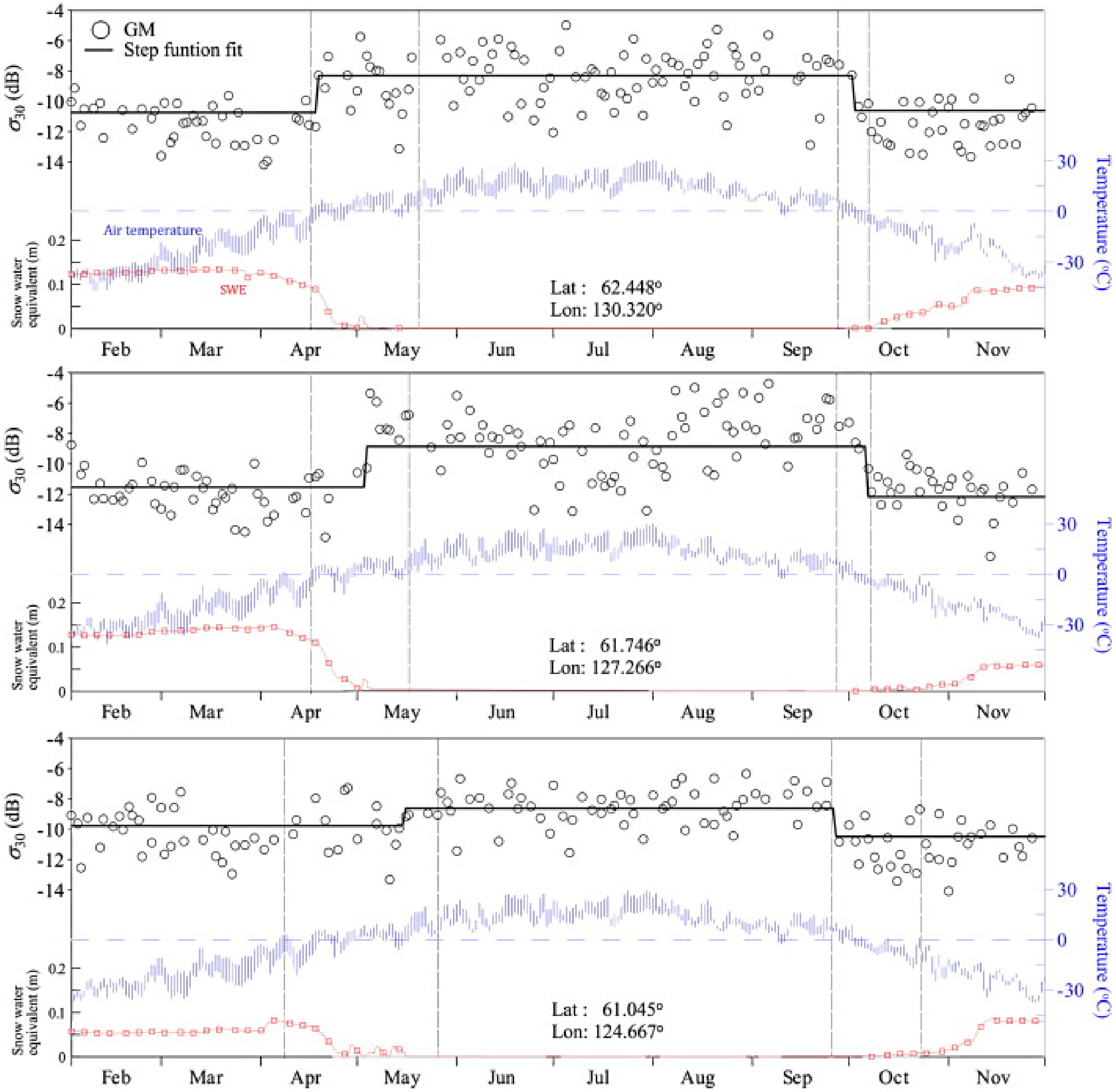

Fig. 6: Park et al., 2011

Melt-freeze detection with SAR

A) spring thaw

B) autumn freeze-up

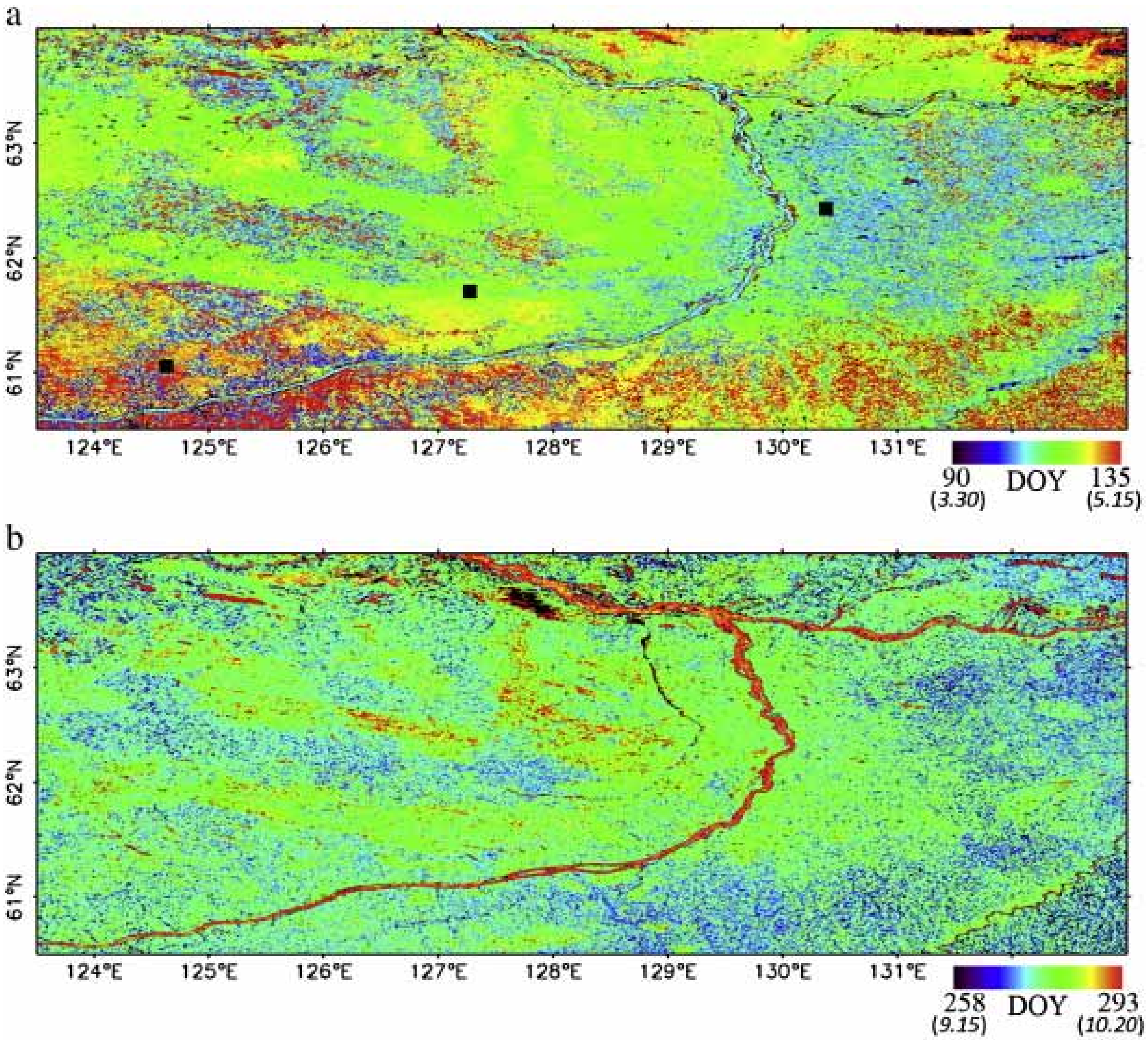

Fig. 5: Park et al., 2011

Subsidence due to Active Layer Drainage (DInSAR)

(a) 25 June 1996 and 30 July 1996 and
(b) 18 September 1995 and 23 September 1997.
Negative rates indicate relative Uplift.

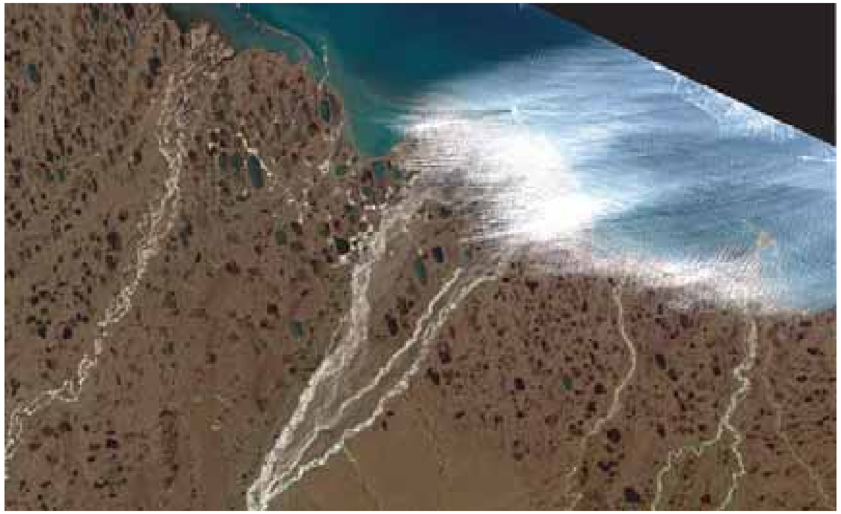

Fig. 11: Liu et al., 2010

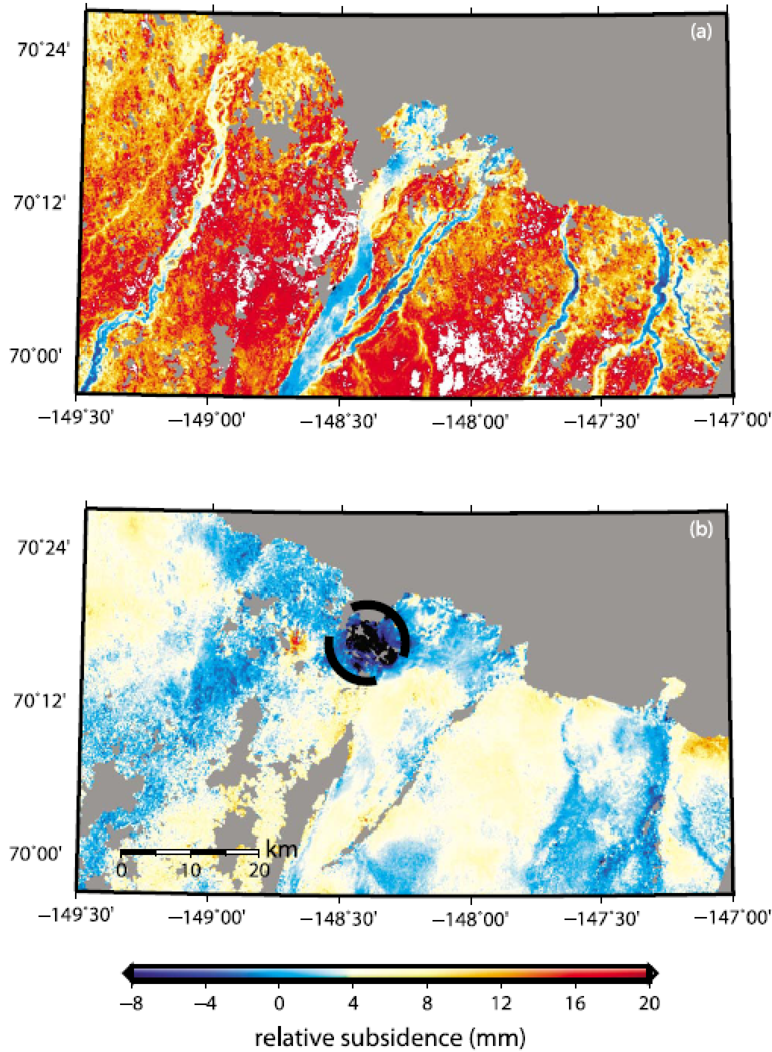

SAREDU

Subsidence due to Active Layer Drainage (DInSAR)

- (a) secular rates in cm/decade and (b) seasonal subsidence in cm within four months.
- Negative rates indicate relative uplift.

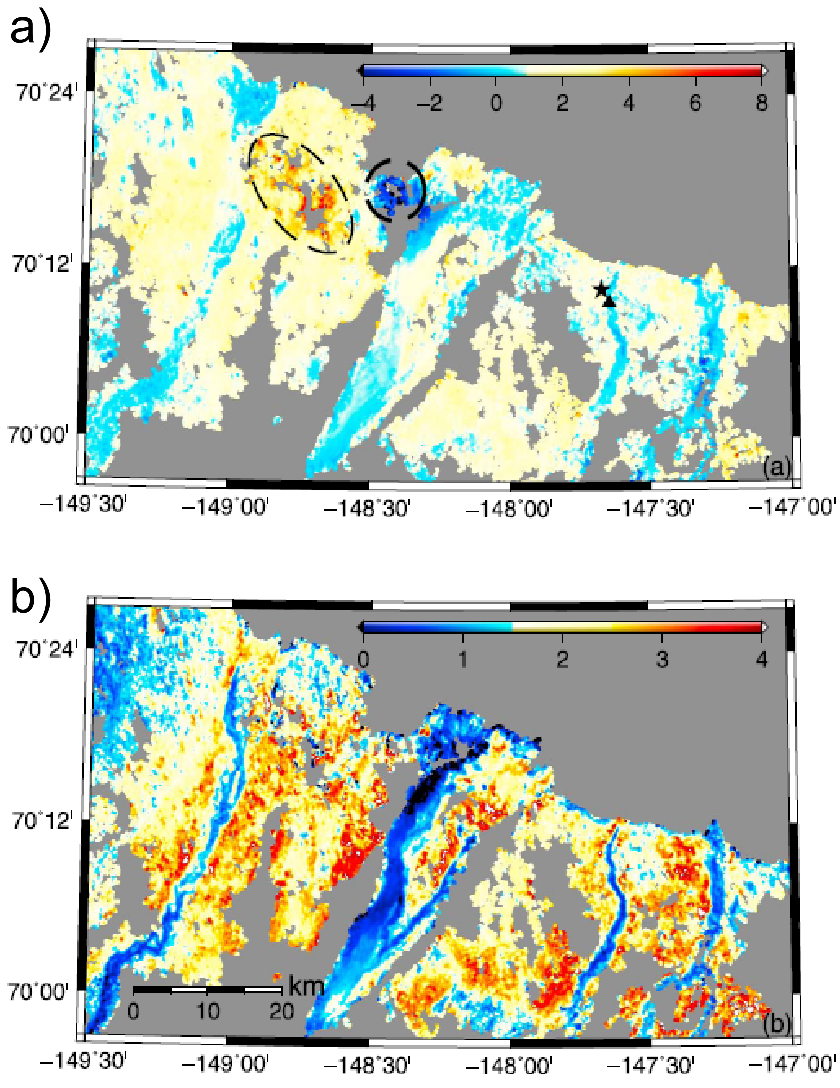

Fig. 12: Liu et al., 2010

Subsidence due to Active Layer Drainage (DInSAR)

- Time series of the differential vertical displacement between a point in the tundra area and one in the floodplain area.

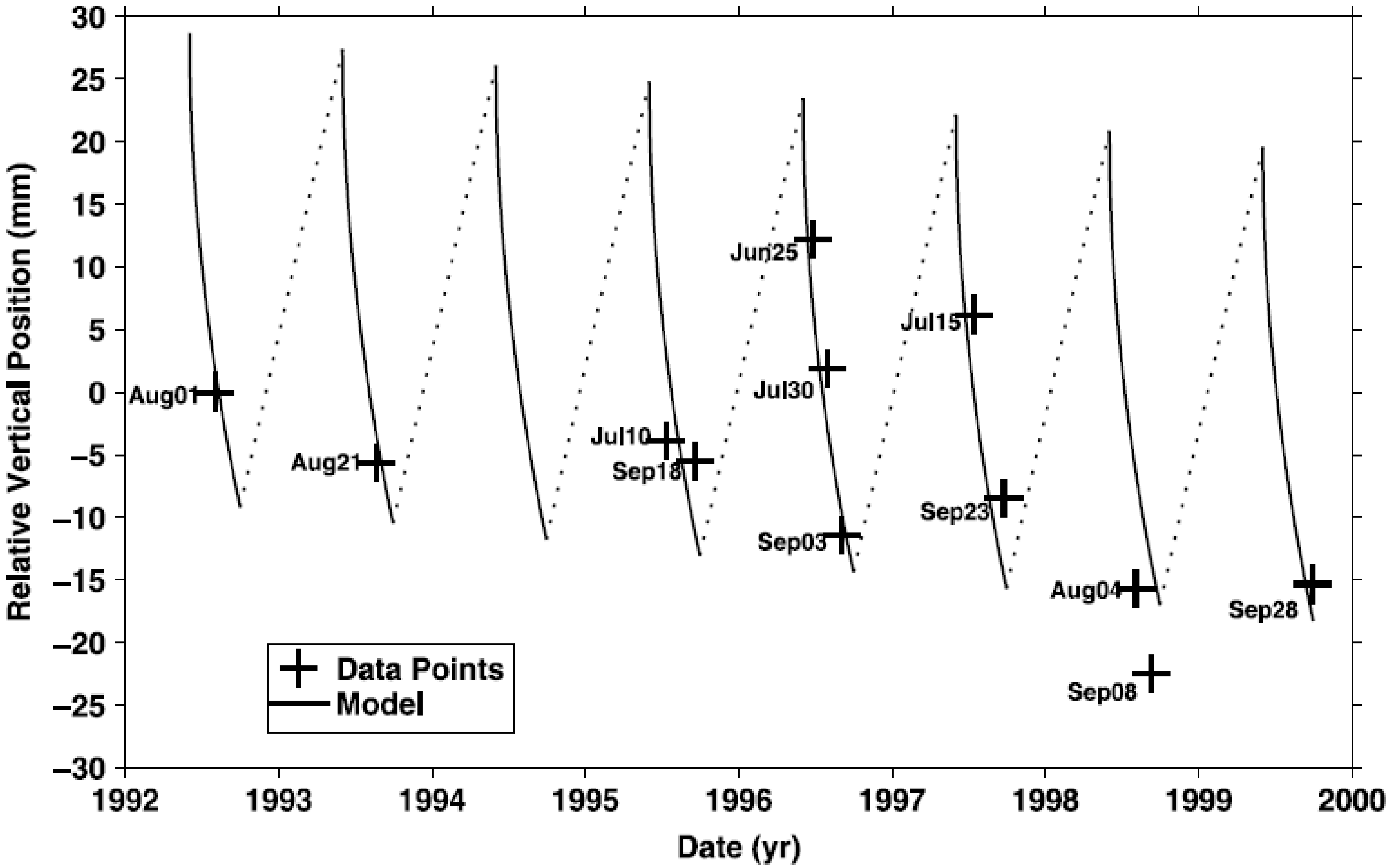

Fig. 13: Liu et al., 2010

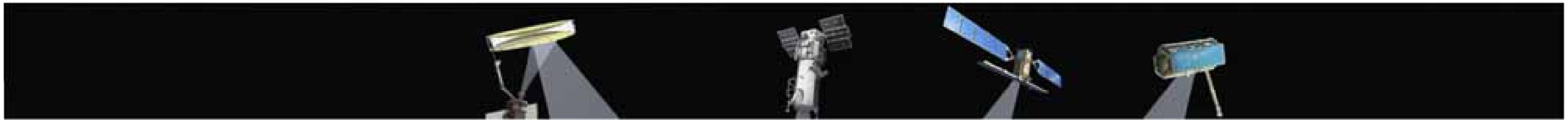

SAR-EDU – SAR Remote Sensing Educational Initiative

https://saredu.dlr.de/

Supported by:

Federal Ministry of Economics and Technology

on the basis of a decision by the German Bundestag